ABSTRACT

Title of Dissertation: ZERO-BIAS CONDUCTANCE PEAKS IN MAJORANA NANOWIRES: THE GOOD, THE BAD, AND THE UGLY

Haining Pan
Doctor of Philosophy, 2022

Dissertation Directed by: Professor Sankar Das Sarma
Department of Physics

Majorana zero modes are neutral zero-energy localized excitations emerging in the low-dimensional condensed matter systems, which are their own antiparticles. These excitations are topological with an intrinsic ground-state degeneracy, belonging to the $(SU_2)_2$ algebra and obeying the non-Abelian anyonic braiding statistics, which provides a possibility to implement the fault-tolerant topological quantum computing. As a result, enormous experimental efforts have focused on the realization of the Majorana zero modes, especially in the one-dimensional semiconductor-superconductor Majorana nanowires during the past decade. Although experiments have observed the zero-bias conductance peaks, these experimentally observed peaks are not robustly quantized as theoretically predicted for the signature of Majorana zero modes, and many other hallmarks of Majorana zero modes are yet to be unambiguously confirmed in experiments, which makes the experimentally observed zero-bias conductance peaks being interpreted as the Majorana zero modes questionable.

Therefore, in this dissertation, we carry out a detailed theoretical analysis of the experimental results, and classify the experimentally observed zero-bias conductance peaks into three types: the good (i.e., the actual topological Majorana zero modes), the bad (i.e., which is the partially-separated quasi-Majorana modes induced by the inhomogeneous potential and quantum dot in the nanowire), and the ugly (i.e., which is the trivial low energy fermionic state induced by random disorder). Our study concludes that almost all the current experimentally observed zero-bias conductance peaks in the publications are the ugly zero-bias conductance peaks, and future experiments should focus on the improvement of the material quality to reduce disorder.

ZERO-BIAS CONDUCTANCE PEAKS IN MAJORANA NANOWIRES: THE GOOD, THE BAD, AND THE UGLY

by

Haining Pan

Dissertation submitted to the Faculty of the Graduate School of the
University of Maryland, College Park in partial fulfillment
of the requirements for the degree of
Doctor of Philosophy
2022

Advisory Committee:
Professor Sankar Das Sarma, Chair/Advisor
Associate Professor Jay Deep Sau
Assistant Professor Alicia Kollár
Associate Professor Maissam Barkeshli
Associate Professor John Cumings

Acknowledgments

I owe my deepest gratitude to my advisor Professor Sankar Das Sarma as a mentor, a scientist, and a philosopher, who has been guiding me, deeply influencing me to reformulate my view on not only physics and academia but also the way to think about things happening every day in real life, which will benefit me for the whole life. My initial contact with him started in March 2017 even before I accepted the offer from the University of Maryland. I boldly sent a cold email to him after viewing the website of the Condensed Matter Theory Center (CMTC) without expecting a reply from a prestigious professor. However, Professor Sankar Das Sarma immediately replied to me with a very friendly email, which made me feel extremely encouraged. This was my first time being impressed by his approachability and responsiveness.

Later I began my first year at the University of Maryland, and I visited his office. As a student who literally knew nothing about condensed matter physics at that time but just had the passion of wanting to work in the field, he did not just open the door of his office and ask me to leave; instead, he introduced me to several research papers, asked me to read and then solve a seemingly-small problem he left to me. After I have produced some results and sent them to him, he responded to me almost immediately, gave me a follow-up question, and asked me if I understand the question. I still remember the time when I expressed confusion, he directly told me to come to the conference room opposite his office, and spent almost the entire afternoon explaining the details and drawing on the blackboard to me, even if I was not his student at that time. I was

both amazed by his wisdom and knowledge from his very fast speech with rigorous logic, and by his patience, when I admitted I did not fully understand what he said. Such experiences happened not once but several times before I became his student. After 8 months of working with him by "solving" the problems he gave to me, I officially became his student, and it turned out that all the seemingly-small problems he gave to me before actually can be integrated into a study on a frontier research problem which later becomes my main research topics in the Ph.D. study, and is also the origin of this dissertation. His role as a successful and professional educator (beyond teaching the mere knowledge of physics) is greatly exemplified by this experience, as he did not simply throw a big problem with unfamiliar languages and complicated math to me. Instead, the way he divided the big problem into multiple small problems, and introduced them, step by step, to me after I finished each one is very efficient and approachable, otherwise I may just be haunted by the monstrous problem in front of me and have nowhere to start.

His teaching to me is not only on physics itself, but also on many things in academia. For example, he taught me the importance of academic integrity just from his answer to one of my very tiny questions. Once I was peer-reviewing a paper that shared similar results with my own paper which was also being peer-reviewed at that time. I asked him whether my decision on this paper would positively or negatively affect the editorial decision of my paper due to the competition. I still remember the reply was that, "This is not the right way to think about writing the referee report, this question itself even should not be asked. The spirit of peer-reviewed paper is absolute neutrality and objectivity, that one should only decide based on the physics in the manuscript— anything other than physics, including connections, friends/foes, or personal interests, is irrelevant."

He also taught and trained me in many "soft skills", such as how to give a vivid and attrac-

tive presentation, which makes it impossible for the audience to wander away; how to explain one's work to a non-expert from another subfield or even non-physicist using simple while profound languages, which extremely benefits me when I tried to introduce my work to other people after a seminar; and the writing skills on how to introduce a large topic top-down, how to explain every important technical details that would otherwise confuse readers, and how to conclude it bottom-up as well as how to extract and emphasize the most eye-catching selling point in the paper.

As I mentioned in the beginning, he is also like a philosopher to me, who always thinks deeply and seriously, and has a unique view of the world. This is because he has particular insight and can directly grasp the essence of a matter. For example, in 2020, I suffered a period of depression and hopelessness about the future due to the pandemic and the politics, so I talked to him. He calmed me down by predicting the future trend and told me what I had been worrying about was very unlikely to happen. I felt much relieved after talking to him, and, amazingly, almost all the predictions he made by his observations on even the tiniest things turned out to be correct (e.g., only from the patterns of COVID cases in different countries over different periods, he predicted the fate the pandemic as early as in June 2020.), which is usually way before other people like the mainstream media begin to realize, and advertise as they find it first. I feel very fortunate for having the opportunity to learn how to think differently and make the correct decision from him by direct witnessing.

It is so fortunate to be mentored by Professor Sankar Das Sarma. He is always supportive in many aspects: the infinite financial support which makes me never need to ever worry about my fellowships, stipends, reimbursements for conferences/workshops/travels/desktop computers/monitors, etc.; the support of the recommendation letter for me to freely apply for any posi-

tions, fellowships, postdocs, internships, and even industry jobs; and the spiritual support when I felt confused and hesitated to make decisions. Not to mention other things like: Driving us to the finest restaurants in DC to have lunches and dinners several times. The free food after the CMTC seminar is always very good; (The foods never let me down, especially compared to those seminars from other places, where usually only sandwiches, and cookies are served and pizza is like the upper bound. Here, at CMTC, pizza is even below the lower bound which we never had—we are always fed with high-standard food, e.g, buffet, barbecue, kebab, lamb, and many other tasty Mexican or Indian dishes that I don't even know their names.) We also had the Nespresso coffee for dozens of flavors for free every day. There are still countless things that I do not have enough space to enumerate unless I am allowed to write a thousand-page dissertation.

I also owe my great gratitude to Janet Das Sarma, who was the official CMTC Administrative Assistant. She was extremely friendly and thoughtful. It is because of her dedication that makes me never have to deal with the administrative and non-academic paperwork by myself. (Actually, I do not even know the complexity behind the paperwork related to the reimbursement/advisor form/travel permission/purchase because of her role until I have to directly do them after Dec. 2019.) Every time she talked to us, I can feel her kindness and caring for us. I still remember that, in the Spring of 2019, when she told me that we would be soon moving to the new office in a new building in August, and I asked her what would the new office be like, she told me that, unlike my current office which was shared by only two people, the new office would be a large one with all the graduate students in it. And I was inadvertently half-joking that "It must be a noisy office to me then because I seem to have misophonia.". I even forgot it after that, but later when we moved to the new office, she told me that she assigned me a desk at the corner of the office, which is the farthest desk in the office from anyone else, simply because she

wanted me to have a quiet workplace as much as possible. I was very touched and grateful for her thoughtfulness at that moment. I still remember many other things that she helped me from things as little as finding a lamp to giving me the choice to customize the specifications when buying a new desktop computer for me. Without her, I cannot be what I am now.

I also want to express my gratitude to my committee members, Professor Alicia Kollár, Professor Maissam Barkeshli, Professor John Cumings, and especially, Professor Jay Deep Sau who spent lots of time discussing with me and answering my technical questions on physics and non-physics things.

CMTC is such a special place that I have benefited a lot from talking to different people, especially the postdocs. I would like to thank Fengcheng Wu for guiding me to a new research area, which otherwise could not have been possible. He is also very knowledgeable with a very solid understanding of condensed matter theory, who has taught me many physical concepts and technical tricks, and is also a very nice man bearing with my ignorant questions. I also would like to thank Chun-Xiao Liu for guiding me on the fundamental concepts in Majorana zero modes in my early stage of academia. I also benefited a lot through the discussions with Rui-Xing Zhang on many physics and non-physics topics, with Xiao Li on the machine learning and many-body localizations, with Dong-Ling Deng on quantum machine learning and the book advice, with Yi-Ting Hsu on machine learning and postdoc advice, and many many other postdocs including Junhyun Lee, William Cole, Shenglong Xu, Yu-An Chen, Jiabin Yu, Yangzhi Chou, Ming Xie, Seongjin Ahn, Shaokai Jian, Shengjie Huang, Xin Wang, Christoper White, Seth David. All these valuable discussions with CTMC postdocs expand my scope and understanding of physics.

I also cannot have an enjoyable time without my friends and colleagues at CMTC including Yingyi Huang, Yi-Hua Lai, Dinhduy Vu, Donovan Buterakos, Ali Lavasani, Benjamin Woods,

Huan-Kwang Wu, Rebecca Cawthorne, Erika Martin, Maya Matava, Nan Zhang, Kwan-Yuet Ho, Shuyang Wang, Kaixin Huang, Haonan Xiong, Fei Wu, Yuxuan Liu, Zhengjing Chu, Weitian Zang, Tianyuan Zhao, Luyan Yu, and many ex-CMTC members including Robert Throckmorton, Tudor Stanescu, Meng Cheng, Qiuzi Li, Fnu Setiawan, Hoi Yin Hui. I also want to express my gratitude to Prof. Na Young Kim who supervised me on the exciton-polariton project, and Prof. Jingbo Wang who supervised me on the quantum walk project.

With the support of Professor Sankar Das Sarma, I was nominated as a graduate fellow at the Kavli Institute of Theoretical Physics in the Spring of 2021. I spent most of my time working with Hassan Shapourian and would like to thank him for bringing me a new research area. I also thank Lars Bilstern, Leon Balents, Matthew Fisher, Sagar Vigay, Cenke Xu, Anthony Zee, Roman Lutchyn, Chetan Nayak, Zhenghan Wang, Zhuxi Luo, Tianci Zhou, Jong Yeon Lee, Mengxing Ye, Grant Remmen, Urban Seifert, Michael Flynn, David Long, Wenping Cui for the personal discussions and making my visit possible.

Finally, I would like to express my gratitude to my mother, Guiqin Zhao, and my father, Dejun Pan, for their nurturing and education, and my uncle, Guiming Zhao, my aunt, Hui Cheng, and my cousin Sinan Zhao for their always support since my childhood.

It is impossible to remember all, and I apologize to those I have inadvertently left out.

Table of Contents

List of Tables

List of Figures

List of Abbreviations

0D	Zero-Dimensional
1D	One-Dimensional
ABS	Andreev Bound State
Al	Aluminum
BCS	Bardeen-Cooper-Schrieffer
BdG	Bogoliubov-de Gennes
InSb	Indium Antimonide
MBS	Majorana Bound State
MZM	Majorana Zero Mode
NS	Normal metal-Superconductor
NbTiN	Niobium-Titanium-Nitride
QD	Quantum Dot
RMT	Random Matrix Theory
SC	Superconductor/Superconductivity/Superconducting
SM	Semiconductor
SOC	Spin-Orbit Coupling/Spin-Orbit Coupled
SSH	Su-Schrieffer-Heeger
TI	Topological Invariant
TQPT	Topological Quantum Phase Transition
TV	Topological Visibility
ZBCP	Zero-Bias Conductance Peak

List of Symbols

P_{tot}	the total fermion parity
P_i	the local fermion parity at Site i
$\|n_1 n_2 \dots n_N\rangle$	the computation basis constructed by the local fermion parity n_i at Site i
U_{ij}	the unitary transformation of braiding two Majorana zero modes, γ_i and γ_j
$\mathcal{U}_{ij}$	the matrix representation of U_{ij} when acting to the computational basis
c_i	the spinless fermionic annihilation operator at Site i in the Kitaev chain
$\tilde{c}_k$	the spinless fermionic annihilation operator at momentum k in the Kitaev chain
H_{SM}	the BdG Hamiltonian for the semiconductor
H_{SC}	the BdG Hamiltonian for the superconductor
$H_{\text{SM-SC}}$	the BdG Hamiltonian for the semiconductor-superconductor coupling
H_{tot}	the BdG Hamiltonian for the total semiconductor-superconductor nanowire
H_{Z}	the BdG Hamiltonian for the Zeeman splitting energy
H_{V}	the BdG Hamiltonian for various effects of disorder and gate potentials
H_0	the BdG Hamiltonian for the minimal model without the self-energy
$H_{0,\text{SE}}$	the BdG Hamiltonian for the minimal model with the self-energy
H_{QD}	the BdG Hamiltonian for a nanowire with a quantum dot without the self -energy
$H_{\text{QD,SE}}$	the BdG Hamiltonian for a nanowire with a quantum dot with the self-energy
H_{inhom}	the BdG Hamiltonian for a nanowire with an inhomogeneous potential without the self-energy
$H_{\text{inhom,SE}}$	the BdG Hamiltonian for a nanowire with an inhomogeneous potential with the self-energy
$H_{\text{disorder},\mu}$	the BdG Hamiltonian for a nanowire in the presence of disorder in μ without the self-energy
$H_{\text{disorder},\mu,\text{SE}}$	the BdG Hamiltonian for a nanowire in the presence of disorder in μ with the self-energy
$H_{\text{disorder},g}$	the BdG Hamiltonian for a nanowire in the presence of disorder in g without the self-energy
$H_{\text{disorder},g,\text{SE}}$	the BdG Hamiltonian for a nanowire in the presence of disorder in g with the self-energy
$H_{\text{disorder},\Delta}$	the BdG Hamiltonian for a nanowire in the presence of disorder in Δ without the self-energy
$H_{\text{disorder},\Delta_0,\text{SE}}$	the BdG Hamiltonian for a nanowire in the presence of disorder in Δ_0 with the self-energy

H_{lead}	the BdG Hamiltonian for the normal lead
G^{R}	the retarded Green's function for the Bogoliubov quasiparticles in the Nambu basis
$\hat{H}_{\text{Kitaev}}$	the second quantized Hamiltonian for the Kitaev chain
$\hat{H}^{\text{BdG}}_{\text{Kitaev}}$	the second quantized BdG Hamiltonian for the Kitaev chain
$\hat{\mathcal{H}}^{\text{BdG}}_{\text{Kitaev}}$	the second quantized BdG Hamiltonian for the Kitaev chain without a constant shift
$\hat{H}^{\text{M}}_{\text{Kitaev}}$	the second quantized Hamiltonian for the Kitaev chain in the Majorana basis
$\hat{H}_{\text{NW}}$	the second quantized Hamiltonian for the SM-SC nanowire
$\hat{H}_{\text{SM}}$	the second quantized Hamiltonian for the semiconductor
$\hat{H}_{\text{SC}}$	the second quantized Hamiltonian for the superconductor
$\hat{H}_{\text{SM-SC}}$	the second quantized Hamiltonian for the semiconductor-superconductor coupling
$\hat{H}_{\text{tot}}$	the second quantized Hamiltonian for the total semiconductor-superconductor nanowire
$\hat{H}_{\text{Z}}$	the second quantized Hamiltonian for the Zeeman splitting energy
$\hat{H}_{\text{V}}$	the second quantized Hamiltonian for various effects of disorder and gate potentials
$\hat{H}_0$	the second quantized BdG Hamiltonian for the minimal nanowire model
h	Planck constant
$\hbar$	reduced Planck constant
V_{Z}	Zeeman field
$V_{\text{Z}c}$	the critical Zeeman field of the collapse of the bulk superconducting gap
μ_B	Bohr magneton
B	the magnetic field along the nanowire
g	the effective Landé g factor in the nanowire
α	the strength of Rashba-type spin-orbit coupling
μ	the chemical potential in the semiconductor
Δ	the proximitized superconducting gap in the semiconductor
Δ_0	the superconducting bulk gap in the superconductor
γ	the effective semiconductor-superconductor coupling (tunneling) strength
$\vec{\boldsymbol{\sigma}}$	components of the Pauli matrices $(\sigma_x, \sigma_y, \sigma_z)$ acting on the spin space
$\vec{\boldsymbol{\tau}}$	x, y, z components of the Pauli matrices (τ_x, τ_y, τ_z) acting on the particle-hole space
m^*	the effective mass in the semiconductor
m_e	the electron rest mass
L	the length of the nanowire
$\Sigma(\omega)$	the self-energy term of the superconductor at energy ω
$V(x)$	the position (x) dependent potential
$V_{\text{imp}}(x)$	the position (x) dependent random potential
η	the positive infinitesimal in the retarded Green's function
V_{D}	the peak of the quantum dot barrier
l	the length of the quantum dot
V_{max}	the height of the confining inhomogeneous potential
σ	the linewidth of the confining inhomogeneous potential

σ_μ	the standard deviation of normally distributed random potential
σ_g	the standard deviation of normally distributed Landé g factor
σ_Δ	the standard deviation of normally distributed proximitized superconducting gap
σ_{Δ_0}	the standard deviation of normally distributed bulk parent superconducting gap
$\mathcal{N}(\mu, \sigma^2)$	the Gaussian distribution with the mean of μ, and the variance of σ^2
$G(V)$	the differential conductance at a bias voltage V
μ_{lead}	the chemical potential in the lead
V_{bias}	the bias voltage
T	temperature
Γ	dissipation
$\hat{\Psi}(x)$	the position-dependent spinor in Nambu basis
$\hat{\psi}_s(x)$	the annihilation operator to annihilate an electron of spin s at x
$\hat{\gamma}_s(x), \hat{\bar{\gamma}}_s(x)$	the Majorana operators to create a Majorana zero mode at x
$\Psi_{E_n}(s, \tau, i)$	the Nambu basis (with s and τ) wave function at Site i for a state with the energy of E_n
$\gamma_n(s, i), \bar{\gamma}_n(s, i)$	the Majorana representation wave function at Site i with spin s for a state with E_n
$\lvert\gamma_n(i)\rvert^2, \lvert\bar{\gamma}_n(i)\rvert^2$	spin-averaged density of Majorana representation wave function at Site i for a state with E_n
E_n	the corresponding energy of nth state in the nanowire
$\mathcal{S}$	S matrix
S_{LL}	the reflection matrix on the left end
S_{RR}	the reflection matrix on the right end
S_{LR}	the transmission matrix from the right to the left end
S_{RL}	the transmission matrix from the left to the right end
$S_{ij}^{\alpha\beta}$	the reflection or transmission matrix from type β to type α
δx	the lattice constant of the tight-binding Hamiltonian
$\mathcal{G}$	the differential conductance matrix
G_{LL}	the local conductance measured from the left end
G_{RR}	the local conductance measured from the right end
G_{LR}	the nonlocal conductance measured from the right to the left end
G_{RL}	the nonlocal conductance measured from the left to the right end
$V_{\text{bias,L}}$	the bias voltage on the left lead
$V_{\text{bias,R}}$	the bias voltage on the right lead
I_{L}	the current entering the left lead from the scattering region
I_{R}	the current entering the right lead from the scattering region
N_i	the number of electron modes in Lead i
$\mathcal{T}_{ij}^{\alpha\beta}$	transmission from Lead j with type β to Lead i with type α

κ	the thermal conductance
κ_0	the quantized thermal conductance
k_{B}	Boltzmann constant
V_g	the tunnel barrier height
V_{TG}	the voltage of the tunnel gate
Γ_n	the tunneling probability of mode n in the lead in the RMT
M	the number of states in the quantum dots in the RMT
N	the number of channels in the normal lead in the RMT
w_n	the coupling strength between the normal lead and class D quantum dot in the RMT
$\mathcal{H}$	the Hamiltonian of the class D random quantum dot in the Majorana basis in the RMT
$\mathcal{W}$	the tunneling matrix in the RMT
δ_0	the average energy-level spacing in the class D quantum dot in the RMT

Chapter 1: Introduction

Over the past 40 years, the topological phenomena have been among the most active research areas in condensed matter physics since the discovery of the quantum Hall effects in the 1980s [1, 2]. These pioneering experiments on quantum Hall effects are spectacular as the experimental measurements of the Hall conductance in units of e^2/h are so precise that they have now become the definition of the official resistance standard to define the "Ohm". This is due to a robust topological effect, where the quantization of Hall conductance is protected by a topological gap in the bulk of the sample along with a gapless edge mode on the boundary of the sample. The reason for the robustness of Hall conductance (i.e., against ubiquitous disorder in the sample) is the large topological gap, because, in general, the larger topological gap provides the better topological protection, and thus more robust and precise quantization— the same reason for that integer quantum Hall effect has better quantization than the fractional quantum Hall effect. Due to the large bulk gap in the quantum Hall effect, the topological theoretical understanding was developed after the experimental discoveries, which is to say, the quantum Hall effect was not a theoretical prediction but an experimentally discovered phenomenon from 1980 to 1982.

By contrast, although the discoveries of quantum Hall effects heralded the blossom of the theory of the topological phases and matters, the topological theoretical predictions have dominated condensed matter physics during the last 20 years with the worldwide extensive experi-

mental search for the specific theoretical predictions of quantization effects. Such well-known predictions being studied experimentally are, for instance, quantum spin Hall effect [3], topological insulator [4], quantum anomalous Hall effect [5], non-Abelian braiding [6], Kitaev spin liquid [7], Majorana zero mode (MZM) [8, 9]. Many of these theoretical predictions have the precise conductance quantization protected by an energy gap in the topological phase, such as the quantum spin Hall effect, quantum anomalous Hall effect, and MZM, or quantization in the electromagnetic and thermal response, such as topological insulator and Kitaev spin liquid. Despite being rigorous and precise in theory, these predictions unwittingly lead to a serious problem in experiments, the potential confirmation bias, where one tends to "verify" the known theoretical prediction through fine-tunings and data selection in experiments. This is particularly problematic for the topological discoveries because (1) the experimental samples are usually complicated, stacked with multiple layers of different materials, which also have the unique and unintentional disorder from sample to sample; (2) the topology, usually theoretically studied in the thermodynamic limit or at zero temperature and zero dissipation, can apply only when the sample size (temperature or dissipation) exceeds (is below) a certain characteristic topological length (the topological gap). Therefore, this leads to the considerable leeway to generously explain the deviation in the experimental observation from the theoretical prediction of the "quantization" as arising from the finite size effect, finite temperature, or finite dissipation.

In this dissertation, we will specifically focus on the experimental observations in the recent experiments pursuing the MZMs, where our theoretical studies classify all experimental observations of zero-bias conductance peaks (ZBCP) into three types— the good, the bad, and the ugly. But before we delve into the experimental and theoretical details, we would like to first clarify the motivation of why we care about whether the MZMs have been confirmed in the first place.

1.1 Topological quantum computing

The Majorana zero mode originates from the Majorana fermion, which was first postulated by Ettore Majorana in 1937 [10] as a real solution to the Dirac equation, describing a charge-neutral fermion being its own antiparticle. Since then, enormous efforts in high-energy physics have worked on the search for the Majorana fermion, especially in determining whether neutrinos are Majorana fermions [11, 12]. However, in condensed matter physics, we do not have neutrinos but only electrons (holes). Therefore, the Majorana fermion, besides being a fundamental particle in high-energy physics, can only exist in condensed matter as a quasiparticle, which is an equal superposition of electron and hole excitations. Rigorously speaking, because these Majorana fermions in the context of condensed matter physics are not fermions since their exchange statistics are anyonic other than fermionic; we refer to them as the MZMs in this dissertation to avoid the confusion with the Majorana fermions in high energy physics.

Besides the fundamental interest in a particle of its own antiparticle, one of the most attractive aspects of the MZMs lies in the potential application to the topological quantum computing, which is an intrinsically fault-tolerant quantum computing, due to its non-Abelian anyonic braiding statistics [13–16]. Therefore, it is worth first introducing topological quantum computing using MZMs.

We start with the definition of the Majorana operators in terms of the fermionic operator as per

$$\gamma = c^\dagger + c, \quad \bar{\gamma} = i\left(c - c^\dagger\right), \tag{1.1}$$

which are manifestly self-adjoint, i.e., $\gamma = \gamma^\dagger$ and $\bar{\gamma} = \bar{\gamma}^\dagger$. Equation (1.1) states that the Majorana

operator creates a quasiparticle which is the equal superposition of "electron" and "hole", and different Majorana operators (e.g., on different sites) anticommute with each other.

1.1.1 Fermion parity as qubits

To implement quantum computing, we first need to encode information into the physical system in some way. Thus, we consider N pairs of MZMs in a chain

$$\gamma_1\ \bar{\gamma}_1\ \gamma_2\ \bar{\gamma}_2\ \cdots\ \gamma_{N-1}\ \bar{\gamma}_{N-1}\ \gamma_N\ \bar{\gamma}_N. \tag{1.2}$$

Since each Majorana γ_i is a zero-energy excitation, a chain composed of N pairs of MZMs forms a ground state manifold with the degeneracy of 2^N. For each pair of MZMs γ_i and $\bar{\gamma}_i$, we define the fermion parity operator as per

$$P_i = i\gamma_i\bar{\gamma}_i, \tag{1.3}$$

whose eigenstates are the two degenerate ground states with eigenvalues $+1$ and -1 with the even and odd parity, denoted by $|0\rangle$ and $|1\rangle$. By generalizing the single pair of MZMs to N pairs of MZMs, we can construct the computational basis in the Hilbert space of the set of N pairs of MZMs as $|n_1 n_2 \ldots n_N\rangle$, where $n_i = 0$ ($n_i = 1$) indicates the i-th fermionic site is empty (occupied). It is easy to verify that the computational basis is not only the eigenstate of the local fermion parity at each site P_i but also of the total parity $P_{\text{tot}} = \prod_{i=1}^{N} P_i$. Therefore, the whole Hilbert space is decomposed into two orthogonal subspaces depending on the total parity, which reduces the number of accessible computation basis from 2^N to 2^{N-1} for N pairs of MZMs. Namely, for N pairs of MZMs, we can express any state $|a\rangle$ in the Hilbert space spanned by the

computation basis with a definite total fermion parity as

$$|a\rangle = \sum_{\substack{\{n_i\}=\{0,1\} \\ \text{subject to } \sum n_i = \text{even or odd}}} \alpha_{n_1,n_2,\ldots,n_N} |n_1 n_2 \ldots n_N\rangle , \tag{1.4}$$

where n_i can be viewed as the topological qubit on each site.

1.1.2 Braiding as gate operations

After encoding the information using the local fermion parity of MZMs as the topological qubit, the next step is to manipulate the qubits to perform logic gates. Therefore, we exchange two MZMs (i.e., braiding), which eventually leads to nontrivial operations acting on the topological qubits.

We first consider the exchange of two MZMs, γ_i and γ_j ($\bar{\gamma}_j$ will also work following the same steps). Considering a dynamic process where we slowly drag the first MZM γ_i around the other MZM γ_j along a complete closed trajectory containing γ_j in a two-dimensional plane, and return them to the initial stage, due to the adiabatic theorem, we will have the final state still lying in the ground state manifold. Therefore, we can explicitly write down the unitary transformation U connecting the initial state and final state, $|\Psi\rangle \mapsto U|\Psi\rangle$, by reasonably assuming (1) it only involves the two exchanged MZMs γ_i and γ_j; (2) the adiabatic process is slow enough to preserve the total parity throughout the exchange. Given these two assumptions, the unitary matrix takes the form of

$$U_{ij} \equiv \exp(\beta\gamma_i\gamma_j) = \cos(\beta) + \sin(\beta)\gamma_i\gamma_j, \tag{1.5}$$

up to an overall U(1) phase factor. Here β is a real parameter, which can be determined in the

Heisenberg picture of the Majorana operator, i.e.,

$$\begin{aligned}\gamma_i &\mapsto U\gamma_i U^\dagger = \cos(2\beta)\gamma_i - \sin(2\beta)\gamma_j \\ \gamma_j &\mapsto U\gamma_j U^\dagger = \cos(2\beta)\gamma_j + \sin(2\beta)\gamma_i.\end{aligned} \tag{1.6}$$

Since we have exchanged γ_i and γ_j through braiding, the final state should have γ_j at the position where it was originally γ_i and vice versa, which gives $\beta = \pm\frac{\pi}{4}$. (The two signs can be thought of as the clockwise and counterclockwise exchange, which we can choose the $+$ sign as a convention in the following results.) Finally, we can write the unitary operator for the braiding of two MZMs γ_i and γ_j as

$$U_{ij} = \exp\Big(\frac{\pi}{4}\gamma_i\gamma_j\Big). \tag{1.7}$$

To illustrate the non-Abelian statistics of MZMs, we study a chain of four MZMs denoted by

$$\gamma_1 \ \bar{\gamma}_2 \ \gamma_2 \ \bar{\gamma}_2 \tag{1.8}$$

with the two computational basis in the odd parity (the same result for the even parity)

$$\begin{aligned}|0\rangle &= |n_1 = 1; n_2 = 0\rangle = c_1^\dagger \,|\text{vac}\rangle \\ |1\rangle &= |n_1 = 0; n_2 = 1\rangle = c_2^\dagger \,|\text{vac}\rangle\,,\end{aligned} \tag{1.9}$$

where $|\text{vac}\rangle$ denotes the vacuum state with zero fermion.

We first consider the braiding of the first pair of MZMs, γ_1 and$\bar{\gamma}_1$. By applying the unitary

operators $U_{1\bar{1}}$ to the two basis, we obtain

$$\begin{aligned} U_{1\bar{1}} \left|0\right\rangle &= \exp\Big(\frac{\pi}{4}\gamma_1\bar{\gamma}_1\Big)c_1^\dagger \left|\text{vac}\right\rangle = e^{i\frac{\pi}{4}} \left|0\right\rangle, \\ U_{1\bar{1}} \left|1\right\rangle &= \exp\Big(\frac{\pi}{4}\gamma_1\bar{\gamma}_1\Big)c_2^\dagger \left|\text{vac}\right\rangle = e^{-i\frac{\pi}{4}} \left|1\right\rangle. \end{aligned} \tag{1.10}$$

Therefore, the braiding of γ_1 and $\bar{\gamma}_1$ effectively performs the gate operation of

$$\mathcal{U}_{1\bar{1}} = \begin{pmatrix} e^{i\frac{\pi}{4}} & 0 \\ 0 & e^{-i\frac{\pi}{4}} \end{pmatrix}, \tag{1.11}$$

when acting on the basis $\{\left|0\right\rangle, \left|1\right\rangle\}$.

Similarly, the final state after braiding the last two MZMs, γ_2 and $\bar{\gamma}_2$, can be calculated as per

$$\begin{aligned} U_{2\bar{2}} \left|0\right\rangle &= \exp\Big(\frac{\pi}{4}\gamma_2\bar{\gamma}_2\Big)c_1^\dagger \left|\text{vac}\right\rangle = e^{-i\frac{\pi}{4}} \left|0\right\rangle, \\ U_{2\bar{2}} \left|1\right\rangle &= \exp\Big(\frac{\pi}{4}\gamma_2\bar{\gamma}_2\Big)c_2^\dagger \left|\text{vac}\right\rangle = e^{i\frac{\pi}{4}} \left|1\right\rangle, \end{aligned} \tag{1.12}$$

which also gives an effective gate operation as per

$$\mathcal{U}_{2\bar{2}} = \begin{pmatrix} e^{-i\frac{\pi}{4}} & 0 \\ 0 & e^{i\frac{\pi}{4}} \end{pmatrix}. \tag{1.13}$$

Both $\mathcal{U}_{1\bar{1}}$ and $\mathcal{U}_{2\bar{2}}$ act trivially on $\left|0\right\rangle$ and $\left|1\right\rangle$ by adding an additional phase factor to each basis.

However, a nontrivial process happens when we braid the middle two MZMs, $\bar{\gamma}_1$ and γ_2,

where the final state becomes

$$
\begin{aligned}
U_{\bar{1}2}\left|0\right\rangle &= \exp\Big(\frac{\pi}{4}\bar{\gamma}_1\gamma_2\Big)c_1^\dagger\left|\text{vac}\right\rangle = \frac{1}{\sqrt{2}}\left(c_1^\dagger - ic_2^\dagger\right)\left|\text{vac}\right\rangle, \\
U_{\bar{1}2}\left|1\right\rangle &= \exp\Big(\frac{\pi}{4}\bar{\gamma}_1\gamma_2\Big)c_2^\dagger\left|\text{vac}\right\rangle = \frac{1}{\sqrt{2}}\left(-ic_1^\dagger + c_2^\dagger\right)\left|\text{vac}\right\rangle.
\end{aligned}
\tag{1.14}
$$

Therefore, the gate operation of braiding the middle two MZMs is

$$
\mathcal{U}_{\bar{1}2} = \frac{1}{\sqrt{2}}\begin{pmatrix} 1 & -i \\ -i & 1 \end{pmatrix}. \tag{1.15}
$$

This is actually the $\sqrt{X}$ up to a global phase factor, which can be used to construct a NOT gate if applying twice (i.e., returning $\bar{\gamma}_1$ and γ_2 back to the initial stage).

To see the non-Abelian statistics, we verify that the order of braiding matters as

$$
\mathcal{U}_{1\bar{1}}\mathcal{U}_{\bar{1}2} = \frac{1}{\sqrt{2}}\begin{pmatrix} e^{i\frac{\pi}{4}} & -ie^{i\frac{\pi}{4}} \\ -ie^{-i\frac{\pi}{4}} & e^{-i\frac{\pi}{4}} \end{pmatrix} \tag{1.16}
$$

is different from

$$
\mathcal{U}_{\bar{1}2}\mathcal{U}_{1\bar{1}} = \frac{1}{\sqrt{2}}\begin{pmatrix} e^{i\frac{\pi}{4}} & -ie^{-i\frac{\pi}{4}} \\ -ie^{i\frac{\pi}{4}} & e^{i\frac{\pi}{4}} \end{pmatrix}. \tag{1.17}
$$

This is the idea behind topological quantum computing that encodes the information in fermion parity, and braids MZMs to perform quantum gates (Clifford gates [17]). The advantage is the topological protection both in the qubit encoding and braiding process because the information is stored and manipulated nonlocally between a pair of MZMs, which is robust against local perturbations by nature. Furthermore, because the building block of topological quantum

computing is composed of a sequence of braidings with each step being exactly a unitary operation $\exp(\pi\gamma_i\gamma_j/4)$, which does not depend on any detail of the exchanging trajectory as long as the process is slow enough to ensure the adiabatic limit; it naturally avoids the nasty scenario of tuning the duration of the π-pulse or Rabi frequency to make an exact flip of a spin in the Bloch sphere for a CNOT gate as in other quantum computing schemes, where errors are inevitable.

Of course, the aforementioned braiding is just the simplest idea to show how to perform the logic gate operation using the non-Abelian statistics of MZMs. In fact, more practical architectures and schemes use ancillary qubits, and braid without "braiding" to perform the complete Clifford gates, such as Majorana hexon architecture [18], and measurement-based braiding [19–21], which are beyond the scope of this dissertation, and, thus, will not be covered.

1.2 Kitaev chain: A toy model to obtain MZMs

Despite being a conceptually attractive method to implement topological quantum computing, the way to "split" an electron into a pair of MZMs remains unclear because the electron is always a stable fermionic bound state in nature. In 2001, it was realized by Kitaev that such MZMs with non-Abelian statistics can emerge as localized zero-energy bound states in an idealized model of one-dimensional (1D) spinless p-wave superconductor (SC), which is later known as the Kitaev chain [22, 23]. The ingredients of the Kitaev chain are composed of a p-wave SC pairing term Δ, a nearest-neighbor hopping term t, and an on-site chemical potential term μ as shown in Fig. 1.1(a), i.e.,

$$\hat{H}_{\text{Kitaev}} = \sum_{i=1}^{L-1} \left(-t c_{i+1}^{\dagger} c_i + \Delta c_{i+1}^{\dagger} c_i^{\dagger} + \text{h.c.} \right) - \sum_{i=1}^{L} \mu c_i^{\dagger} c_i, \tag{1.18}$$

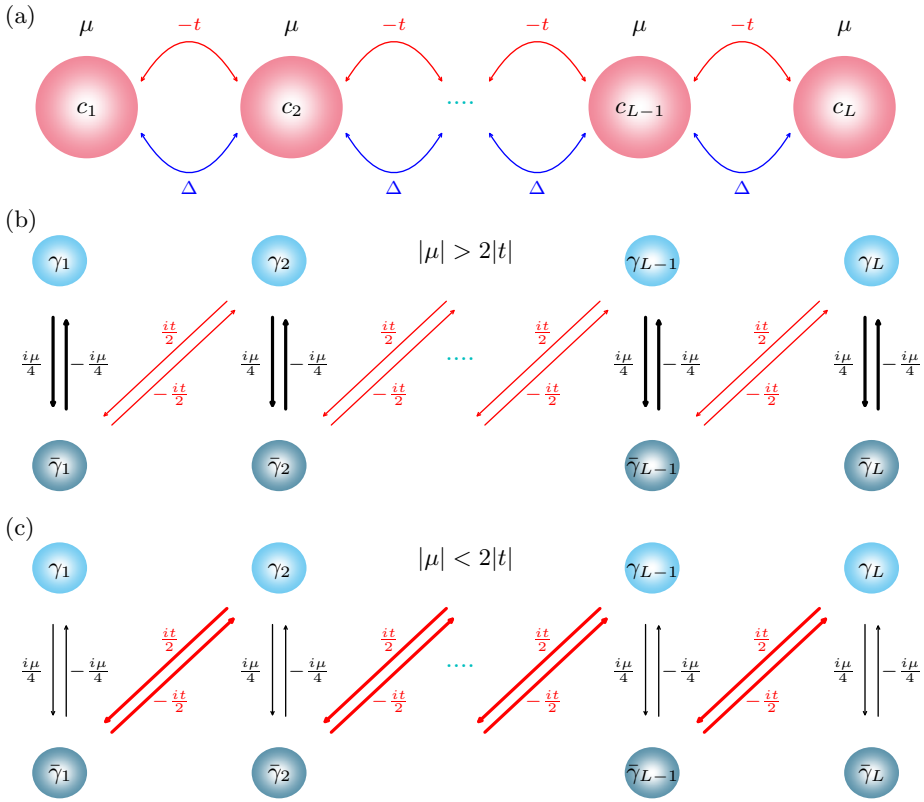

Figure 1.1: (a) Schematic of a Kitaev chain in the fermionic basis c_i; (b) trivial phase of the Kitaev chain in the Majorana basis γ_i and $\bar{\gamma}_i$ with $|\mu| > 2|t|$. The thickness of the arrow indicates the hopping amplitude; (c) topological phase of the Kitaev chain in the Majorana basis γ_i and $\bar{\gamma}_i$ with $|\mu| < 2|t|$

where $c_i^\dagger$ (c_i) creates (annihilates) a spinless fermion at i-th site in an N-site chain, and $\Delta = |\Delta|e^{i\theta}$. Here, we simply choose $\theta = 0$ such that $\Delta > 0$ without loss of generality, as the phase factor can be absorbed into the creation operators anyway.

Through a Bogoliubov-de Gennes (BdG) transformation, we can rewrite the Hamiltonian Eq. (1.18) as per

$$\hat{H}^{\text{BdG}}_{\text{Kitaev}} = \frac{1}{2}\sum_{i=1}^{L-1}\begin{pmatrix} c_{i+1}^\dagger & c_{i+1}\end{pmatrix}(-t\tau_z + \Delta i\tau_y)\begin{pmatrix} c_i \\ c_i^\dagger\end{pmatrix} + \text{h.c.} - \frac{\mu}{2}\sum_{i=1}^{L}\begin{pmatrix} c_i^\dagger & c_i\end{pmatrix}\tau_z\begin{pmatrix} c_i \\ c_i^\dagger\end{pmatrix} - \frac{\mu L}{2}. \tag{1.19}$$

We can ignore the last term as it is simply a constant shift of the total energy, and rewrite the remaining terms in the momentum space by imposing the periodic boundary condition with the Fourier transformation $c_j = \frac{1}{\sqrt{N}}\sum_k \tilde{c}_k e^{-ikj}$, which yields the BdG Hamiltonian

$$\hat{\mathcal{H}}^{\text{BdG}}_{\text{Kitaev}} = \frac{1}{2}\sum_k \begin{pmatrix} \tilde{c}_k^\dagger & \tilde{c}_{-k}\end{pmatrix}\begin{pmatrix} -2t\cos k - \mu & 2i\Delta\sin k \\ -2i\Delta\sin k & 2t\cos k + \mu\end{pmatrix}\begin{pmatrix} \tilde{c}_k \\ \tilde{c}_{-k}^\dagger\end{pmatrix}. \tag{1.20}$$

Therefore, the energy spectrum of the BdG Hamiltonian Eq. (1.20) is

$$E_\pm = \pm\sqrt{(2t\cos k + \mu)^2 + 4\Delta^2\sin^2 k}. \tag{1.21}$$

By tracking the gap between $E_\pm$, we can identify that topological quantum phase transition (TQPT) happens at $\mu = 2t$ ($\mu = -2t$) when the two bands touch at $k = \pi$ ($k = 0$).

In principle, we can always track the winding number as k crosses the Brillouin zone or calculate the Chern number of the filled valence bands to identify which side is topological;

however, we will follow a more intuitive approach that clearly shows which side is topological by converting the Hamiltonian Eq. (1.18) into the Majorana basis as per,

$$\hat{H}^{\mathrm{M}}_{\mathrm{Kitaev}} = -\frac{1}{2}\sum_{i}^{L-1}\left[(t+\Delta)\, i\gamma_{i+1}\bar{\gamma}_i + (\Delta - t) i\bar{\gamma}_{i+1}\gamma_i\right] - \frac{\mu}{2}\sum_{i=1}^{L} i\gamma_i\bar{\gamma}_i - \frac{\mu L}{2}. \tag{1.22}$$

Therefore, if we set $\Delta = t$, the class BDI Hamiltonian Eq. (1.18) can be viewed as a class AIII Su-Schrieffer-Heeger (SSH) chain [24] in the Majorana basis with the "intra-atom coupling" of $\pm\frac{i\mu}{4}$, and "inter-atom coupling" of $\pm\frac{it}{2}$ (see Fig. 1.1). Thus, the two limits— the trivial limit [Fig. 1.1(b)] and the topological limit [Fig. 1.1(c)]— depend on the competition between the inter-atom and intra-atom couplings of the two neighboring Majorana sites. It is straightforward to see that, given the finite SC gap, $|\mu| < 2|t|$ corresponds to the topological limit where two isolated Majorana modes dangle at both ends of the chain, while $|\mu| > 2|t|$ corresponds to the trivial limit, where no edge mode exists.

1.3 Semiconductor-Superconductor nanowire: an engineered spinless p-wave superconductor

However, the Kitaev chain suffers from two problems in reality because p-wave SC is hard to find in nature as well as the electron always carries the spin which is a spinful system. Therefore, several realistic proposals were made for the laboratory realization of effective spinless p-wave SC and the associated MZMs in different 2D and 1D systems [25–31]. One of the most studied and most prevailing proposals is Semiconductor-Superconductor (SM-SC) nanowire system [27, 29, 30]. The SM requires a large Rashba-type spin-orbit coupling (SOC) and

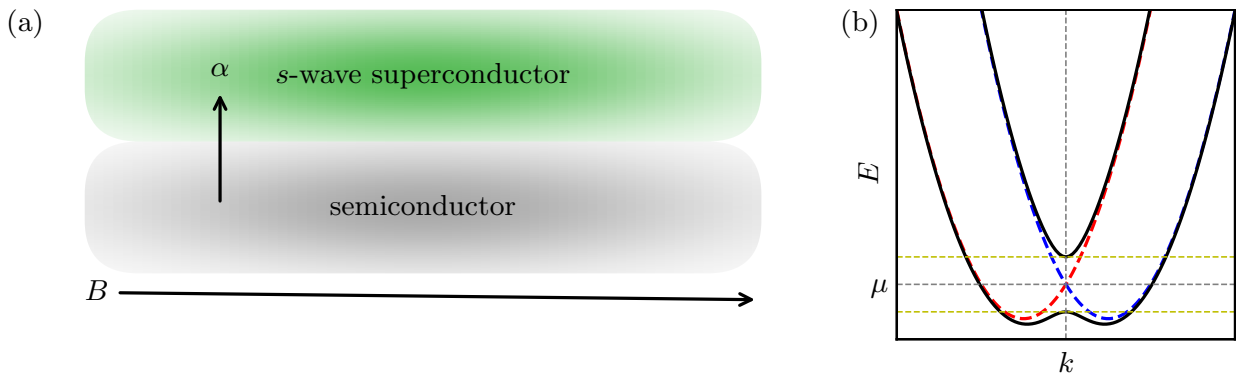

Figure 1.2: (a) The schematic for the SM-SC nanowire in the presence of an external magnetic field B. α is the Rashba-type spin-orbit coupling perpendicular to B. (b) The band structure for the SM part with SOC for the zero magnetic field (dashed lines) and a finite magnetic field (solid lines). μ is the chemical potential. The spinless regime exists when the chemical potential μ lies between the Zeeman-induced gap at $k = 0$ (between the two yellow lines).

Zeeman field to explicitly break the spin-rotational symmetry and time-reversal symmetry. The SM also acquires an effective p-wave SC pairing by a proximitized s-wave SC in the presence of Rashba-type SOC and Zeeman spin splitting. The schematic of the SM-SC nanowire is shown in Fig. 1.2(a).

The essence of this heterostructure is the proximitized superconductivity from the covering s-wave SC in the SM, namely, the SM can inherit Copper pairing from a nearby long-ranged ordered superconductor [32, 33]. We consider a 1D SM system with the Hamiltonian in the general form of

$$\hat{H}_{\text{1D}} = \sum_{s,s'} \int \frac{dk}{2\pi} \hat{\psi}_s^\dagger(k) \left[H_{\text{1D}}(k)\right]_{s,s'} \hat{\psi}_{s'}(k), \tag{1.23}$$

and a 3D conventional s-wave SC as per

$$\hat{H}_{\text{SC}} = \int \frac{d\boldsymbol{k}}{2\pi} \left[\sum_s E_s^{\text{SC}}(k) \hat{\eta}_s^\dagger(\boldsymbol{k}) \hat{\eta}_s(\boldsymbol{k}) + \Delta_{\text{SC}} \left(\hat{\eta}_\uparrow(\boldsymbol{k}) \hat{\eta}_\downarrow(-\boldsymbol{k}) + \text{h.c.} \right) \right], \tag{1.24}$$

where $\hat{\psi}_s(k)^\dagger$ and $\hat{\eta}_s^\dagger(\boldsymbol{k})$ create an electron with spin s at the 1D electronic system and supercon-

ductor, respectively, and $E_s^{\text{SC}}(k) = \frac{\hbar^2 k^2}{2m_{\text{SC}}} - \mu_{\text{SC}}$ and Δ_{SC} are the kinetic energy and s-wave pairing in the bulk superconductor. The proximity effect can be modeled by

$$H_\lambda = -\lambda \sum_s \int dx \left(\hat{\psi}_s^\dagger(x) \eta_s(x,0,0) + \text{h.c.} \right), \tag{1.25}$$

where λ characterizes the hopping strength with the dimension of energy $\times$ length. We treat the coupling term H_λ between the SC and SM perturbatively, and assume the Fermi wavevector of SC, k_{F}^{SC}, is much longer than that of the 1D system. Therefore, the first order process, which describes the single electron hopping, is strongly suppressed as $\lambda k_{\text{F}}^{\text{SC}} \ll \Delta_{\text{SC}}$. The second order process generates an effective Copper pair hopping term using the dimensional analyses as per

$$\hat{H}_\lambda^{(2)} = \frac{\lambda^2}{k_{\text{F}}^{\text{SC}} \Delta_{\text{SC}}} \int dx \left[\hat{\psi}_\uparrow(x) \hat{\psi}_\downarrow(x) \hat{\eta}_\downarrow^\dagger(x,0,0) \hat{\eta}_\uparrow^\dagger(x,0,0) + \text{h.c.} \right]. \tag{1.26}$$

In lower energies, we can treat it in the mean-field level by replacing $\hat{\eta}_\downarrow^\dagger(x,0,0)\hat{\eta}_\uparrow^\dagger(x,0,0)$ with $\left\langle \hat{\eta}_\downarrow^\dagger(x,0,0)\hat{\eta}_\uparrow^\dagger(x,0,0) \right\rangle \propto \rho_{\text{SC}} \Delta_{\text{SC}}$. Therefore, we can define the proximitized s-pairing gap as

$$\Delta \propto \frac{\lambda^2 \rho_{\text{SC}}}{k_{\text{F}}^{\text{SC}}}. \tag{1.27}$$

Therefore, the Hamiltonian of the SM-SC nanowire with a length of L can be described as per

$$\begin{aligned} \hat{H}_{\text{NW}} = & \sum_{s,s'} \int_0^L dx \hat{\psi}_s^\dagger(x) \left(-\frac{\hbar^2 \partial_x^2}{2m^*} - \mu - i\alpha\sigma_y \partial_x + V_{\text{Z}} \sigma_x \right)_{s,s'} \hat{\psi}_{s'}(x) \\ & + \int_0^L dx \left(\Delta \hat{\psi}_\uparrow^\dagger(x) \hat{\psi}_\downarrow^\dagger(x) + \text{h.c.} \right), \end{aligned} \tag{1.28}$$

where $\hat{\psi}_s^\dagger(x)$ [$\hat{\psi}_s(x)$] creates (annihilates) an electron with spin s at x, m^* is the effective mass of the conduction band, μ is the chemical potential in the SM, $V_\mathrm{Z} = \frac{1}{2}g\mu_B B$ is the Zeeman field with μ_B being the Bohr magneton and B being the magnetic field along the wire, α is the strength of Rashba-type SOC perpendicular to the wire, and Δ is the proximitized SC gap in the SM. Through a Bogoliubov transformation of the $\hat{\psi}_s(x)$, one can solve the Hamiltonian Eq. (1.28) and find that the topological regime requires high magnetic fields such that $V_\mathrm{Z} > \sqrt{\mu^2 + \Delta^2}$.

To see why the SM-SC nanowire in the presence of a magnetic field is an effective p-wave spinless system, we first consider the SM part. In Fig. 1.2(b), we show the band structure of the SM without the magnetic field in the red and blue dashed lines corresponding to two states with spin aligned with $+y$ and $-y$ respectively due to the spin-orbit coupling. At this point, no "spinless'' regime exists as there are always two pairs of Fermion points for any chemical potential μ. However, the magnetic field solves the problem by lifting the degeneracy at $k = 0$ because if the chemical potential μ lies in between the Zeeman-induced gap (indicated by the yellow dashed lines), there is only one pair of Fermion points, which can be thought of as the spinless regime. In this spinless regime, we turn on the s-wave SC pairing, which can create an effective p-wave pairing. To see this point, we need to project the Hamiltonian Eq. (1.28) onto the lower band by diagonalizing the Hamiltonian for the SM. The band energies for the Hamiltonian for the SM are

$$E_\pm(k) = \frac{\hbar^2 k^2}{2m^*} - \mu \pm \sqrt{(\alpha k)^2 + h^2}, \tag{1.29}$$

with the transformed basis as per

$$\hat{\psi}_\pm(k) = \frac{1}{\sqrt{2}}\left(\pm\frac{V_\mathrm{Z} + i\alpha k}{\sqrt{V_\mathrm{Z}^2 + \alpha^2 k^2}}\hat{\psi}_\uparrow(k) + \hat{\psi}_\downarrow(k)\right). \tag{1.30}$$

Here $\hat{\psi}_+^\dagger(x)$ and $\hat{\psi}_-^\dagger(x)$ create an electron on the upper band $E_+(k)$ and lower band $E_-(k)$, respectively. Therefore, the low energy effective model after the projection can be obtained by substituting Eq. (1.30) into Hamiltonian (1.28) as per

$$\hat{H}_{\text{eff}} = \int \frac{dk}{2\pi} E_-(k)\hat{\psi}_-^\dagger(k)\hat{\psi}_-(k) + \frac{i\alpha\Delta k}{\sqrt{V_Z^2 + \alpha^2 k^2}}\hat{\psi}_-^\dagger(k)\hat{\psi}_-^\dagger(-k) + \text{h.c.}, \tag{1.31}$$

where the first term comes from the SM part and the last term is the effective p-wave SC pairing.

Two years after the original theoretical proposal, the first Majorana experiment on the SM-SC nanowire [8] came out with the observation of zero-bias tunneling conductance peaks, which are the hallmark of MZMs. Although the maximal conductance of such ZBCPs was far below the theoretically predicted quantization of $2e^2/h$ [34] in Ref. [8], it inspired many follow-up experiments [9, 35–62] producing better ZBCPs by improving the quality of samples. Recently, a maximal conductance of almost $2e^2/h$, which is so far the closest one to the predicted Majorana quantized value, was reported in Refs. [9, 46, 57]. These reported "almost-quantized" ZBCPs are, however, not very stable as a function of system parameters (such as the temperature, applied magnetic field, and gate voltage) casting doubts on their topological Majorana origin [57].

With these mysteries in experiments, we will introduce real experimental devices, and explain the issues in experiments in the next section.

1.4 Experiments on pursuing the MZMs

The schematic of the experimental setup is a normal metal-superconductor (NS) junction as shown in Fig. 1.3 (a) and (b) from Ref. [57], where the SM, Indium antimonide (InSb), in grey is covered by the SC shell, aluminum (Al). in green, and the normal lead in yellow is the contact to

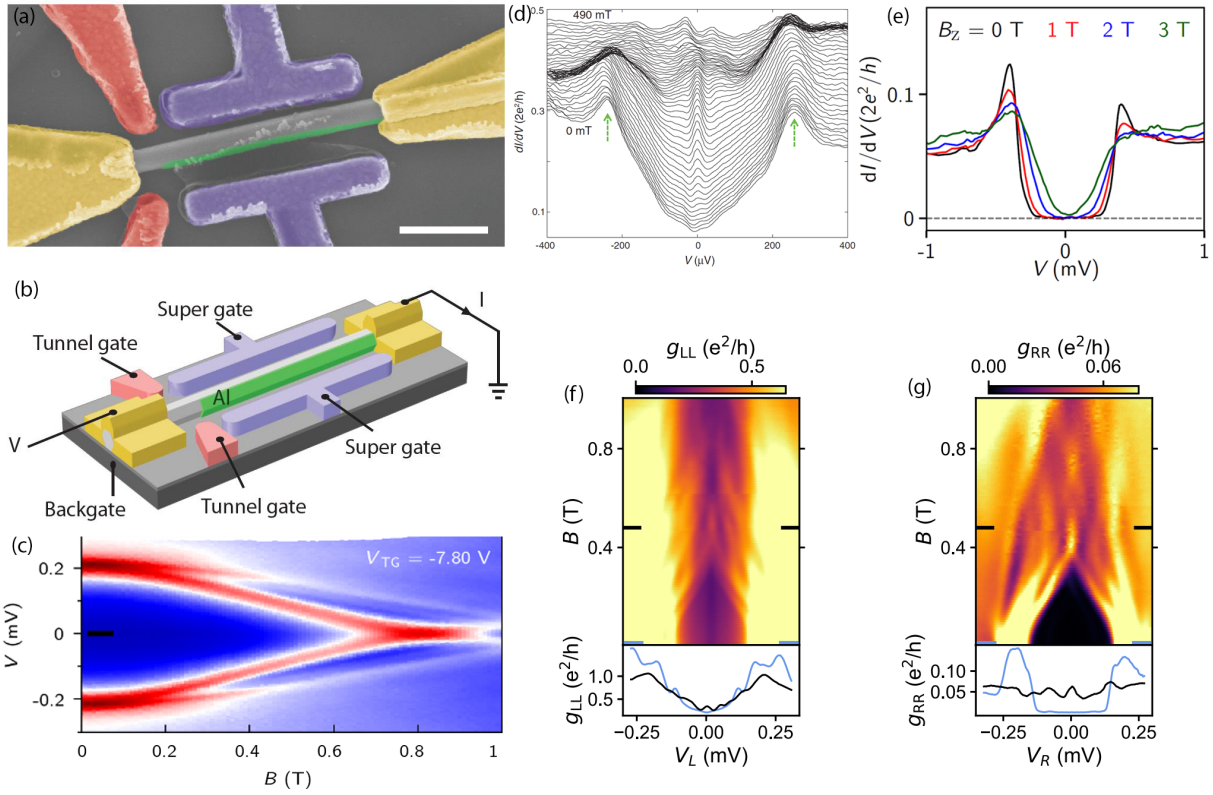

Figure 1.3: (a) Schematic and (b) experimental setup of an NS junction (from Ref. [57]); (c) The tunneling conductance as a function of bias voltages and magnetic field (from Ref. [57]); (d) The tunneling conductance as a function of bias voltage and magnetic field in the "waterfall" plot in 2012 (from Ref. [8]); (e) The tunneling conductance as a function of bias voltage for several magnetic fields in 2022 (from Ref. [62]); (f) and (g) show the left and right tunneling conductance as a function of bias voltage and magnetic field in a three-terminal device (from Ref. [55]).

measure the transport property by applying a bias voltage. Several gate voltages are used to tune the system parameters such as the tunnel gates in red to control the tunneling energy between the nanowire and the lead, and the super-gates in purple used to tune the chemical potential and other parameters in the device.

In experiments, the procedure to search for the ZBCPs can be summarized in these three steps. First, it involves a coarse search over a large parameter space spanned by super-gates, magnetic fields, tunnel gates, etc., to identify any signs of the ZBCPs with an otherwise clean, featureless spectrum below the parent SC gap. Once such a sign is identified in experiments, one can fine-tune the parameters to obtain the quantized ZBCPs of $2e^2/h$. Finally, with the demonstration of a quantized ZBCP, one further fine-tunes the gate voltages within a small region to show the robustness of such ZBCPs as a function of external fields, such as tunnel gates and magnetic fields.

Such a protocol may seem promising as it almost always guarantees to find ZBCPs in experiments. However, the observed ZBCPs [8, 9, 35–62], although observed some theoretical predicted features, lack several critical features of the MZMs, including the increasing Majorana oscillation with increasing magnetic fields [63], the bulk gap closing and reopening [29–31], the robustness of the quantized ZBCP against gate voltage and magnetic field [64], and the end-to-end correlation of the ZBCPs from both ends of the wire [65–67], which we will discuss in detail in the following subsections. The absence of these critical features makes the experimentally observed ZBCPs arising from topological MZMs highly unlikely, and many theoretical papers have attributed these ZBCPs to the trivial ABSs arising from the inhomogeneous potential [64, 68–78] or disorder [71, 77, 79–94] in the system. Therefore, in the following subsections, we clarify several critical issues in experiments.

1.4.1 Confirmation bias

The first and foremost issue in experiments to emphasize is confirmation bias. The confirmation bias that we are referring to here is that— when one knows exactly that one is looking for the quantized ZBCPs, one has considerable freedom in what one may report in the experimental publications through unjustified fine-tunings and cherry-picking data selections in order to "verify" the known theoretical predicted quantized ZBCPs.

It may be unfair to only mention the confirmation bias in the experiments using SM-SC nanowire to search for MZMs because this issue has been widely existing in topological condensed matter physics. For example, the somewhat unsatisfactory situation existing in the quantum spin Hall [95] conductance quantization has recently been discussed in-depth, and a recent claim [96] for Majorana modes in the quantum anomalous Hall scenario has been debunked [97]. Similarly, experimental claims of MZMs in ferromagnetic chains [98] were persuasively shown to be likely innocuous signatures of nontopological Shiba states in a rather complicated situation [99–101]. Similarly, a compelling claim for the observation of non-Abelian quasiparticle interference in the $\nu = 5/2$ fractional quantum Hall state has never been reproduced and is generally ignored in the literature despite the singular importance of the claim itself [6]. Another important claim [40] for the observation of exponential protection of topological Majorana modes in nanowires has been shown to be arising from trivial modes with the claimed exponential wire length dependence being an artifact of having too few samples [102, 103].

In all of these situations, the experiment data by itself is not so spectacular (unlike the astonishing precise quantization of Hall conductance in quantum Hall effect [1, 2] in the early 1980s), however, they merit the great interest only because there were compelling earlier theoretical pre-

dictions. Therefore, the attention and the guarding against the data selection and confirmation bias are critical. Especially, it is imperative to trenchantly analyze the claimed discovery, not only through extensive independent data analyses, but also through rigorous theoretical scrutiny, to ensure that all possible trivial explanations can be unambiguously ruled out.

1.4.2 Soft gaps

Besides the confirmation bias that generically exists in the topological condensed matter physics to some extent, we also point out issues specifically in the SM-SC Majorana nanowire experiments. The first is the soft gap existing in the early stage of experiments [8, 35–38]. The soft gap means a substantial subgap conductance forming a smooth in-gap conductance background as shown in the bottom red curve for zero magnetic field in Fig. 1.3(d) because of the interface disorder [91, 104, 105]. However, there has been enormous progress in the sample quality since 2012, with the emergence of hard zero-field gaps with no obvious features of deleterious subgap fermionic states, e.g., a recent experiment in 2022 as shown in Fig. 1.3(e).

1.4.3 Majorana oscillations

Another typical issue is the absence of the Majorana oscillation— the increasing of the splitting amplitude of the zero energy with increasing magnetic fields in the finite nanowire due to the overlapping between the two Majorana modes at both ends of the wires— which is the smoking gun evidence of the topological MZM [63] [see Fig. A.1]. The period and amplitude of the oscillation depend on details such as SC coherence length and Fermi wavevector in the SM. There are several reasons for the absence of the Majorana oscillations in the local conduc-

tance [70, 72, 73, 77, 79, 106–110], e.g., the SC bulk gap collapses too early below the putative TQPT, the self-energy effect is too strong so that it suppresses the amplitude of the oscillation, the omnipresent trivial ZBCP in class D ensemble due to the disorder in the nanowire [111, 112], etc. The total absence of MZM oscillations in experimental observed ZBCPs, however, remains a serious problem, particularly since the nanowires used in the experiments are generally rather short, and some oscillatory behavior is expected in the conductance even in the presence of self-energy effects. For example, Figure 1.3(c) shows a typical experimentally observed ZBCP without any Majorana oscillations.

1.4.4 SC gap collapse

As mentioned before, the SC gap collapsing too early below the putative TQPT is another serious issue. The topological regime for the SM-SC nanowire is defined as the regime where the Zeeman field is larger than $\sqrt{\Delta^2 + \mu^2}$ with Δ being the proximitized SC the nanowire and μ being the chemical potential. Therefore, in principle, one can apply a sufficiently high magnetic field to enter the topological regime eventually. However, this is impractical because the bulk SC gap, on the other hand, is suppressed as the magnetic field increases. Therefore, if the bulk gap collapses at some characteristic fields below the putative TQPT, one can neither access the topological regime nor observe the signature of the reopening of the bulk gap because the parent bulk SC gap has already collapsed due to the high magnetic field. For example, in Fig. 1.3(c), the parent bulk SC gap closes at $B \sim 1$ T, beyond which the system becomes completely trivial due to the vanishing SC gap.

1.4.5 Instability

The MZMs are a pair of topological delocalized states protected by a topological gap existing in the entire topological regime for $V_Z > \sqrt{\mu^2 + \Delta^2}$. Therefore, MZMs should manifest a quantized conductance of $2e^2/h$ due to the perfect Andreev reflection at the NS junction in the local conductance measurement [83, 113, 114], showing the robustness against the change of many parameters in the device, including the magnetic field (within the topological regime), tunnel voltage, etc., as long as they remain in the topological regime. However, this quantization condition is only a necessary condition but not a sufficient one to deduce the topological MZMs, due to many other mechanisms that can also trivially induce seemingly quantized ZBCPs arising from ABSs [68, 72, 73, 75–77, 115–118]. However, unlike the robust topological MZM-induced quantized ZBCPs, these trivial ZBCPs are usually unquantized because there is no such topological property to ensure a perfect Andreev reflection at the NS junction. Therefore, it can, in principle, manifest any conductance depending on the number of electron modes in the normal lead and the tunneling transparency at the NS junction. Furthermore, even if sometimes a (nearly) quantized ZBCPs appear by accident, they are not guaranteed to be robust in the sense that the ZBCPs cannot persist at high magnetic field increases and will disappear and bifurcate. For example, the ZBCP disappears at around $B \sim 1$ T along with the close of the parent bulk gap in Fig. 1.3(c),

1.4.6 Short wires

In topological condensed matter physics, the topological invariant (TI) is usually only defined in the thermodynamic limit. Therefore, it becomes ambiguous to carry any physical mean-

ings if the system is simply too short, e.g., the TI of the Pfaffian defined in the Kitaev's original paper [23] may not correspond to the topology of a short wire in the presence of disorder, instead, it quickly switches between $+1$ and -1, indicating a finite-size fermion parity switch [92]. Note that long wire and short wire refer specifically to the actual physical lengths of SM-SC nanowires used in the current experiments— since the SC coherence length is unknown in the topological regime, it is possible that all experimental systems so far are in the "short" wire limit as the topological gap in the experimental nanowires has not been measured or even detected so far experimentally.

1.4.7 End-to-end nonlocal correlation

The absence of the perfect end-to-end nonlocal correlation [65–67] of the conductance from both ends of the wire is another critical feature of the MZMs missing in experiments. Because the MZMs appear in pairs at both ends of the wire, we will expect the simultaneous response of the conductance spectrum measured from both ends of the wire if the wire enters the topological regime. However, if the ZBCP is induced by the trivial low-energy ABSs. There is no such an end-to-end correlation since the fermionic subgap state is not spatially delocalized at the wire ends, where the two Majorana modes highly overlap. In experiments, the end-to-end correlated measurements have become available very recently [51, 54, 55, 59–62]. By comparison of the left-right conductance spectra, we find that the end-to-end correlation is yet to be manifested. For example, in Fig. 1.3(f) and (g) from Ref. [55], the local conductance spectrum from the left and the right end does not manifest the perfect end-to-end correlation as they manifest the ZBCPs at different magnetic fields.

1.4.8 Inhomogeneous potential and disorder

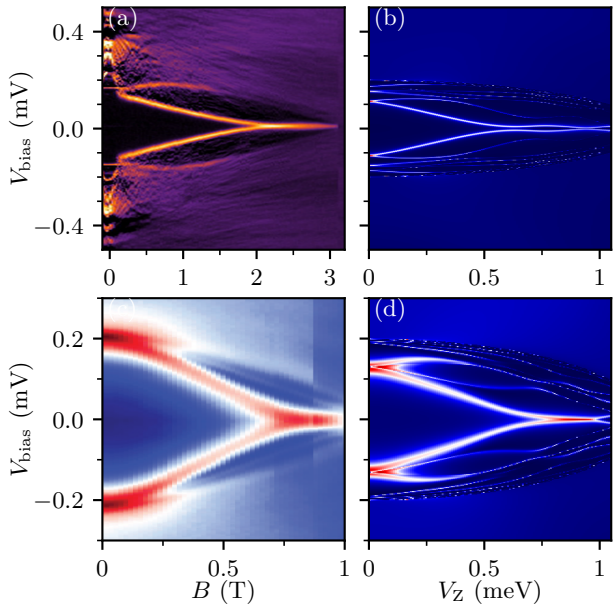

Figure 1.4: (a) and (c) are experimentally measured tunneling conductance as a function of the magnetic field and bias voltage from Refs. [46] and [9]. The redder color indicates the larger conductance; (b) and (d) are theoretically fine-tuned results to fit (a) and (c).

Finally, even if all aforementioned issues do not exist, there are still other trivial alternative explanations of the experimentally observed ZBCPs, the inhomogeneous potential- and disorder-induced ZBCPs, which are the bad ZBCPs and ugly ZBCPs dubbed in this dissertation. These ZBCPs are trivially arising from low-energy fermionic subgap states, and are referred to as the Andreev bound states (ABS), as opposed to the Majorana bound states (MBS). For example, we show two experimental observed ZBCPs in Figs. 1.4(a) and (c) from experiments Refs. [46] and [9], respectively, along with the two corresponding theoretical reproductions in Figs. 1.4(b) and (d) using nanowires in the presence of disorder in the chemical potential. We find that the experimental results (left column) and simulations (right column) are hard to distinguish as both experimental observations are qualitatively reproduced by the trivial ZBCPs in the presence of a

certain disorder through fine-tuning, including the vanishing amplitude of the ZBCP oscillation with an increasing magnetic field, and the instability of the ZBCP over regimes of high magnetic fields. The fact that the most experimentally-observed features can be qualitatively reproduced by the disorder-induced ZBCPs leaves the suspicious origin of the experimentally observed ZBCPs being interpreted as the topological MZMs. This conundrum necessitates a thorough study in full detail as we will discuss from Chapters 2- 5 in this dissertation.

1.5 Outline

The remaining part of the dissertation is arranged as follows. In Chapter 2, we construct a microscopic model for the SM-SC Hamiltonian in the real experimental situation, taking into account various effects arising from the inhomogeneous potential and disorder. By simulating the local differential tunneling conductance as a function of Zeeman field and bias voltage, we define three types of ZBCPs— the good, the bad, and the ugly ZBCPs— that are possible to be observed in the experiments, which are the most important concept and contribution of our work. The good ZBCPs are the topological MZMs, which only exist in the pristine limit, or in the presence of weak disorder. The bad ZBCPs are the quasi-MZMs induced by the quantum dot (QD), or the inhomogeneous potential. The ugly ZBCPs are trivial ABSs arising from strong disorder, which, we believe, are the observations of current experiments. We will elaborate on these three types of ZBCPs in more detail in Chapter 2.

In Chapter 3, beyond the local tunneling conductance, we proceed to the nonlocal conductance in the hope of probing the bulk information of the SM-SC nanowire, as we will present in Chapter 2 that the mere local conductance of ZBCP is incapable of distinguishing among the

three types of ZBCPs due to the lack of bulk information. Thus, we study the thermal conductance and propose a practical protocol, which combines the local electrical conductance, nonlocal electrical conductance, and thermal conductance, to decisively classify all three ZBCPs.

In Chapter 4, we study and comment on the real experimental observations in recent literature, and provide a compelling theoretical analysis with concrete simulations to show that even the best tunneling conductance in experiments so far is consistent with a disorder-induced trivial ZBCPs in the theory.

In Chapter 5, we revisit the simulations of the transport properties from a random matrix theory (RMT) approach, which is beyond the microscopic model constructed in Chapters 2- 4, to generalize our existing conclusion in SM-SC nanowires into all potential class D SC experimental platforms pursuing MZMs because the particle-hole symmetry is the only thing that is assumed in our RMT. We find that the quantized ZBCPs are generic in the class D ensemble by introducing a protocol that is guaranteed to find the trivial quantized ZBCPs.

Finally, we conclude in Chapter 6, and provide three pieces of guidance for future experiments. More examples of the good, the bad, and the ugly ZBCPs along with the wave functions are shown in Appendix A, B and C. The code for producing all results in this dissertation is shown in Appendix D.

Chapter 2: Physical mechanisms for zero-bias conductance peaks

In this chapter, we take a broad view within the single-subband 1D nanowire model for the SM-SC structure, considering all possibilities, both trivial and topological which produce ZBCPs, critically comparing the results in different situations in order to shed light on how to discern MZM-induced topological ZBCPs from the trivial ones. We critically compare four distinct physical situations producing ZBCPs within one unified formalism keeping all the SM-SC parameters fixed (except for the specific mechanism leading to the ZBCP in each case), discuss similarities and differences between various cases, and comment on possible methods for distinguishing between trivial and topological phases as a matter of principle. Given the proliferation of many different proposed physical mechanisms leading to trivial ZBCPs in different contexts, it is important to compare them all under one uniform model to understand their relevance and properties. In addition, we carefully study the nonperturbative stability and robustness of pristine MZMs in nanowires to different types of disorder, which leads to the interesting conclusion that, while strong disorder by itself could produce trivial ZBCPs, pristine ZBCPs arising from topological MZMs, if they exist in the system, are immune to weak disorder. Immunity of topological MZMs to weak disorder and complete suppression of topological SC with the consequent generic appearance of trivial ZBCPs (some of which may be accidentally "quantized") is the unfortunate dichotomy making it a difficult challenge to interpret the existing tunneling conductance data in

SM-SC hybrid nanowires since *a priori* no quantitative information is available on whether the disorder in the currently existing samples is strong or weak compared with the topological SC gap (which has not yet been clearly seen in any experiment).

We consider three distinct physical situations (i.e., ZBCP origins) with ZBCPs in the SM-SC hybrid nanowires, referred to as "good"/"bad"/"ugly", which differ qualitatively in the way the ZBCPs arise in each case. All the considered situations apply to the same physical system, namely, a 1D SM (InSb) nanowire with SOC in proximity to an ordinary metallic SC (Al) subjected to an external magnetic field, described by the same 1D BdG Hamiltonian with the differences among the three cases arising from extra terms in the Hamiltonian representing either inhomogeneous chemical potential ("bad") with or without QDs or quenched disorder ("ugly"). The "good" situation is pristine without these extra terms, and has been the standard model for studying topological SC and Majorana modes in SM-SC structures ever since it was introduced in Refs. [29, 30]. The "bad" situation is further subdivided into two physically distinct cases, depending on how the inhomogeneity in the chemical potential arises in the nanowire. One bad situation arises from having an unintentional QD in the system, which often happens near the wire end because of the complex materials science of creating the hybrid system [116]. The other bad situation arises from the presence of an inhomogeneous potential along the wire, arising presumably from the presence of charged impurities in the environment [68]. These two bad situations are not qualitatively different as they both give rise to near-zero fermionic subgap states leading to trivial ZBCPs, but their physical origins are different and there are significant quantitative differences between the two so considering them separately is sensible. The "ugly" is the fluctuation in the nanowire due to the unintentional (mostly) charged impurities invariably present in the nanowire. Since the charge fluctuation is very sensitive to the gate voltages, tem-

perature, subband occupancy, etc., it is intractable when multiple gate voltages are being tuned simultaneously. Thus, it can be treated as a random disorder in the 1D SM-SC nanowire. The random disorder also arises from disorder in the parent SC, the dielectric substrates, and the various leads and gates necessary to produce the hybrid system. The precise source of this strong disorder in the ugly case is unimportant for our considerations since we parametrize it simply as a random disorder as described below.

We construct the SM-SC nanowire Hamiltonian taking into account various aspects (see Fig. 2.1), including the pristine wire, QD, inhomogeneous potential, disorder in the chemical potential, in the SC gap, and the effective g factor. We theoretically calculate the tunneling conductance spectra through an NS junction as a function of the Zeeman field V_{Z} (magnetic field B) by calculating the S matrix (Fig. 2.1).

Apart from the tunneling conductance results as a function of the Zeeman field, we additionally calculate the tunneling conductance spectrum at zero Zeeman field as a function of the chemical potential. At zero magnetic field, where everything observed inside the gap should be topologically trivial, the "bad" and "ugly" ZBCPs may still manifest fermionic subgap states. This observation of the fermionic subgap states would thus become an indicator of inhomogeneous chemical potential or strong disorder, and therefore, samples showing subgap states at a zero field are unsuitable for MZM studies.

In addition, we also study the correlation measurement of tunneling conductance from both ends of the nanowire. In principle, this method, by virtue of the nonlocal nature of the topological MZM, can serve to distinguish Majorana bound states from trivial ABSs in the "bad" and "ugly" situations, since the topological state will be correlated but the trivial one will not [66]. However, this proposal will work only if the nanowire is sufficiently long. Therefore, by comparing

the long nanowire results ($L \sim 3$ μm) with the short ones ($L \sim 1$ μm), we show that in the short nanowire it is not feasible to distinguish between trivial and topological even utilizing the correlation measurement because the end-to-end correlation may be trivially manifested due to wave-function overlaps from the two ends.

2.1 Theory

When considering the real experimental situation, we can construct the most general form of the second quantized Hamiltonian to describe an SM-SC hybrid nanowire as per [119]

$$\hat{H}_{\text{tot}} = \hat{H}_{\text{SM}} + \hat{H}_{\text{Z}} + \hat{H}_{\text{V}} + \hat{H}_{\text{SC}} + \hat{H}_{\text{SM-SC}}, \tag{2.1}$$

where $\hat{H}_{\text{SM}}$ is the Hamiltonian for SM component, $\hat{H}_{\text{Z}}$ describes the contribution from the applied magnetic field (entering as the Zeeman splitting energy), $\hat{H}_{\text{V}}$ contains various effects of disorder and gate potentials, $\hat{H}_{\text{SC}}$ quantifies the parent SC, and $\hat{H}_{\text{SM-SC}}$ is the SM-SC coupling. This model has been studied extensively since its introduction in Refs. [29, 30], but usually with some of the terms (e.g., $\hat{H}_{\text{V}}$) left out to emphasize one or other physical mechanisms. In this dissertation, we keep all the terms to study and contrast the different situations within one comprehensive framework.

2.1.1 Minimal effective model

We start with the minimal effective Hamiltonian of a pristine nanowire without any QD, inhomogeneous potential, or disorder, which implies $\hat{H}_{\text{V}} = 0$. (This, by definition, corresponds to the "good" case where isolated topological MZMs arise at two wire ends for suffi-

ciently large Zeeman splitting and sufficiently long wires, i.e., above the TQPT.) The pristine nanowire is then described by the "standard" minimal BdG Hamiltonian [27, 29, 31] $\hat{H}_0 = \frac{1}{2}\int_0^L dx\ \hat{\Psi}^\dagger(x) H_0(x) \hat{\Psi}(x)$, with

$$H_0(x) = \left(-\frac{\hbar^2}{2m^*}\partial_x^2 - i\alpha\partial_x\sigma_y - \mu\right)\tau_z + V_{\rm Z}\sigma_x + \Delta\tau_x. \tag{2.2}$$

Here, $\hat{\Psi}(x) = \left(\hat{\psi}_\uparrow(x), \hat{\psi}_\downarrow(x), \hat{\psi}_\downarrow^\dagger(x), -\hat{\psi}_\uparrow^\dagger(x)\right)^{\mathsf{T}}$ represents a position-dependent spinor; $\vec{\boldsymbol{\sigma}}$ and $\vec{\boldsymbol{\tau}}$ denote the vectors of Pauli matrices acting on the spin and particle-hole space, respectively. The magnetic field is applied along the longitudinal direction of the nanowire providing a Zeeman term $H_{\rm Z} = V_{\rm Z}\sigma_x$, where $V_{\rm Z} = \frac{1}{2}g\mu_B B$ and μ_B is the Bohr magneton. Rashba-type SOC with strength α is assumed to be perpendicular to the wire length [120]. We emphasize the pristine nanowire aspect by imposing a spatially constant chemical potential μ with an effective g-factor and an SC proximitized gap Δ in the weak SM-SC coupling limit [32, 121]. Thus, $H_{\text{SM-SC}}$ here is given simply by the last term $\Delta\tau_x$ in Eq. (2.2). Unless otherwise specified, the values of effective parameters in Eq. (2.2) are [9, 41, 44, 47, 53, 122, 123] $m^* = 0.015\ m_e$ (for the effective mass), where m_e is the electron rest mass, $\Delta = 0.2$ meV (for the proximity-induced SC gap), $\mu = 1$ meV (for the chemical potential), $\alpha = 0.5$ eVÅ (for the SOC) and the length of the nanowire $L = 1\ \mu$m [46, 48–50] (for the short wire) or $3\ \mu$m (for the long wire). (This choice of parameters corresponds approximately to the InSb-Al hybrid SM-SC systems.) We calculate all the energy spectra numerically by discretizing the continuum Hamiltonian into a finite-difference tight-binding model [124] and then exactly diagonalizing the corresponding Hamiltonian matrix. The tight-binding model is diagonalized for different values of $V_{\rm Z}$ to obtain the corresponding eigenvalues and eigenvectors utilizing Arnoldi iteration technique [125] for sparse matrices (ex-

cept for the Hamiltonian in the presence of the self-energy discussed next). The schematic of a pristine nanowire ("good") model is shown in Fig. 2.1(a).

2.1.2 Self-energy

Under real experimental conditions, the weak SM-SC coupling limit, i.e., $H_{\text{SM-SC}} = \Delta\tau_x$ as in Eq. (2.2), may not be sufficient to describe the system, especially for those involving epitaxial Al as the parent SC [36, 126, 127]. Therefore, we consider the proximity effect in an intermediate regime within a Green's function approach [30, 32, 121]. The retarded Green's function $G^{\text{R}}(\omega)$ for the Bogoliubov quasiparticles in the Nambu basis, which allows us to compute all time-dependent response functions for an effectively noninteracting theory, can be written in terms of the effective Hamiltonian,

$$H_{0,\text{SE}}(x,\omega) = \left(-\frac{\hbar^2}{2m^*}\partial_x^2 - i\alpha\partial_x\sigma_y - \mu\right)\tau_z + V_{\text{Z}}\sigma_x + \Sigma(\omega). \tag{2.3}$$

where $G^{\text{R}}(x,\omega) = [H_{0,\text{SE}}(x,\omega+i\eta) - (\omega+i\eta)]^{-1}$ (η being the standard positive infinitesimal required to ensure causality). The last term $\Sigma(\omega)$ arises from the SC proximity effect, which represents the tunneling effect between the SC and the SM as $H_{\text{SM-SC}}$. By integrating out the SC degrees of freedom, we obtain the self-energy term [32, 72, 119, 121, 128, 129]

$$\Sigma(\omega) = -\gamma\frac{\omega + \Delta_0\tau_x}{\sqrt{\Delta_0^2 - \omega^2}}, \tag{2.4}$$

where γ is the effective SM-SC coupling (tunneling) strength, ω is the energy, and Δ_0 is the bulk parent SC gap. Unless otherwise specified, these values of parameters are used throughout:

$\gamma = 0.2$ meV and $\Delta_0 = 0.2$ meV [129].

Since the Hamiltonian (2.3) is ω-dependent in the presence of the self-energy, it can be solved self-consistently in an iterative manner for each energy state [130]. Note that the self-energy term $\Sigma(\omega)$ in Eq. (2.3) represents the coupling term $H_{\text{SM-SC}}$ of Eq. (2.1).

One of the practical problems encountered in experiments is that the bulk SC gap of the parent SC is suppressed by the applied magnetic field, and often in fact vanishes for sufficiently large Zeeman fields [107]. To better simulate the real experimental situation [9, 42, 43, 46, 48–50, 52], we therefore further consider a V_{Z}-dependent bulk SC gap, where it collapses at some experimentally determined non-universal $V_{\text{Z}c}$, namely, the constant Δ_0 in Eq. (2.4) is then replaced by [72]

$$\Delta_0(V_{\text{Z}}) = \Delta_0(V_{\text{Z}} = 0)\sqrt{1 - \left(\frac{V_{\text{Z}}}{V_{\text{Z}c}}\right)^2}\,\theta(V_{\text{Z}c} - V_{\text{Z}}), \tag{2.5}$$

where $\theta(\dots)$ is the Heaviside-step function indicating that the SC gap will never reopen once it has collapsed since the parent bulk SC gap has vanished causing a complete disappearance of the proximity effect in the SM. As such regimes of gap collapsing V_{Z} are not of our interest, we do not extend Zeeman field V_{Z} in the numerical calculated tunneling conductance spectra beyond the SC collapse field $V_{\text{Z}c}$ (i.e., the theory throughout this chapter is only discussed within $V_{\text{Z}} < V_{\text{Z}c}$, and should not be applied to the regime of $V_{\text{Z}} > V_{\text{Z}c}$). Thus the Hamiltonian with the self-energy Eq. (2.4) then becomes

$$H_{0,\text{SE}}(x, \omega; V_{\text{Z}}) = \left(-\frac{\hbar^2}{2m^*}\partial_x^2 - i\alpha\partial_x\sigma_y - \mu\right)\tau_z + V_{\text{Z}}\sigma_x + \Sigma(\omega; V_{\text{Z}}), \tag{2.6}$$

where

$$\Sigma(\omega; V_{\rm Z}) = -\gamma \frac{\omega + \Delta_0(V_{\rm Z})\tau_x}{\sqrt{\Delta_0^2(V_{\rm Z}) - \omega^2}}. \tag{2.7}$$

Equation (2.6) along with Eqs. (2.7) and (2.5) are the Hamiltonian to produce most of the numerical results in the main text. In essence, the reason for including the self-energy with the bulk $V_{\rm Z}$-dependent SC gap collapse is to introduce the renormalization effects by the parent SC. The functional form of the SC gap collapse Eq. (2.5) is chosen merely because it phenomenologically simulates well the real experimental situation – any other smooth form of the parent SC gap collapse does not change any aspect of our results or conclusions.

We will show results both with and without the self-energy term to distinguish weak- and intermediate-coupling SM-SC systems in Appendix A. In the main text, only results with the self-energy are presented since the self-energy effect is crucial under real experimental conditions. (Note that we call the results with self-energy "intermediate-coupling" rather than "strong-coupling" since the strongly coupled SM-SC represents the situation where the SC completely overwhelms the SM nanowire, leading to very unfavorable conditions for the creation of MZMs– weak-coupling and intermediate-coupling situations, without and with the self-energy respectively, are the experimentally relevant situations.)

2.1.3 Quantum dot

The previous Hamiltonian in Eq. (2.2) describes a pristine "good" nanowire without any disorder, i.e., $\hat{H}_{\rm V} = 0$. However, the presence of an unintentional QD at the end of the nanowire may be inevitable under real experimental conditions due to the mismatch of Fermi energy between the normal lead and the SM nanowire by creating a Schottky barrier [72, 75]. There-

fore, although the QD may not be intentionally introduced in experiments, it is expected to be quite ubiquitous in many SM-SC nanowire experimental setups [9, 42, 46, 53]. Theoretically, the "QD" is a potential fluctuation at the end of the nanowire which is a short segment uncovered by the parent SC. Since it is a zero-dimensional (0D) object, the QD usually appears at the contact point connecting the SM nanowire to the lead. Thus, the QD will play a role in $H_{\rm V}(x) = V(x)$, where $V(x)$ is simply chosen as a Gaussian barrier. Namely, the QD potential is given by

$$V(x) = V_{\rm D} \exp\left(-\frac{x^2}{l^2}\right) \theta(l-x), \tag{2.8}$$

where $V_{\rm D}$ defines the peak of the dot barrier and l is the length of the QD. Here $V_{\rm D}$ and l are the parameters modeling the QD. By intensive numerical calculations, we ensure that the specific form of the QD potential does not qualitatively modify the results [72, 76]. Consequently, the BdG Hamiltonian of SM-SC nanowire with a QD then becomes

$$H_{\rm QD}(x) = \left[-\frac{\hbar^2}{2m^*}\partial_x^2 - i\alpha\partial_x\sigma_y - \mu + V_{\rm D}e^{-\frac{x^2}{l^2}}\theta(l-x)\right]\tau_z + V_{\rm Z}\sigma_x + \Delta\theta(x-l)\tau_x, \tag{2.9}$$

Eq. (2.9) where $\theta(x-l)$ is included to account for the partially covering parent SC (i.e., the SC is absent over a length l at the end of the nanowire). For the same reason, we incorporate the self-energy Eq. (2.4) as well for the finer simulation of experimental results in the presence of the QD. Thus, the Hamiltonian in the presence of the QD and the self-energy then becomes

$$\begin{aligned} H_{\rm QD,SE}(x,\omega;V_{\rm Z}) = &\left[-\frac{\hbar^2}{2m^*}\partial_x^2 - i\alpha\partial_x\sigma_y - \mu + V_{\rm D}e^{-\frac{x^2}{l^2}}\theta(l-x)\right]\tau_z + V_{\rm Z}\sigma_x \\ &- \gamma\frac{\omega + \Delta_0(V_{\rm Z})\tau_x}{\sqrt{\Delta_0^2(V_{\rm Z}) - \omega^2}}\theta(x-l). \end{aligned} \tag{2.10}$$

The schematic of the nanowire with a QD is shown in Fig. 2.1(b). This is one of our "bad" situations, with the possibility of ZBCPs arising from the QD. The second "bad" situation with an inhomogeneous potential along the whole wire, in contrast to a potential fluctuation just at the end, is discussed below.

2.1.4 Inhomogeneous potential

The inhomogeneous potential is an alternative mechanism producing ZBCP in the trivial regime [68, 69, 71, 74, 75, 78]. This is the second type of "bad" situation we consider. To be specific, the inhomogeneous potential is a smooth confining potential in the SM due to charged impurities in the environment or the gate voltage [8, 9, 36, 42, 53]. In the theoretical model, we use, similar to the QD case above, a Gaussian smooth confining potential [68, 78]

$$V(x) = V_{\text{max}} \exp\left(-\frac{x^2}{2\sigma^2}\right), \tag{2.11}$$

where V_{max} defines the height of confining potential and σ controls the linewidth of the inhomogeneous potential. Therefore, the BdG Hamiltonian of the nanowire with an inhomogeneous potential is

$$H_{\text{inhom}}(x) = \left(-\frac{\hbar^2}{2m^*}\partial_x^2 - i\alpha\partial_x\sigma_y - \mu + V_{\text{max}}e^{-\frac{x^2}{2\sigma^2}}\right)\tau_z + V_{\text{Z}}\sigma_x + \Delta\tau_x. \tag{2.12}$$

We note that both types of "bad" situations, the QD and inhomogeneous potential, can be construed to produce an effective spatially varying chemical potential $\mu - V(x)$ in the BdG equations defined by Eqs. (2.9) and (2.12) respectively, with the only difference between the two "bad"

cases being the way inhomogeneous potential in $V(x)$ arises. A slight difference in the theoretical model between the QD and the inhomogeneous potential case lies in the spatial extent of the parent SC segment covering the nanowire. Unlike the QD case, the parent SC fully covers the SM nanowire in the "bad" situation of the inhomogeneous potential. We may also incorporate the self-energy Eq. (2.4) here, and the Hamiltonian then becomes

$$H_{\text{inhom,SE}}(x,\omega;V_{\text{Z}}) = \left(-\frac{\hbar^2}{2m^*}\partial_x^2 - i\alpha\partial_x\sigma_y - \mu + V_{\text{max}}e^{-\frac{x^2}{2\sigma^2}}\right)\tau_z + V_{\text{Z}}\sigma_x - \gamma\frac{\omega + \Delta_0(V_{\text{Z}})\tau_x}{\sqrt{\Delta_0^2(V_{\text{Z}}) - \omega^2}}. \tag{2.13}$$

The schematic of the nanowire with the inhomogeneous potential is shown in Fig. 2.1(c). This is our second type of "bad" situation.

2.1.5 Disorder

There are two completely distinct aspects of disorder we study in this chapter. We show that the pristine MZM-induced topological ZBCPs, if they exist in the system, are to a large extent immune to the effects of disorder by virtue of their topological robustness. Thus, the "good" ZBCPs are robust to disorder effects. By contrast, disorder by itself can produce trivial ZBCPs, which mimic MZM-induced ZBCPs, complicating the interpretation of experimentally-observed ZBCPs.

Under real experimental conditions, unintentional disorder is unavoidable, and therefore, disorder may also play an important role in the emergence of topologically-trivial ZBCP [70, 71, 79, 81, 84–91, 106]. In essence, the SC nanowire which hosts the Majorana modes acts like an effective p-wave SC [131–133] which is not necessarily immune to nonmagnetic disorder [80, 134]. We first introduce disorder in the chemical potential as $V_{\text{imp}}(x)$ in Eq. (2.1) [70],

i.e., $H_{\mathrm{V}}(x) = V_{\mathrm{imp}}(x)$. $V_{\mathrm{imp}}(x)$ is a short-ranged random potential drawn from an uncorrelated Gaussian distribution with zero mean value and standard deviation σ_μ, i.e.,

$$\langle V_{\mathrm{imp}}(x) V_{\mathrm{imp}}(x') \rangle = \sigma_\mu^2 \delta(x - x'), \tag{2.14}$$

where $\delta(\dots)$ denotes the Dirac δ function and the variance σ_μ^2 represents the strength of disorder. We clarify that the impurity potential is randomly generated and the results in Sec. 2.2 are shown for a specific configuration of randomness without averaging over disorder. Thus, the Hamiltonian Eq. (2.2) then becomes

$$H_{\mathrm{disorder},\mu}(x) = \left[-\frac{\hbar^2}{2m^*}\partial_x^2 - i\alpha\partial_x\sigma_y - \mu + V_{\mathrm{imp}}(x) \right] \tau_z + V_{\mathrm{Z}}\sigma_x + \Delta\tau_x, \tag{2.15}$$

and the Hamiltonian in the presence of the self-energy Eq. (2.4) then becomes

$$H_{\mathrm{disorder},\mu,\mathrm{SE}}(x,\omega;V_{\mathrm{Z}}) = \left[-\frac{\hbar^2}{2m^*}\partial_x^2 - i\alpha\partial_x\sigma_y - \mu + V_{\mathrm{imp}}(x) \right] \tau_z + V_{\mathrm{Z}}\sigma_x - \gamma\frac{\omega + \Delta_0(V_{\mathrm{Z}})\tau_x}{\sqrt{\Delta_0^2(V_{\mathrm{Z}}) - \omega^2}}. \tag{2.16}$$

The schematic of disorder in the chemical potential is shown in Fig. 2.1(d). This is the "ugly" situation in the presence of a large amount of disorder. Here we can think of the chemical potential itself having random spatial disorder with the effective random chemical potential being $\mu - V_{\mathrm{imp}}(x)$.

For completeness, we additionally introduce disorder in the effective g factor and the SC gap in our theoretical model. Since the Zeeman field is related to the applied magnetic field and the definite value of g in experiments is unknown [130], we avoid directly handling the random g

factor by transferring its randomness to V_{Z}. Thus we define a normalized factor $\tilde{g}(x) = g(x)/\bar{g}$, where $g(x)$ is the random g factor and $\bar{g}$ stands for its mean value. Since V_{Z} is linearly proportional to g, $\tilde{g}(x)$ also equals $V_{\mathrm{Z}}(x)/\bar{V}_Z$. We randomize $\tilde{g}(x)$ in the form of Gaussian distribution $\mathcal{N}(1, \sigma_g^2)$ as before. Note that, to avoid the possibility of a physically meaningless negative g factor, the standard deviation σ_g cannot be set too large. With the random $V_{\mathrm{Z}}(x) = \tilde{g}(x)\bar{V}_Z$, the Hamiltonian Eq. (2.2) becomes

$$H_{\text{disorder},g}(x) = \left(-\frac{\hbar^2}{2m^*}\partial_x^2 - i\alpha\partial_x\sigma_y - \mu\right)\tau_z + V_{\mathrm{Z}}(x)\sigma_x + \Delta\tau_x \tag{2.17}$$

and the Hamiltonian with the self-energy Eq. (2.3) then becomes

$$H_{\text{disorder},g,\text{SE}}(x,\omega;V_{\mathrm{Z}}) = \left(-\frac{\hbar^2}{2m^*}\partial_x^2 - i\alpha\partial_x\sigma_y - \mu\right)\tau_z + V_{\mathrm{Z}}(x)\sigma_x - \gamma\frac{\omega + \Delta_0(V_{\mathrm{Z}})\tau_x}{\sqrt{\Delta_0^2(V_{\mathrm{Z}}) - \omega^2}}. \tag{2.18}$$

The schematic of disorder in the effective g factor is shown in Fig. 2.1(e). This type of Zeeman disorder in the effective g factor is the second mechanism leading to creating "ugly" ZBCPs.

The last type of disorder we consider is in the SC gap. It can be defined as $\Delta(x) \sim \mathcal{N}(\Delta, \sigma_\Delta^2)$ in Eq. (2.2) without the self-energy or $\Delta_0(x) \sim \mathcal{N}(\Delta_0, \sigma_{\Delta_0}^2)$ in Eq. (2.3) with the self-energy. Again, to avoid any unphysical negative SC gap, the standard deviation should not be too large. Thus the Hamiltonian (2.2) then becomes

$$H_{\text{disorder},\Delta}(x) = \left(-\frac{\hbar^2}{2m^*}\partial_x^2 - i\alpha\partial_x\sigma_y - \mu\right)\tau_z + V_{\mathrm{Z}}\sigma_x + \Delta(x)\tau_x \tag{2.19}$$

and the Hamiltonian utilizing the self-energy term (2.4) becomes

$$H_{\text{disorder},\Delta_0,\text{SE}}(x,\omega;V_\text{Z}) = \left(-\frac{\hbar^2}{2m^*}\partial_x^2 - i\alpha\partial_x\sigma_y - \mu\right)\tau_z + V_\text{Z}\sigma_x - \gamma\frac{\omega + \Delta_0(x;V_\text{Z})\tau_x}{\sqrt{\Delta_0^2(x;V_\text{Z}) - \omega^2}}. \quad (2.20)$$

The schematic of disorder in the SC gap is shown in Fig. 2.1(f). In Sec. 2.2, we will show that neither the topological MBS-induced ZBCP is destroyed due to this gap disorder nor any trivial ABS-induced ZBCP is created in the presence of disorder in the SC gap. Thus this is another subcategory of the "good" ZBCPs in contrast to both chemical potential and Zeeman disorder which lead to ugly ZBCPs. Although the topological MZMs are protected against some gap disorder [135], a very large gap disorder obviously destroys the MZMs since it suppresses the topological SC itself [86, 91].

2.1.6 Wave functions

Since all of our foregoing models, after discretization, are based on the tight-binding approximation, we can obtain the wave functions by diagonalizing the $4N \times 4N$ BdG Hamiltonian for an N-site system, where the factor of 4 comes from the Nambu spinor basis.

Because the trivial ABSs are distinct from the topological MBSs in the spatial separation between the localized bound states in the nanowire— ABSs in the trivial regime are two highly overlapping (or only partially separated) Majorana modes at one end of the nanowire; while MBSs in the topological regime are two well-separated MZMs at both ends of the nanowire [78, 118, 136]. Thus, the trivial ABSs here are in fact quasi-MZMs that are not well-separated to be considered as two isolate modes. Therefore, to explicitly identify the ABS-induced ZBCP, we are motivated to decompose the wave functions of the BdG Hamiltonian in the Nambu space to

the wave functions in the Majorana basis as per,

$$\begin{aligned}\gamma_n(s,i) &= \frac{1}{\sqrt{2}}\sum_{\tau}\left[\Psi_{E_n}(s,\tau,i)+\Psi_{-E_n}(s,\tau,i)\right],\\ \bar{\gamma}_n(s,i) &= \frac{i}{\sqrt{2}}\sum_{\tau}\left[\Psi_{E_n}(s,\tau,i)-\Psi_{-E_n}(s,\tau,i)\right],\end{aligned} \tag{2.21}$$

where $\Psi_{E_n}(s,\tau,i)$ is the wave function at Site i with the spin $s=\{\uparrow,\downarrow\}$ for the state with the energy of E_n in the particle channel ($\tau=e$) or hole channel ($\tau=h$), and $\Psi_{-E_n}(s,\tau,i)$ is its negative energy counterpart connected via a particle-hole transformation $\mathcal{P}=\sigma_y\tau_y\mathcal{K}$ with $\mathcal{K}$ being the complex conjugate (note the different form of the particle-hole transformation than the usual one due to the Nambu spinor $\hat{\Psi}$). The two wave functions, $\gamma_n(s,i)$ and $\bar{\gamma}_n(s,i)$, in the Majorana basis are defined by the Majorana transformation in Eq. (1.1).

We sum over all spins on Site i to obtain the spin-averaged density of wave functions projecting to the Majorana basis,

$$\begin{aligned}|\gamma_n(i)|^2 &= \sum_s |\gamma_n(s,i)|^2,\\ |\bar{\gamma}_n(i)|^2 &= \sum_s |\bar{\gamma}_n(s,i)|^2,\end{aligned} \tag{2.22}$$

as shown in Appendix B, along with its corresponding energy spectrum E_n.

2.1.7 Differential conductance spectrum

To simulate the experimental measurement of tunneling conductance $G(V=V_{\text{bias}})=dI/dV\big|_{V=V_{\text{bias}}}$ [9, 42, 43, 48–50, 52, 53] at a bias voltage V_{bias}, we attach a normal lead to the end of the nanowire and numerically calculate the tunneling conductance through the NS junction

using the S matrix method. The normal lead has the same Hamiltonian as the SM-SC nanowire except for the absent SC term, i.e.,

$$H_{\text{lead}} = \left(-\frac{\hbar^2}{2m^*}\partial_x^2 - i\alpha\partial_x\sigma_y - \mu_{\text{lead}} \right) \tau_z + V_{\text{Z}}\sigma_x \tag{2.23}$$

where $\mu_{\text{lead}} \sim 25$ meV is the chemical potential in the lead controlled by the voltage of the tunnel gate [72]. The tunnel barrier $V_g \sim 10$ meV is added on at the interface of the NS junction [137]. We use KWANT to compute the S matrix [138]. Since the calculation technique is well-established, we refer the reader to existing references for technical details [65, 69, 105, 115, 124, 138–147]. The schematic for the simulated model is in Fig. 2.1 under six distinct aforementioned situations [from (a) to (f)]: the pristine nanowire, the nanowire in the presence of the QD, the nanowire in the presence of the inhomogeneous potential, the nanowire in the presence of disorder in the chemical potential, the nanowire in the presence of disorder in the effective g factor, and the nanowire in the presence of disorder in the SC gap.

We insert a set of discrete V_{Z} into the Hamiltonian and calculate the differential conductance as a function of V_{bias} from -0.3 to 0.3 mV. The conductance varies between $G = 0$ and $4e^2/h$ because of the two spin channels in general [142]. We present two-dimensional false-color plots, where the two axes are V_{Z} and V_{bias}, to visualize the pattern of conductance spectra, with white indicating quantized conductance $2e^2/h$, blue indicating zero conductance, and red indicating the maximally possible conductance of $4e^2/h$ in this single occupied subband model. The numerical results for the tunneling conductance are presented in Sec. 2.2.

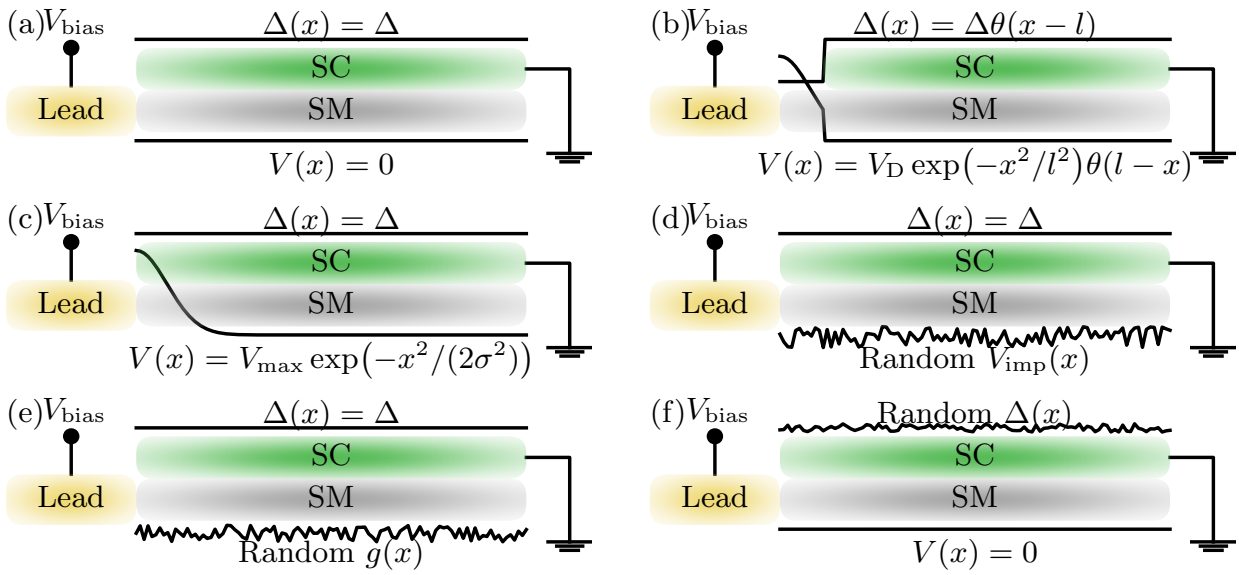

Figure 2.1: The schematic of the NS junction composed of a lead and (a) pristine nanowire with a constant SC gap Δ in the clean limit $V(x)=0$; (b) nanowire with a QD $V(x)$ and a partially-covered parent SC; (c) nanowire with an inhomogeneous potential $V(x)$ and a constant SC gap Δ; (d) nanowire with disorder $V(x)$ in the chemical potential; (e) nanowire with disorder $\tilde{g}(x)$ in the effective g factor; and (f) nanowire with disorder in the SC gap $\Delta(x)$.

2.1.8 Dissipation and temperature

In the experimental situation, there is invariably some dissipation in the nanowire because of coupling to the environment, which we simulate phenomenologically by adding a dissipative term to the diagonal part of the BdG Hamiltonian [139]. Dissipation also introduces a particle-hole asymmetry in the observed tunneling conductance at finite voltages which is not present in the dissipationless BdG formalism by virtue of the exact particle-hole symmetry [139]. In reality, the experiments are at the temperature $T\sim 20$ mK [49, 50]. To include the finite temperature effect, the conductance spectrum is calculated as a convolution with the derivative of Fermi distribution at finite temperature. The dissipation and finite temperature effects are already taken into account by following recent works in the literature [30, 69, 70, 76, 84, 106, 124, 137, 139, 148]. Thus, we do not intend to discuss the effect of the dissipation and finite temperature

throughout this chapter by sticking to zero temperature and small dissipation ($\Gamma = 10^{-4}$ meV) in the numerical results in this chapter.

2.2 Results

We emphasize that our definitions for good, bad, and ugly physical mechanisms are both mathematically and physically sharply defined with no ambiguity as shown clearly in Fig. 2.1. Physically, the good situation is pristine MZM with little background disorder and a constant chemical potential; the bad situation has a spatially varying (but deterministic) chemical potential with no random disorder; the ugly case has strong random disorder. Mathematically, the three situations are distinguished by the term $H_{\rm V}(x)$ in the Hamiltonian defining the BdG equation [see Eq. (2.1)] with $H_{\rm V}(x)$ being a constant ("good"), spatially varying in a deterministic manner ("bad"), and strongly random ("ugly"). Thus the three situations, good/bad/ugly, are both physically and mathematically distinct.

In this section, we show representative numerical results for the calculated differential tunneling conductance as a function of $V_{\rm bias}$ and $V_{\rm Z}$ in Figs. 2.2-2.6. The complete correlation conductance measurements from both ends of the nanowire are shown in Appendix A. Our goal is to simulate stable ZBCPs as observed experimentally, taking into account various possible experimental situations, including the pristine nanowire, the nanowire in the presence of the QD, in the presence of the inhomogeneous potential, in the presence of disorder in the chemical potential, in the presence of disorder in the effective g factor, and the presence of disorder in the SC gap, within a unified formalism keeping all system parameters the same except for the specific mechanism leading to that ZBCP. Based on the nature of the ZBCP sticking to zero energy (as

well as the underlying physical mechanism), we classify the conductance results into three types: the good (in Sec. 2.2.1), the bad (in Sec. 2.2.2), and the ugly (in Sec. 2.2.3). We emphasize that all ZBCPs other than the good ones are topologically trivial since the ZBCPs begin to stick to zero energy in these trivial cases before the nominal TQPT. This triviality is reinforced by the wave functions in the Majorana basis in Appendix B, where the two Majorana modes are not well-separated for the bad and the ugly cases in spite of the occurrence of ZBCPs.

In addition, we notice that by including the self-energy with a gradual-collapsing SC gap (as happens experimentally), the amplitude of the ZBCP oscillation is significantly suppressed as V_Z increases. For each type of ZBCP, the left-right correlation conductance measurements are also discussed. Although the end-to-end correlation measurement can be, in principle, used to distinguish MBS from ABS in long wires, we show that the nonlocal end-to-end measurements in short wires can trivially manifest such correlations. Besides presenting the conductance spectrum as a function V_Z, we also present conductance results for zero magnetic field in Sec. 2.2.4, which qualitatively reproduce the experiments in Ref. [51]. Obviously, the observed existence of subgap states at the zero magnetic field indicates the presence of substantial disorder in the system which casts serious doubt on the topological nature of the corresponding finite field ZBCPs.

2.2.1 The good ZBCP

The good ZBCP arises from the genuine topological Majorana mode which occurs beyond the TQPT. First, we present the results of good ZBCPs in the pristine nanowire model in Figs. 2.2(a) and 2.2(b). The schematic of the pristine model is shown in Fig. 2.1(a). In Figs. 2.2(a) and 2.2(b), the chemical potential and the SC gap are all simply constant without any disor-

der. The identical nonlocal conductance correlated between the two ends as shown in Fig. 2.2 manifests the most ideal theoretical instance of the good ZBCP, where the ZBCP is completely topological and appears only beyond the TQPT [136].

The good ZBCP arising from MZM remains immune to some finite amount of disorder as shown in Figs. 2.2(c) and 2.2(d). In Figs. 2.2(c) and 2.2(d), we provide an example of the good ZBCP in the presence of weak disorder in the chemical potential with a Gaussian distribution of variance $\sigma_\mu = 0.4$ meV, which accounts for 40% of the chemical potential. The corresponding schematic is in Fig. 2.1(d). We find no ZBCP emerging in the trivial regime below TQPT, and the topological ZBCP with the Majorana oscillation emerging beyond the TQPT in the usual manner. The nonlocal conductance measurements are almost identical from both ends exhibiting the expected Majorana correlations from the two ends.

Another type of disorder is also found to have a modest impact on the good ZBCP as in Figs. 2.2(e)(f), where we show the calculated conductance for SC gap disorder. The corresponding schematic is in Fig. 2.1(f). The strength of the random gap disorder is parameterized by the standard deviation of 0.06 meV, which accounts for 30% of the mean SC gap. Note that, we avoid using a very large strength of disorder to preserve the SC gap, otherwise, the SC gap has a possibility to be negative which would be unphysical. In the presence of disorder in the SC gap, we again find that the topological ZBCP, occurring beyond the TQPT, is relatively immune to disorder, and no trivial ZBCP is induced below the TQPT. To show that we are not deliberately choosing particular random configurations, we provide more disorder-averaged conductance spectra in Appendix A, where we observe a robust ZBCP beyond the TQPT. Thus, the good ZBCP survives weak disorder in the chemical potential and the SC gap.

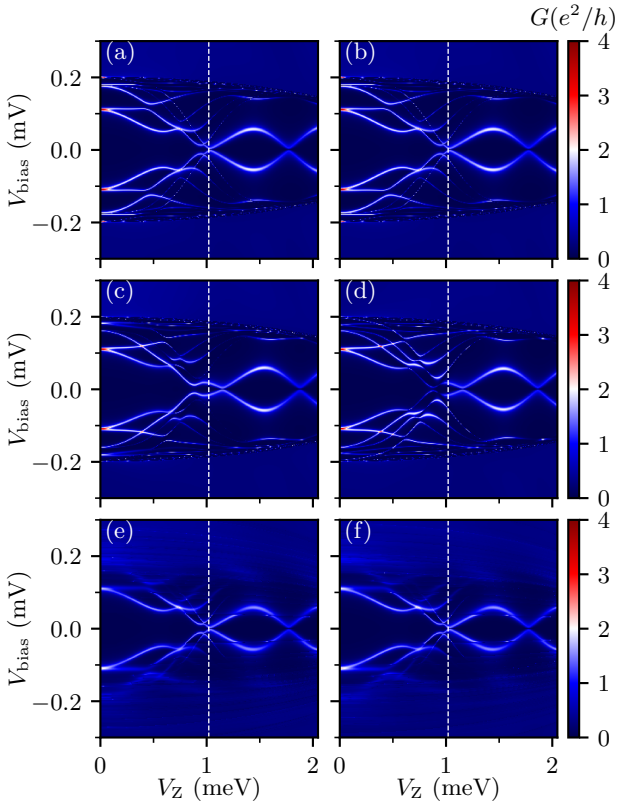

Figure 2.2: (a) and (b) show an example of the good ZBCP in a pristine nanowire with the self-energy in a 1 μm wire. The color plots show the differential tunneling conductance G as a function of V_{Z} (x axis) and V_{bias} (y axis) from the left lead (left column) and the right lead (right column). The SC gap collapses $V_{\text{Z}c} = 3$ meV. The TQPT is labeled in the white dashed line at $V_{\text{Z}} = 1.02$ meV. The complete correlation conductance measurements are shown in Fig. A.1; (c) and (d) show an example of the good ZBCP in the presence of a small amount of disorder in the chemical potential in a 1 μm wire. The parameters are: standard deviation of disorder in the chemical potential $\sigma_\mu = 0.4$ meV, SC gap collapse $V_{\text{Z}c} = 3$ meV. The TQPT is labeled in the white dashed line at $V_{\text{Z}} = 1.02$ meV. The complete correlation conductance measurements are shown in Fig. A.2; (e) and (f) show an example of the good ZBCP in the presence of disorder in the SC gap in a 1 μm wire. The parameters are: standard deviation of disorder in the gap $\sigma_\Delta = 0.06$ meV, mean parent SC gap $\Delta_0 = 0.2$ meV, and SC gap collapse $V_{\text{Z}c} = 3$ meV. The TQPT is labeled in the white dashed line at $V_{\text{Z}} = 1.02$ meV. The complete correlation conductance measurements are shown in Fig. A.3.

2.2.2 The bad ZBCP

The bad ZBCP is topologically trivial because it exists below the TQPT. In Fig. 2.3, we present the calculated conductance spectra for the nanowire in the presence of a QD at its end, as shown in Fig. 2.1(b). In Figs. 2.3(a)(b), we find that two ABSs coalesce into a zero-energy bound state producing a stable ZBCP from $V_{\rm Z} = 0.6$ to 0.9 meV. These two ABSs cross at zero energy several times before $V_{\rm Z}$ reaches the TQPT. If the amplitudes of crossings are tiny, within the finite energy resolution scale in experiments (where thermal broadening also provides a finite energy resolution around zero energy), these crossings may be incorrectly identified as ZBCPs although they arise from almost-zero-energy trivial ABSs, not from isolated MBSs. Apart from the fact that the trivial ZBCPs arise below the TQPT, the trivial ZBCPs also differ from the topological ZBCPs in the amplitude of the ZBCP oscillation. In short nanowires ($L = 1$ μm), the true Majorana-induced ZBCP should have a prominent oscillation in the topological regime [as shown in the right of the white dashed line in Figs. 2.2(a)(b)]. However, in Figs. 2.3(a) and 2.3(b), the ZBCP only has a small amplitude of the ZBCP oscillation. Admittedly, one could go to a very high magnetic field to measure the amplitude of the ZBCP oscillation, but this may not be feasible because the SC gap may collapse at such a high magnetic field. Thus, if the SC gap collapses even below the TQPT (e.g., $V_{\rm Zc} = 1$ meV shown in Fig. 2.3 is smaller than the nominal TQPT 1.02 meV), one will never expect to observe the real Majorana mode under such a situation. We believe that in most of the current experimental samples, the bulk SC gap collapse happens before the TQPT is reached, dooming any manifestation of the MZMs.

Besides the QD, the inhomogeneous potential [as shown in Fig. 2.1(c)] can also induce the bad ZBCP as shown in Figs. 2.3(c) and 2.3(d). We take the same Gaussian form of $V(x)$ in the

inhomogeneous potential case as in the QD case except that the potential is now extended over the bulk of the nanowire instead of being confined to the end as it is for the QD. Thus, both QDs and inhomogeneous potential induce bad ZBCPs below the TQPT.

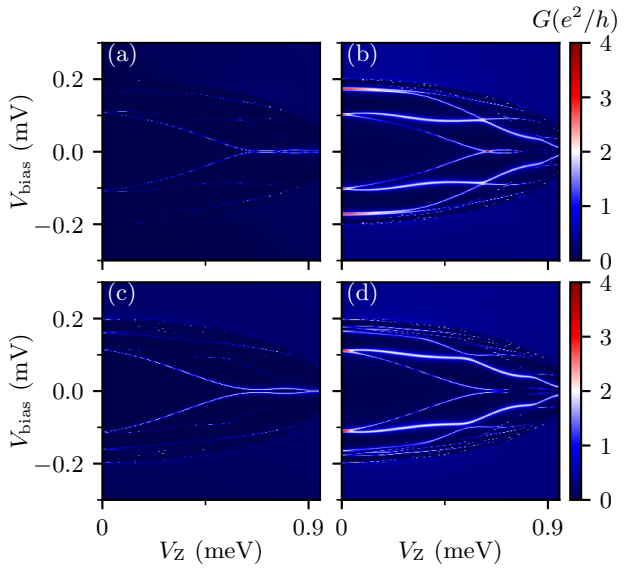

Figure 2.3: Two examples of the bad ZBCP due to the QD in (a) and (b) and the inhomogeneous potential in (c) and (d) respectively with the self-energy in a 1 μm wire. The left (right) column shows the conductance measured from the left (right) lead. For the QD case [(a) and (b)], the parameters are: SC gap collapse $V_{\rm Zc} = 1$ meV, the peak value of the Gaussian-shaped QD $V_{\rm D} = 1.7$ meV, and the size of the QD $l = 0.2$ μm. For the inhomogeneous potential case [(c) and (d)], the parameters are: SC gap collapse $V_{\rm Zc} = 1$ meV, the peak value of the Gaussian-shaped potential confinement $V_{\rm max} = 1.4$ meV, and the linewidth $\sigma = 0.15$ μm. The complete correlation conductance measurements are shown in Fig. A.4 for the QD and Fig. A.5 for the inhomogeneous potential respectively.

2.2.3 The ugly ZBCP

The ugly ZBCP induced by disorder is also topologically trivial. In Fig. 2.4, we present two distinct configurations of the random disorder in the chemical potential, where the schematic is shown in Fig. 2.1(d). Figures 2.4[(a) and (b)], which are calculated conductance from the left and right lead, respectively, share a common disorder configuration; Figs. 2.4(c) and (d) share another common configuration. The disorder-induced ugly ZBCPs are ubiquitous. We note that

the disorder configuration in a given sample is not necessarily fixed and most likely changes as various gate voltages are tuned to optimize the ZBCPs, as is the common experimental practice. (The same happens also in thermal cycling.) For example, the occurrence of the disorder-induced ZBCP in Fig. 2.4(a) could shift from the left lead to the right lead as shown in Fig. 2.4(d). In addition, under the same configuration of disorder [e.g., Fig. 2.4(a) versus (b), and Fig. 2.4(c) versus (d)], we also find the end-to-end correlation from both ends, although this arises here simply due to the shortness of the wire. Thus, random disorder is capable, particularly when gate voltages are tuned so as to modify the disorder configuration in a given sample, of producing well-correlated ZBCPs in nanowires although these ZBCPs are completely trivial. Of course, it is possible that the end-to-end correlations are absent for ugly ZBCPs in a given situation (even for a short wire) since the correlations in the trivial ZBCPs depend on many details and are not universal nonlocal properties. More examples are provided in Appendix A.

For completeness, we also study the nanowire in the presence of disorder in the effective g factor and obtain qualitatively similar results as presented in Fig. 2.5. This corresponds to the schematic shown in Fig. 2.1(e). Again, Figs. 2.5(a) and 2.5(b) share a common disorder configuration; Figs. 2.5(c) and 2.5(d) share another common configuration. Therefore, we conclude that, in the short wire, the disorder-induced trivial ABS not only resembles Majorana-induced ZBCP but also manifests the pseudo-end-to-end correlation from two ends, which could be very misleading in experiments. We emphasize again that whether end-to-end correlations are present for ugly ZBCPs depends on many details, and short wires may or may not manifest end-to-end correlations for ugly ZBCPs in specific instances. The important point is that the existence of end-to-end conductance oscillations cannot be construed to be smoking-gun evidence for good ZBCPs since ugly ZBCPs manifest them (as do the bad ZBCPs also) in many instances.

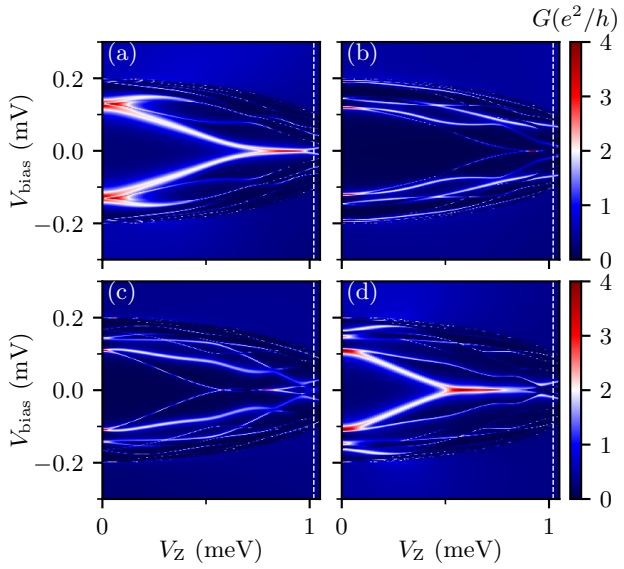

Figure 2.4: Two examples of the ugly ZBCP in the presence of a large amount of disorder in the chemical potential with the self-energy in the 1 μm wire. (a) and (b) share a common configuration of disorder; (c) and (d) share another common one. The left(right) column shows the conductance measured from the left(right) lead. The parameters are: standard deviation of disorder in the chemical potential $\sigma_\mu = 1$ meV, SC gap collapse $V_{\rm Zc} = 1.2$ meV. The nominal TQPT is labeled in the white dashed line at $V_{\rm Z} = 1.02$ meV. The complete correlation conductance measurements are shown in Fig. A.6.

2.2.4 Zero magnetic field

All preceding conductance spectra are calculated for a fixed chemical potential μ as a function of $V_{\rm Z}$; however, we additionally show the nonlocal end-to-end conductance measurement at zero magnetic fields as a function of the chemical potential in Fig. 2.6 to theoretically reproduce the experiment in Ref. [51]. In Fig. 2.6, the left (right) lead measurements are shown in the first (second) row. All three mechanisms (good, bad, ugly) discussed in this article are presented in Fig. 2.6. The first column is for the pristine nanowire; the second and third columns are in the presence of the QD and inhomogeneous potential respectively; the fourth and fifth columns are both in the presence of disorder in the chemical potential. Two separate conductance spectra in the ugly case due to two different configurations are presented here again to demonstrate that the

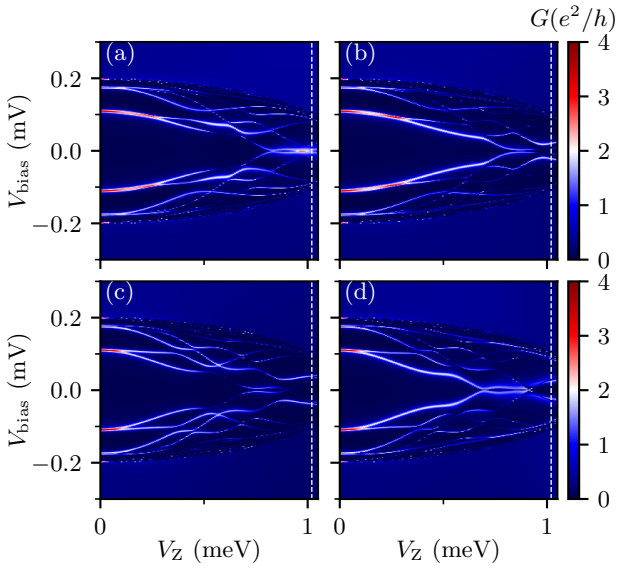

Figure 2.5: Two examples of the ugly ZBCP in the presence of disorder in the effective g factor with the self-energy in the 1 μm wire. (a) and (b) share a common configuration of disorder; (c) and (d) share another common one. The left (right) column shows the conductance measured from the left (right) lead. The parameters are: standard deviation of disorder in the effective g factor is $\sigma_g = 0.8$, SC gap collapse $V_{\rm Zc} = 1.2$ meV. The nominal TQPT is labeled in the white dashed line at $V_{\rm Z} = 1.02$ meV. The complete correlation conductance measurements are shown in Fig. A.7.

specific disorder choice is not important for the physics being discussed. Since the nanowire is short ($L = 1$ μm), the nonlocal conductance measurements are trivially correlated. In addition, we notice that the bad and ugly cases will bring down the fermionic subgap states to lower energies as opposed to the good case. This is particularly noticeable for the bad case in Fig. 2.6 where the subgap trivial states at zero field happen to be almost near zero energy although the system is simply a non-topological s-wave Bardeen-Cooper-Schrieffer (BCS) SC by construction. Therefore, whenever there is strong disorder in the nanowire, there could be prominent fermionic subgap bound states at both ends of the wire, even at the zero magnetic field. This further implies that if one already finds fermionic subgap states in the system, the chance of seeing an ABS mimicking MBS will be highly enhanced at finite magnetic fields, because those fermionic subgap states could move to zero, and then cross with each other, which could produce

trivial ZBCPs within the finite experimental energy resolution. Thus, it is important to ascertain that there are no low energy subgap states in the nanowire at zero field before embarking on the V_Z-dependent search for ZBCPs in the hybrid system.

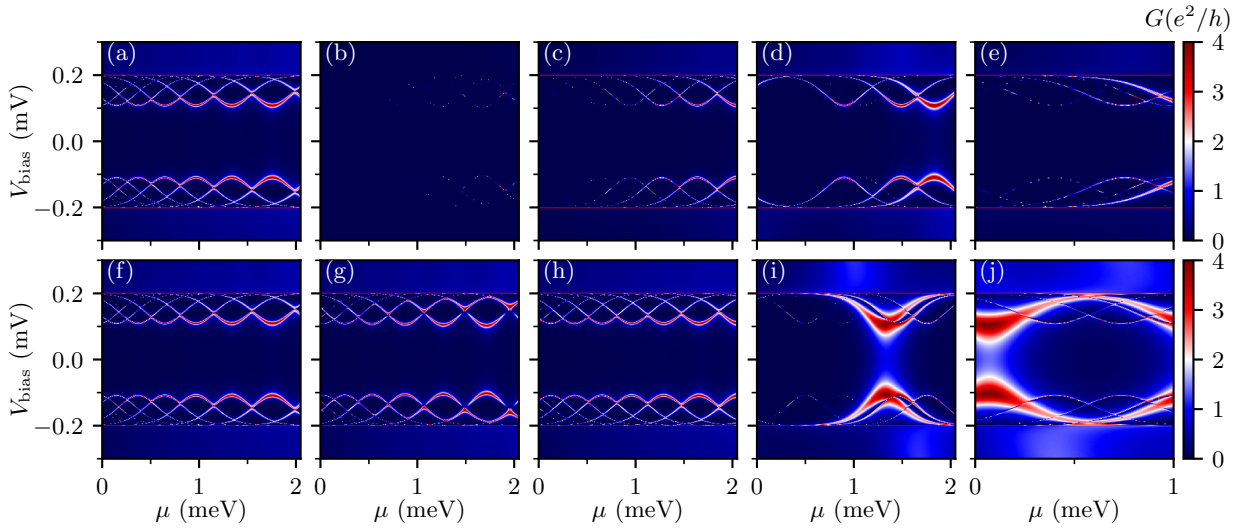

Figure 2.6: The conductance spectra as a function of the chemical potential μ and V_{bias} at zero magnetic field in the 1 μm wire with the self-energy. The first (second) row shows the conductance measured from the left (right) lead. (a) and (f) are in the pristine nanowire case; (b) and (g) are in the presence of a QD with the peak value of $V_{\text{D}} = 1.7$ meV and the size of $l = 0.2$ μm; (c) and (h) are in the presence of an inhomogeneous potential with the peak value of $V_{\text{max}} = 1.4$ meV and the linewidth $\sigma = 0.15$ μm; (d), (i) and (e), (j) are in the presence of disorder in the chemical potential with two distinct configurations. The standard deviation of disorder is $\sigma_\mu = 3$ meV.

2.3 Discussion

In addition to the conductance spectra from the lead at a particular end, we compare the nonlocal correlation measurements in the short wire ($L = 1$ μm) with the one in the long wire ($L = 3$ μm). We note that the long and short here refer only to the actual physical length of the wire. The nonlocal correlation measurements for each case ("good"/"bad"/"ugly") in the short wire are shown in Figs. 2.2-2.6. We additionally provide the nonlocal conductance measure-

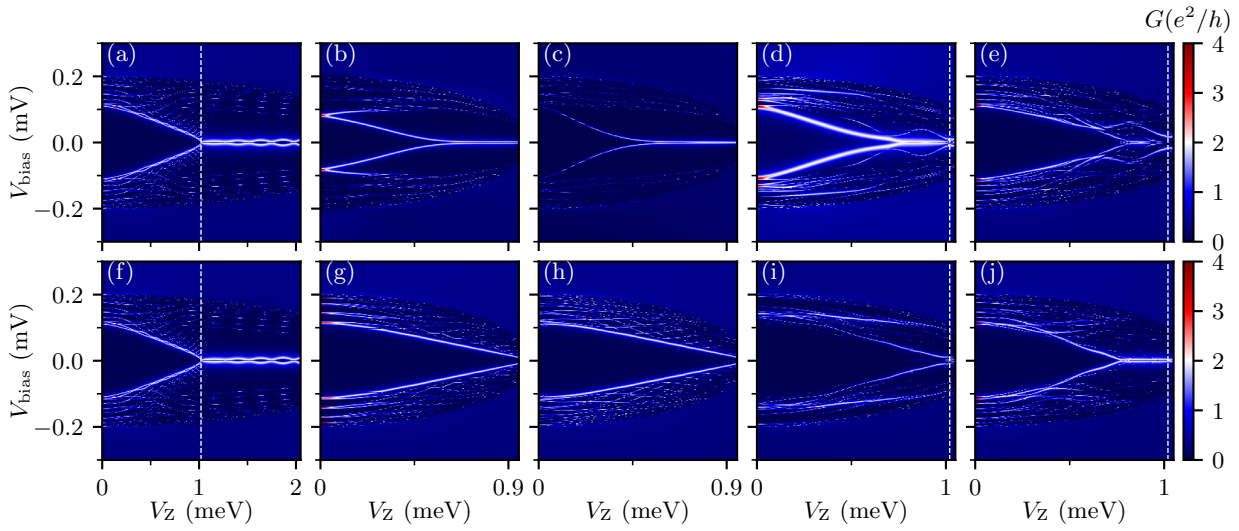

Figure 2.7: Conductance spectra measured from the left lead (the first row) and the right lead (the second row) in the long wire $L = 3$ μm. (a) and (f) are the good ZBCP in the pristine nanowire with the SC gap collapse $V_{\rm Zc} = 3$ meV; (b) and (g) are the bad ZBCP in the presence of the QD with the peak value of $V_{\rm D} = 0.6$ meV and the size of $l = 0.4$ μm. The SC gap collapse is $V_{\rm Zc} = 1$ meV; (c) and (h) are the bad ZBCP in the presence of the inhomogeneous potential with the peak value of $V_{\rm max} = 1.2$ meV and the linewidth of $\sigma = 0.4\mu$m. The SC gap collapse is $V_{\rm Zc} = 1$ meV; (d) and (i) are the ugly ZBCPs in the presence of disorder in the chemical potential, where $\sigma_\mu = 1$ meV. The SC gap collapse is $V_{\rm Zc} = 1.2$ meV; (e) and (j) are the ugly ZBCP in the presence of disorder in the effective g factor, where $\sigma_g = 0.6$. The SC gap collapse is $V_{\rm Zc} = 1.2$ meV.

ments in the long wire in Fig. 2.7. The left lead and right lead measurements are in the first and second row respectively. In Fig. 2.7, the first column is for the pristine nanowire; the second to the fifth column is in the presence of the QD, inhomogeneous potential, disorder in the chemical potential, and disorder in the effective g factor respectively. These nonlocal measurements inform us of the properties of ZBCPs and the corresponding likely mechanisms; for instance, in Fig. 2.7(a) and 2.7(f) (the good case), the left and right measurements show conclusively identical conductance spectra. For the bad and ugly cases in the long wire, the ABS-induced ZBCPs are completely uncorrelated as they are determined by the detailed shape of the QD, inhomogeneous potential, or disorder profile at both ends of the nanowire. However, it is a different scenario in the short wire limit; for instance, in Fig. 2.4 (the ugly case), the ZBCPs measured from both ends will be trivially correlated just because of the short wire. Imagine a scenario where none of the physics being discussed here was known theoretically and the very first experimental paper reported results like Fig. 2.4, everything would be temptingly deemed to be well-established as the discovery of topological MZMs since it is a quantized ZBCP and it is nonlocal. Unfortunately, this conclusion would be most likely incorrect as we know from the results presented in this chapter where we find that disorder-induced ZBCPs mimic many features of the MZM-induced ZBCPs, particularly in short wires. The same is true for Fig. 2.5, where Figs. 2.5(a) and 2.5(b) as well as Fig. 2.5(c) and 2.5(d) appear to manifest similar ZBCPs from both ends although the ZBCPs are purely ugly and nontopological— thus reinforcing the conclusion that the mere fine-tuned observation of end-to-end ZBCP correlations by itself cannot be construed to be a signature or evidence for topological MZMs. Purely ugly disorder-induced ZBCPs could manifest end-to-end correlations just accidentally. A key problem is that there is no way to know *a priori* whether the experimental wires are long or short since the nanowire coherence length is

completely unknown (and long or short is defined with respect to the coherence length) although the current experimental samples with $L \sim 1$ micron are most likely in the short wire regime. For the results of long wires in Fig. 2.7, which are longer than the SC coherence length, only the real MZM would have the perfect end-to-end correlation. The trivial ABS, on the other hand, may have a pseudo-end-to-end correlation in the short wire (typically shorter than 1 μm). This leads to the conundrum that although the nonlocal correlation measurement, in principle, can serve as a reliable diagnostic for MZMs, the prerequisite for this indicator being the long nanowire limit may not be satisfied in the experimental samples. Unless sufficiently long nanowires (at least longer than the SC coherence length) can be fabricated, the observation of the end-to-end correlation can never prove the existence of topological MZMs. In fact, as a cautionary note, we emphasize that such accidental end-to-end correlations could happen for ugly ZBCPs even in the long wire limit as shown in Figs. A.6 and A.7 in Appendix A. This is of course purely accidental with no significance except that if one post-selects and fine-tunes experimental results, a certain fraction of ugly ZBCPs will manifest apparent nontopological end-to-end correlations which could be mistaken for the nonlocal correlation of real topological MZMs. Of course, generically, short wires do not manifest any end-to-end conductance correlations arising from trivial ZBCPs as shown in Appendix A, but the important point here is that trivial ZBCPs in short (or even, long) wires can be correlated from the two ends under suitable conditions, making the correlation test not conclusive unless one can be sure that the experiment is indeed being carried out in the no-disorder limit.

2.4 Conclusion

We have provided extensive numerical simulations for the Majorana properties of SM nanowires in the SM-SC hybrid structures, taking into account the essential effects, including QDs and inhomogeneous potentials along the wire as well as random disorder in the chemical potential or the SC gap or the effective g factor. We find three different types of tunneling ZBCPs: the good, the bad, and the ugly. The good ZBCPs arise from the intrinsic topological properties of the system for the Zeeman field above the TQPT point, with the ZBCPs from the two ends of the wire showing a high level of correlations even in long wires by the nonlocal topological properties of the system. We show that good ZBCPs are immune to weak disorder in the chemical potential and the SC gap, and are robust to system parameters such as the chemical potential or Zeeman field provided one is the topological regime (i.e., Zeeman field above the TQPT value). The bad ZBCPs arise from QDs or other inhomogeneous potentials in the nanowire, and are essentially quasi-Majorana modes where the two MZMs, instead of being well-separated as in the good case, overlap with each other giving rise to near-zero-energy ABSs. These ABSs produce trivial ZBCPs for Zeeman field values below TQPT, mimicking many properties of good ZBCPs, including even the end-to-end correlation properties in short wires. Since experimentally neither the TQPT critical field nor the SC coherence length is known, the mere observation of ZBCPs by themselves (or even the observation of end-to-end correlations) hardly could be construed to be evidence supporting the existence of MZMs in nanowires since bad ZBCPs are capable of mimicking the properties of the good ZBCPs. The situation becomes worse when strong random disorder is considered to lead to "ugly" ZBCPs, which are trivial, but may mimic all the properties of good ZBCPs, including end-to-end correlations. Our direct comparison with the

available experimental data indicates that most experimental ZBCP observations are consistent with the ZBCPs being ugly although one can never be sure without knowing what the TQPT field is and whether the nanowire is long or short from a topological viewpoint. The fact that subgap conductance and even some end-to-end conductance correlations have been observed already for the zero magnetic field in nanowires [51] suggests that strong disorder is playing a key role in the existing SM-SC samples, and the observed ZBCPs are likely to be of the undesirable ugly type.

A key difference between the bad and the ugly ZBCPs is the fact that the system manifesting bad ZBCPs should, in principle, eventually manifest good ZBCPs at larger magnetic field values above the TQPT. By contrast, the strongly disordered systems manifesting ugly ZBCPs cannot manifest topological properties at any Zeeman field since disorder has eliminated the TQPT. It may therefore appear that one should be able to observe good ZBCPs in a system manifesting bad ZBCPs simply by increasing the magnetic field so that the bad ZBCPs below TQPT transmute to good ZBCPs above TQPT. The same can also be achieved in principle by tuning the chemical potential through the TQPT. Although theoretically appealing, this crossover of trivial ZBCPs arising from ABS to topological ZBCPs arising from MBS has never been experimentally achieved because of the SC bulk gap collapse problem in real nanowires, where with increasing field, the bulk gap eventually collapses at some characteristic field ($\sim$ 1 T), thus severely restricting the field range of the topological regime. In particular, if the gap collapse happens at a field below TQPT, there is no hope ever of observing the topological regime with true Majorana modes. Current experiments suggest that this is the likely scenario, making the gap collapse a very serious problem preventing the existence of topological Majorana modes.

An equally serious problem is that most experimental nanowires may be in the "short wire" ($\sim$ 1 μm) regime, where the concept of topology simply does not apply even if the system is

fairly disorder-free. In such a situation, the MBSs overlap producing near-zero-energy ABSs which then produce bad ZBCPs. The fact that experimentally Majorana oscillations are never seen, however, indicates that this situation may not be the dominant scenario in the current experimental samples, where strong random disorder and the associated ugly ZBCPs arising purely from random disorder is the dominant physical mechanism.

Our most important finding in this chapter is that although weak disorder does not adversely affect the topological properties of the MZMs, strong random disorder, with the root mean square fluctuation of disorder being comparable to or larger than the average system parameter such as the SC gap or the chemical potential, not only suppresses all topological properties but also introduces relatively stable ZBCPs with conductance values $\sim 2e^2/h$, closely mimicking recent experimental results.

Chapter 3: Nonlocal conductance in three-terminal devices

In the last chapter, we establish the definition of the good, the bad, and the ugly ZBCPs, which paves the way for the answer to the next natural question: how to differentiate the three types of ZBCPs through their transport properties. Therefore, we resort to the three-terminal nonlocal conductance in Majorana nanowires, and focus on the key question that whether such nonlocal conductance can decisively distinguish between trivial and topological Majorana scenarios in the presence of chemical potential inhomogeneity and random impurity disorder.

As we discussed in Chapter 2, the measurement of local conductance through NS tunneling, just by itself, is useless in determining the good, bad, and ugly ZBCP, because many accidental ABS have nearly zero energy in the nanowire [136]. Even if the disorder is weak, the problem of ABS itself is already notoriously serious [72]. Without any bulk information (e.g., the bulk gap as a function of the Zeeman field), the local conductance cannot distinguish whether the Andreev state is perfect or not (the MBS, is simply a "perfect" ABS, being a precise zero energy state, the MZM), and thus whether the system is in the topological regime or not. What is even worse, the nanowire system is often highly disordered, and the strong disorder creates ubiquitous trivial "class D" ZBCP that can even appear to be quantized through careful fine-tuning of system parameters (e.g., various gate voltages) [112]. Therefore, the local conductance measurement is not sufficient in distinguishing ABS from MBS.

One crucial drawback of the two-terminal ZBCP tunneling measurements is that the experiment does not probe bulk properties and cannot, therefore, provide any direct information on nonlocality, which is the characteristic signature of topological MZMs. There have been suggestions and efforts to circumvent this problem by doing tunneling measurements from both ends and looking for correlations in the ZBCPs produced from the two ends and/or carrying out local conductance measurements using tunnel probes throughout the nanowire. But, as already known, such inherently two-terminal measurements are incapable of providing information about the bulk gap closure and reopening, which, along with the appearance of a quantized ZBCP, is the hallmark of MZM physics. In this chapter, we analyze a promising candidate, a direct measurement of the three-terminal nonlocal conductance, as a possible probe for MZMs— this measurement is in principle capable of providing the bulk gap information missing in the two-terminal NS tunneling measurement.

A conceptually clean way to detect the bulk property is the nonlocal conductance measuring the tunneling conductance from one end to the other. Several experiments have already performed measurements in three-terminal devices [54, 55], though they are incomplete and inconclusive, because only a few situations are studied, and no complete picture has emerged with characteristic MZM signatures. Given the potential importance of nonlocal three-terminal experiments in the MZM observation, we develop a complete theory for nonlocal conductance in nanowires including effects of potential inhomogeneity (e.g., QDs or a smoothly varying chemical potential) and random disorder, comparing these realistic results with the pristine situation. Our theory, comparing "good" (i.e., pristine), "bad" (i.e., inhomogeneous potential and QDs), and "ugly" (i.e. random disorder) cases [77], should serve as a guide for forthcoming nonlocal conductance measurements. We already know that disorder can create accidental almost-quantized ZBCP on

its own in the local conductance from Chapter 2, but the behavior of nonlocal conductance in the presence of inhomogeneous potential and random disorder has not been studied systematically in the literature, and therefore, it is unclear at this stage whether the bulk signatures in the nonlocal conductance of pristine systems survive inhomogeneous potential and/or disorder.

In principle, the nonlocal conductance should be decisive in establishing the existence or not of MZMs since it contains the bulk information and thus can identify the proximity gap as well as its closing and reopening associated with the TQPT: The conductance is vanishingly small above the bulk parent SC gap and below the proximity gap. Therefore, we may directly see where the bulk gap is and how the bulk gap closes (and then reopens) as the magnetic field increases. However, the measurement of nonlocal conductance poses a problem that the signal is too weak since the measurement is nonlocal (and thus of higher order in strength). In this chapter, we will show explicitly how small the nonlocal conductance could be compared to the local conductance, especially in the presence of disorder, which usually dominates in experiments. Therefore, one should be careful not to confuse the background noise with the small signal of nonlocal conductances. Our proposal provides a quantitative guide on the expected signal strength of nonlocal conductance.

Despite the ambiguities in interpreting the nonlocal conductance in practice, we have an advantage in theory that we can directly calculate the TI [114] to identify the topological property. This is impossible in experiments— we explicitly know by construction whether a particular calculated conductance feature, no matter how weak, arises from topological or trivial physics. We calculate the topological visibility (TV) which is only well defined for the gapped state. To determine whether it is gapped or not, we resort to thermal conductance, which measures the total transmission of electrons and holes. The thermal conductance should peak at a quantized

value [83] at the TQPT. Therefore, in theory, we can unambiguously separate the three situations, the good, the bad, and the ugly, because we know by construction which results belong to which category. In experiments, however, one only has the final conductance results, where distinguishing between topological ("good") and trivial ("bad" or "ugly") may be a huge challenge, particularly if the nonlocal conductance signals are so low that they are overwhelmed by noise leading to all three situations producing qualitatively similar conductance. We already know from the situation in the local conductance, as obtained by two-terminal NS tunneling, even ZBCPs which appear to be quantized may be generically "bad" or "ugly", so one should be very careful in interpreting the nonlocal conductance experimental results when they come out.

We first present the electrical conductance and thermal conductance of a pristine nanowire (good ZBCP) to provide a general picture of what the nonlocal conductance in the three-terminal device should ideally look like. Next, we consider a more complicated case— the bad ZBCP in the presence of the QD and an inhomogeneous chemical potential. Then we add disorder to the wire to study the disorder effect, where we find weak disorder preserves the good ZBCP while intermediate disorder can induce the trivial ugly ZBCP. When disorder is very strong, the whole concept of the topological SC is pointless since the SC gap is destroyed leading to Anderson localization. Therefore, the strongly disordered nanowire just breaks into a series of QDs, which should be described by the RMT [111, 112, 149–152]. (We will revisit this issue from RMT in Chapter 5.) Finally, we consider a more realistic scenario by combining the QD and the disorder. To correspond to the realistic experimental scenarios, we also consider short wire lengths as well as the magnetic field-induced bulk gap collapse situations to investigate realistic complications expected to arise in the experiments. We present a few sets of the representative results of the good and ugly ZBCP in the main text, and relegate the rest to Appendix C, where most of our

detailed results are provided.

3.1 Theory

The most general model for the SM-SC nanowire has already been established in the last chapter in Sec. 2.1. Here, the additional part in the model is the extra lead that provides the possibility for the nonlocal conductance and thermal conductance, which we will explain as follows.

3.1.1 Electrical conductance, thermal conductance, and topological invariant

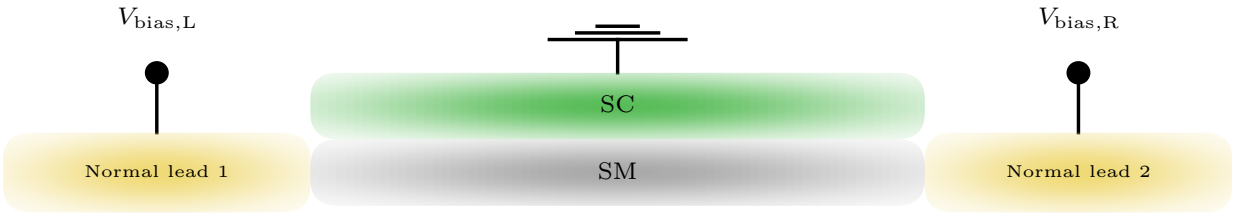

Figure 3.1: The schematic of the three-terminal device with two normal leads in yellow and one grounded SC in green. The corresponding two-terminal device for measuring the local tunneling conductance simply removes one of the contacts at the wire ends (i.e., either lead 1 or lead 2 is present for the two-terminal whereas both are present for the three-terminal).

We show the three-terminal device to measure the nonlocal conductance in Fig. 3.1. The SM (gray) as a scattering region is covered by a grounded SC lead (green) and separated by two normal leads (yellow). We apply a bias $V_{\mathrm{bias,L}}$ on the left normal lead and $V_{\mathrm{bias,R}}$ on the right normal lead. The normal lead is described by a Hamiltonian in Eq. (2.23).

Here, we first want to clarify the ambiguity of the two-terminal device and three-terminal device due to the inconsistent nomenclature used in this community: The two-terminal device in Refs. [75, 83] is essentially the three-terminal device in Refs. [54, 65]. In this chapter, we reserve

the term "two-terminal"—one grounded SC lead covering SM plus one normal lead at the end—to denote the usual local conductance measurement, as initially proposed in theory and performed in experiments. However, the "three-terminal device"—one grounded SC lead covering SM plus two normal leads at both ends— measures the nonlocal conductance, i.e., the conductance matrix in Eq. (3.3), which is recently suggested in theory [65, 75] and performed in experiments [51, 54]. In the two-terminal device, we can still perform the correlation measurement as in Chapter 2 by isolating one lead when measuring from the other. On the contrary, both normal leads are always attached to the SM when measuring conductance in the three-terminal device. The local conductance in the two schemes will be slightly different, but the nonlocal conductance is only achievable in the three-terminal device.

To calculate the electrical and thermal conductance in the three-terminal device, we use the S matrix formalism with [153]

$$\mathcal{S} = \begin{pmatrix} S_{\mathrm{LL}} & S_{\mathrm{LR}} \\ S_{\mathrm{RL}} & S_{\mathrm{RR}} \end{pmatrix}, \tag{3.1}$$

where each block of the scattering matrix connecting lead j to lead i is

$$S_{ij} = \begin{pmatrix} S_{ij}^{ee} & S_{ij}^{eh} \\ S_{ij}^{he} & S_{ij}^{hh} \end{pmatrix}. \tag{3.2}$$

Here the superscript represents a process of transmission from type β to type α, where $\alpha, \beta = e, h$ stand for the electron and hole. The numerical calculation of the S matrix (3.1) is performed [16, 138, 140, 141, 147, 154] with the help of KWANT [138]. We discretize the continuum Hamiltonian into a finite-difference tight-binding model [124] by setting the lattice constant $\delta x = 10$ nm. We also model the chemical potential of the lead $\mu_{\mathrm{lead}} = 25$ meV and the

height of the barrier at the NS junction equaling 5 meV [137] to match the normal conductance in experiments [9].

The local conductance (G_{LL} and G_{RR}) and nonlocal conductance (G_{LR} and G_{RL}) in the differential conductance matrix $\mathcal{G}$ at zero temperature is [51, 54, 141, 153]

$$\mathcal{G} = \begin{pmatrix} G_{\mathrm{LL}} & G_{\mathrm{LR}} \\ G_{\mathrm{RL}} & G_{\mathrm{RR}} \end{pmatrix} = \begin{pmatrix} \frac{\partial I_{\mathrm{L}}}{\partial V_{\mathrm{bias,L}}} & -\frac{\partial I_{\mathrm{L}}}{\partial V_{\mathrm{bias,R}}} \\ -\frac{\partial I_{\mathrm{R}}}{\partial V_{\mathrm{bias,L}}} & \frac{\partial I_{\mathrm{R}}}{\partial V_{\mathrm{bias,R}}} \end{pmatrix}, \tag{3.3}$$

where I_{L} (I_{R}) is the current entering the left (right) normal lead from the scattering region, and $V_{\mathrm{bias,L}}$ ($V_{\mathrm{bias,R}}$) is the bias applied on the left (right) normal lead. Note that different sign conventions may be adopted [65] on the nonlocal conductance, though it does not affect any real physical conclusion as long as we stick to one convention consistently. In Blonder-Tinkham-Klapwijk formalism [140], the local conductance is

$$G_{ii} = \frac{e^2}{h}\left(N_i - \mathcal{T}_{ii}^{ee} + \mathcal{T}_{ii}^{eh}\right), \tag{3.4}$$

and the nonlocal conductance is

$$G_{ij} = \frac{e^2}{h}\left(\mathcal{T}_{ij}^{ee} - \mathcal{T}_{ij}^{eh}\right), \qquad i \neq j, \tag{3.5}$$

where $N_i = 2$ is the number of the electron mode in each single channel lead, and the transmission $\mathcal{T}_{ij}^{\alpha\beta} = \mathrm{tr}\left(\left[S_{ij}^{\alpha\beta}\right]^{\dagger} S_{ij}^{\alpha\beta}\right)$ [$\mathrm{tr}(..)$ for the trace].

The local conductance combined with the nonlocal conductance may be insufficient to distinguish the MBS from ABS in realistic cases, which are dominated by disorder effect. Therefore,

we additionally calculate the thermal conductance which is defined as [83, 152]

$$\kappa_{ij} = \kappa_0(\mathcal{T}_{ij}^{ee} + \mathcal{T}_{ij}^{eh} + \mathcal{T}_{ij}^{he} + \mathcal{T}_{ij}^{hh}), \qquad i \neq j, \tag{3.6}$$

where the quantized peak $\kappa_0 = \pi^2 k_B^2 T/6h$ at temperature T happens at TQPT [155–157] (h for the Planck constant and k_B for the Boltzmann constant). Here, the thermal conductances from both ends are manifestly equal.

To identify the TI in finite-length nanowires, we refer to the TV [114, 124] defined as $\det(S_{\text{LL}})$ and $\det(S_{\text{RR}})$ with a positive value (+1, ideally) indicating trivial regime and a negative value (-1, ideally) indicating topological regime. Therefore, the TQPT is indicated by the zero crossings of the TV when the unitarity of $\det(S_{\text{LL}})$ or $\det(S_{\text{RR}})$ breaks. We additionally impose a phenomenological dissipation term $i\Gamma$ with $\Gamma = 10^{-3}$ meV [124, 139, 148] in the Hamiltonian to circumvent potential numerical singularities from local bound states in the middle of the wire. Such a small dissipation is invariably present in the experiments. We also set the height of the barrier at the NS junction interface to be 0 when calculating the TV.

3.1.2 Quantum dots and inhomogeneous potential

The minimal effective model in Hamiltonian (2.6) shows a pristine nanowire example resulting in good ZBCPs. However, ZBCPs in nanowires used in present experiments are potentially more consistent with the so-called "bad" and "ugly" ZBCPs as we discussed in Chapter 2. We first start with the bad ZBCP and will discuss the ugly ZBCP in the next subsection.

The two main sources that can induce the bad ZBCP are (1) the QD, which we model in the same form as Eq. (2.8), and (2) the inhomogeneous potential, which also takes the same form

as in Eq. (2.11). They only differ in their physical mechanisms. Therefore, they both induce bad ZBCP, mimicking MZM, in a similar manner.

3.1.3 Onsite random disorder

For the ugly ZBCP, unlike the QD and inhomogeneous potential, which both induce the bad ZBCP, the onsite random disorder has threefold effects on the ZBCP: (1) weak disorder can leave the topological regime unchanged, preserving the good ZBCP; (2) strong disorder itself can induce trivial ugly ZBCP. The ugly ZBCP can mimic the good ZBCP in the local conductance measurement; (3) very strong disorder will simply destroy all SC in nanowire and leave the system in the Anderson localized phase [158]. We have already shown the first two effects in Chapter 2, and we will extensively study the third effect in this chapter. The onsite disorder may arise in the chemical potential, parent SC gap, and effective g factor. In this chapter, we will mainly discuss the effects of the disorder in the chemical potential in the same form as in Eq. (2.14), which is the leading disorder in SM nanowire [53, 56].

3.2 Results

In this section, we first show representative electrical conductance, thermal conductance, and TV of the good, bad, and ugly ZBCPs in the three-terminal long nanowire in Secs. 3.2.1, 3.2.2, and 3.2.3. In Sec. 3.2.4, we add disorder to a bad ZBCP case with the QD for a more realistic simulation. We also present results for the short wire in Sec. 3.2.5 for the pristine wire and the nanowire in the presence of intermediate disorder with and without the parent SC gap collapse. Other examples of the bad and ugly ZBCP are presented in Appendix C. We provide most of

our results in Appendix C to help with the readability of the text and not because the results in Appendix C are less important.

3.2.1 Pristine nanowire

We start with the good ZBCP in a pristine nanowire as presented in Fig. 3.2 to show how this proposal works since the good ZBCP provides a milestone of what the real Majorana should ideally look like in the three-terminal device in future experiments. We present the local conductance (G_{LL}, G_{RR}) and nonlocal conductance (G_{LR}, G_{RL}), respectively, from the first column to the last column along with the line cut of the conductance at different V_{Z}.

The conductance in the first row is plotted in their "intrinsic" (i.e., defined by the maximum and minimum values in the plot) color scales—the color bar ranges from 0 to $4e^2/h$ for the local conductance [Figs. 3.2(a) and (b)] and the color bar ranges from $-0.1e^2/h$ to $0.1e^2/h$ for the nonlocal conductance [Figs. 3.2(c) and (d)]. The conductances G_{LL} and G_{RR} plotted in Figs. 3.2(a) and 3.2(b) show the appearance of a quantized ZBCP at the TQPT (cyan line) [29]. The nonlocal conductances (G_{LR}, G_{RL}) shown in Figs. 3.2(c) and 3.2(d) provide a more direct measurement of gap closure as opposed to the local conductance G_{ii}. The gap closure features seen in G_{ii} have been identified previously to be associated with ABSs localized at each end of the nanowire. By contrast, the conductance G_{LR} seen in Fig. 3.2 can only represent contributions from states that are delocalized across the nanowire. Thus, the transport gap closing and reopening seen in Figs. 3.2(c) and 3.2(d) provide direct evidence for a gap closure and reopening associated with TQPT.

In the second row, we present the same calculated conductance data in the opposite way:

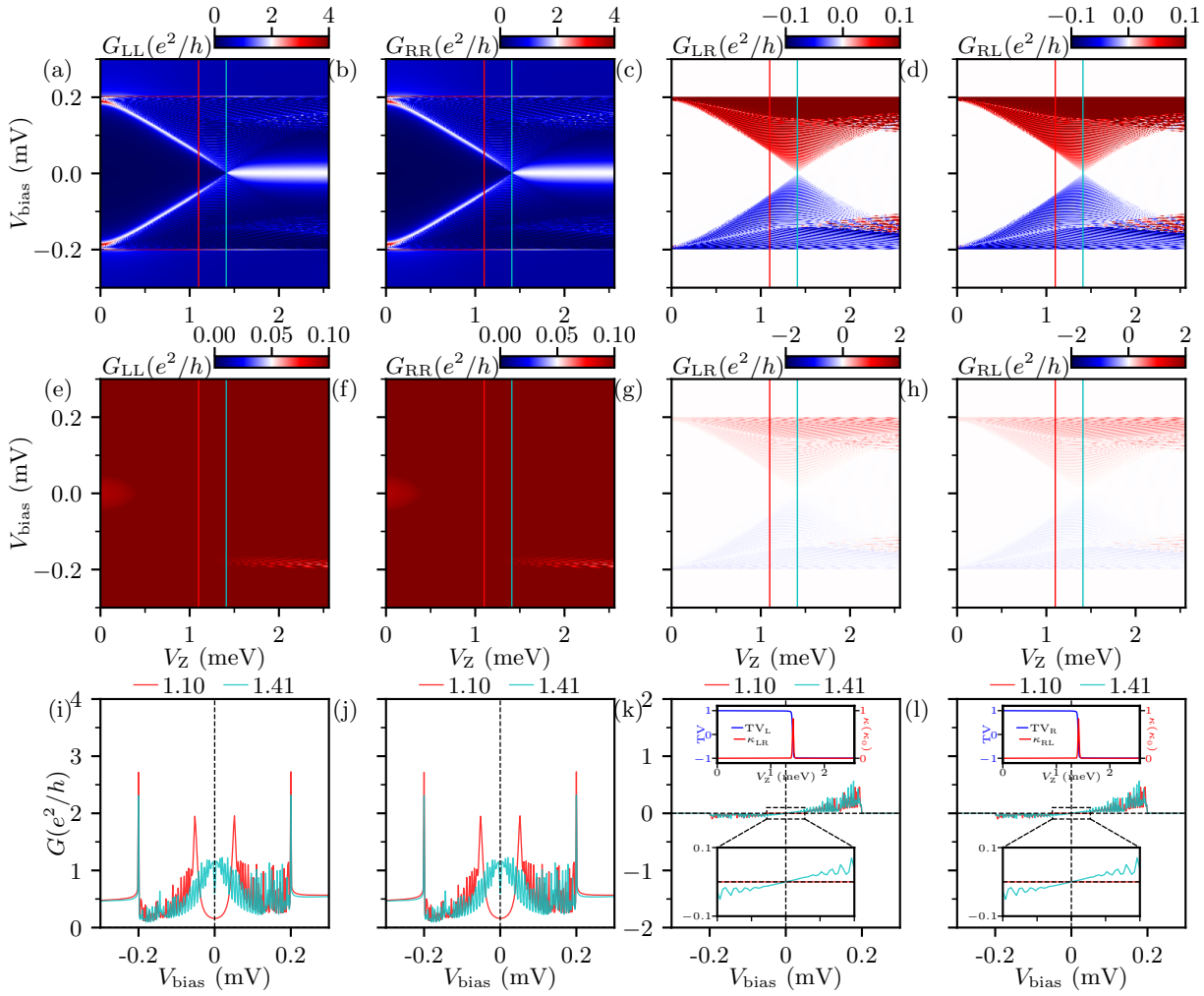

Figure 3.2: The good ZBCP in a pristine nanowire; (a)-(d) show the local and nonlocal conductance in the "intrinsic" color scale. (e)-(h) show the same conductance in the opposite color scale; (i)-(j) show line cuts of the conductance as a function of bias at $V_{\rm Z} = 1.1$ meV and 1.41 meV. The parameters are: chemical potential $\mu = 1$ meV, parent SC gap $\Delta_0 = 0.2$ meV, SM-SC coupling strength $\gamma = 1$ meV, SOC $\alpha = 0.5$ eVÅ, the height of the barrier is 5 meV, and wire length $L = 3$ μm. The corresponding TV from the left (right) and thermal conductance $\kappa_{\rm LR}$ ($\kappa_{\rm RL}$) are shown in the inset of (k) [(l)].

The local conductance is colored with the "intrinsic" scale for nonlocal conductance and vice versa. Although this may look absurd at the first glance— the local conductance is almost saturated at the ZBCP and the nonlocal conductance is nearly invisible everywhere— we still want to emphasize that this is what Majorana would look like in experiments of the three-terminal measurement. Even in the pristine wire, without any disorder or inhomogeneous potential, we almost see nothing in the nonlocal conductance because the nonlocal conductance [Figs. 3.2(g) and (h)] is several orders of magnitudes smaller than the local conductance. The only way we can observe any signature is to measure the conductance with very high precision ($\sim 10^{-2}e^2/h$). This is the premise of the three-terminal measurement. Recent experiments [54, 55] report such nonlocal conductance measurements with the precision of up to $10^{-3}e^2/h$, in an attempt to use three-terminal measurements to distinguish the MBS from ABS. We emphasize that if the signal in any nonlocal three-terminal conductance measurement is comparable to (or even just an order of magnitude less than e^2/h) the local conductance, then the only possible conclusion is that the measurement is dominated by noise and artifacts.

In the third row, we show the line cuts at a specific magnetic field V_{Z} for the local and nonlocal conductance. The red line intersects a trivial regime and the cyan line is at the TQPT (we follow this convention throughout the chapter). By presenting the four conductance plots "redundantly", we emphasize that the local conductance G_{LL} and G_{RR} are identical, and the same for nonlocal conductance G_{LR} and G_{RL}. The inset at the critical point shows a linear dependence of the conductance on the bias voltage.

The measurement of thermal transport provides another indication of gap closure. As seen in the insets of Fig. 3.2(k) and (l), the thermal conductance shows a clear quantized peak [83] indicating the TQPT. While the thermal conductance might be intrinsically more challenging to

measure, we note that the thermal conductance does not show any of the suppression near zero bias that the nonlocal electrical conductance shows.

The degree to which the pristine nanowire is topological can be characterized by the TV, which is plotted in the insets of Figs. 3.2(k) and 3.2(l). The calculated TV for the pristine wire shows a clear transition from -1 to 1 at the TQPT (cyan line), which occurs at the theoretically expected critical Zeeman field $\sqrt{\gamma^2 + \mu^2}$. Thus, in this case, the cyan line represents the unambiguous characterization of when the nanowire is topological. The other panels of Fig. 3.2 that show conductances that are in principle measurable in experiments show the expected characteristics of the topological, nontopological phase, as well as the TQPT. Unfortunately, TV, being a purely theoretical construct, cannot be measured in the laboratory, but it does enable the theory in ascertaining whether a particular experimental sample can in principle manifest topological properties.

3.2.2 Quantum dot and inhomogeneous potential

Once we establish the protocol of three-terminal measurement in the pristine nanowire, we proceed to use this protocol in more realistic models. In this subsection, we consider the effect of a QD and inhomogeneous potential on the nanowire, which can lead to a ZBCP similar to the pristine topological nanowire seen in Figs. 3.2(a) and (b). This ZBCP may be good (i.e., topological) or bad (i.e., trivial) depending on the situation— just looking at the ZBCP itself would not tell us whether the ZBCP is good or bad; one needs to know whether the ZBCP is below or beyond the TQPT to figure out its topological nature.

We first add a QD at the left end of the nanowire, and present the electrical conductance in

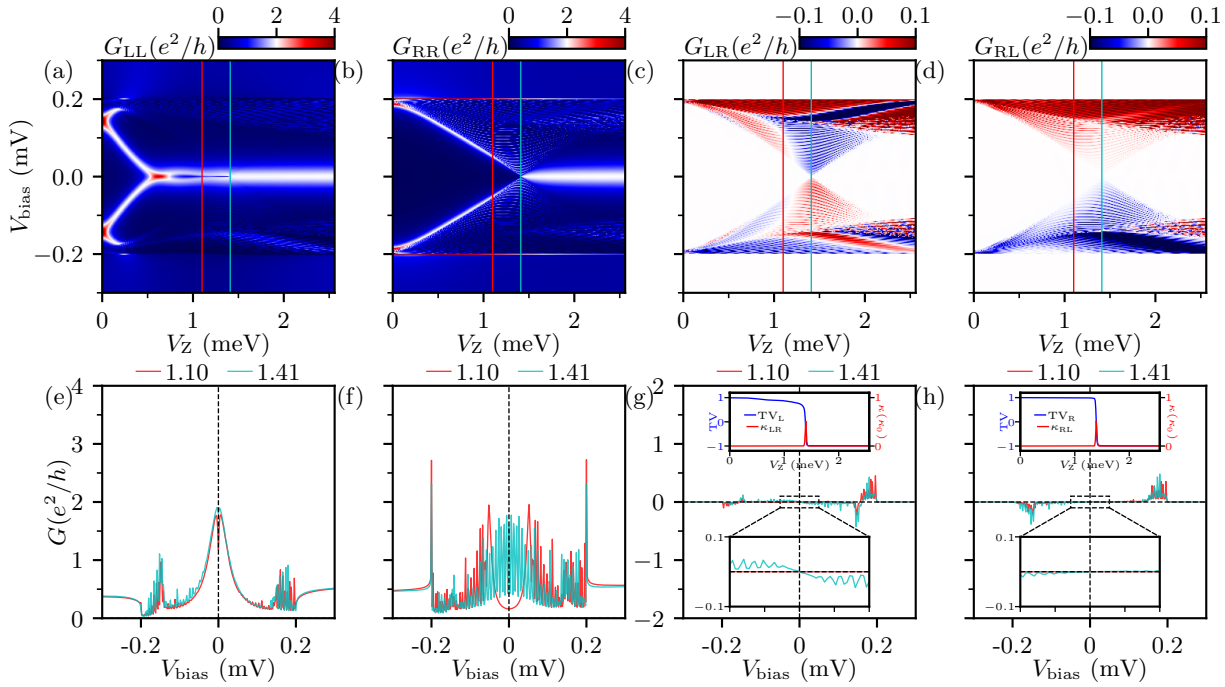

Figure 3.3: The bad ZBCP in a nanowire with the QD at the left end. (a)-(d) show the local and nonlocal conductance in the "intrinsic" color scale; (e)-(h) are the corresponding line cuts of the conductance as a function of bias at $V_{\rm Z} = 1.1$ meV and 1.41 meV. The height of the QD $V_{\rm D} = 0.4$ meV and the size $l = 0.15$ μm. The other parameters are the same as Fig. 3.2. The corresponding TV from the left (right) and thermal conductance $\kappa_{\rm LR}$ ($\kappa_{\rm RL}$) are shown in the inset of (g) [(h)].

Fig. 3.3. In the local conductance Fig. 3.3(a), we notice that the ZBCP starts to emerge below TQPT at $V_{\mathrm{Z}} \sim 0.5$ meV, which shows a quantized and robust ZBCP without oscillations. In the nonlocal conductance as presented in Figs. 3.3(c) and (d), we find that the bulk gap does not collapse until the advent of real TQPT at $V_{\mathrm{Z}} = 1.41$ meV.

In the second panel, we show the line cuts of two V_{Z} with the red being in the trivial regime, and the cyan being real TQPT determined by the peak of thermal conductance. In Figs. 3.3(g) and (h), the nonlocal conductance at the left end is much more prominent than that of the right end due to the presence of the QD at the left end but not at the right end. Thus, the measurement of the "bad" quantized ZBCP from a QD can, in principle, be distinguished from an MBS by the lack of an associated gap closure in Fig. 3.3(c) at the value of the Zeeman field where the ZBCP starts in Fig. 3.3(a). At the same time, Fig. 3.3(c) shows that the presence of the QD might make the gap closure harder to see compared to the pristine case.

As in the pristine case, the thermal conductances in the insets in Figs. 3.3(g) and 3.3(h) show quantized peaks at exactly the TQPT. For reference, we plot the TV in the inset as well, which indicates the position of the TQPT by where the TV vanishes. The deviations from quantization for both the thermal quantization and TV are a result of the finite dissipation which we use to stabilize our numerical calculations.

The second source of the bad ZBCP is the inhomogeneous potential. We present the results of the inhomogeneous potential with one potential barrier at the left end in Fig. 3.4. The local conductance in Fig. 3.4(a) is similar to the QD situation in Fig. 3.3(a), where we also observe a quantized and robust ZBCP without any Majorana oscillation. However, in the nonlocal conductance in Figs. 3.4(c) and 3.4(d), we find that the gap closure and reopening feature is not salient— the minimal gap does not completely close at the putative TQPT. Nevertheless, we can

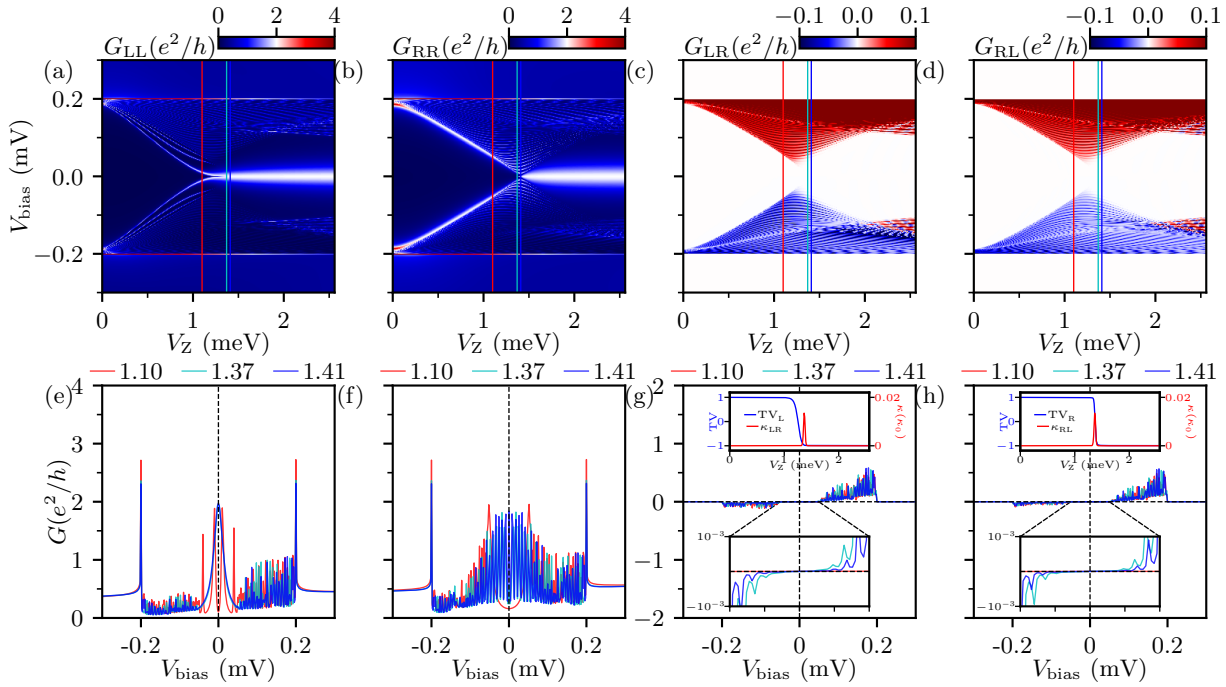

Figure 3.4: The bad ZBCP in a nanowire with the Gaussian inhomogeneous confinement at the left end. (a)-(d) show the local and nonlocal conductance in the "intrinsic" color scale; (e)-(h) are the corresponding line cuts of the conductance as a function of bias at $V_{\rm Z} = 1.1$ meV, 1.37 meV, and 1.41 meV. The height of the confining potential $V_{\rm max} = 1$ meV and linewidth $\sigma = 0.45$ μm. The other parameters are the same as Fig. 3.2. The corresponding TV from the left (right) and thermal conductance $\kappa_{\rm LR}$ ($\kappa_{\rm RL}$) are shown in the inset of (g) [(h)].

still distinguish the trivial zero-energy ABS from the MBS by the lack of associated gap closure at where ZBCP starts to emerge in Fig. 3.4(a).

In the second panel, we additionally show the blue line of the nominal TQPT which is always fixed at $V_{\mathrm{Z}} = 1.41$ meV. Here, unlike the pristine wire and the QD case, the value of the real TQPT determined from the peak of thermal conductance is smaller than that of the nominal TQPT, but the discrepancy is only slight (i.e., within the width of the thermal conductance peak and thus can be thought of as a finite size effect). The nonlocal conductance at the real TQPT [cyan in the insets of Figs. 3.4(g) and 3.4(h)] is also slightly larger than that at the nominal TQPT [large blue in the insets of Figs. 3.4(g) and (h)] near zero bias.

Similar to the pristine wire and QD, we again calculate the TV and the thermal conductance in the insets of Figs. 3.4(g) and 3.4(h). We find that the thermal conductance, though not quantized due to the finite dissipation, accurately indicates the position of TQPT where the TV flips the sign.

3.2.3 Disorder in the chemical potential

Finally, we present the effect of disorder and show what the nonlocal conductance will look like in the presence of disorder. Since the weak disorder (typically $\sigma_\mu/\mu \leq 1$ in this configuration) preserves the good ZBCPs as shown in Fig. A.1 in Sec. 2.2, we will skip our results for the nonlocal conductance in the weak disorder case, which is similar to the pristine case in Fig. 3.2. Weak disorder poses no problem to the detection of MZMs.

We first add the intermediate disorder in the chemical potential with $\sigma_\mu/\mu = 1.5$ as shown in Fig. 3.5. In the first row, we find that the trivial ZBCP emerges below the TQPT in G_{LL} [see

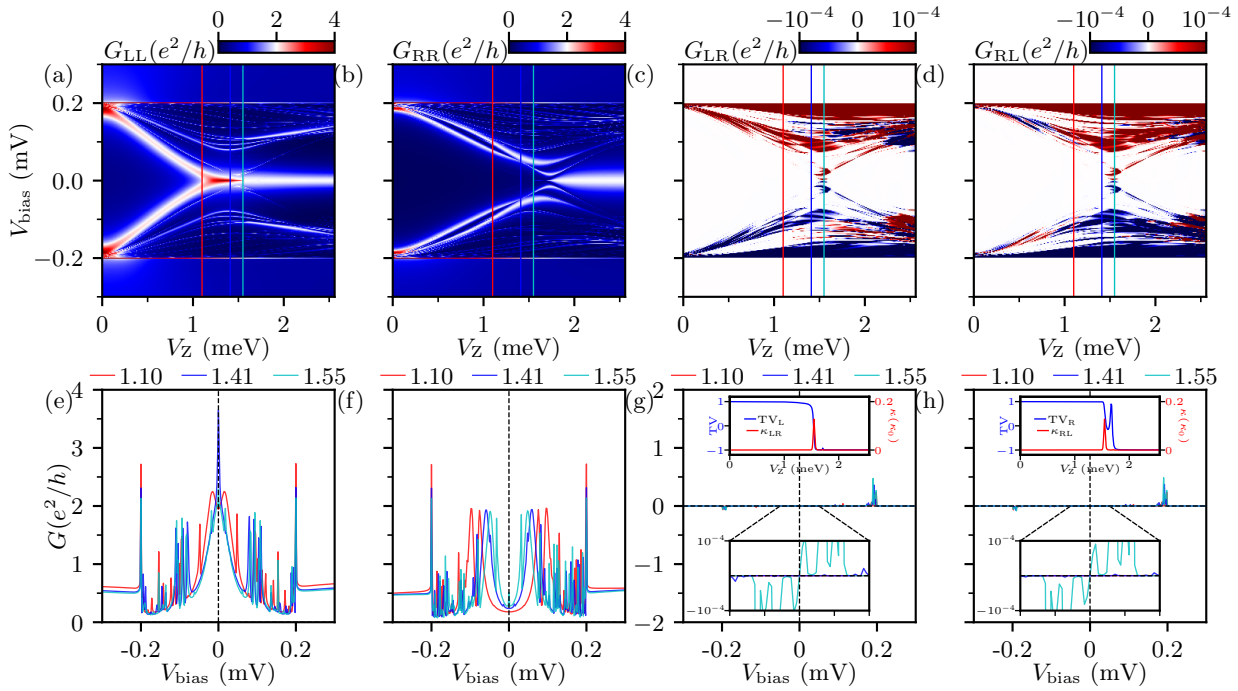

Figure 3.5: The ugly ZBCP in a nanowire in the presence of intermediate disorder with $\sigma_\mu/\mu = 1.5$. (a)-(d) show the local and nonlocal conductance in the "intrinsic" color scale; (e)-(h) are the corresponding line cuts of the conductance as a function of bias at $V_{\rm Z} = 1.1$ meV, 1.41 meV, 1.55 meV. The other parameters are the same as Fig. 3.2. The corresponding TV from the left (right) and thermal conductance $\kappa_{\rm LR}$ ($\kappa_{\rm RL}$) are shown in the inset of (g) [(h)].

Fig. 3.5(a)] and beyond the TQPT in G_{RR} on the right [Fig. 3.5(b)]. The left-right symmetry breaking in this case is accidental. Thus the local conductance resembles Figs. 3.3(a) and 3.3(b). In the nonlocal conductance, it looks like a signal of gap closure and gap reopening, though the signal is very small (we use a much smaller scale of the color bar here). Similar to the case of the pristine and bad ZBCPs the nonlocal conductance shown in Figs. 3.5(c), 3.5(d), 3.5(g), and 3.5(h) still shows a gap closure at the TQPT, though the signal is reduced by three orders of magnitudes compared to the already difficult to measure pristine case.

In the second row of Fig. 3.5, we present the line cuts of the color plots from the first row at Zeeman values representing the trivial regime (red), the nominal TQPT (blue), and the real TQPT determined by the peak of thermal conductance (cyan). The nonlocal conductance near zero bias also manifests an antisymmetric shape in the insets of Figs. 3.5(g) and 3.5(h).

The insets of Figs. 3.5(g) and 3.5(h) show the thermal conductance (plotted in red). The thermal conductance here shows a peak at the TQPT as in the pristine case. The TVs [plotted in blue in the insets in Figs. 3.5(g) and (h)] show a well-defined topological regime, though there are a few small spikes due to the disorder in the TV. The topological regime here is also narrower than that in the pristine wire in the sense that the trivial regime extends above the nominal TQPT ($\sqrt{\mu^2+\gamma^2} = 1.41$ meV). Of course, the nominal TQPT does not indicate a real phase transition here. Nevertheless, we still show this line cut [dark blue lines in Figs. 3.5(g) and (h)] to emphasize that the real disorder-renormalized TQPT more and more deviates from the nominal TQPT (1.41 meV) in the pristine limit as disorder increases.

Next, we increase the disorder to $\sigma_\mu/\mu = 3$ as shown in Fig. 3.6. In the first row of Fig. 3.6, the trivial ZBCP emerges while the topological ZBCP is destroyed at the left end due to the large disorder. In the nonlocal conductance, the signature of gap-closing is very faint and the signature

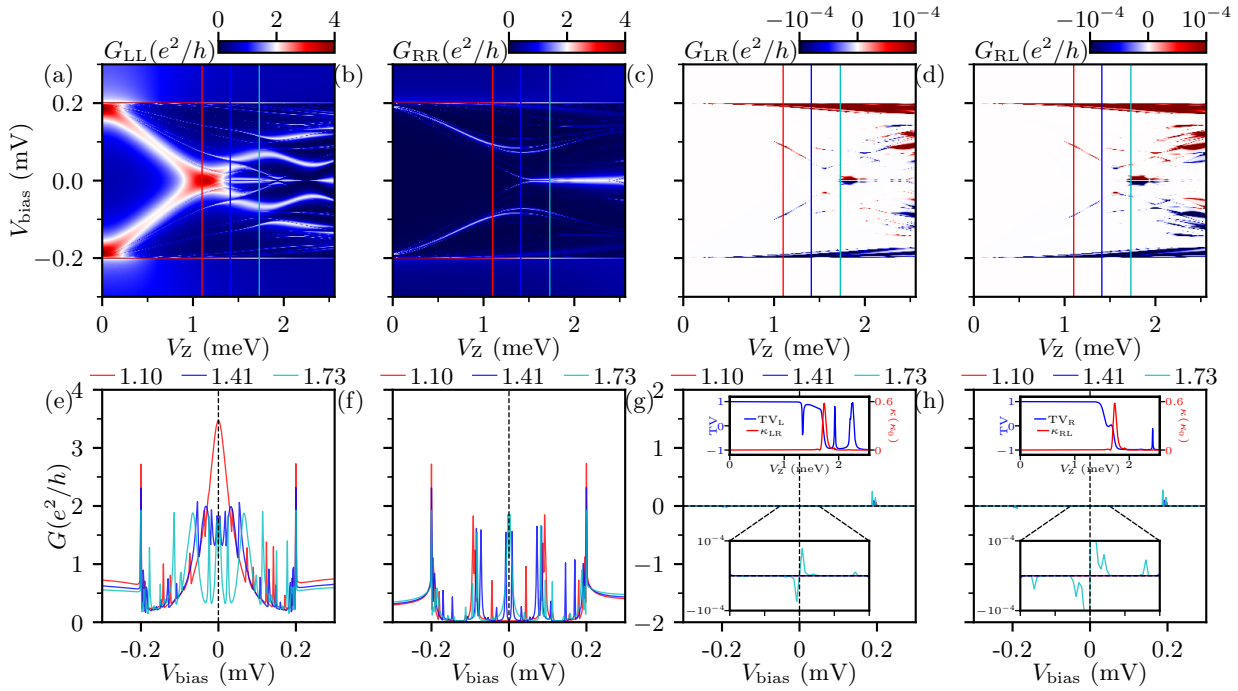

Figure 3.6: The ugly ZBCP in a nanowire in the presence of strong disorder with $\sigma_\mu/\mu = 3$. (a)-(d) show the local and nonlocal conductance in the "intrinsic" color scale; (e)-(h) are the corresponding line cuts of the conductance as a function of bias at $V_{\rm Z} = 1.1$ meV, 1.41 meV, 1.73 meV. The other parameters are the same as Fig. 3.2. The corresponding TV from the left (right) and thermal conductance $\kappa_{\rm LR}$ ($\kappa_{\rm RL}$) are shown in the inset of (g) [(h)].

of gap reopening is absent even if we use a color scale with a very small range of conductance.

In the second row of Fig. 3.6, we present the line cuts of the color plots of the nonlocal conductance from the first row and find vanishingly small signals almost everywhere. The upper insets of Figs. 3.6(g) and 3.6(h) show the thermal conductance (red line). The thermal conductance has a peak with a height smaller than the quantized value due to the finite dissipation. The TV (blue line) in the insets of Figs. 3.6(g) and 3.6(h) oscillates abruptly as the magnetic field increases.

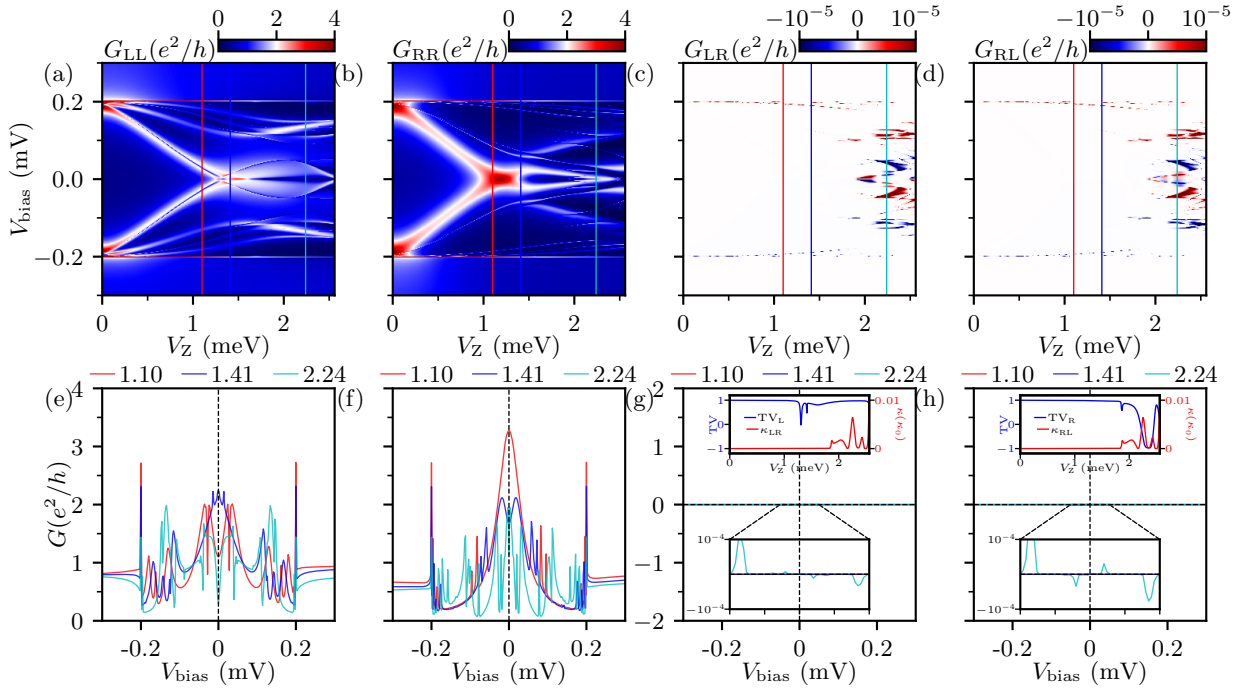

Figure 3.7: The ugly ZBCP in a nanowire in the presence of very strong disorder with $\sigma_\mu/\mu = 5$. (a)-(d) show the local and nonlocal conductance in the "intrinsic" color scale; (e)-(h) are the corresponding line cuts of the conductance as a function of bias at $V_{\rm Z} = 1.1$ meV, 1.41 meV, 2.24 meV. The other parameters are the same as Fig. 3.2. The corresponding TV from the left (right) and thermal conductance $\kappa_{\rm LR}$ ($\kappa_{\rm RL}$) are shown in the inset of (g) [(h)].

Finally, we use a very large disorder $\sigma_\mu/\mu = 5$ and present the electrical and thermal conductance in Fig. 3.7. In the local conductance in the first row, the ZBCP are all trivially induced by disorder; the ZBCP above the nominal TQPT is completely absent. The nonlocal conduc-

tances in Figs. 3.7(c) and (d) are featureless: Almost everywhere is measured a tiny conductance within $10^{-5}e^2/h$.

In the second row of Fig. 3.7, we present the line cuts of the color plots of the nonlocal conductance from the first row, where, again, the conductance is almost zero. The upper insets of Figs. 3.7(g) and 3.7(h) show the thermal conductance (red line). The predicted thermal conductance in this strong disorder case goes from essentially vanishing at a low Zeeman field to an irregular structure with many peaks, suggesting suppression of the SC transmission gap with the magnetic field. Thus, the thermal conductance here does not appear to indicate any topological phase. This is consistent with the TV [blue line in the insets of Figs. 3.7(g) and (h)], which does not flip to -1.

In fact, the ugly ZBCP in Fig. 3.5 continuously transmutes to Anderson localization in Fig. 3.7 when disorder increases from the intermediate level to the very strong level. To show this continuous development, we additionally present other examples of intermediate and strong disorder with σ_μ/μ ranging from 2 up to 4.5 in Appendix C for a direct comparison.

Before ending this subsection, we note that the scale of the disorder σ_μ/μ where disorder effects become substantial is significantly higher compared to the previous Chapter 2 on the subject. This is largely due to our using a larger tunnel coupling strength γ ($\gamma = 1$ meV as opposed to $\gamma = 0.2$ meV in Chapter 2). In general, the effect of chemical potential disorder on the system depends on other parameters, e.g., the tunnel coupling (which is usually unknown in experiments) and the lattice constant of discretization (which is purely artificial). The tunnel coupling strength γ sets the overall strength of the conductance and also determines the effective SC gap at zero energy [32]; therefore, it changes the effective coherence length. Since we use a larger tunnel coupling strength $\gamma = 1$ meV other than the previous 0.2 meV, the critical value

increases due to the larger SC gap protection. Therefore, one should not take the value of disorder $\sigma_\mu/\mu = 1.5$ and conclude that these results are in the strong disorder limit. In fact, in our simulations, since we choose the disorder and keep other parameters fixed throughout, we can directly compare them and the relative results are sensible. However, the matter of how to directly map this disorder in our theory to experimental disorder values in real samples is unknown at this stage. Each sample will have its own weak to intermediate to strong disorder regime depending on the unknown details of various sample parameters such as tunnel coupling, SC gap, etc.

3.2.4 Quantum dot with disorder in the chemical potential

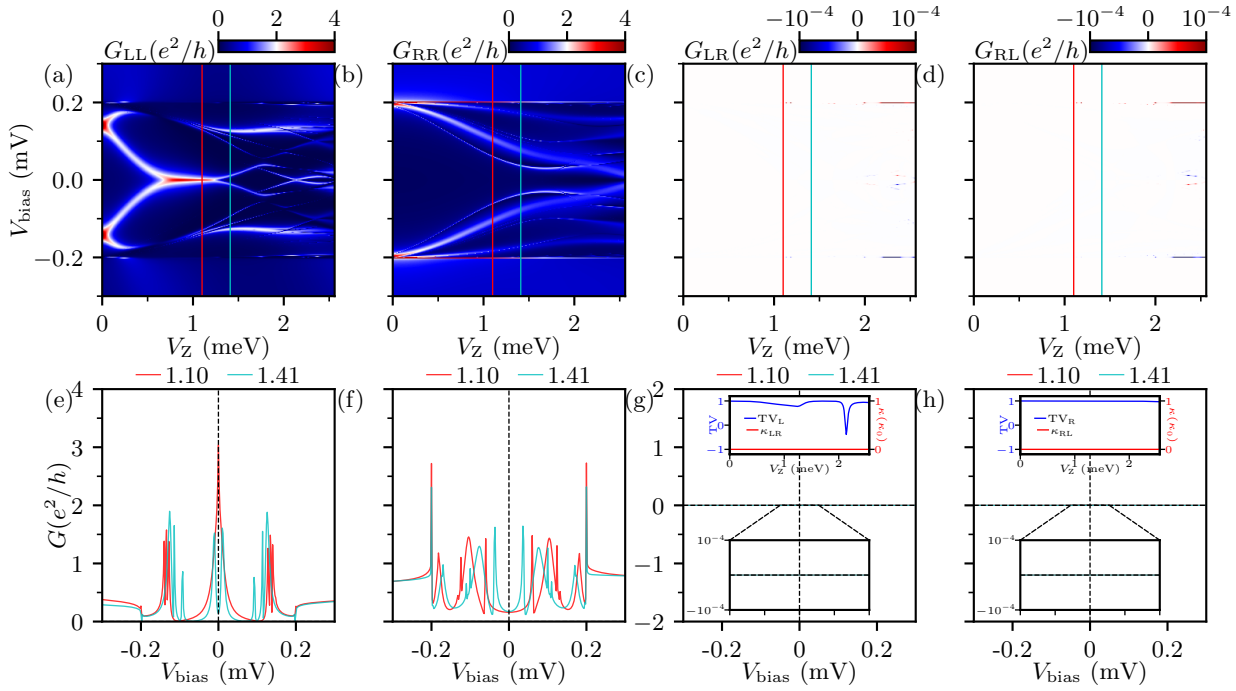

Figure 3.8: The wire in the presence of the QD and very strong disorder with $\sigma_\mu/\mu = 5$. (a)-(d) show the local and nonlocal conductance in the "intrinsic" color scale; (e)-(h) are the corresponding line cuts of the conductance as a function of bias at $V_Z = 1.1$ meV, and 1.41 meV. The QD is the same as Fig. 3.3 with $V_D = 0.4$ meV and $l = 0.15$ μm. The other parameters are the same as Fig. 3.2. The corresponding TV from the left (right) and thermal conductance κ_{LR} (κ_{RL}) are shown in the inset of (g) [(h)]. The nonlocal conductance is very small in this situation.

Finally, we consider a more complicated, and more realistic, situation where the QD and

disorder coexist. This is like mixing the bad ZBCP with the ugly ZBCP. Although we deliberately isolate them and attribute them to different mechanisms, e.g., QDs or disorder, this is just for the better instructive purpose and there is no reason that only one of these mechanisms would happen one at a time. Therefore, it is natural to consider their combined effects on the nanowire. For example, we impose the disorder on the nanowire in the presence of a fixed QD in Fig. 3.3. The size of the QD $l = 0.15$ μm and the height $V_{\rm D} = 0.4$ meV as defined in Eq. (2.8) the disorder in the chemical potential exists only in the region $[l, L]$ of the nanowire, leaving the QD intact.

By tuning the magnitude of disorder, we find that: If the disorder is weak, the bad ZBCP almost remains the same as if no disorder is present, which is expected. We present weak disorder results in Fig. C.6 in Appendix C and skip it in the main text because it is qualitatively the same as Fig. 3.3. If the disorder is intermediate, e.g., $\sigma_\mu/\mu = 3$ as shown in Fig. C.7 in Appendix C, we can still see the imprint of the QD since the wire is still dominated by the QD.

However, if the disorder is very large, for example, $\sigma_\mu/\mu = 5$ as shown in Fig. 3.8, apart from some ZBCP signatures of the QD, the local conductance of the wire is qualitatively similar to the strongly disordered wire [see Figs. 3.7(a) and (b)]. In $G_{\rm LL}$, the remnant effect of the QD still shows up in the low-lying state near $V_{\rm Z} = 0.5$ meV while the topological regime is destroyed by the strong disorder. In Figs. 3.8(c) and 3.8(d), the nonlocal conductance is also very small everywhere, which is the same scenario as the strong disorder case discussed in Sec. 3.2.3.

In the second row, the line cuts of the color plots of the nonlocal conductance from the first row also show vanishingly small conductance. The thermal conductances [red lines in the insets of Figs. 3.8(g) and 3.8(h)] remain vanishingly small, which is consistent with the TV. We find the TV [blue lines in the insets of Figs. 3.8(g) and 3.8(h)] does not flip to -1, which again indicates that the wire continues to remain in the topologically trivial phase.

3.2.5 Short nanowires

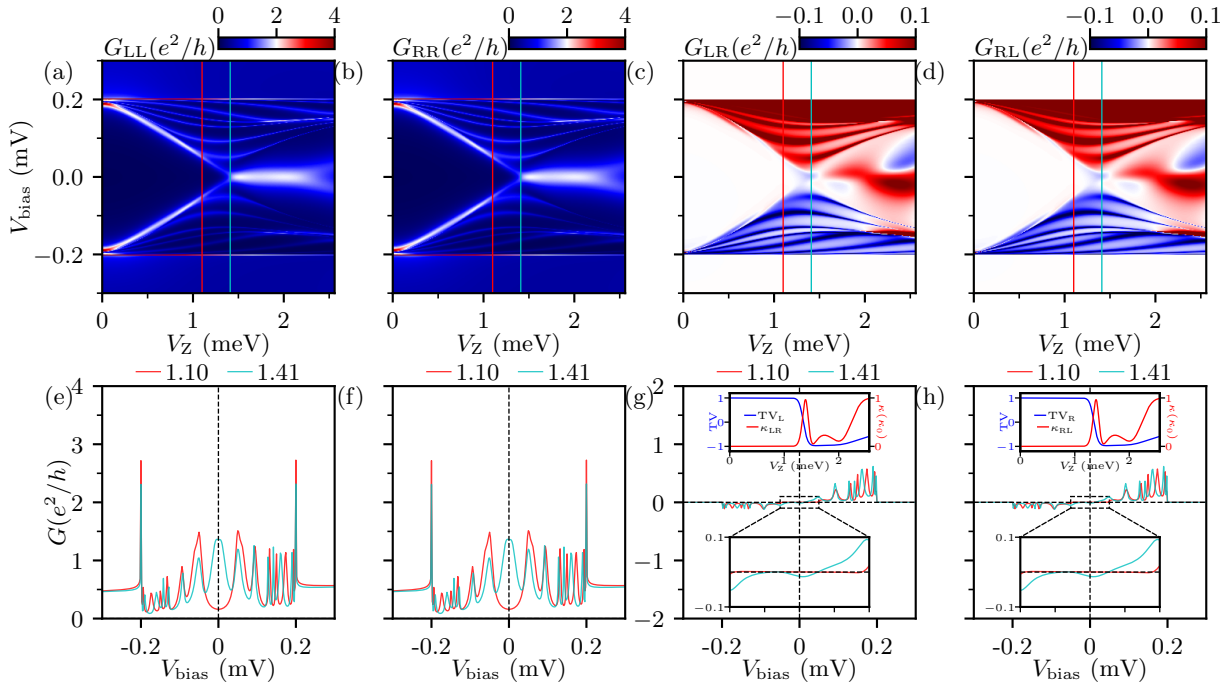

Figure 3.9: The short pristine nanowire ($L = 0.5$ μm). (a)-(d) show the local and nonlocal conductance in the "intrinsic" color scale; (e)-(h) show line cuts of the conductance as a function of bias at $V_Z = 1.1$ meV and 1.41 meV. The other parameters are the same as Fig. 3.2. The corresponding TV from the left (right) and thermal conductance κ_{LR} (κ_{RL}) are shown in the inset of (g) [(h)].

Previously, our results of the good, bad, and ugly ZBCP are all calculated under the long wire limit, where the magnitude of TV was close to unity so that wires could be precisely characterized as either topological or trivial. However, at the current stage of experiments, nanowires are of effective length up to $0.5 \sim 1$ μm [9, 46], which is closer to the short wire limit (smaller than SC coherence length), even if some parameters that determine the coherence length in the nanowire are unknown in experiments, e.g., the SM-SC coupling strength and chemical potential. Therefore, we also present four representative short wire results in Fig. 3.9 to Fig. 3.12 and show the other examples of short wires in Appendix C.

In Fig. 3.9, we use the pristine wire again in a shorter wire $L = 0.5$ μm. The local conductance [Figs. 3.9(a) and (b)] has a larger Majorana oscillation (which bifurcates at around $V_Z \sim 2.5$ meV) compared to the long wire situation in Fig. 3.2. In the nonlocal conductance [Figs. 3.9(c) and (d)], we also see gap closure and reopening features but the minimal gap at the TQPT (see in the color plot) is not as small as that in the long wire limit.

In the second row, we present the line cuts of the color plots of the nonlocal conductance from the first row, and find the nonlocal conductance shows significant nonlinearity at the TQPT around zero bias [cyan line in Figs. 3.9(g) and 3.9(h)], as opposed to the long wire limit in Fig. 3.2. Although the thermal conductance [red lines in the insets of Figs. 3.9(g) and (h)] peaks at the quantized value at TQPT $V_Z = 1.41$ meV, it grows again at a larger Zeeman field $V_Z = 2.5$ meV as a result of the highly-overlapped Majorana. The TV [blue lines in the insets of Figs. 3.9(g) and 3.9(h)] also becomes less topological (more deviation from -1) at larger magnetic fields. This is because the coherence length generally increases as V_Z increases; therefore, the effective length of the wire becomes shorter at large magnetic fields.

In experiments, the parent SC bulk gap often collapses as the magnetic field increases (most likely because of the penetration of the magnetic field into the parent Al). Therefore, we additionally introduce a phenomenological bulk gap collapse in the short wire as shown in Fig. 3.10. The corresponding modification to the Hamiltonian (2.3) is the change of the parent SC bulk gap, which closes in the form of Eq. (2.5). Here, we manually set SC gap collapse at $V_{Zc} = 3$ meV.

In the local conductance in Figs. 3.10(a) and 3.10(b), we find the topological ZBCP is not affected by the collapse of the parent SC gap as long as the parent SC gap does not vanish below TQPT. In the nonlocal conductance in Figs. 3.10(c) and 3.10(d), we find qualitatively similar

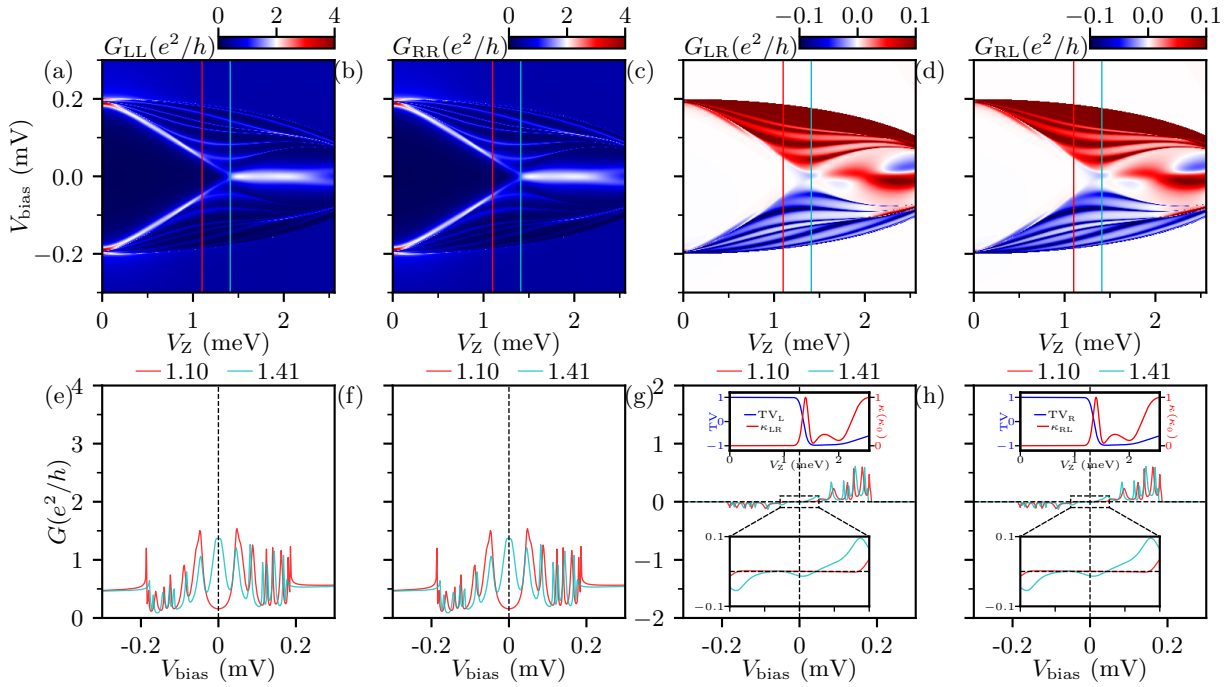

Figure 3.10: The short pristine nanowire ($L = 0.5$ μm). The SC bulk gap collapses as $V_{\rm Z}$ increases and closes completely at $V_{\rm Z} = 3$ meV (not shown here). (a)-(d) show the local and nonlocal conductance in the "intrinsic" color scale; (e)-(h) show line cuts of the conductance as a function of bias at $V_{\rm Z} = 1.1$ meV and 1.41 meV. The other parameters are the same as Fig. 3.2. The corresponding TV from the left (right) and thermal conductance $\kappa_{\rm LR}$ ($\kappa_{\rm RL}$) are shown in the inset of (g) [(h)].

results as in Fig. 3.9 with suppressed oscillations from overlapping Majoranas.

In the second row, we present the line cuts (cyan lines) of the color plots of the nonlocal conductance from the first row and find that the conductance at zero bias is not altered by the collapse of the SC gap. However, the whole range of finite nonlocal conductance is suppressed as a result of a smaller parent SC gap. The thermal conductance [red lines in the upper insets of Figs. 3.10(g) and 3.10(h)] shows the exact same conductance as in Fig. 3.9 where the SC bulk gap does not collapse. The TV [blue lines in the upper insets of Figs. 3.10(g) and 3.10(h)] shows a peak around $V_Z = 1.41$ meV and grows a second peak at $V_Z = 2.5$ meV again. This implies that the effect of SC gap collapse is only quantitative— it will not change the topological properties of the nanowire as long as the SC gap does not vanish already below TQPT.

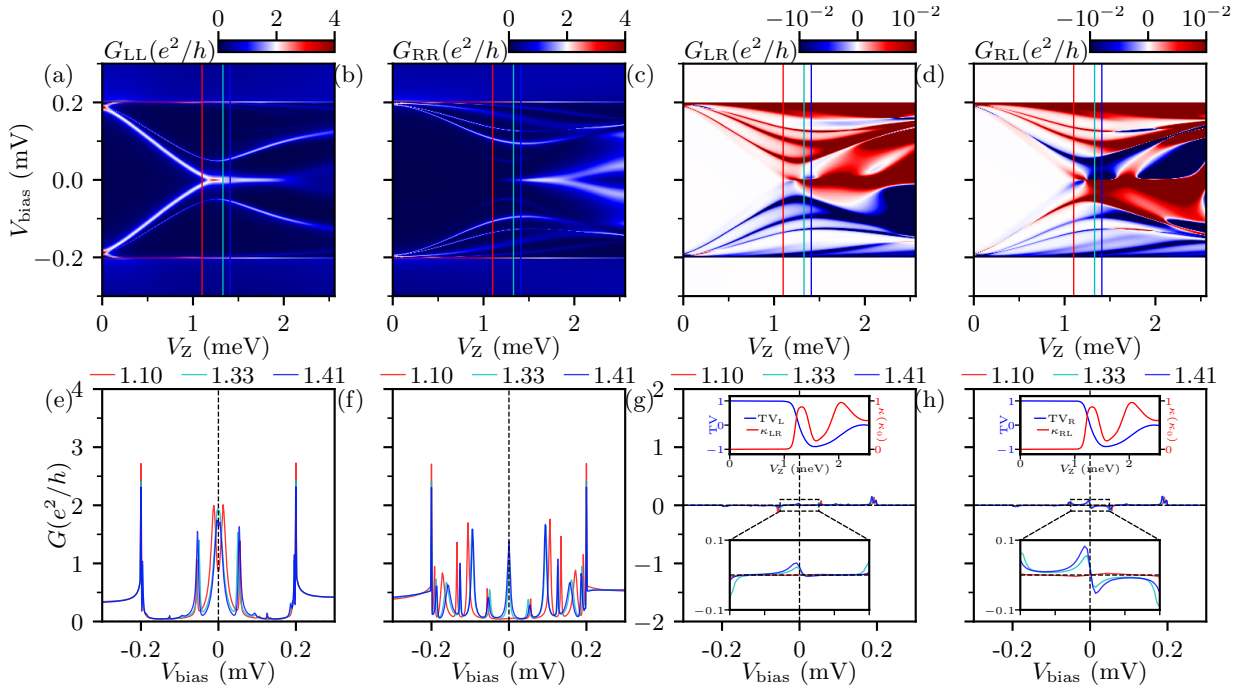

Figure 3.11: The short wire ($L = 0.5$ μm) in the presence of strong disorder with $\sigma_\mu/\mu = 3$. (a)-(d) show the local and nonlocal conductance in the "intrinsic" color scale; (e)-(h) are the corresponding line cuts of the conductance as a function of bias at $V_Z = 1.1$ meV, 1.33 meV, 1.41 meV. The other parameters are the same as Fig. 3.2. The corresponding TV from the left (right) and thermal conductance κ_{LR} (κ_{RL}) are shown in the inset of (g) [(h)].

In Fig. 3.11, we present the strong disorder with $\sigma_\mu/\mu = 3$ in the short wire $L = 0.5$ μm, as a comparison to its long wire counterpart in Fig. 3.6. The local conductance in Fig. 3.11(a) shows a trivial ZBCP emerging below the nominal TQPT, and the putative topological ZBCP is destroyed in Fig. 3.11(b). The nonlocal conductance shows a vague signature of gap-closing but without the gap reopening.

In the second row, we present the line cuts of the color plots of the nonlocal conductance from the first row, and find that the nonlocal conductance (blue lines) is also much smaller than the pristine short wire case in Fig. 3.10. The thermal conductances [red lines in the upper insets of Figs. 3.11(g) and 3.11(h)] remain finite after the induced gap closes, and oscillate as the magnetic field increases. The TV [blue lines in the upper insets of Figs. 3.11(g) and 3.11(h)] also does not completely flip to -1, which indicates that the topology is not well-defined as expected from the lack of gap reopening seen in Figs. 3.11(c) and 3.11(d).

Similar to Fig. 3.10, we show results in a short wire in the presence of strong disorder with the collapse of the parent SC bulk gap in Fig. 3.12. In the local conductance in Figs. 3.12(a) and 3.12(b), we find that the conductances at small magnetic fields are not altered while the conductances at large magnetic fields are more easily affected. In the nonlocal conductance in Figs. 3.12(c) and 3.12(d), the amplitude of the oscillation (anticrossings of two ABS with low energies) above $V_{\rm Z} = 1.41$ meV is much suppressed by the collapse of the parent SC gap.

In the second row, we present the line cuts of the color plots of the nonlocal conductance from the first row, and find that the nonlocal conductance [blue lines in Figs. 3.12(g) and 3.12(h)] near zero bias is almost the same as the one without SC gap collapse [Figs. 3.11(g) and 3.11(h)]. The thermal conductances [red lines in the upper insets of Figs. 3.12(g) and 3.12(h)] also remain finite after the induced gap closes, and oscillate as the magnetic field increases. The TV

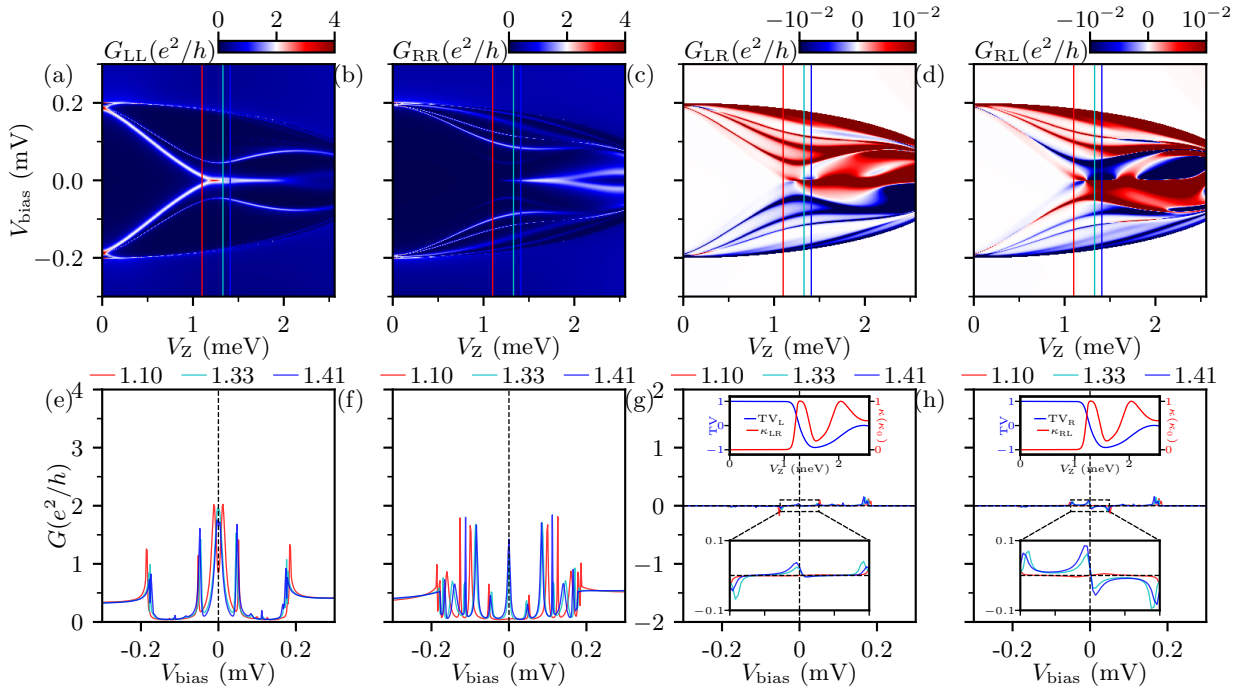

Figure 3.12: The short wire ($L = 0.5$ μm) in the presence of strong disorder with $\sigma_\mu/\mu = 3$. The SC bulk gap collapses as $V_{\rm Z}$ increases and closes completely at $V_{\rm Z} = 3$ meV (not shown here). (a)-(d) show the local and nonlocal conductance in the "intrinsic" color scale; (e)-(h) are the corresponding line cuts of the conductance as a function of bias at $V_{\rm Z} = 1.1$ meV, 1.33 meV, 1.41 meV. The other parameters are the same as Fig. 3.2. The corresponding TV from the left (right) and thermal conductance $\kappa_{\rm LR}$ ($\kappa_{\rm RL}$) are shown in the inset of (g) [(h)].

[blue lines in the upper insets of Figs. 3.12(g) and 3.12(h)] does not flip to -1 completely, which supports the same conclusion of the ill-defined topology in short wires.

We add as a sobering reminder that the short-wire and highly disordered situation with the bulk gap collapse appears to be the most consistent interpretation for the recent measurements of nonlocal conductance in SM nanowires [55]. Thus, more nonlocal conductance measurements are necessary for progress in the field.

3.3 Discussion

We discuss now the possible experimental situation and the efficacy of observing MZMs in nanowires based on our results in this chapter.

The local conductance is not a reliable technique to distinguish the ABS from the MBS. Although in the pristine wire in Fig. 3.2 the topological ZBCP has a quantized value of $2e^2/h$, the opposite assertion is not true. A quantized ZBCP is necessary but not sufficient. In the situation of the QD and inhomogeneous potential in Figs. 3.3 and 3.4, the bad ZBCP is also induced at one end of the nanowire by the barrier of the QD or inhomogeneous potential, and it transmutes into the real MBS beyond TQPT. After the phase transition, the topological regime shows up as the magnetic field increases. This bad ZBCP is sometimes referred to as the quasi-MZMs[118]: It generically manifests a quantized and stable conductance peak without oscillation in the trivial regime due to the partial separation of the two Majorana modes [75, 76, 78], unlike the ugly ZBCP, where the quantized value of conductance is purely by accident and unstable as a result of the Anderson localization [158]. Thus, the local conductance is not sufficient to confirm the MBS. This has already been discussed in the literature.

The nonlocal conductance should be more informative because it contains the bulk information. In the good ZBCP, the conductances at the bias above the parent gap and below the proximity gap are nearly zero; therefore, we can directly observe the gap closure and gap reopening in the nonlocal conductance. However, in the bad ZBCP in Figs. 3.3 and 3.4, the nonlocal conductance is too small to observe any signature near zero bias, which restates the need for very high precision in the three-terminal measurement. This situation becomes worse in the ugly ZBCP in the presence of disorder. Disorder generally suppresses the magnitude of the nonlocal conductance everywhere. For very strong disorder, the topological regime is not well defined; the system just enters the Anderson localization regime. Therefore, the discussion of topology in such a case is meaningless since the wire is just composed of a bunch of QDs that cannot be described by the nanowire model effectively. Thus, the nonlocal conductance will not affirmatively tell us whether a system is in the topological regime or not; on the other hand, if a very weak signal is detected in experiments, it may indicate that the underlying disorder is very strong and the ZBCP in the local conductance, if any, would be the ugly ZBCP induced by disorder. The invariable presence of noise in experiments may become a real challenge in the context of detecting such weak nonlocal signals.

The thermal conductance provides more reliability in determining the topological regime. In the good ZBCP, the thermal conductance sharply peaks at the vanishing point of TV, which retains a quantized thermal conductance at that point. This peak does not go away even if we add the inhomogeneous potential and QD, although the quantization may not manifest due to finite dissipation. In the presence of disorder, the thermal conductance is still quite robust, though may not be quantized again due to the combined effect of finite dissipation and disorder. Of course, the thermal conductance cannot be helpful in the very strong disorder limit since the topology itself

is not well defined— we do not see a peak of thermal conductance in this situation. Other than this strong disorder situation, we would consider thermal conductance as a robust and accurate indicator of the TQPT. On the other hand, if we always find negligible thermal conductance when sweeping the magnetic field, it indicates that the disorder is so large that the topological regime may not even exist. Nothing useful will happen in experiments if the samples are in the strong disorder regime since all one is exploring is the physics of Anderson localization, and not the physics of topological SC.

From the good ZBCP in the pristine wire to the bad ZBCP in the inhomogeneous potential and QD, and ugly ZBCP in the presence of disorder, we conclude that the local conductance is useless in distinguishing the ABS from the MBS; the nonlocal conductance— which may provide more bulk information— is, in principle, useful, but is, unfortunately, more fragile to the inhomogeneous potential and disorder; therefore, it may not serve as a very practical tool. However, thermal conductance is a more reliable technique to predict the topology of the nanowire.

In short wires, all the conductances— local, nonlocal or thermal— are not illuminating since the topological regime itself is not well-defined from a practical viewpoint. Therefore, we emphasize that all the discussions of the electrical and thermal conductance above should be considered only in the context of the long wire limit.

3.4 Conclusion

In this chapter, we exhaustively simulate the electrical and thermal conductance in the three-terminal SM-SC hybrid Majorana nanowire device in various situations, including pristine nanowire, QDs, inhomogeneous potential, and onsite disorder in the chemical potential. The goal

Table 3.1: Summary of different measurements in different situations.

	G_{ii}	G_{ij}	κ	TV
Good-pristine	✓	✓	✓	✓
Bad-QD	×	✓	✓	✓
Bad-inhomogeneous potential	×	✓*	✓	✓
Ugly-intermediate disorder	×	✓*	✓	✓
Ugly-strong disorder	×	×	×	×
Short wires	×	×	×	×

is to provide extensive results so that forthcoming experimental nonlocal conductance data can be validated through a direct comparison with our theory. To better simulate experiments, we also change the long wire limit to the short wire, and introduce the parent SC bulk gap collapse at a high magnetic field. We summarize the efficacy of all four measurements (although the TV is only theoretically measured) to distinguish each situation in Table 3.1. The check ✓ (cross ×) means a possible (impossible) measurement to distinguish a particular situation. The extra star $*$ after the check ✓ indicates a possible measurement but with a significantly weaker signal compared to the pristine case. The four columns are local conductance G_{ii}, nonlocal conductance G_{ij}, thermal conductance κ , and the TV.

This chapter generalizes the previous Chapter 2 on the good, bad, and ugly ZBCP in the local conductance to the nonlocal conductance and thermal conductance. We first present the nonlocal conductance in the pristine nanowire, which results in the good ZBCP, to give a general idea of what the nonlocal conductance will look like if it is the real topological Majorana in a clean long wire. This serves as a guide for future experiments which may report the observation of topological Majorana in nonlocal conductance. The local conductance has a quantized peak at $2e^2/h$ in the topological regime; the nonlocal conductance shows an apparent gap closure and reopening signal at TQPT, but in general the signal is much weaker than the local conductance.

This TQPT, which is determined by the sign flip of the TV, can be captured clearly by the peak of thermal conductance. It may therefore be necessary to carry out local conductance, nonlocal conductance, and thermal conductance measurements in the same sample for conclusive results. This becomes particularly significant given disorder considerably complicates and weakens the nonlocal conductance signal.

We also investigate the bad ZBCP arising from inhomogeneous potential including QDs. This may induce the quasi-Majorana ABS in the trivial regime with a quantized ZBCP. As the magnetic field increases, the trivial bad ZBCP finally transmutes into the topological ZBCP. We find that the local conductance here becomes misleading and the nonlocal conductance, while still showing the gap closure and reopening feature near TQPT, has much weaker signals than the local conductance. It is unclear if such a weak signal is experimentally detectable in the presence of noise, but such measurements are necessary for progress since these nonlocal measurements are capable of detecting bulk topological properties. However, the peak of the thermal conductance can still provide evidence for the real TQPT. Thus, measuring thermal conductance along with nonlocal conductance is warranted for decisive conclusions.

Most relevant to experiments, we consider the role of disorder in nonlocal conductance. This is crucial since, based on the previous Chapter 2, we believe that the existing NS tunneling, measurements may be observing disorder-induced ZBCP effects. We study a nanowire in the presence of disorder in the chemical potential and find that weak disorder does not destroy topological effects: The electrical conductance and thermal conductance in the weak disorder resemble those in the pristine wire. In the presence of the intermediate disorder, we find that the trivial ZBCP emerges in the local conductance below the putative TQPT which is misleading if one decides only based on the local conductance (since local conductance measurement knows

nothing about TQPT, and there is no way to tell whether a ZBCP is above or below the TQPT based only on local conductance data). A decisive measurement of three-terminal conductance as proposed in this chapter may enable the observation of bulk topological properties, but one must be careful about the weak strength of the nonlocal signal. However, if we measure the thermal conductance, we notice that the thermal conductance still peaks at the real TQPT, which can be determined by the zero TV. The only difference is that the range of the topological regime now becomes small compared to the pristine case. The worst case is strong disorder, which destroys the topological regime. The system dominated by the strong disorder (and not SC) enters the Anderson localization regime, where the local conductance is purely random as in the class D ensemble, the nonlocal is very small, and thermal conductance shows irregular structures with many peaks. Thus, it is not meaningful to discuss the topological or nontopological in such a strong disorder situation, and the only possible conclusion then would be that the sample quality must improve before MZMs can manifest.

We also consider a realistic situation by combining disorder and QD. We find two limits based on the magnitude of disorder. For the weak disorder, the nanowire is still dominated by the QD, which manifests the bad ZBCP as if the disorder is absent. For the strong disorder, the nanowire is dominated by disorder so that the bad ZBCP becomes the ugly ZBCP. The local conductance now becomes arbitrary, and the putative topological regime disappears.

Finally, simulating the current experimental short wire situations, we perform the same calculation in a short wire ($L = 0.5$ μm) and introduce the phenomenological parent SC bulk gap collapse which happens in the experiment. In the short wire, there is no distinction between the topological and trivial regime from a practical standpoint since the topology itself is not well defined when the wire is much shorter than the coherence length. The overlap of Majorana from

both ends in the short wire is so large that the thermal conductance remains finite even after the proximity gap closes. This is a situation that should be avoided in experiments, although we believe that all experiments so far, unfortunately, may be in this undesirable short wire limit.

Our extensive results presented in this chapter establish that nonlocal three-terminal conductance along with the standard two-terminal tunneling spectroscopy could distinguish between topological and trivial regimes in Majorana nanowires provided the wires are not too short and not too dirty, in particular, any observation of gap closure and reopening features in the nonlocal conductance, even if the signal is weak, along with a stable quantized tunneling conductance peak should be reasonable evidence for topological MZMs. If thermal conductance measurements can also be carried out simultaneously and manifest our predicted signatures, one could be more assured that the nanowire is indeed in the topological regime, and one could then proceed toward the goal of braiding the Majorana modes in order to create a protected topological qubit.

Chapter 4: Disorder-induced zero-bias conductance peaks

In the previous two chapters, we have both defined and compared the methods of nonlocal conductances and thermal conductances to distinguish the three types of ZBCPs. In this chapter, we focus on the real experiments, especially on the recently retracted experiment Ref. [9], and the related recently available correctly analyzed data from this Delft experiment [57], to discuss the general problem of confirmation bias in experiments verifying various theoretical topological quantization predictions.

Reference [9] was published in *Nature* in 2018 reporting the quantized Majorana conductance, but has been retracted in 2021 as the authors concluded on the reanalysis and recalibration of the original data that the original claim might have suffered from confirmation bias with fine-tuned data selection unwittingly preferring false positives in favor of the known theoretical prediction [30]. This retraction [159] of the high-profile article [9] in favor of a new detailed article [57] with corrected data and analysis has led to the conclusion that the original claim of the Majorana quantization observation is untenable. We show that this Majorana experiment [9] is most likely dominated by disorder, which produces trivial (but quite sharp and large) zero-bias Andreev tunneling peaks with large conductance $\sim 2e^2/h$ in the theory, closely mimicking the data. Thus, although the corrected Delft data are by far the best tunnel spectroscopy results available in the literature, manifesting large and sharp ZBCPs rising above the background with

an impressive hard SC gap, our theory shows that the most natural explanation for these ZBCPs is that they are disorder-induced and not topological Majorana modes. One characteristic of the disorder-induced trivial peaks is that they manifest little stability as a function of the Zeeman field, chemical potential, and tunnel barrier, distinguishing their trivial behavior from the expected topological robustness of non-Abelian MZMs.

Although our theory and analysis in this work are specific only to the Majorana nanowire physics of [57], we believe that our conclusions are far-reaching and may have substantial relevance to the somewhat unsatisfactory aspect of various experimental claims in the whole field of topological condensed matter physics. Our results apply to most of the Majorana experiments since 2021 in the literature, which were trying to verify precise theoretical predictions made in 2010 [23, 27, 29–31] claiming evidence in support of the existence of MZMs in 1D nanowires. Therefore, we also provide a brief analysis of another very recent nanowire experiment with small peaks, which most obviously arises from disorder [56]. The data presented in this recent experiment [56] are taken on samples with a very high amount of disorder, with substantial subgap conduction and a very soft gap, but still manifesting small conductance peaks which can occasionally be fine-tuned to values of $O(2e^2/h)$.

4.1 Theory

The theory is still based on the standard free-fermion BdG Hamiltonian introduced in Sec. 2.1 and 3.1. We use the same parameters for the InSb/Al system as in Chapter 2. We show in Fig. 4.1 the experimental structure [reproduced directly from Fig. 1(a) of [57]] as well as the corresponding 1D theoretical idealization studied in this section. An SM (InSb) nanowire

is in contact with an SC (Al) so that the nanowire becomes SC due to the proximity effect [160]. The experiment (and our theory) studies tunneling spectroscopy through the nanowire using the standard NS tunneling structure at one end (left end in Fig. 4.1) by controlling a tunnel barrier (seen in red as tunnel gates in Fig. 4.1) in the presence of a magnetic field applied parallel to the nanowire.

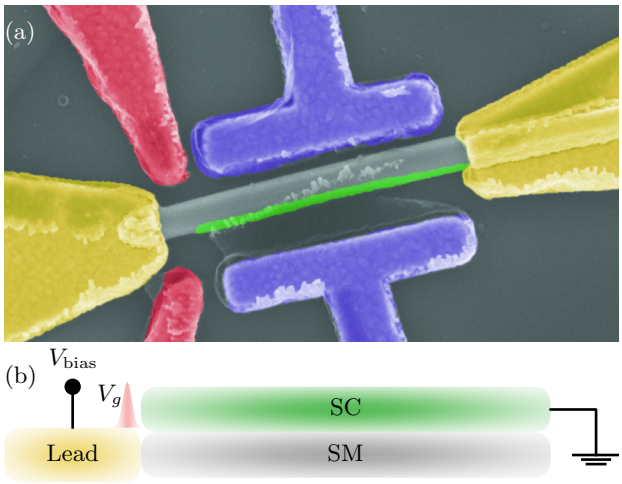

Figure 4.1: (a) The experimental device from Fig. 1 of Ref. [57]. The InSb nanowire (gray) is covered by the Al shell (green). The tunnel gate (red) controls the tunnel barrier V_g in (b). The super gate (purple) controls the chemical potential. The normal lead (yellow) is attached to one end of the nanowire; (b) The schematic of the SM-SC hybrid nanowire in the theory, which is essentially the same device as Fig. 2.1(a), except for the explicit inclusion of the tunnel barrier V_g.

4.2 Results

The most important aspect of our theory, which is also the key physics underlying the ZBCPs reported in Majorana experiments, is the inclusion of a model spatially random potential, $V_{\text{imp}}(x)$, added to the constant chemical potential μ as discussed in Sec. 2.1.5. This random term represents the disorder that invariably exists in the nanowire due to the presence of quenched random impurities and interface imperfections. The presence of $V_{\text{imp}}(x)$ in the BdG Hamiltonian

makes our theory correspond to the "ugly" situation in the terminology in Chapter 2, whereas for $V_{\rm imp}(x) = 0$ the system is pristine, corresponding to the "good" situation, which is the situation the experimentalists always have in their mind as the theoretical prediction to be emulated. The good situation is the standard theoretical Majorana scenario [23, 27, 29–31], where topological ZBCPs appear in the tunneling spectra for $V_{\rm Z} > V_{\rm Zc}$, whereas for $V_{\rm Z} < V_{\rm Zc}$ the subgap conductance is basically zero. The presence of random disorder is the key physical mechanism in our theory which, in our opinion, produces much of the physics showing up in the experimental ZBCPs reported in Refs. [9, 56, 57, 159]. We contend that the physics of Majorana nanowires at this point is dominated by disorder rather than topology as discussed in the next studies of two real experiments.

4.2.1 Intermediate disorder: InSb/Al SM-SC nanowire

We start with Ref. [57], which is deemed to carry an intermediate amount of disorder, and reproduce Fig. 2 exactly as it appears in this experimental work with no modification because these results in Fig. 4.2 are what we are trying to explain theoretically. In Fig. 4.2, we show the measured conductance spectra as a function of the magnetic field, bias voltage, and tunnel barrier. The theory must be able to reproduce all dependence of the three parameters faithfully for us to claim the understanding. The experimental measurement temperature is very low ($\sim$ 20 mK), therefore, we show our theoretical results at $T = 0$ with no loss of generality. Thermal effects are easy to include but would not modify the results as long as the thermal broadening is smaller than the tunneling energy, which is easily checked in the experiment by ensuring that the ZBCP saturates with the lowering of temperature.

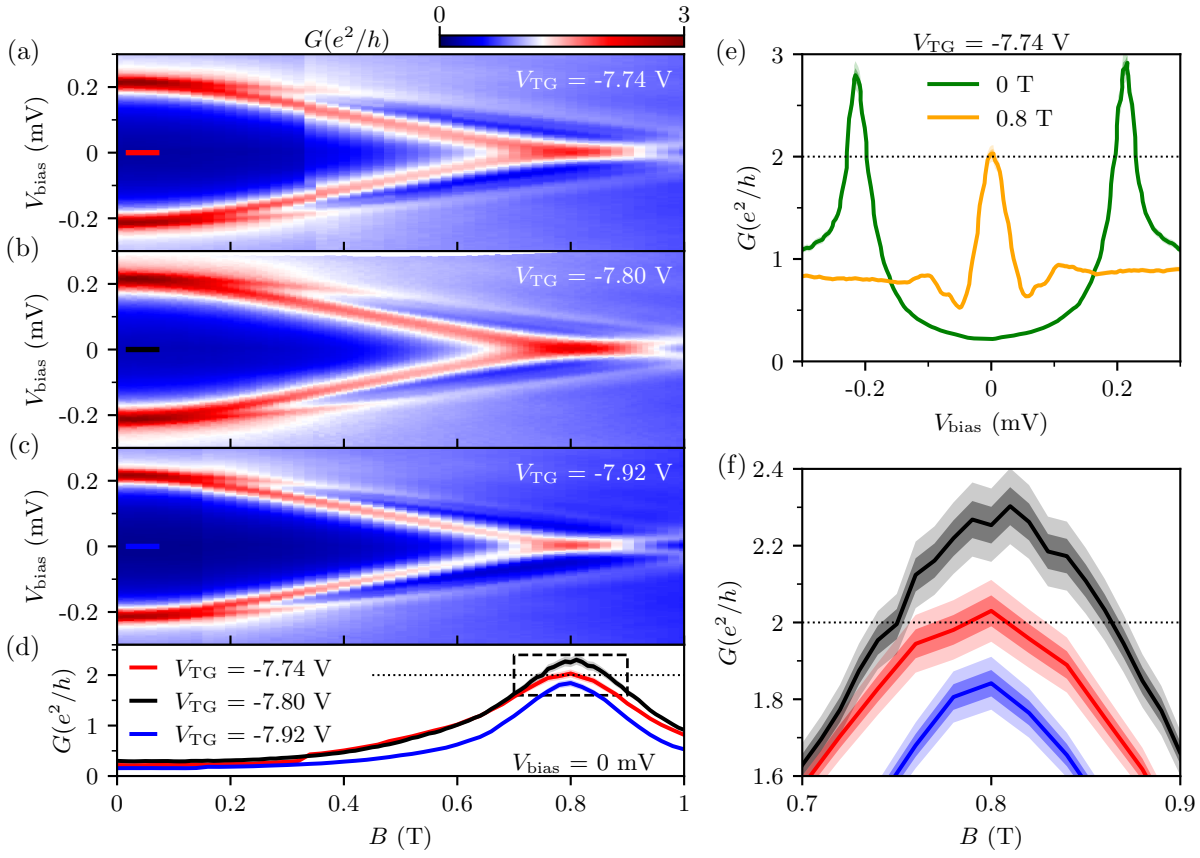

Figure 4.2: The experimental tunneling conductances from Ref. [57]. Panels (a)-(c) are tunneling conductances as a function of the bias voltage and magnetic field at various tunnel gate voltages V_{TG}=-7.74, -7.80, -7.92 V, respectively; (d) The horizontal line cuts at zero bias as a function of magnetic field corresponding to (a)-(c); (e) The vertical line cuts at zero magnetic field (red) and finite magnetic field (orange) at $V_{\mathrm{TG}} = -7.74$ V; (f) The closed-up view of the conductance peak near $2e^2/h$, indicated by the dashed rectangle in (d). The shading regions indicate the error bar of 1σ (darker) and 2σ (lighter). Refer to Ref. [57] for the other parameters of gate voltages.

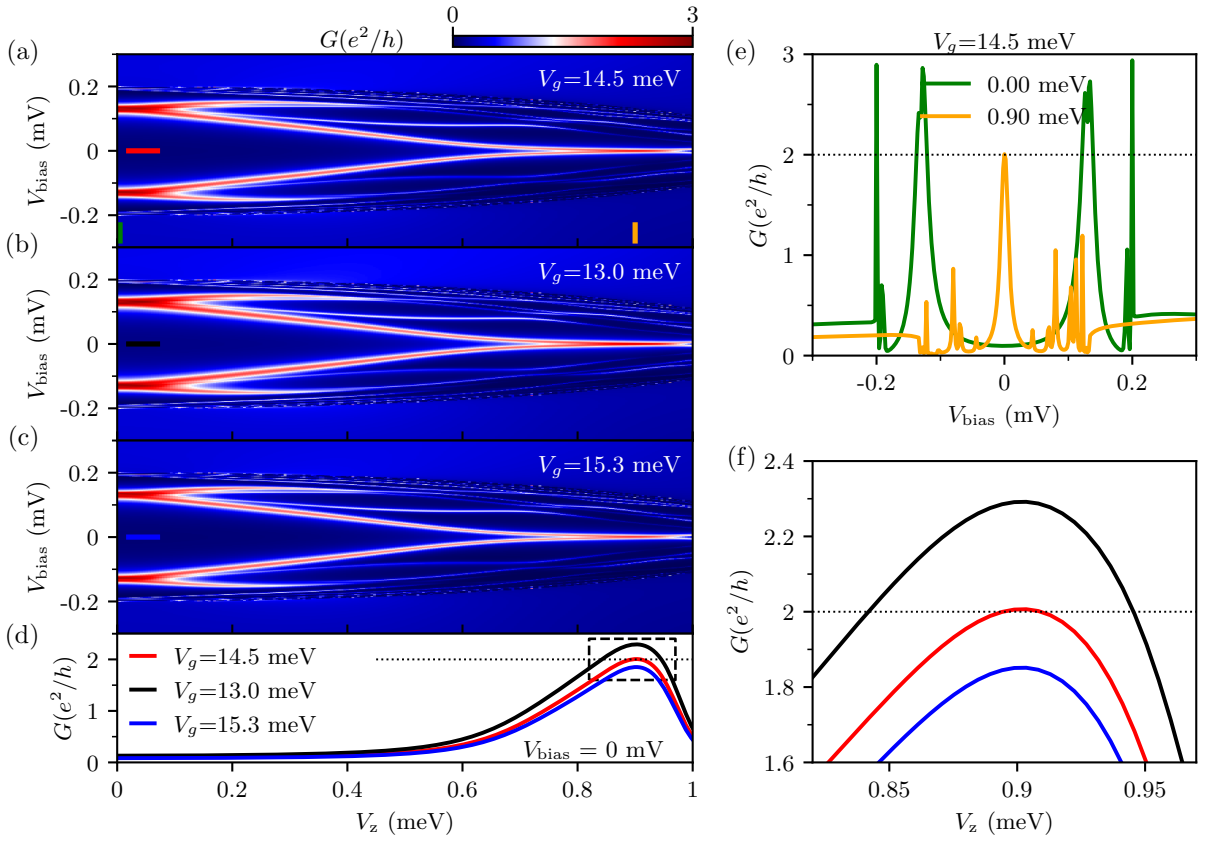

Figure 4.3: The theoretical tunneling conductances in the trivial regime which qualitatively reproduce the experimental measurements in Fig. 4.2. Panels (a)-(c) are tunneling conductances as a function of the bias voltage and Zeeman field at different tunnel barriers V_g=14.5, 13.0, and 16.5 meV, respectively; (d) The horizontal line cuts at zero bias as a function of Zeeman field corresponding to (a)-(c); (e) The vertical line cuts at zero magnetic field (red) and finite magnetic field (orange) at $V_g = 14.5$ meV; (f) The closed-up view of the conductance peak near $2e^2/h$. Note that the error bar is not applicable here compared to Fig. 4.2 because it is purely the theoretical calculation. The parameters are as follows: the wire length is 1 μm, the chemical potential $\mu = 1$ meV, the standard deviation of disorder $\sigma_\mu = 1$ meV, the parent SC gap $\Delta_0 = 0.2$ meV [122], the SM-SC coupling strength $\gamma = 0.2$ meV, the parent SC gap closes at $V_{\rm Z} = 1.2$ meV, the SOC $\alpha = 0.5$ eVÅ, the phenomenological dissipation is 3×10^{-3} meV [139], and zero temperature.

In Fig. 4.3, we show our calculated conductance spectra corresponding to the experimental results shown in Fig. 4.2 using a Gaussian disorder distribution for $V_{\rm imp}(x)$ with the disorder parameters shown in the figure caption. Note that the disorder is spatially fixed once chosen using the Gaussian distribution (for Fig. 4.3). We adjust the strength of the disorder to get the striking agreement between our theoretical results in Fig. 4.3 with the experimental results of Fig. 4.2, but we do not vary the disorder strength once chosen and all the results shown in Fig. 4.3 use identical disorder. There is no disorder averaging here, just one fixed disorder configuration, characterized by the single parameter of disorder strength, since the low experimental temperature implies that ensemble averaging is unnecessary. The striking agreement between Figs. 4.2 and 4.3 in both the magnetic field and the tunnel barrier dependence between experiment and theory is remarkable at a qualitative and semiquantitative level. A quantitative comparison is impracticable since the experimental disorder parameters are unknown including experimentally $V_{\rm Z}$ and μ. (We note that knowing the experimental magnetic field is not equivalent to knowing the Zeeman energy since the precise Landé g factor is not known under the actual experimental conditions [130].) So, what we do here with a model disorder potential, obtaining excellent qualitative agreement as a function of several different tuning parameters, is the best one can do.

The most important physical point about Fig. 4.3, and by inference about the experimental results in Fig. 4.2, is that the sharp ZBCPs with large conductance $\sim 2e^2/h$ are trivial peaks occurring below the TQPT in the trivial $V_{\rm Z} < V_{{\rm Z}c}$ regime. Note that in our theory we know the TQPT location $V_{{\rm Z}c}$ analytically by construction (the bulk gap closes and then reopens at $V_{{\rm Z}c}$) whereas the TQPT is unknown in the laboratory since a gap reopening is not observed experimentally. For our parameters in Fig. 4.3, the TQPT is at $V_{{\rm Z}c} = 1.02$ meV whereas the ZBCPs are at $V_{\rm Z} \sim 0.90$meV $< V_{{\rm Z}c}$. In addition, the ZBCP values in Fig. 4.3 (as in the experiments shown in

Fig. 4.2) are slightly (by about 10%) larger than the Majorana quantization value of $2e^2/h$, further reinforcing the fact that these are not MZM-induced topological ZBCPs, but disorder-induced trivial ZBCPs [64]. The fact that one can have large (and even sharp) ZBCPs of $O(2e^2/h)$ arising just from disorder has recently been emphasized [112] (which will also be discussed in the next chapter), nevertheless, the agreement between Figs. 4.2 and 4.3 is surprising, giving us confidence in claiming that it is possible, even likely, that the best Majorana nanowire experiments are disorder-limited even though the induced gap is hard rather than soft as was common in the earlier Majorana experiments [8, 35–38], where the role of strong disorder was obvious just by very soft induced gap implying the presence of considerable subgap fermionic states. The fact that disorder may dominate the ZBCPs even when the zero-field-induced gap is hard (and the ZBCPs themselves are sharp and large) is sobering. There have been earlier theoretical works in the literature on disorder effects in Majorana nanowires, mostly emphasizing class D antilocalization peaks and soft gap arising from the disorder-induced fermionic subgap states as well as on the stability of the MZMs against weak disorder [70, 79, 81, 82, 86, 87, 90, 91, 104, 106, 161–164]. The fact that disorder by itself can, under certain circumstances, give rise to large and sharp trivial ZBCPs closely mimicking the Majorana ZBCPs, even when the gap is hard, was not realized before. Certainly, no earlier theory presented such a convincing agreement between theory (Fig. 4.3) and experiment (Fig. 4.2) based on trivial disorder-induced theoretical ZBCPs.

In Fig. 4.4, we further study and discuss the (lack of) stability of the trivial ZBCPs of Fig. 4.3 by showing [Fig. 4.4(a)] the calculated zero-bias conductance, at fixed tunnel barrier and Zeeman splitting, as a function of the chemical potential, taking care to ensure that the system stays in the trivial phase with $V_Z < V_{Zc}$ always in the whole range of the chemical potential. We show the calculated chemical-potential-dependent conductance for three values of V_Z. We find

that the conductance can be tuned almost at will by changing the chemical potential (which is experimentally controlled by various gate voltages, such as the side gate and back gate voltages in Refs. [9, 57]). Although the dependence on the chemical potential is complicated and non-monotonic, in Fig. 4.4 the key feature is that the calculated conductance can be tuned by tuning chemical potential, with no stability, as also seen experimentally [57]. In Fig. 4.4(b), we depict the calculated zero-bias conductance as a function of the tunnel barrier potential for fixed Zeeman energy and chemical potential, showing that the trivial ZBCPs of Fig. 4.3 vary smoothly with a varying tunnel barrier, indicating its trivial character. The topological MZM manifests a constant $2e^2/h$ ZBCP for all tunnel barrier values as long as the temperature is lower than the tunneling energy. The fact that the ZBCP varies with the tunnel barrier means that it is not quantized, and does not arise from MZMs. One point to note here is that it is a challenge to connect our theoretical parameters V_g and μ to various gate voltages in the experimental situation, and it is likely that a variation in any of the experimental gate potentials varies both μ and V_g in some complex manners. For our discussion, however, this is irrelevant because the point we are making is that even when a fine-tuned ZBCP is apparently "quantized" (see Fig. 4.3), it is simply a feature of fine-tuning and postselection, and the conductance can be tuned to almost any value between 0 and $4e^2/h$ by carefully tuning $V_{\rm Z}$, μ, and V_g in the theory (and, equivalently, by the magnetic field, various gate voltages, and the tunnel barrier in the experiments).

In Fig. 4.5 we show the calculated energy spectra (and the lowest and the second-lowest wave functions) with and without the disorder potential to emphasize what is going on at the microscopic quantum-mechanical level. Figure 4.5(a) shows the energy spectrum in the presence of disorder corresponding to Figs. 4.3(a)-4.3(c) (since they only differ by the height of the tunnel barrier). The pair of low-lying states emerging from $V_{\rm Z} = 0.75$ to 1 meV is trivial be-

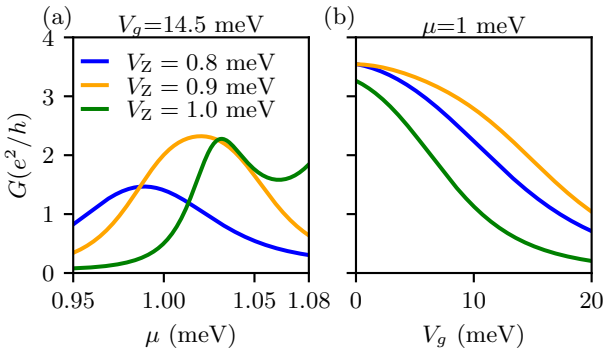

Figure 4.4: (a) The calculated zero-bias tunneling conductance as a function of the chemical potential μ at a fixed tunnel barrier $V_g = 14.5$ meV for V_Z =0.8 meV (blue), 0.9 meV (orange), 1 meV (red); (b) The calculated zero-bias tunneling conductance as a function of the tunnel barrier V_g at a fixed chemical potential $\mu = 1$ meV for $V_Z = 0.8$ meV (blue), 0.9 meV (orange), 1 meV (red). Refer to Fig. 4.3 for the rest parameters.

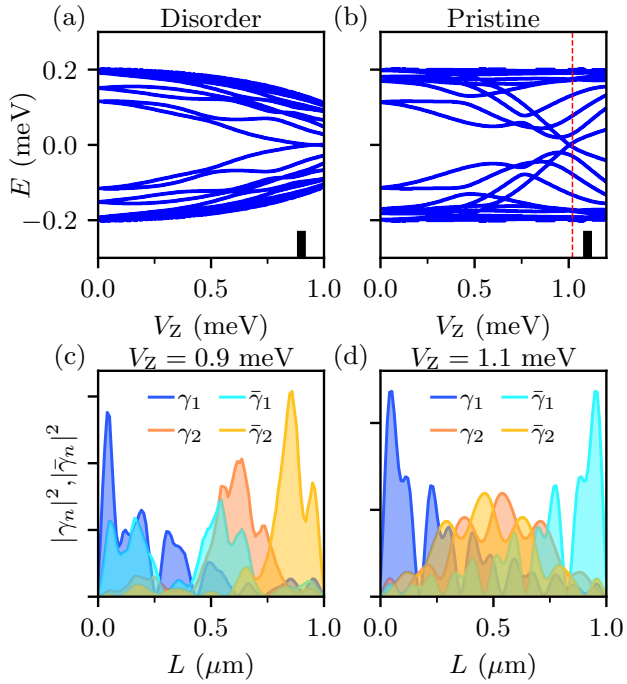

Figure 4.5: The energy spectra (upper panels) and wave functions (lower panels) of the disordered (left panels) and pristine nanowires (right panels) InSb/Al hybrid nanowire. (a) The energy spectrum as a function of Zeeman field in the presence of disorder, which corresponds to Fig. 4.3; (b) The energy spectrum as a function of the Zeeman field in a pristine nanowire for comparison. The topological regime is where $V_Z > 1.02$ meV, indicated by the vertical red dashed line. The SC gap always persists as the Zeeman field increases; (c) shows the lowest and second-lowest wave functions in the trivial regime at $V_Z = 0.9$ meV corresponding to the black line in (a); (d) shows the lowest and second-lowest wave functions in the topological regime at $V_Z = 1.1$ meV corresponding to the black line in (b). Refer to Fig. 4.3 for the other parameters (except for the tunnel barrier and dissipation, which are absent here).

cause it is below the putative TQPT at 1.02 meV. Given the finite dissipation (or even low, but finite, temperature), this pair of low-lying states may merge into a single peak and thus manifest the ZBCPs in Fig. 4.3. We also plot the corresponding wave function in the Majorana basis at $V_{\mathrm{Z}} = 0.9$ meV below the TQPT in Fig. 4.5(c). The wave functions of the lowest state in the Majorana basis $(\gamma_1, \bar{\gamma}_1)$ as defined in Eqs. (2.21) and (2.22) are in blue and cyan while the wave functions of the second-lowest state in the Majorana basis $(\gamma_2, \bar{\gamma}_2)$ are in red and orange. We find that the two Majorana modes are highly overlapping, which indicates a trivial fermionic state. For comparison, we also present the energy spectrum of the corresponding disorder-free pristine nanowire in Fig. 4.5(b). The TQPT happens at $V_{\mathrm{Z}} = 1.02$ meV (red dashed line); thus, the corresponding wave function at $V_{\mathrm{Z}} = 1.1$ meV [Fig. 4.5(d)] is in the topological regime. The wave function of the lowest state is localized at two ends of the nanowire, while the wave function of the second-lowest state is localized in the bulk region of the nanowire.

Several aspects of our disordered Majorana nanowire results need to be emphasized in order to avoid any misunderstanding. First, there is no ensemble averaging, the quenched spatial disorder is one fixed random configuration chosen from a Gaussian distribution, consistent with the experiment being done at very low temperatures. Second, most disorder configurations with the same strength and variance do not produce large zero-bias trivial peaks— in fact, most disordered results have small ZBCPs or no peaks at all; only a few configurations give rise to large ZBCPs. This is also consistent with the experimental situation where the protocol is to go through many samples by varying tuning parameters until large ZBCPs appear in the measurements, and once such a peak appears, it is fine-tuned to produce the desired results. Both the experiment [57] and our theory produce only of the order of $\sim$2% samples manifesting large ZBCPs with conductance $\sim O(2e^2/h)$. Large ZBCPs are not guaranteed by any means either in the experiment

or in the theory with disorder, only for the pristine nanowires with real topological Majorana modes, ZBCPs with conductance $2e^2/h$ appear generically for $V_{\rm Z}$ above the TQPT. We mention as an aside that very stable trivial ZBCPs with values pinned at $2e^2/h$ may arise from certain types of smooth deterministic potential-induced trivial tunneling peaks, but such stable peaks do not go above $2e^2/h$ [64]. We believe that the measurements of Refs. [9, 56, 57], as well as all the earlier nanowire Majorana experiments, are dominated by random disorder effects and not by any smooth potential-induced quasi-Majorana behavior. The other thing to emphasize is that even our disordered system eventually would manifest topological ZBCPs at a large enough Zeeman field well above the TQPT so that the Zeeman field can overcome the disorder effect. But, experimentally such a high-field regime is currently inaccessible since the bulk SC is completely suppressed at the high field in the experiment, most likely because the parent Al SC is quenched by the high magnetic field. The ZBCPs in Fig. 4.3 in our theory are all nontopological occurring below TQPT, which are induced entirely (but only occasionally, not generically) by disorder. No experiment has ever reported either ZBCPs $\sim 2e^2/h$ values stable over a large magnetic field range or reentrant ZBCPs with $\sim 2e^2/h$ conductance at high magnetic fields, so we can safely conclude that the existing experimental data do not provide evidence for any topological ZBCP at $V_{\rm Z} > V_{\rm Zc}$. We emphasize that the good MZM-induced topological ZBCPs could manifest conductance $< 2e^2/h$ (e.g., because of temperature effect), but not $> 2e^2/h$, as in Fig. 4.2 and Ref. [57].

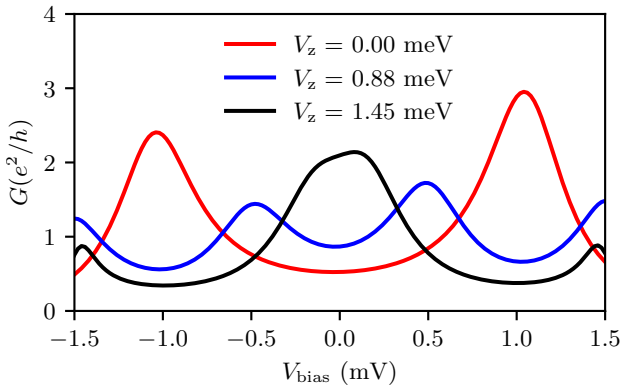

Figure 4.6: The tunneling conductances in the trivial regime as a function of bias voltages at fixed Zeeman fields 0 meV (red), 0.88 meV (blue), and 1.45 meV (black) to reproduce Fig. 3(c) in Ref. [56] using exactly the same Hamiltonian as in Fig. 4.3 but only with a different set of SC parameters corresponding NbTiN: the parent SC gap is 3 meV and the SM-SC coupling strength is 1.5 meV (hence the induced SC gap is around 1 meV) [122]. The other parameters are as follows: the wire length is 0.4 μm, the chemical potential is $\mu = 5$ meV, the standard deviation of disorder $\sigma_\mu = 20$ meV, the parent SC gap closes at $V_{\rm Z} = 10$ meV, the SOC $\alpha = 0.5$ eVÅ, the phenomenological dissipation is 0.1 meV, and the tunnel barrier height V_g is 10 meV. We also verify that the conductance at the other end [left end in Fig. 4.8(c)] of the nanowire has no feature, namely, no subgap states emerge and the conductances are almost zero everywhere inside the parent SC gap.

4.2.2 Strong disorder: InSb/NbTiN SM-SC nanowire

Now, we briefly discuss another recent experiment, where very small ZBCPs $\sim 2e^2/h$ are reported in Indium Antimonide/Niobium-Titanium-Nitride (InSb/NbTiN) SM-SC structures, with the system being well-known to be very highly disordered [56]. Very similar (essentially identical) tunneling data to what is reported in [56] were already reported extensively in the early experiments on Majorana nanowires [8, 35–38], where the characteristic features were the existence of a soft SC gap (indicating strong disorder in the system) and very non-sharp small peaks over the large background tunneling conductance because of the presence of considerable subgap fermionic states (the same states leading to the gap being soft). In addition, the new experiment emphasizes the fact that tunneling from only one end manifests ZBCPs, not from

both ends, further reinforcing the trivial nature of these small (above the background) ZBCPs.

In Fig. 4.6, we show our fine-tuned simulated theoretical results corresponding to the observations of [56] using nanowire parameters corresponding to the InSb/NbTiN system, where the parent SC gap is larger (than in Al) and so are disorder and dissipation (arising from the copious presence of vortices in the rather poor quality NbTiN material). We reproduce disorder-induced small ZBCPs above the background which are not sharp at all (similar to the experiment in [56]), but have conductance values $\sim 2e^2/h$. Our results of Fig. 4.6 look very similar to the results shown in Figs. 2(c) and 3(c) of [56]. We note that neither experiment [56] nor our theory generically produces ZBCPs $\sim O(2e^2/h)$ — both are fine-tuned results without much significance. The characteristic features are as follows: the ZBCPs are trivial arising entirely from disorder, a strong asymmetry in the peaks arising from dissipation [139], very soft SC gap because of disorder-induced subgap states, and small non-sharp ZBCPs above the background with conductance $\sim O(2e^2/h)$. We have checked that the tunneling from the other end here does not produce any ZBCPs in our simulations as expected, and we have also checked that these calculated ZBCPs are not robust against the tunnel barrier potential. The tunnel barrier potential has to be carefully tuned both in our theory and in the experiment of [56] in order to find small peaks with $2e^2/h$ values: it is a result of precise fine-tuning in the magnetic field, tunnel barrier, and disorder potential. The peaks in the experiment of [56] and in our Fig. 4.6 are similar to the ones seen in the early 2012 nanowire tunneling spectroscopies [8, 35–38], and are not similar to the results in Figs. 4.2 and 4.3, i.e., in Ref. [57], where the gap is hard and the ZBCPs are large and sharp. We do not believe that the experimental observations of Refs. [56, 57] are equivalent as the latter is reporting results in extremely highly disordered systems with a huge amount of subgap fermionic states as was the situation in 2012. It is clear that sample improvement from

2012 to 2021 has vastly improved the quality of the data in Majorana nanowires, and we believe that further improvement in sample quality will lead to the observation of topological Majorana modes.

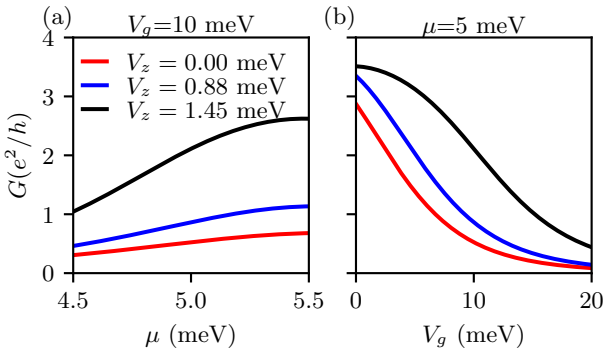

Figure 4.7: (a) The calculated zero-bias tunneling conductance as a function of the chemical potential μ at a fixed tunnel barrier $V_g = 10$ meV for V_Z =0 meV (red), 0.88 meV (blue), and 1.45 meV (black); (b) The calculated zero-bias tunneling conductance as a function of the tunnel barrier V_g at a fixed chemical potential $\mu = 5$ meV for V_Z =0 meV (red), 0.88 meV (blue), 1.45 meV (black). Refer to Fig. 4.6 for the rest parameters.

In Fig. 4.7 (see Fig. 4.4 for comparison with the same results for Ref. [57] parameters), we show our calculated conductance for Ref. [56] parameters as a function of chemical potential and tunnel barrier keeping all other quantities fixed (and ensuring that the system is always trivial, i.e., $V_Z < V_{Zc}$ throughout). As expected, the conductance at zero bias varies smoothly as a function of either the chemical potential [Fig. 4.7(a)] or the tunnel barrier [Fig. 4.7(b)], reflecting their trivial unstable character, similar to what we find in Fig. 4.4 for the Delft sample. Thus, trivial ZBCP, arising at $V_Z < V_{Zc}$, could possibly be tuned to $\sim 2e^2/h$ (or to any value between 0 and $4e^2/h$) by fine-tuning the chemical potential and/or the tunnel barrier strength, but such a fine-tuned $2e^2/h$ ZBCP is neither stable nor meaningful. Of course, for the extremely disordered samples used in Ref. [56], these peaks are very small and are additionally misleadingly fine-tuned by carrying out an arbitrary contact resistance subtraction, making the whole fine-tuning exercise meaningless

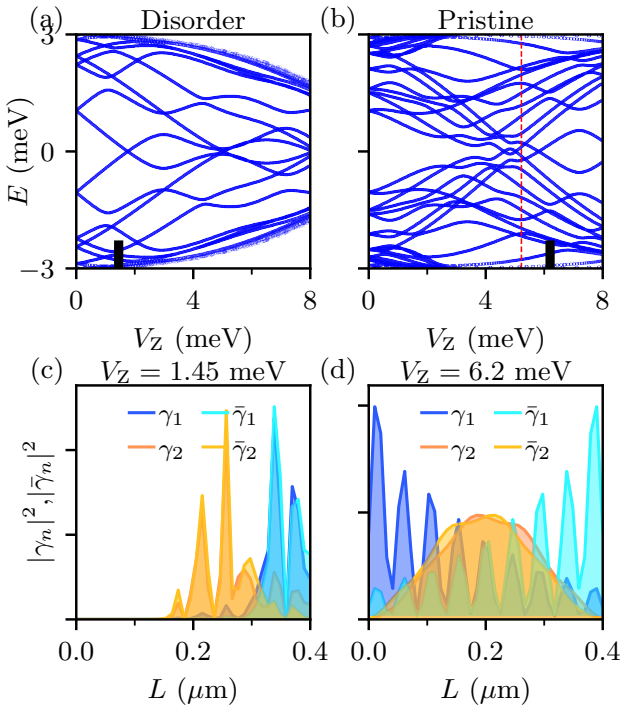

Figure 4.8: The energy spectra (upper panels) and wave functions (lower panels) of the disordered (left panels) and pristine nanowires (right panels) in InSb/NbTiN hybrid nanowire. (a) The energy spectrum as a function of the Zeeman field in the presence of disorder, which corresponds to Fig. 4.6; (b) The energy spectrum as a function of the Zeeman field in a pristine nanowire for comparison. The topological regime is where $V_Z > 5.22$ meV, indicated by the vertical red dashed line. The SC gap always persists as the Zeeman field increases; (c) shows the lowest and second-lowest wave functions in the trivial regime at $V_Z = 1.45$ meV corresponding to the black line in (a); (d) shows the lowest and second-lowest wave functions in the topological regime at $V_Z = 6.2$ meV corresponding to the black line in (b). Refer to Fig. 4.6 for the other parameters (except for the tunnel barrier and dissipation, which are absent here).

and bizarre.

In Fig. 4.8 (c.f., Fig. 4.5 for the corresponding results for the corresponding Delft [57] results) we show our calculated energy spectra and low-lying wave functions for the typical parameters of Ref. [56]. The important point of Fig. 4.8 is that disorder mixes the Majorana states from the two ends strongly, and depending on the details of this overlap, it is possible to have a trivial zero-bias tunneling peak from one end, but not from the other end.

4.3 Discussion

We have provided in this chapter detailed Majorana nanowire theoretical simulations, showing that trivial ZBCPs with sharp and large $\sim O(2e^2/h)$ values may appear in the tunneling spectra mimicking aspects of topological MZMs, thus misleading the experimentalists. These large trivial peaks arise from random disorder with fine-tuning very similar to the experimental protocol used in the experimental data analysis searching for MZMs through tunneling spectroscopy. Just as not all laboratory samples manifest large ZBCPs, not all random disorder configurations produce large trivial peaks, and therefore the possibility of confirmation bias is considerable because the inevitable presence of disorder in the experimental samples may very well produce large zero-bias tunneling conductance peaks through extensive data selection, which is the current laboratory protocol for the Majorana search. For example, Zhang *et al.* [9, 57] find the reported large ZBCPs, which they originally mistakenly attributed as "Majorana quantization", only in 2 out of around 80 samples they looked at. This is a $\sim$2% yield on the desired outcome one is trying to find, and should always be taken with considerable suspicion as possibly being "false positives" arising from the inherent nature of the confirmation bias syndrome. We believe that it

is likely that all existing claims of Majorana observations in the literature are trivial peaks arising from disorder, but of course, we can only suggest this as a real possibility, we cannot prove it. Something negative, i.e., true MZMs have not yet been experimentally observed, can only be persuasively suggested by our theory, by definition, it cannot be proven. The fact that the observed ZBCPs never manifest any robust stability in experimental tuning parameters, e.g., the magnetic field, gate voltage, and tunnel voltage, which is consistent with our disorder-induced trivial peaks in this chapter, where we find that the disorder-induced trivial ZBCPs show smooth variations in Zeeman energy, chemical potential, and barrier potential, and inconsistent with topological zero modes also lends credence to our suggestion that Majorana experiments are dominated by random disorder. We would speculate that this disorder problem is prevalent in most, if not all, topological experiments in the literature. Although our current work focuses on SM-SC nanowire platforms, because the best and the most quantitatively compelling tunneling spectroscopy data are extensively available in Majorana nanowires, other systems, where the ZBCPs are studied at vortex cores using scanning tunneling microscopy, manifest ZBCPs of extreme small values which are much more consistent with disorder-induced subgap Andreev states in the vortex cores than with topological MZMs.

The most important finding in this chapter is its remarkable agreement with the reported data in Ref. [57]: both experiment [57] and our theory find similar-looking large and sharp fine-tuned zero-bias tunneling conductance peaks which are not robust against variations in Zeeman field, chemical potential, and tunnel barrier, and both manifest peaks which could go above $2e^2/h$ quantization value, but can be fine-tuned (by adjusting parameters such as magnetic field and gate voltages) to $2e^2/h$, enhancing the unfortunate possibility of a confirmation-bias-induced claim for Majorana quantization. Also, our trivial ZBCPs generically exist only for tunneling from one end,

and not the other end, although that can occasionally happen accidentally [66, 77]. Therefore, we urge experimentalists to try simultaneous tunnel spectroscopies from both ends as an additional distinguishing aspect of trivial versus topological.

4.4 Conclusion

This chapter suggests that serious vigilance is necessary to guard against claims of topological discoveries based on confirmation bias arising from precise existing theoretical predictions. In particular, all such experimental claims should necessarily release all data collected in the experiment (including data that are inconsistent with the topological predictions) so that the community could go through the data to ensure that the outcome is not generated by confirmation bias achieved through fine-tuned data selection. The fundamental problem here is that, given a sufficient number of tunable parameters (magnetic field, tunnel barrier, gate voltage) in the experiment, it is often, if not always, possible to keep on tuning parameters until one finds precisely what one is looking for. What we show here is that disorder produces trivial peaks, which on sufficient fine-tuning, would produce $\sim 2e^2/h$ peaks, and this by itself is no discovery, it is simply confirmation bias.

One specific and concrete conclusion of our extensive theoretical studies on Majorana nanowires including effects of disorder is that topological MZMs in all likelihood have not yet been observed in the laboratory since even the very best currently available experimental data [57] appear consistent with disorder-induced ZBCPs in the theory.

The other key general conclusion of this chapter is that confirmation bias is almost inevitable in claiming topological discoveries if one looks for something precise among a huge

amount of data, particularly if there are many parameters to tune and many samples to use.

Chapter 5: Generic quantized zero-bias conduct peaks: a random matrix theory study

In Chapters 2-5, we have studied the transport properties of the SM-SC nanowires from a microscopic model. However, one may argue that because the emergence of ZBCPs may explicitly depend on the details of the specific platform, the conclusion cannot generalize to the other platforms for searching for the MZMs. To address this issue, we revisit the problem from a random matrix approach, and show that quantized ZBCPs should be ubiquitous in any class D ensemble.

As a quick reminder, the experimental methodology for reporting candidate MZMs based on single-junction NS conductance typically involves: (1) a search over the experimental parameter space (e.g., Zeeman field, tunnel barrier, and various gate voltages to tune the chemical potential) to identify any ZBCPs with an otherwise clean, featureless spectrum below the parent SC gap; (2) additional parameter fine-tuning to obtain $2e^2/h$ conductance; then finally (3) a demonstration that this conductance is quantized through the stability of the ZBCP as external parameters (e.g., gate voltage and Zeeman field) are tuned (i.e., a quantized conductance "plateau"). In this chapter, we conclusively establish that even step (3) of the protocol above is generally unable to rule out the trivial non-MZM ZBCP scenario.

Theoretically, we establish compellingly that ZBCPs of trivial origin are generic in systems

with no symmetry other than particle-hole symmetry that these peaks can stick to zero energy over extended regions of the parameter space, and finally that some finite fraction of these peaks manifests stable and robust quantized conductance. In other words, the experimental procedure of searching for quantized ZBCPs by fine-tuning experimental parameters (e.g., Zeeman field, gate voltages, and tunnel barrier) in a systematic way is practically guaranteed to produce these "false positive" apparently quantized, nevertheless, trivial ZBCPs. Our theoretical starting point is a class D random matrix ensemble [79, 106, 111, 165]. The model is maximally generic since we impose no constraint other than particle-hole symmetry on the Hamiltonian, which holds for every experimental Majorana platform. We do not claim that any previous experiment is precisely described by such a random matrix in its full details: The RMT can only predict the most generic features due to fluctuations in different Hamiltonians governed by the same symmetry (i.e., particle-hole symmetry here) [150]. Thus, this should be only understood as a null hypothesis applied to all 1D and two-dimensional Majorana platforms, including SM-SC devices [9, 46, 49, 53], iron-based SCs [166, 167], etc. We then calculate the NS tunneling conductance spectra of an essentially 0D QD system (see Fig. 5.1). Our central result expands and substantially generalizes on the generic class D "sticking ZBCP" [111] scenario— i.e., a nonquantized conductance peak that remains at zero bias as a single continuous parameter is tuned (this was also called a "*Y*-shaped Andreev resonance" in Ref. [111]). In a higher-dimensional parameter space as consistent with the experimental methodology searching for MZMs, we show here that sticking ZBCPs can evolve into extended plateaulike regions enclosed by contours with $2e^2/h$ conductance. We establish that it is typical to find completely generic random Hamiltonians that produce sticking ZBCPs over some fraction of the parameter space *and* with stable near-quantized conductance but which never correspond to spatially isolated MZMs by construction. If we are allowed some

additional postselection over the space of random class D matrices as can be performed by tuning several parameters in the experimental protocol, these plateaus can even be made remarkably large. We also show that varying the tunneling amplitude leads to qualitatively similar results to those reported in experiments by changing the barrier gate voltage [9].

We choose the Gaussian ensemble to simulate the QD so that each element of the random Hamiltonian is distributed independently, which simplifies the later calculation [149, 165]. We mention also that our random matrix model, whereas being the most generic theoretical model of the hybrid system from the perspective of symmetry, is also a reasonably physical model of the currently available experimental samples where the nanowire is typically short with many discrete energy levels being occupied. This guarantees the prerequisite of a valid random matrix approach that the energy states in the Hamiltonian spectrum should be sufficiently large [149]. In essence, nanowires that have a high chemical potential and, thus, occupy many subbands act like an effective random matrix system because any changes in the system parameters (e.g., various gate voltages) can drastically alter the Hamiltonian of the system during the measurement, even though the material itself is in the clean limit [168].

5.1 Theory

The region in Fig. 5.1 enclosed by the dashed line is mainly composed of a 0D SC QD appearing in a proximitized SM nanowire, which can be described by a class D $M \times M$ Hermitian random matrix. We adopt the Majorana basis for simplicity, where the Hamiltonian is

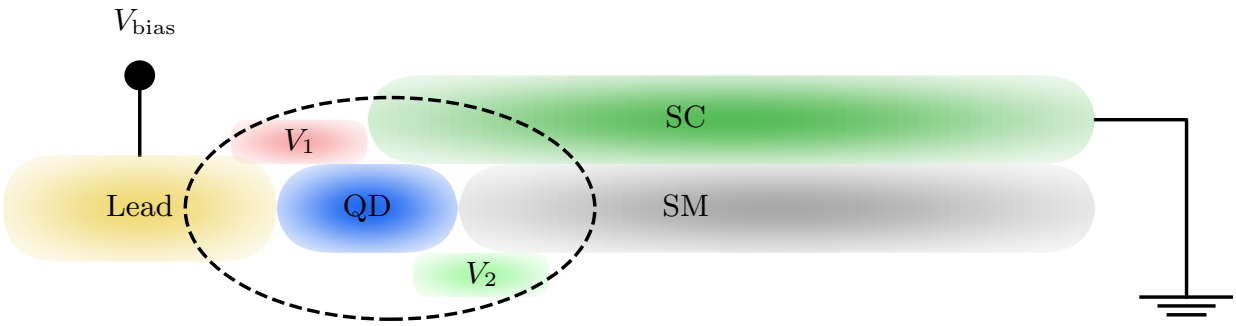

Figure 5.1: Schematic of an SM-SC hybrid structure coupled to a normal metal lead. V_1 and V_2 represent two gate voltages. The dashed circle highlights the QD region arising from the proximitized SM nanowire, which is described by the random matrix Hamiltonian.

characterized by a particle-hole symmetry as per,

$$\mathcal{H} = -\mathcal{H}^*. \tag{5.1}$$

It is then convenient to take $\mathcal{H} = iA$, where A is real and anti-symmetric. In the large-M limit [111, 149, 150, 165, 169], we can assume a Gaussian distribution for $\mathcal{H}$,

$$P(\mathcal{H}) \propto \exp\left(-\frac{\pi^2}{4\delta_0 M}\,\mathrm{tr}\left(\mathcal{H}^2\right)\right), \tag{5.2}$$

where $\mathrm{tr}(\cdots)$ is the matrix trace and mean energy-level spacing $\delta_0 = 0$ for simplicity. Equation (5.2) can be further simplified to independent Gaussian distributions for each element of A,

$$P(\{A_{nm}\}) \propto \prod_{1=n<m}^{M} \exp\left(-\frac{\pi^2 A_{nm}^2}{2M\delta_0^2}\right). \tag{5.3}$$

To calculate the conductance, we follow the formalism of Ref. [111], which we reproduce here to make the presentation self-contained. To simulate the NS tunneling geometry, the M states of the QD are coupled to an N-channel lead through the $M \times N$ tunneling matrix $\mathcal{W}$.

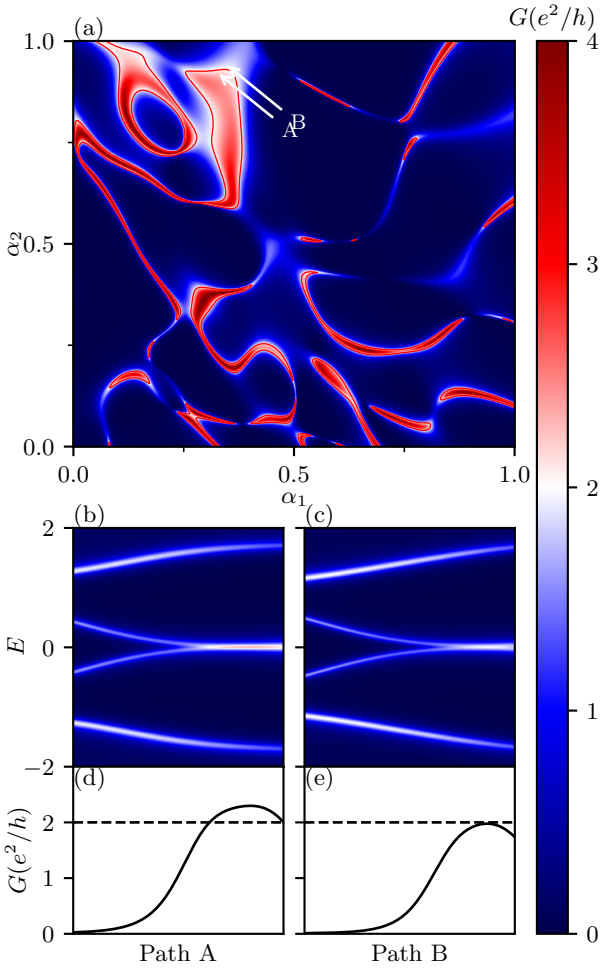

Figure 5.2: (a) Color plot of the differential conductance at zero-bias voltage, as a function of tuning parameters α_1 and α_2. The red solid lines are the contours of the zero-bias conductance of $2e^2/h$. Here, we set the temperature $T = 0$. The marked wite solid lines A and B indicate the paths of varying α mimicking the tuning of gates in experiments; (b-c) The conductance as a function of the bias voltage and position following along Path A and Path B. The bias voltage is normalized by the mean level spacing δ_0. This is an example of the gap closing feature followed by trivial nearly quantized ZBCP; (d-e) are the corresponding ZBCP heights.

Since the choice of the basis of $\mathcal{H}$ does not affect the distribution of $\mathcal{H}$, we can, without loss of generality, simply choose the basis where the tunneling matrix $\mathcal{W}$ is diagonal [111], i.e.,

$$\mathcal{W}_{mn} = w_n \delta_{m,n}, \quad 1 \leq m \leq M, \quad 1 \leq n \leq N, \tag{5.4}$$

where w_n is determined by the tunneling probability $\Gamma_n \in [0, 1]$ as [149, 150]

$$|w_n|^2 = \frac{M\delta_0}{\pi^2 \Gamma_n} \left(2 - \Gamma_n - 2\sqrt{1 - \Gamma_n}\right). \tag{5.5}$$

For simplicity, we assign an identical tunneling probability for each channel in the lead, following Ref. [111].

The differential conductance $G(V) = dI/dV$ is then determined by calculating the $N \times N$ scattering matrix [72, 115, 142] according to the Mahaux-Weidenmüller formula [149, 150, 170–172],

$$\mathcal{S}(E) = \mathbf{1_N} + 2i\pi \mathcal{W}^\dagger (\mathcal{H} - i\pi \mathcal{W}\mathcal{W}^\dagger - E)^{-1} \mathcal{W}. \tag{5.6}$$

We then obtain the differential conductance in the Majorana basis as

$$G(V) = \frac{e^2}{h} \left(\frac{N}{2} - \frac{1}{2} \operatorname{tr}\left[\mathcal{S}(eV) \tau_y \mathcal{S}(eV)^\dagger \tau_y\right] \right) \tag{5.7}$$

where τ_y is the Pauli matrix acting on the particle-hole space.

Another useful tool for understanding the sticking of ZBCPs is the non-Hermitian "effective Hamiltonian",

$$\mathcal{H}_{\text{eff}} = \mathcal{H} - i\pi \mathcal{W}\mathcal{W}^\dagger, \tag{5.8}$$

where the imaginary term is a self-energy acquired from the coupling to the lead. When the tunneling probability Γ_n is small, the energy spectrum of $\mathcal{H}_{\text{eff}}$ approaches that of the original $\mathcal{H}$. Note that the eigenvalues of $\mathcal{H}_{\text{eff}}$ are distributed in the lower half of the complex plane due to the positive definiteness of $\mathcal{W}\mathcal{W}^\dagger$. In addition, the particle-hole symmetry in $\mathcal{H}$ constrains the eigenvalues to come in pairs ϵ and $-\epsilon^*$. Therefore, the eigenvalues will be symmetrically distributed along the imaginary axis, unless purely imaginary. Thus, the nondegenerate eigenvalue on the imaginary axis has a range of stabilities [173, 174] against perturbations since there is no way to obtain a nonzero real part without breaking the particle-hole symmetry. This kind of stability is responsible for the zero energy sticking of the trivial ZBCPs. An intuitive way to understand this is that a purely imaginary eigenvalue of $\mathcal{H}_{\text{eff}}$ corresponds to the presence of an exact zero eigenvalue in $\mathcal{H}$. Consequently, one will observe a corresponding ZBCP, especially when Γ_n is small. In what follows, we use $M = 80$ and $N = 4$ (i.e., a single transport channel with particle-hole and spin degrees of freedom). Our results are sensitive to the choice of N, so we choose it to reflect the experimental situation; our results are not sensitive to the choice of M, once sufficiently large. The tunneling probability is $\Gamma_n = 0.1$ by default unless stated otherwise. We emphasize that all of our results, quantized conductance or not, are, by construction, topologically trivial since M is even [175–177].

Finally, our conceptual break with Ref. [111] is that we simulate the manipulation of several independent parameters (simulating the role of gate voltages in experiments), describing the QD with a parametric Hamiltonian in a higher-dimensional parameter space (i.e., Zeeman field plus gate voltages),

$$\mathcal{H} = \alpha_1\mathcal{H}_1 + \alpha_2\mathcal{H}_2 + (1 - \alpha_1 - \alpha_2)\mathcal{H}_3, \tag{5.9}$$

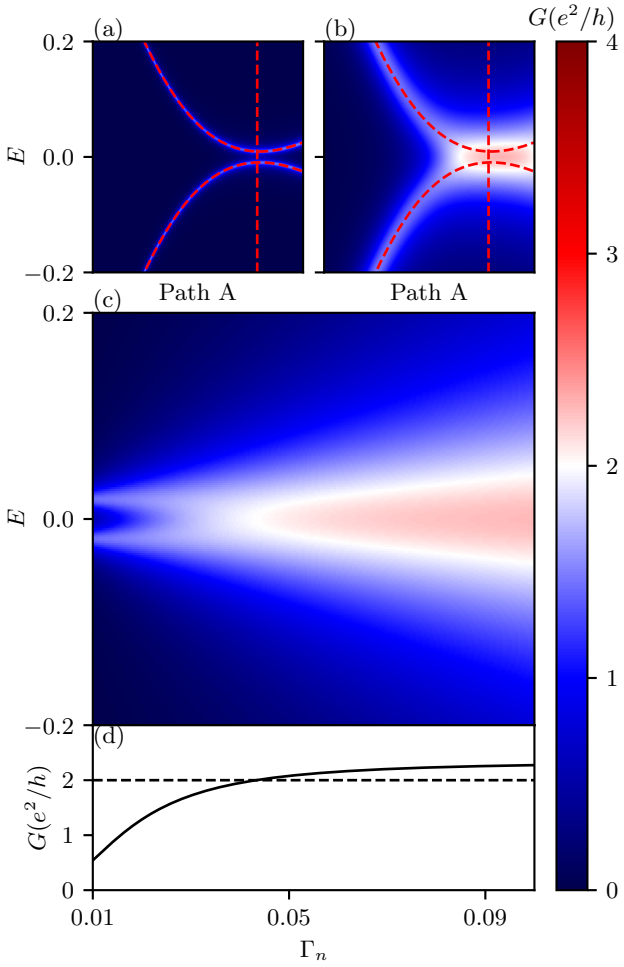

Figure 5.3: Conductance spectra near zero energy following along Path A as in Fig. 5.2 for (a) $\Gamma_n = 0.01$ and (b) $\Gamma_n = 0.1$. The red dashed lines are the eigenvalues of $\mathcal{H}$. For sufficiently large Γ_n, the corresponding conductance smears the level structure into a stuck ZBCP. Fixing $\alpha_{1,2}$ at the vertical red dashed line, the conductance as a function of transparency is shown in (c), and the ZBCP height is shown in (d).

where $\mathcal{H}_{1-3}$ are three randomly drawn matrices and $\alpha_{1,2} \in [0,1] \times [0,1]$ are two tuning parameters. This two-dimensional parameter space can be considered as an isomorphism to a space spanned by magnetic-field B and another gate voltage (V_1 or V_2) in the experiment through a certain deterministic mapping (which does not have to be orthogonal or linear). However, we also clarify that, since there are typically several gates in experiments, the manner in which we introduce two parameters $\alpha_{1,2}$ does not forbid the possibility of a higher-dimensional parameter space. In fact, it is very straightforward to generalize the two-parameter-dependent Hamiltonian to a higher-dimensional one. We find, however, that the two-dimensional parameter space is already sufficient to establish our main conclusions, and any higher-dimensional parameter space representation only reinforces the generic results presented here.

5.2 Results

We now emulate the "Majorana search" protocol of tuning parameters to find sticking ZBCPs. We do this systematically by finding the purely imaginary eigenvalues of Eq. (5.8). We randomly draw 125000 independent triplets for $\mathcal{H}_{1-3}$, and then we post-select a $\mathcal{H}$ that maximizes the region of $\alpha_{1,2}$ with sticking ZBCP by choosing the particular set of $\mathcal{H}_{1-3}$ which yields the largest number of purely imaginary eigenvalues. To determine the occurrence frequency of purely imaginary eigenvalues over realizations of $\mathcal{H}$, we discretize the parameter space $\alpha_{1,2} \in [0,1] \times [0,1]$ and sweep over each grid point of $\alpha_{1,2}$ to evaluate the corresponding $\mathcal{H}$ in Eq. (5.9). By enumerating the occurrences of purely imaginary eigenvalues, we indirectly know the likelihood that one can find the sticking ZBCP in such a configuration. In Fig. 5.2(a), we plot the differential conductance at the zero-bias voltage for the $\mathcal{H}$ selected by this procedure. The

conductance varies continuously from 0 (dark blue) to $4e^2/h$ (dark red), the maximum possible for $N = 4$ [34]. Thus, searching for the sticking quantized ZBCP is equivalent to finding the region of $2e^2/h$ conductance in the color plot. To compare with experimental results [9, 46, 49, 53], we highlight the contour of $2e^2/h$ conductance in Fig. 5.2(a) in red. From this, we can immediately identify two types of regions with high conductance: the *plateaulike* regions on the upper left versus the *ridgelike* regions on the right of Fig. 5.2(a). The plateaulike regions are characterized by small gradients in the conductance and are reminiscent of the theoretical expectation for a topological region of a phase diagram. In Figs. 5.2(b) and 2(c), we show the full conductance spectra following along the two paths marked A and B in the plateaulike region of Fig. 5.2(a). The conductance spectra in Figs. 5.2(b) and (c) show a remarkable resemblance to experimental candidate Majorana ZBCPs [9, 46, 49, 53], i.e., an in-gap conductance peak coming down to zero-bias voltage, followed by a stable ZBCP of $2e^2/h$. More importantly, this nearly quantized ZBCP can even be stable in a certain region of parameters. Shifting Path A slightly to obtain Path B, the conductance spectrum is hardly affected as long as the path remains within the plateaulike region. These ZBCPs in the plateaulike region can manifest a "robust nature" in experiments. Again, we emphasize that, by construction, these nearly quantized ZBCPs shown in the conductance spectra do not arise from a spatially isolated MZM. Furthermore, these trivial nearly quantized ZBCPs are ubiquitous in Fig. 5.2; plateaulike regions are not rare in the color plot, and any path that crosses a plateaulike region (such as paths A and B) will result in similar conductance spectra to Figs. 5.2(b) and 2(c).

We also investigate the effect of tuning the barrier transparency through Γ_n. We first vary Γ_n from 0.01 to 0.1 following along Path A of Fig. 5.2(a). In Figs. 5.3(a) and 3(b), we compare the conductance spectra for two values of Γ_n, overlaid with the eigenvalues of $\mathcal{H}$. As Γ_n increases,

the ZBCP broadens and appears more stuck to the zero voltage axis [111], whereas for small Γ_n, the peak becomes steeper and fainter, and the origin of this ZBCP as a parabolic near touching becomes apparent. This phenomenon is consistent with experiment [9] in the sense that the zero-bias conductance looks nearly quantized for larger transparency but vanishes at small Γ_n where it is accompanied by a peak splitting as shown in Fig. 5.3(c).

Although the previous plots were all produced for a single particular realization of $\mathcal{H}$, we emphasize that the qualitative behavior is typical as we have verified explicitly: Our main results are that the existence of plateaus is generic and these plateaus can be easily obtained by following the generally accepted Majorana search experimental methodology. To quantify this, we calculate the fraction of the parameter space (α_1, α_2) where $\mathcal{H}_{\text{eff}}$ has purely imaginary eigenvalues, which, in turn, roughly corresponds to the fraction of parameter space covered by plateaulike ZBCPs. We histogram this fraction over independent realizations of $\mathcal{H}$, shown in Fig. 5.4. This coverage fraction has a distribution that is peaked around 4% — i.e., when performing a search for MZMs through a two-parameter conductance map (for example, to construct a topological phase diagram), one should *a priori* expect around 4% of the map to feature trivially almost-quantized conductance. In the inset of Fig. 5.4, we show the typical statistics for the expected values of these ZBCPs within $\pm 20\%$ of the putative quantized value of $2e^2/h$. Clearly, quantized stable trivial ZBCPs are generic in class D SC systems.

5.3 Discussion

We have generalized the crucial insight of Ref. [111] that distinguishes *X*- versus *Y*-shaped Andreev resonances (the latter being our sticking ZBCPs) to a higher-dimensional parameter

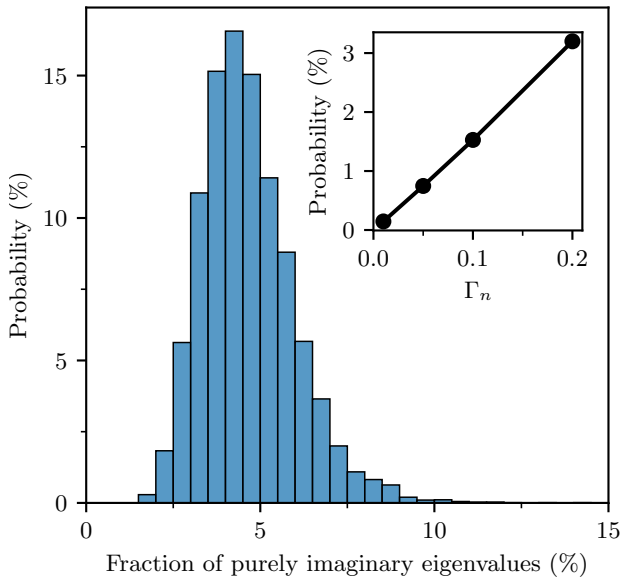

Figure 5.4: Distribution (over the ensemble of $\mathcal{H}$) of the fraction of the parameter space (α_1, α_2) where $\mathcal{H}_{\text{eff}}$ [Eq. (5.8)] possesses purely imaginary eigenvalues. This is proportional to the area of parameter space covered by plateaulike ZBCPs. The inset shows the almost-quantized ZBCP statistics as a function of Γ_n which is determined by the tunnel barrier voltage.

space where the distinction becomes one between ridgelike and plateaulike regions in the parameter space. Although *Y*-shaped resonances of a single parameter might not be quantized in general, the quantized plateaulike higher-dimensional regions are generic, and if we allow even more parameters α_i, the parameter space that realizes nearly quantized trivial ZBCPs can only increase. This implies that more gate voltages being independently tuned to optimize experimental ZBCPs necessarily leads to the observation of generic and trivial quantized ZBCPs. Our simulated results for conductance spectra in the 0D random matrix model resemble the existing experimental NS conductance results, regardless of the proposed Majorana or quasi-Majorana interpretations. The nearly quantized ZBCP is, therefore, ubiquitous in theory in multidimensional parameter space, requiring no input other than class D symmetry— a symmetry that any platform pursuing Majorana should possess— and can be easily observed in conductance color plots, such as Fig. 5.2(a), i.e., modeling the multiparameter tuning involved in Majorana search procedures.

5.4 Conclusion

Our results clarify that even stable apparently quantized ZBCPs do not provide conclusive evidence for topological MZMs; the observation of such peaks does not necessarily imply a topological phase nor does the peak merging or splitting as a function of electrostatic gate manipulation (especially local gates near the junction) imply entering or exiting such a phase. We emphasize that our theory applies to all class D SC platforms where ZBCPs have been reported, which include, in addition to the well-studied SM-SC nanowires [9, 46, 178], also ferromagnetic chains [145], topological insulator-based structures [179], and Fe-based SCs [166, 167].

Chapter 6: Conclusion

In this chapter, we summarize what we have discussed in the previous chapters. In Chapter 1, we start with the introduction of topological quantum computing and introduce the motivation for searching for the MZMs as topological qubits. We then introduce the Kitaev chain as a toy model to host the MZMs at the ends of the chain. However, because the Kitaev chain requires a p-wave SC to pair the fermions between two neighboring sites, which is not naturally found, we introduce the SM-SC nanowire which only requires an SM with a large SOC strength being covered by a conventional s-wave SC and the magnetic field perpendicular to the direction of SOC. Such an SM-SC nanowire should manifest a quantized conductance of $2e^2/h$ in the transport experiment as a signature of MZMs. However, these signatures were only partially observed in experiments as they are neither quantized nor robust, which led to the alternative explanations of the mechanism as trivial ABSs other than the topological MZMs. These ambiguous experimentally observations are the original motivation of this dissertation.

In Chapter 2, we construct the SM-SC nanowire Hamiltonian by taking into account various aspects, including the pristine wire, QD, inhomogeneous potential, disorder in the chemical potential, the SC gap, and the effective g factor. By theoretically calculating the tunneling conductance spectra through an NS junction as a function of the Zeeman field V_{Z}, we classify all the ZBCPs into three types: the "good", the "bad", and the "ugly", which are the most significant

results in this dissertation. The "good" ZBCPs are the true topological MZMs only existing in pristine nanowires or a small amount of disorder which, however, have never been observed in experiments. The "bad" ZBCPs are induced by the QD or the inhomogeneous potential, where a trivial ZBCP emerges from a pair of fermionic ABSs below the TQPT approaching zero energy, and splitting again at a higher magnetic field. The "ugly" ZBCPs are induced by the intermediate to large disorder in the chemical potential or the effective g factor. These types of disorder completely alter the pattern of the conductance spectrum by creating the trivial ZBCPs with arbitrary zero-bias conductance from 0 to $4e^2/h$ below the putative TQPT, and even suppressing the real topological ZBCPs which could have been induced by MZMs beyond the TQPT.

We also discuss the efficacy of the correlation measurement in the two-terminal device, where the left and right local conductances are obtained by isolating the lead at the other end, respectively. In principle, the perfect correlation of ZBCPs on both ends should serve as a reliable diagnostic for the topological MZMs. However, the prerequisite for this indicator to work is the long wire limit, which is not satisfied in the experimental samples at the current stage. Therefore, we conclude that even the observation of the end-to-end correlation cannot prove the existence of topological MZMs by showing that the correlation can be trivially manifested because of the short absolute wire length, and the long SC coherence length due to the small SC gap at large magnetic fields.

Although the local conductance in two-terminal devices by itself is incapable of distinguishing the trivial states from the topological states since ZBCPs are generic in the presence of disorder and inhomogeneous potential, in Chapter 2, in Chapter 3, we develop a new theory in three-terminal devices aiming to answer the question of whether the combination of local, nonlocal electrical conductance, as well as the thermal conductance, can separate the good, the bad,

and the ugly ZBCPs in finite-length wires.

We first present the nonlocal conductance of the good, the bad, and the ugly ZBCPs, and show that the nonlocal conductance, which in principle is capable of providing the bulk gap closing and reopening information at the TQPT, is far too weak in the magnitude to be practically useful in the presence of disorder and inhomogeneous potential. Therefore, we resort to the thermal conductance which shows a quantized peak at the TQPT as an accurate indicator. However, the thermal conductance may also be not quantized or even fail to show a unique single peak in the presence of large disorder, which is expected because the very strong disorder destroys the topological ZBCPs by creating a very large coherence length since the SC gap may collapse. In this situation, the system transmutes from a topological SC into a trivial Anderson insulator, and talking about the topology, therefore, becomes pointless.

Chapter 3 aims to provide a guide to future experiments, and we conclude that a combination of all three measurements would be necessary for a decisive demonstration of topological MZMs in nanowires because the positive signals corresponding to just one kind of measurement are likely to be false positives arising disorder and inhomogeneous potential.

With a full understanding of the three types of ZBCPs in theory, in Chapter 4, we provide a thorough yet compelling theoretical analysis with concrete simulations of the recent experiments. Since the corrected results [57] are by far the best tunneling conductance in the literature, because of the very large and sharp ZBCPs values $\sim 2e^2/h$, we develop a theoretical analysis to understand the underlying physics. We apply the standard disorder theory to Ref. [56, 57] and establish convincingly, through a detailed comparison with the experimental data, that the large ZBCPs reported in these experiments are likely to be disordered-induced trivial peaks. Our results reiterate that seeing occasional large ZBCPs is not evidence of the existence of topological

Majorana modes. The qualitative and semiquantitative agreement with the experimental observations indicates the need for producing much higher-quality nanowire samples with much less disorder for future Majorana experiments.

Chapter 4 also signifies the novelty of a series of our previous works [64, 67, 77, 92–94, 112, 180–182], which differs from the earlier works in inhomogeneous potential [64, 68–78] or disorder [71, 79–91] in the sense that our extensive simulations since 2019, when compared to the latest as well as the best experimental ZBCPs [9, 46, 57], presented in this dissertation suggest that most, if not all, experimentally observed ZBCPs are in fact "ugly" ZBCPs arising from strong random disorder present in the currently available SM-SC nanowire Majorana platforms. Our claim of the experimental ZBCPs being induced by the random disorder, instead of the smoothly varying deterministic background potential, distinguishes our work from the earlier theoretical works, which attribute the experimental ZBCPs to be all inhomogeneous potential induced.

Besides the simulations from a microscopic model, to generalize our conclusion, in Chapter 5, we also simulate the transport properties of the SM-SC nanowire from an RMT approach and find that all features in experiments can be also reproduced, including the quantized conductance with certain degrees of robustness, by preparing a contour plot of conductance over several independent tuning parameters, mimicking the effect of Zeeman splitting and voltages on gates near the NS junction. This suggests that even stable quantized ZBCPs do not provide conclusive evidence for topological MZM; rather, the *a priori* expectation should be that such quantized peaks generically occupy a significant fraction of the high-dimensional tuning parameter space that characterizes the NS tunneling experiments. Such trivial ZBCPs are generic in class D systems [112], and are inevitably present if the results are postselected from a large amount of data.

In summary, we believe that almost all existing experimentally observed ZBCPs in nanowires arise from strong disorder in the system, particularly because the observed experimental behavior of these ZBCPs as functions of magnetic fields and gate voltages belong to what we find in the "ugly" ZBCPs calculations. Therefore, we provide three pieces of guidance for future experiments as follows.

First, we urge that further progress in the field should focus on reducing the disorder in the system, as our work has reinforced the need for the very pristine limit of the nanowire. In order to realize the topological MZM, one has to measure the 2D mobility in the SM part (e.g., InSb) of the nanowires, which should at least increase to $100000 - 300000$ cm^2/V$\cdot$s, as we estimated in Ref. [94].

Second, we point out that one must control the gap collapse problem so that higher magnetic fields can be applied to the system without suppressing the bulk SC completely.

Third, we emphasize the importance of the long wire limit in order to make all the discussions on the trivial ABSs versus MBSs meaningful. Therefore, one has to estimate the actual SC coherence length in the nanowires to guarantee that the system is in the long wire regime.

On the other hand, we list the caveats that experimentalists should avoid in future experiments: The most important caveat is that one refrains from the obsession to search for the "quantized conductance". Any effort to build the topological qubits based on the apparent "quantized conductance" is doomed to failure unless the background disorder is reduced substantially, and the system is sufficiently long at zero temperature with small dissipations. As a result, one also needs to avoid mere fine-tunings to obtain the quantized conductance in experiments. Such fine-tuning and postselection merely to fit the data to the known prediction is dangerous, unless done with great care and rigor, as the retraction of Ref. [9] demonstrates [159]. Let this be a

cautionary tale for the topological condensed matter physics since this field is currently all about experiments chasing precisely known theoretical predictions.

Appendix A: Correlation of local conductance at both ends

In this section, the complete nonlocal correlation of conductance spectra are presented including the pristine nanowire in Fig. A.1, a small amount of disorder in the chemical potential in Fig. A.2, disorder in the SC gap in Fig. A.3, the presence of a QD in Fig. A.4, the presence of the inhomogeneous potential in Fig. A.5, a large disorder in the chemical potential in Fig. A.6, disorder in the effective g factor in Fig. A.7, and the short but uncorrelated instances in Fig. A.8.

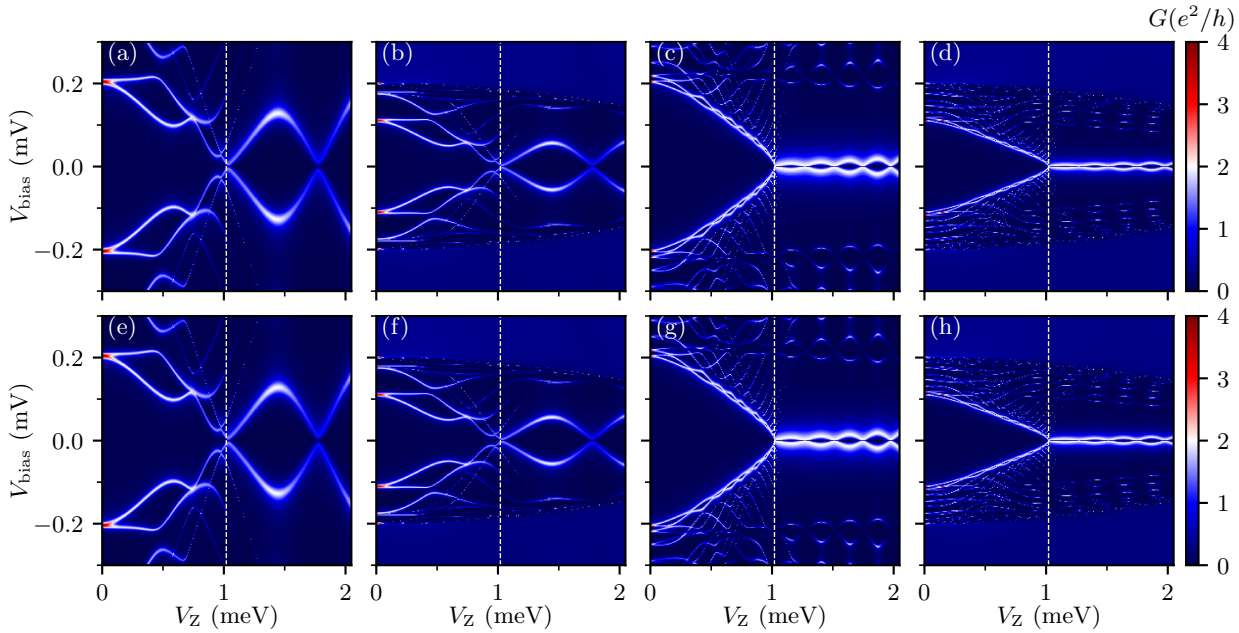

Figure A.1: The good ZBCP in two 1 μm pristine wires [shown in (a)-(d)] and two 3 μm pristine wires [shown in (c)-(h)]. The color plots show the differential tunneling conductance G as a function of $V_{\rm Z}$ (x axis) and $V_{\rm bias}$ (y axis) measured from the left lead (in the first row) and the right lead (in the second row). Nanowires with the self-energy are shown in (b), (f), (d), and (h) and without the self-energy are shown in (a), (c), (e), and (g). The SC gap collapse $V_{\rm Zc} = 3$ meV for the self-energy case. The TQPT is labeled in the white dashed line at $V_{\rm Z} = 1.02$ meV. The corresponding wave functions and energy spectra are shown in Fig. B.1.

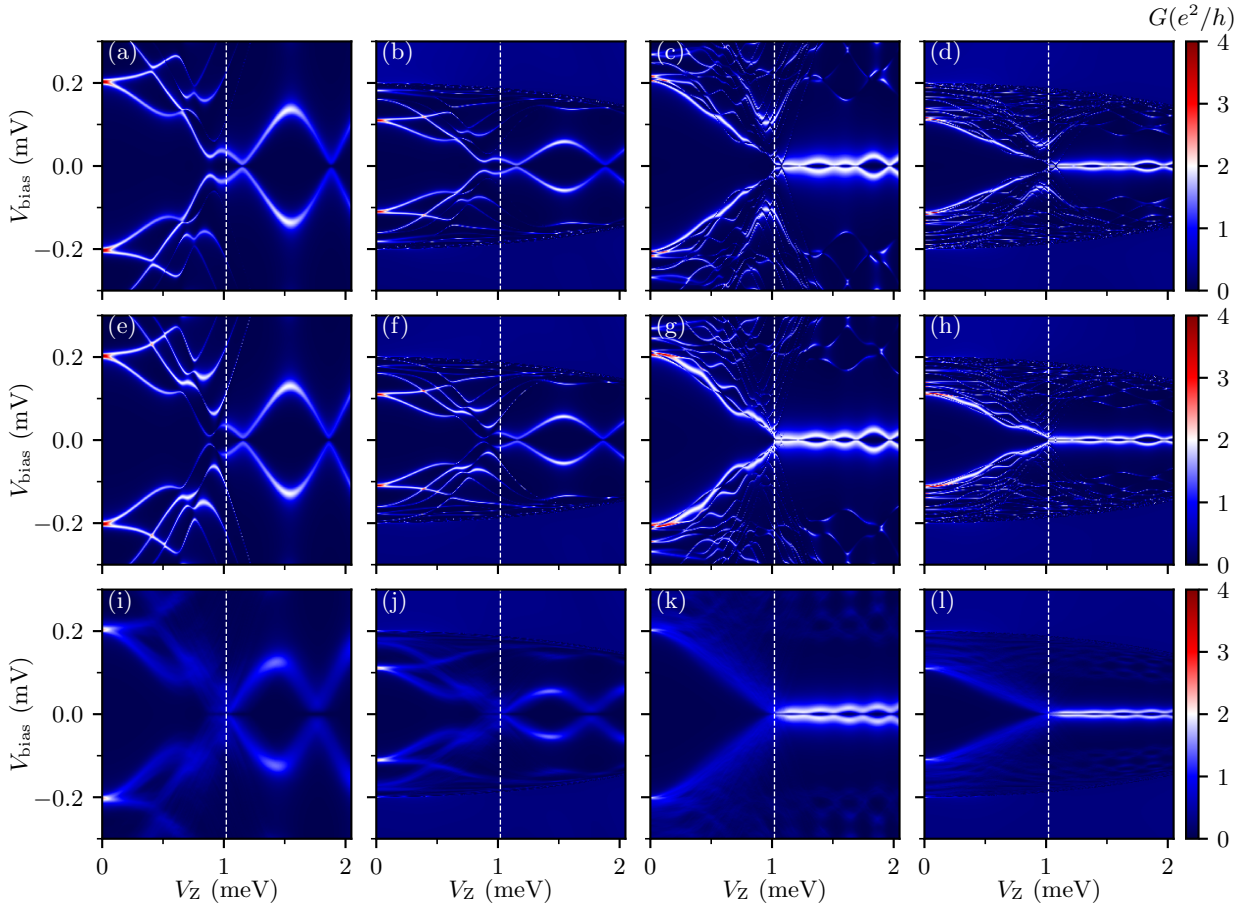

Figure A.2: The good ZBCP in the presence of a small amount of disorder in the chemical potential for 1 μm wires [shown in (a), (b), (e), (f), (i), and (j)] and 3 μm wires [shown in (c), (d), (g), (h), (k), and (l)]. The color plots show the differential tunneling conductance G as a function of V_{Z} (x axis) and V_{bias} (y axis) measured from the left lead (in the first row) and the right lead (in the second row). The third row shows the disorder-averaged conductance over 200 samples; the first two rows are the conductance spectra under one specific configuration of disorder. The standard deviation of disorder in the chemical potential $\sigma_\mu = 0.4$ meV for wires both with the self-energy shown in (b), (d), (f), (h), (j), and (l) and without the self-energy shown in (a), (c), (e), (g), (i), and (k). The SC gap collapse $V_{\text{Z}c} = 3$ meV for the self-energy case. The TQPT is labeled in the white dashed line at $V_{\text{Z}} = 1.02$ meV. The corresponding wave functions and energy spectra are shown in Fig. B.2.

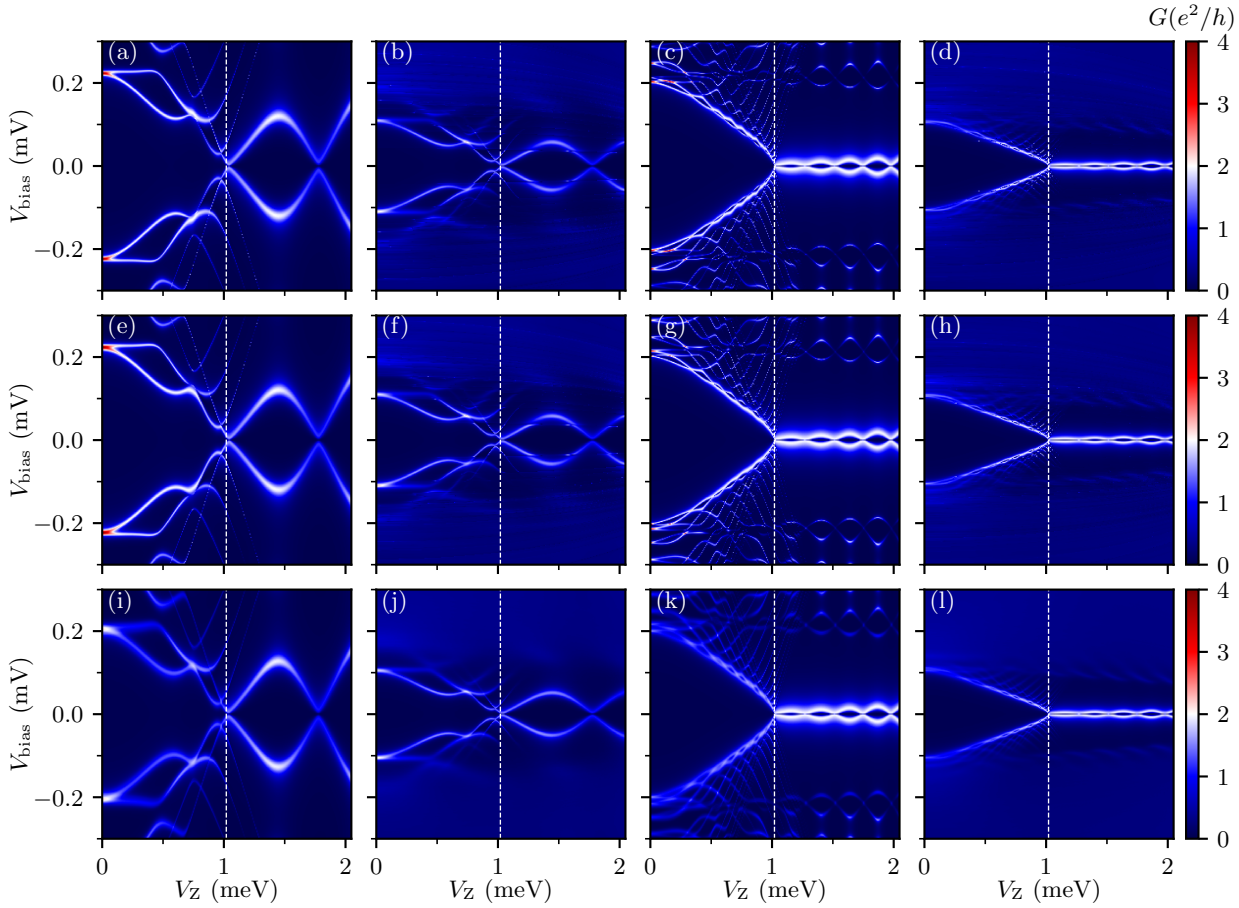

Figure A.3: The good ZBCP in the presence of a small amount of disorder in the SC gap for 1 μm wires [shown in (a), (b), (e), (f), (i), and (j)] and 3 μm wires [shown in (c), (d), (g), (h), (k), and (l)]. The color plots show the differential tunneling conductance G as a function of V_{Z} (x axis) and V_{bias} (y axis) measured from the left lead (in the first row) and the right lead (in the second row). The third row shows the disorder-averaged conductance over 200 samples; the first two rows are the conductance spectra under one specific configuration of disorder. Mean proximity-induced SC gap $\Delta = 0.2$ meV/parent SC gap $\Delta_0 = 0.2$meV and the standard deviation of disorder in the SC gap $\sigma_\Delta = 0.06$ meV are for wires both with the self-energy shown in (b), (d), (f), (h), (j), and (l) and without the self-energy shown in (a), (c), (e), (g), (i), and (k). The SC gap collapse $V_{\text{Z}c} = 3$ meV for the self-energy case. The TQPT is labeled in the white dashed line at $V_{\text{Z}} = 1.02$ meV. The corresponding wave functions and energy spectra are shown in Fig. B.3.

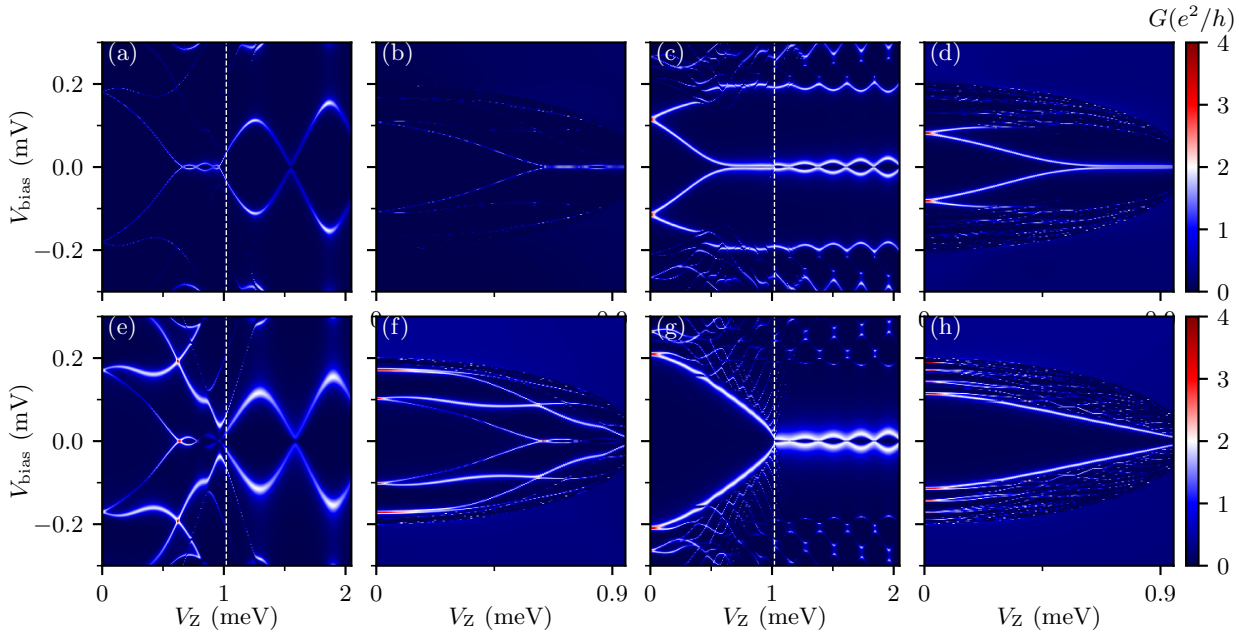

Figure A.4: The bad ZBCP due to the QD in two 1 μm pristine wires [shown in (a), (b), (e), and (f)] and two 3 μm pristine wires [shown in (c), (d), (g), and (h)]. The color plots show the differential tunneling conductance G as a function of V_{Z} (x axis) and V_{bias} (y axis) measured from the left lead (in the first row) and the right lead (in the second row). For the short wire $L = 1$ μm, the peak value of the QD $V_{\text{D}} = 1.7$ meV and size $l = 0.2$ μm for wires both with the self-energy shown in (b) and (f) and without the self-energy shown in (a) and (e). For the long wire $L = 3$ μm, the peak value of the QD $V_{\text{D}} = 0.6$ meV and size $l = 0.4$ μm for wires both with the self-energy shown in (d) and (h) and without the self-energy shown in (c) and (g). The SC gap collapse $V_{\text{Z}c} = 1$ meV for the self-energy case. The TQPT is labeled in the white dashed line at $V_{\text{Z}} = 1.02$ meV. The corresponding wave functions and energy spectra are shown in Figs. B.4 and B.5.

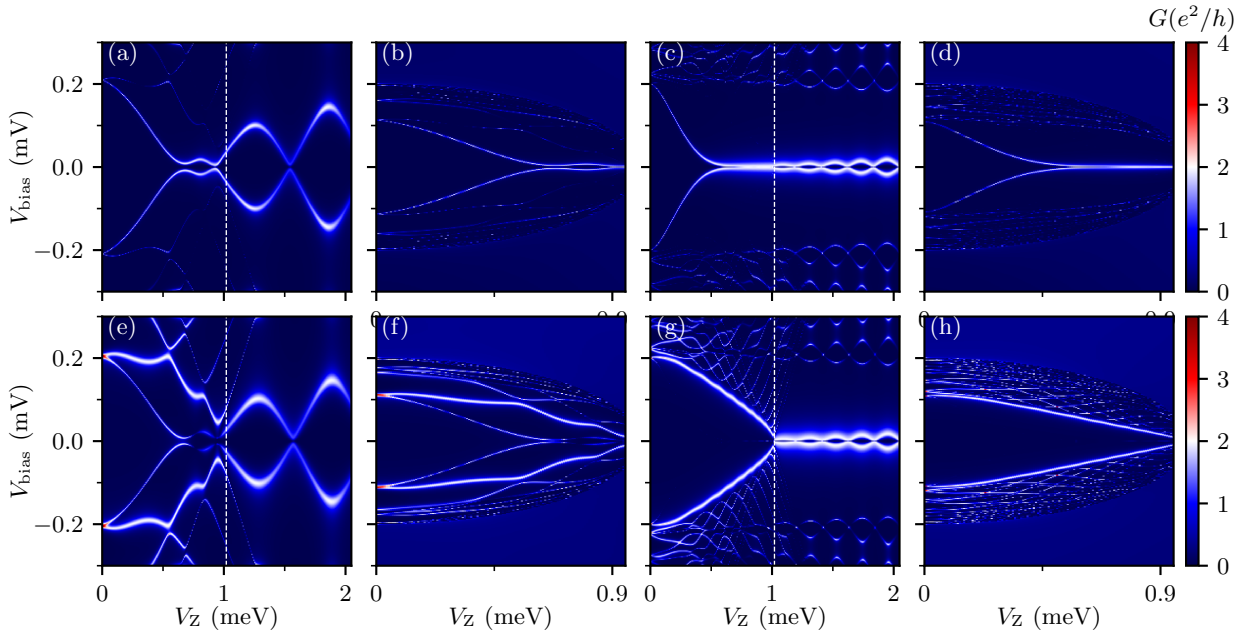

Figure A.5: The bad ZBCP due to the inhomogeneous potential in two 1 μm pristine wires [shown in (a), (b), (e), and (f)] and two 3 μm pristine wires [shown in (c), (d), (g), and (h)]. The color plots show the differential tunneling conductance G as a function of $V_{\rm Z}$ (x axis) and $V_{\rm bias}$ (y axis) measured from the left lead (in the first row) and the right lead (in the second row). For the short wire $L = 1$ μm, the peak value of the inhomogeneous potential $V_{\rm max} = 1.4$ meV and linewidth $\sigma = 0.15$ μm for wires both with the self-energy shown in (b) and (f) and without the self-energy shown in (a) and (e). For the long wire $L = 3$ μm, the peak value of the inhomogeneous potential $V_{\rm max} = 1.2$ meV and linewidth $\sigma = 0.4$ μm for wires both with the self-energy shown in (d) and (h) and without the self-energy shown in (c) and (g). The SC gap collapse $V_{{\rm Z}c} = 1$ meV for the self-energy case. The TQPT is labeled in the white dashed line at $V_{\rm Z} = 1.02$ meV. The corresponding wave functions and energy spectra are shown in Figs. B.6 and B.7.

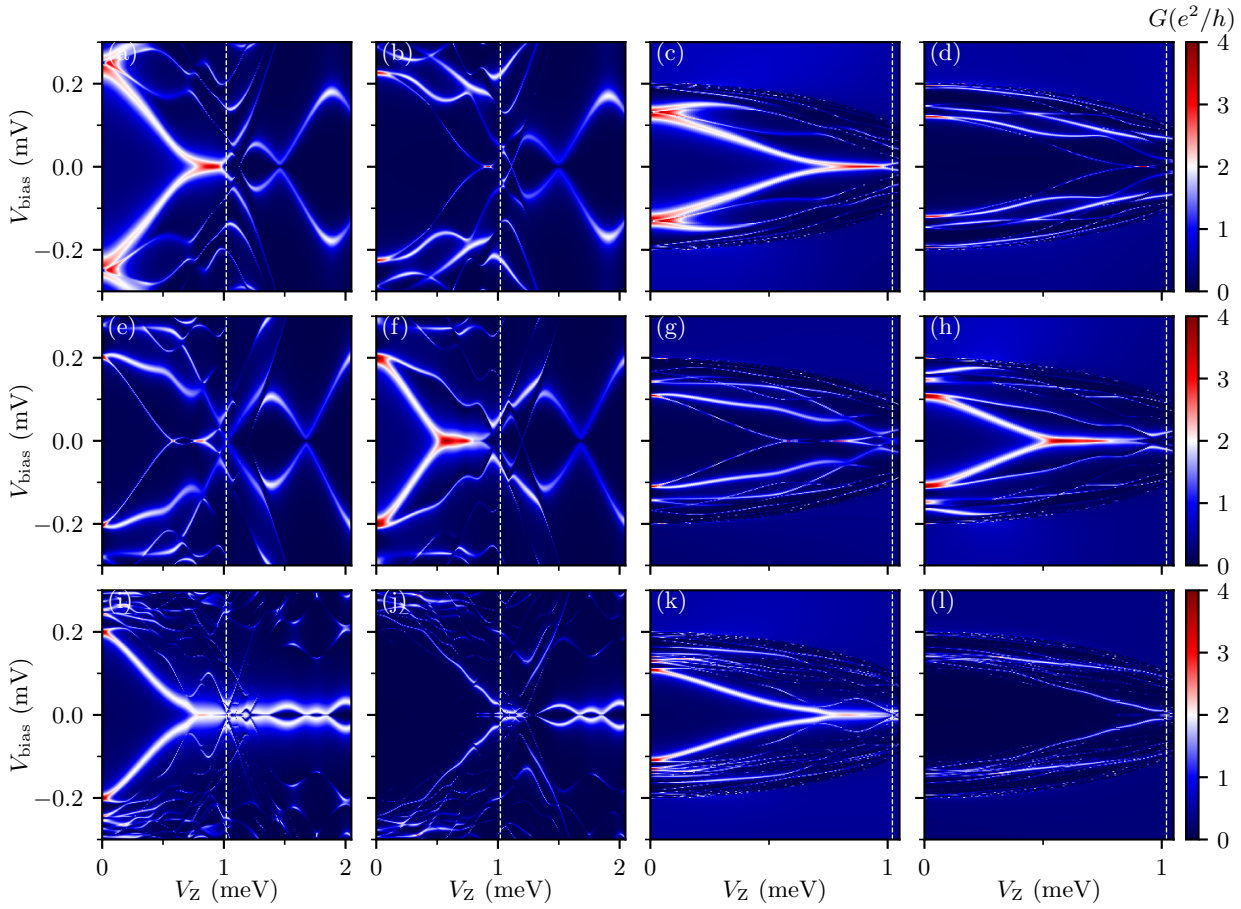

Figure A.6: The ugly ZBCP in the presence of a large amount of disorder in the chemical potential for two 1 μm wires (shown in the first two rows) and for one 3 μm wire (shown in the third row). The color plots show the differential tunneling conductance G as a function of V_{Z} (x axis) and V_{bias} (y axis) measured from the left lead (shown in the first and third columns) and the right lead (shown in the second and fourth columns). The conductance spectra in the first row share a common configuration of disorder; the ones in the second row share another. The standard deviation of the chemical potential $\sigma_\mu = 1$ meV for wires both with the self-energy shown in (c), (d), (g), and (h) and without the self-energy shown in (a), (b), (e), and (f). For $L = 3$ μm wire, the standard deviation of the chemical potential $\sigma_\mu = 1$ for wires both with the self-energy shown in (k) and (l) and without the self-energy shown in (i) and (j). The SC gap collapse $V_{\text{Z}c} = 1.2$ meV for the self-energy case. The TQPT is labeled in the white dashed line at $V_{\text{Z}} = 1.02$ meV. The corresponding wave functions and energy spectra are shown in Figs. B.8 and B.9.

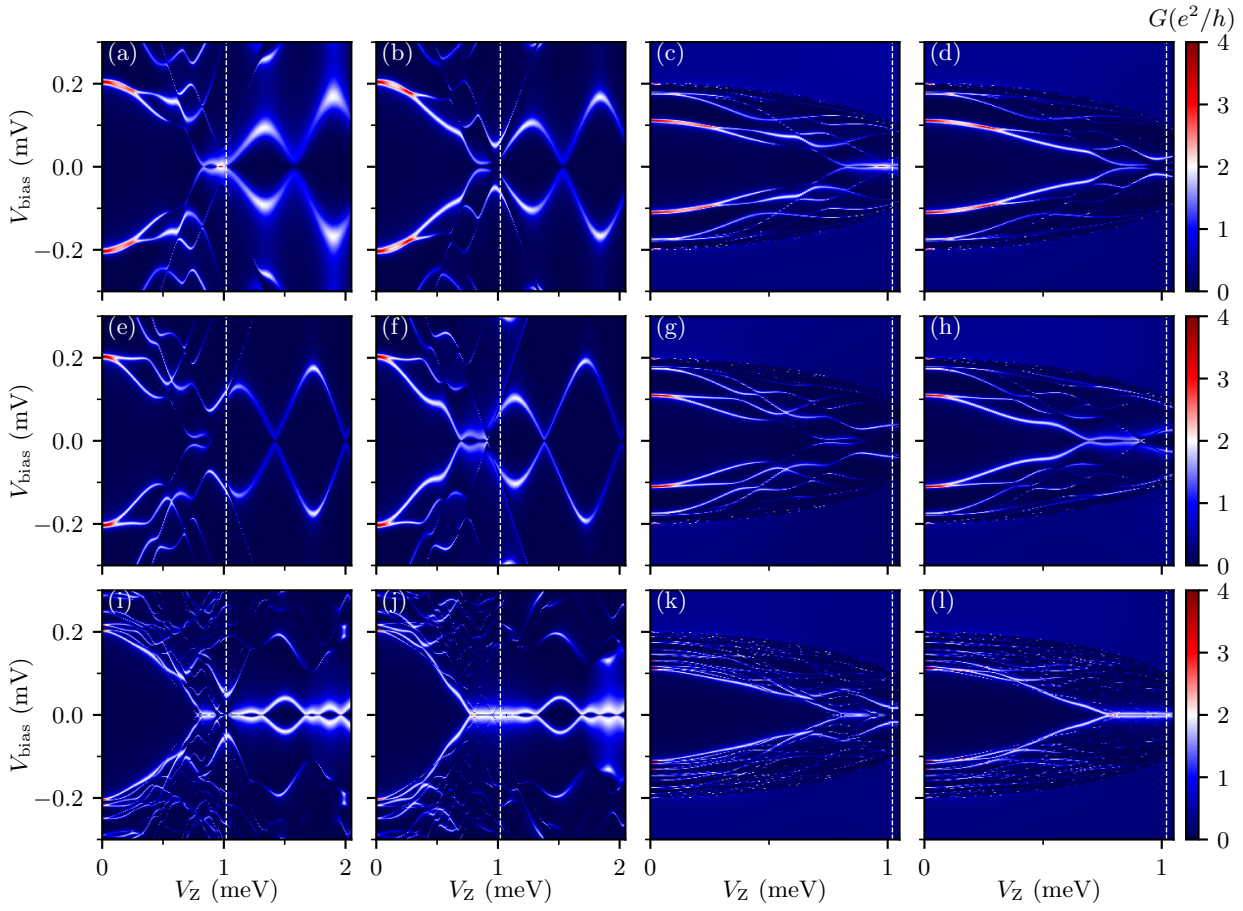

Figure A.7: The ugly ZBCP in the presence of disorder in the effective g factor for two 1 μm wires (shown in the first two rows) and for one 3 μm wire (shown in the third row). The color plots show the differential tunneling conductance G as a function of V_{Z} (x axis) and V_{bias} (y axis) measured from the left lead (shown in the first and third columns) and the right lead (shown in the second and fourth columns). The conductance spectra in the first row share a common configuration of disorder; the ones in the second row share another. The standard deviation of disorder in the effective g factor is $\sigma_g = 0.8$ for wires both with self-energy shown in (c), (d), (g), and (h) and without the self-energy shown in (a), (b), (e), and (f). For $L = 3$ μm wire, the effective g factor is $\sigma_g = 0.6$ for wires both with the self-energy shown in (k) and (l) and without the self-energy shown in (i) and (j). The SC gap collapse $V_{\text{Z}c} = 1.2$ meV for the self-energy case. The TQPT is labeled in the white dashed line at $V_{\text{Z}} = 1.02$ meV. The corresponding wave functions and energy spectra are shown in Figs. B.10 and B.11.

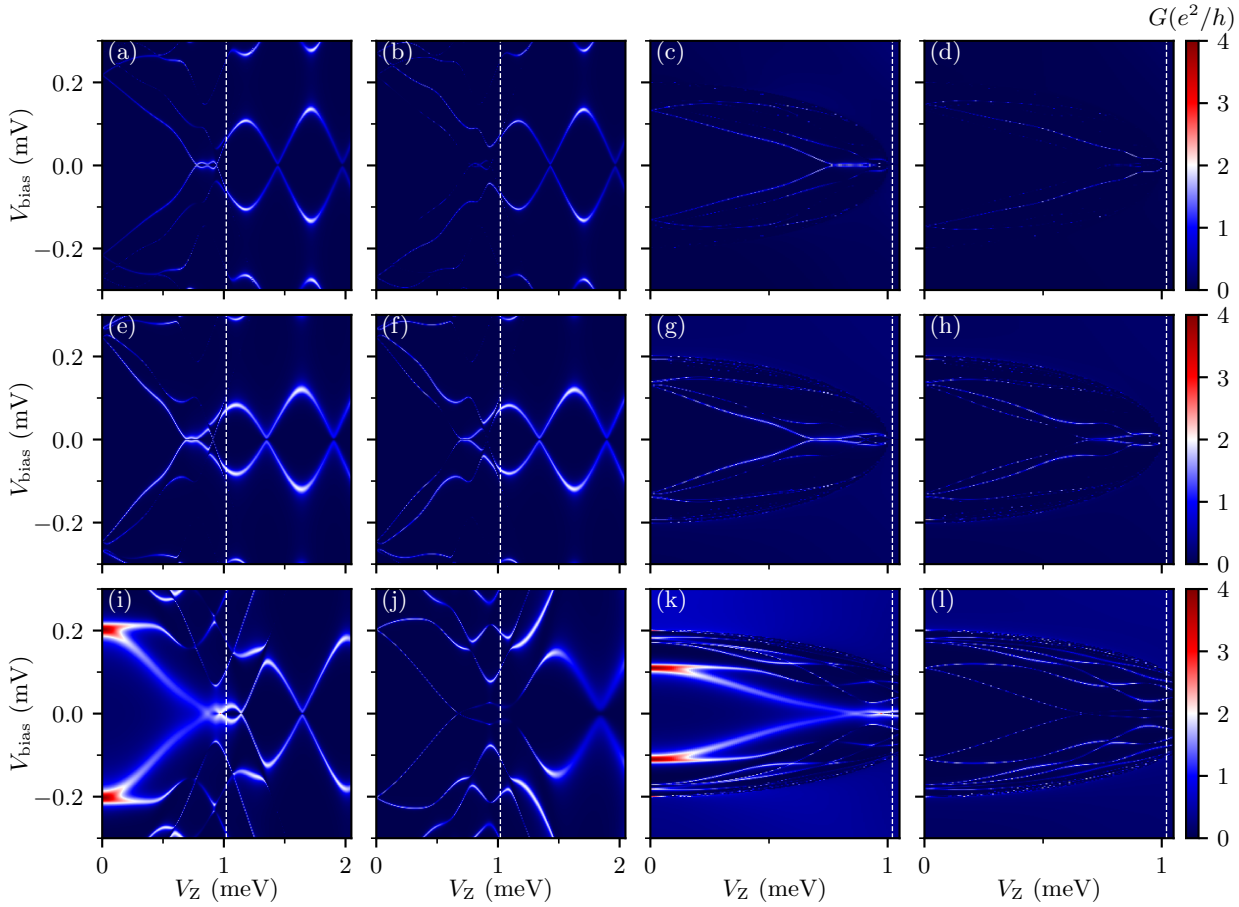

Figure A.8: The short but uncorrelated occasions in bad (the first and second rows) and ugly (the third row) ZBCPs. The color plots show the differential tunneling conductance G as a function of V_{Z} (x axis) and V_{bias} (y axis) measured from the left lead (in the first and third columns) and the right lead (in the second and fourth columns). The bad ZBCPs due to the two QDs at both ends in 1 μm wires are shown in (a)-(d). The peak value of the QD is $V_{\text{D,L}} = 1.7$ meV on the left and $V_{\text{D,R}} = 2.3$ meV on the right, the size of the QD is $l_{\text{L}} = 0.2$ μm on the left and $l_{\text{R}} = 0.15$ μm on the right for both wires with the self-energy shown in (c) and (d) and without the self-energy shown in (a) and (b). The SC collapse $V_{\text{Z}c} = 1$ meV. The bad ZBCPs due to the inhomogeneous potential with the Gaussian barriers on both ends are shown in (e), (f), (g), and (h). The peak value of the Gaussian barrier is $V_{\text{max,L}} = 1.4$ meV on the left and $V_{\text{max,R}} = 1.8$ meV on the right, the linewidth of the Gaussian barrier is $\sigma_{\text{L}} = 0.15$ μm on the left and $\sigma_{\text{R}} = 0.1$ μm on the right for both wires with the self-energy shown in (g) and (h) and without the self-energy shown in (e) and (f). The SC collapse $V_{\text{Z}c} = 1$ meV. The ugly ZBCPs due to the disorder in the chemical potential are shown in (i), (j), (k), and (l). The standard deviation of the chemical potential $\sigma_{\mu} = 1$ meV for wires both with the self-energy shown in (k) and (l) and without the self-energy shown in (i) and (j). The SC collapse $V_{\text{Z}c} = 1.2$ meV. The corresponding wave functions and energy spectra are shown in Fig. B.12.

Appendix B: Energy spectra and wave functions

In this section, the energy spectra as a function of the Zeeman field V_{Z} are shown in the first column and the corresponding wave functions at several representative V_{Z} in the Majorana basis defined in Eq. (2.21) are presented in the second to the fourth columns. In energy spectra, the energies have identical ranges as those in conductance spectra and the red dashed lines are for the nominal TQPT. The two Majoranas are labeled with blue and cyan in the lowest state while red and orange in the second state.

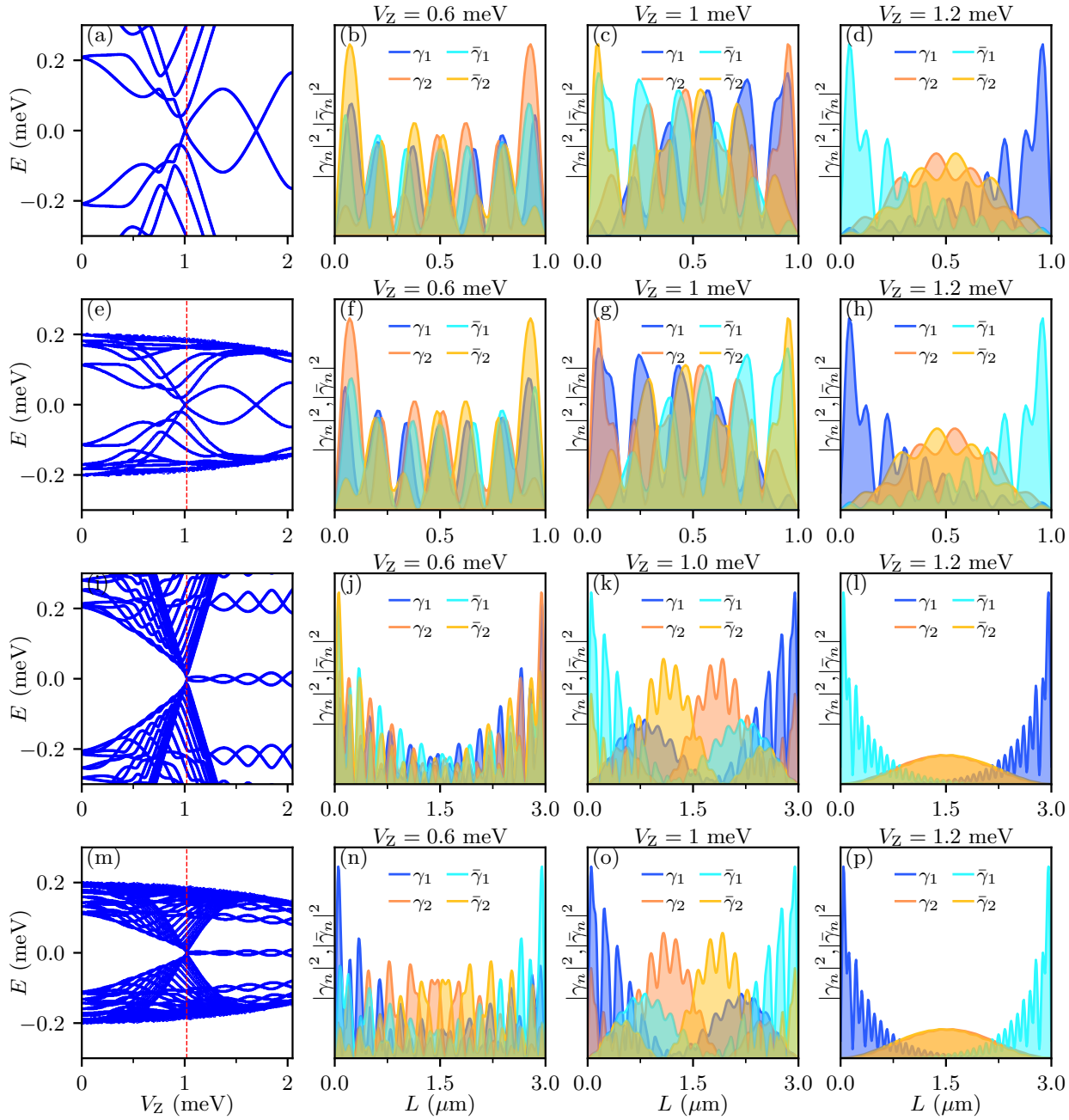

Figure B.1: (a), (b), (c), and (d) correspond to Figs. A.1(a) and A.1(e); (e), (f), (g), and (h) correspond to Figs. A.1(b) and A.1(f). (i), (j), (k), and (l) correspond to Figs. A.1(c) and A.1(g). (m), (n), (o), and (p) correspond to Figs. A.1(d) and A.1(h).

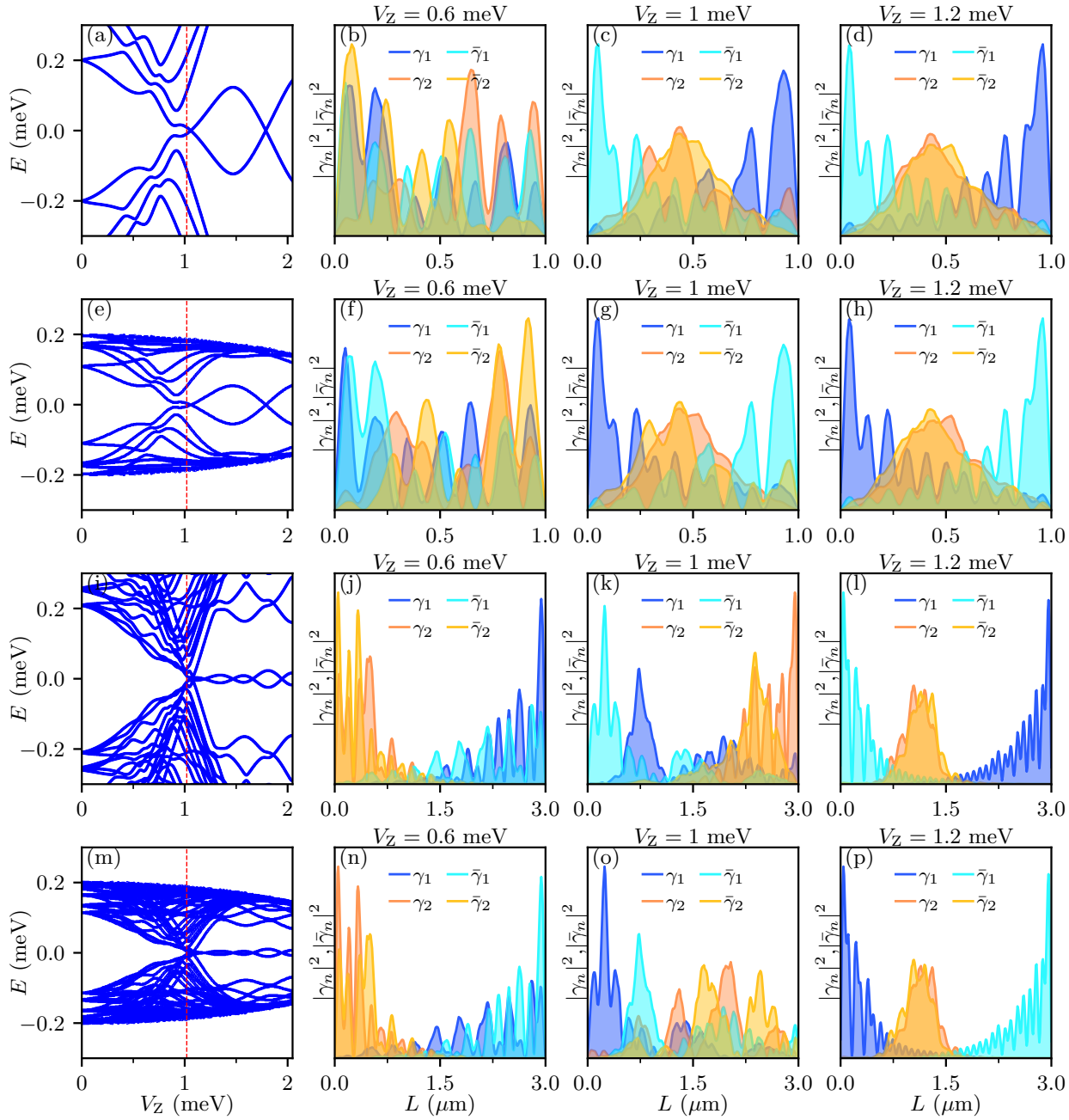

Figure B.2: (a), (b), (c), and (d) correspond to Figs. A.2(a) and A.2(e); (e), (f), (g), and (h) correspond to Figs. A.2(b) and A.2(f). (i), (j), (k), and (l) correspond to Figs. A.2(c) and A.2(g). (m), (n), (o), and (p) correspond to Figs. A.2(d) and A.2(h).

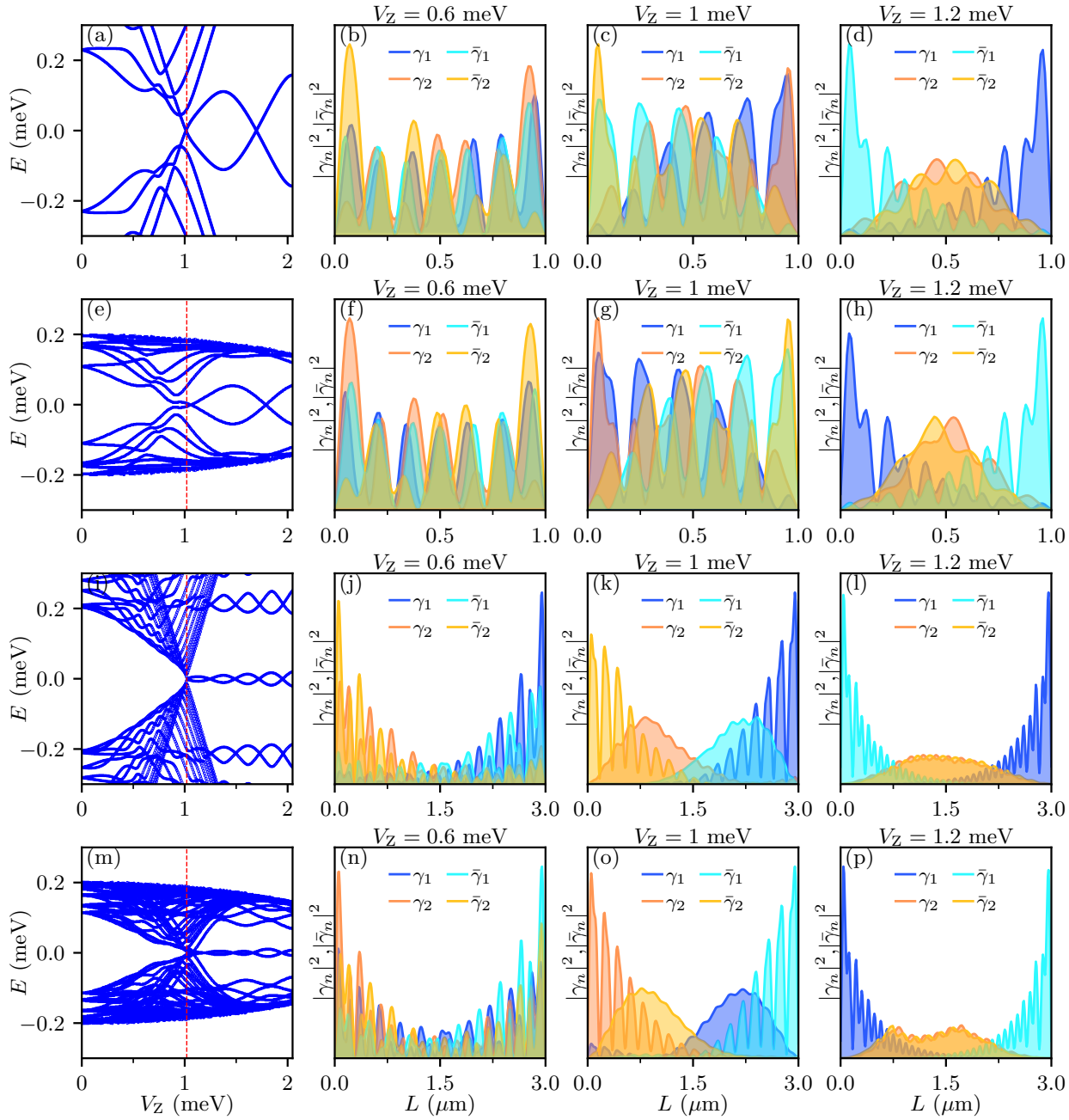

Figure B.3: (a), (b), (c), and (d) correspond to Figs. A.3(a) and A.3(e); (e), (f), (g), and (h) correspond to Figs. A.3(b) and A.3(f). (i), (j), (k), and (l) correspond to Figs. A.3(c) and A.3(g). (m), (n), (o), and (p) correspond to Figs. A.3(d) and A.3(h).

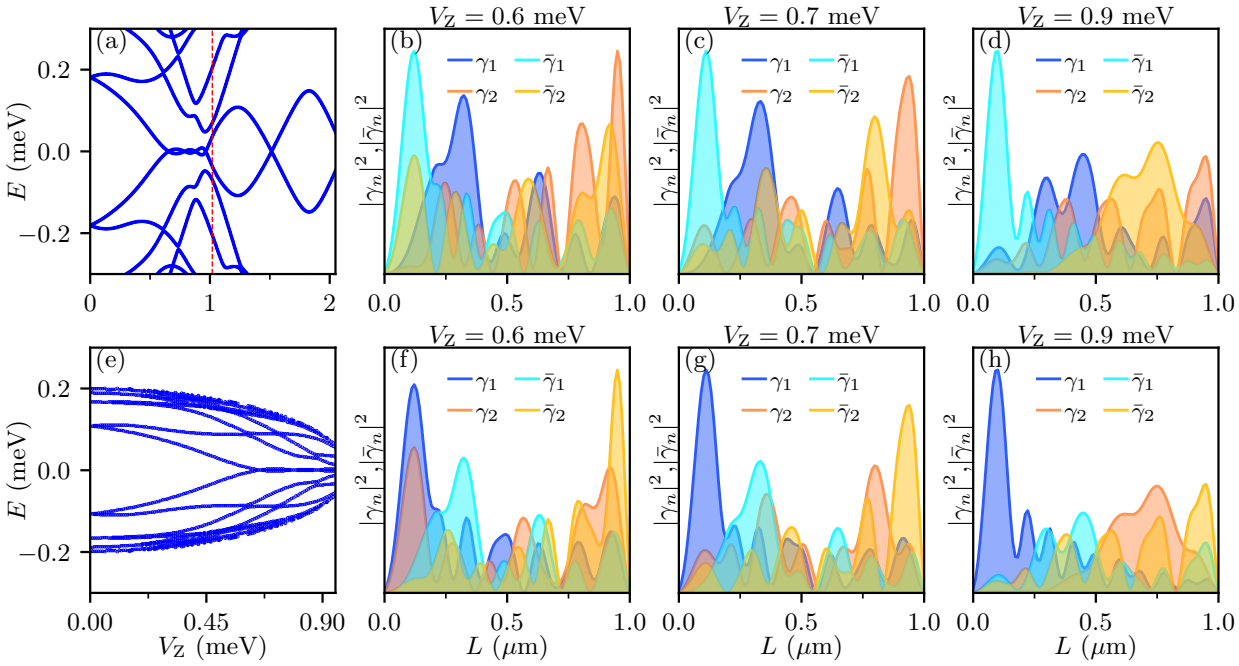

Figure B.4: (a), (b), (c), and (d) correspond to Figs. A.4(a) and A.3(e); (e), (f), (g), and (h) correspond to Figs. A.4(b) and A.3(f).

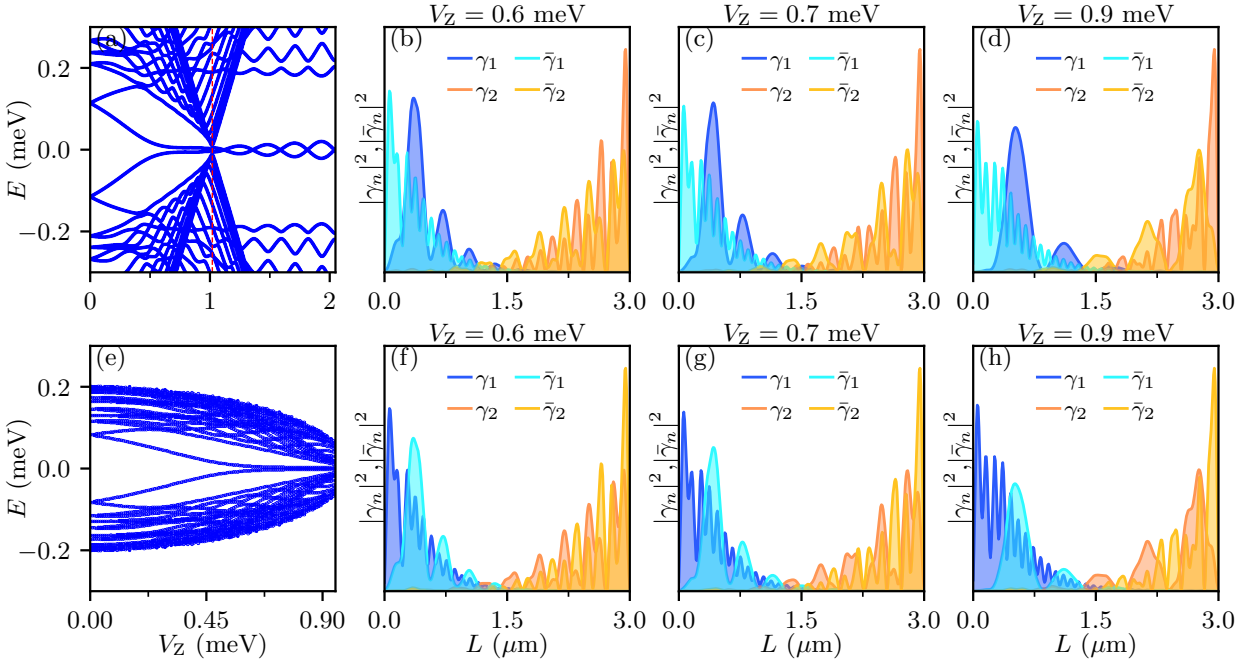

Figure B.5: (a), (b), (c), and (d) correspond to Figs. A.4 (c) and A.4(g); (e), (f), (g), and (h) correspond to Figs. A.4(d) and A.4(h).

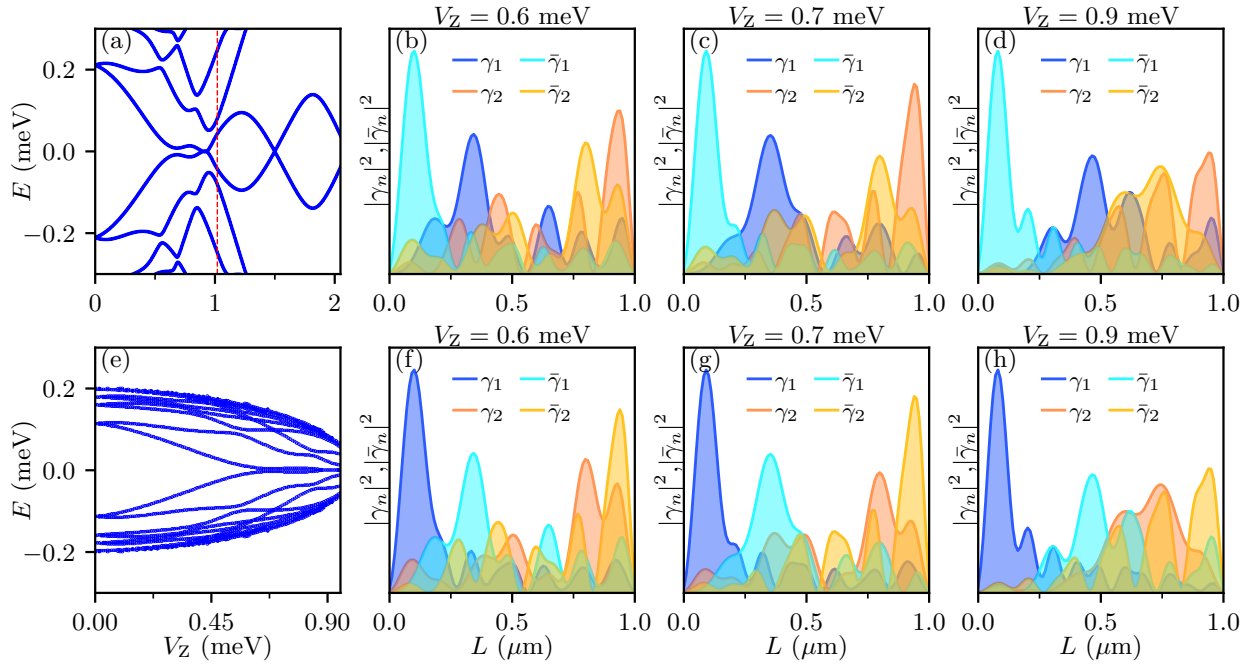

Figure B.6: (a), (b), (c), and (d) correspond to Figs. A.5(a) and A.5(e); (e), (f), (g), and (h) correspond to Figs. A.5(b) and A.5(f).

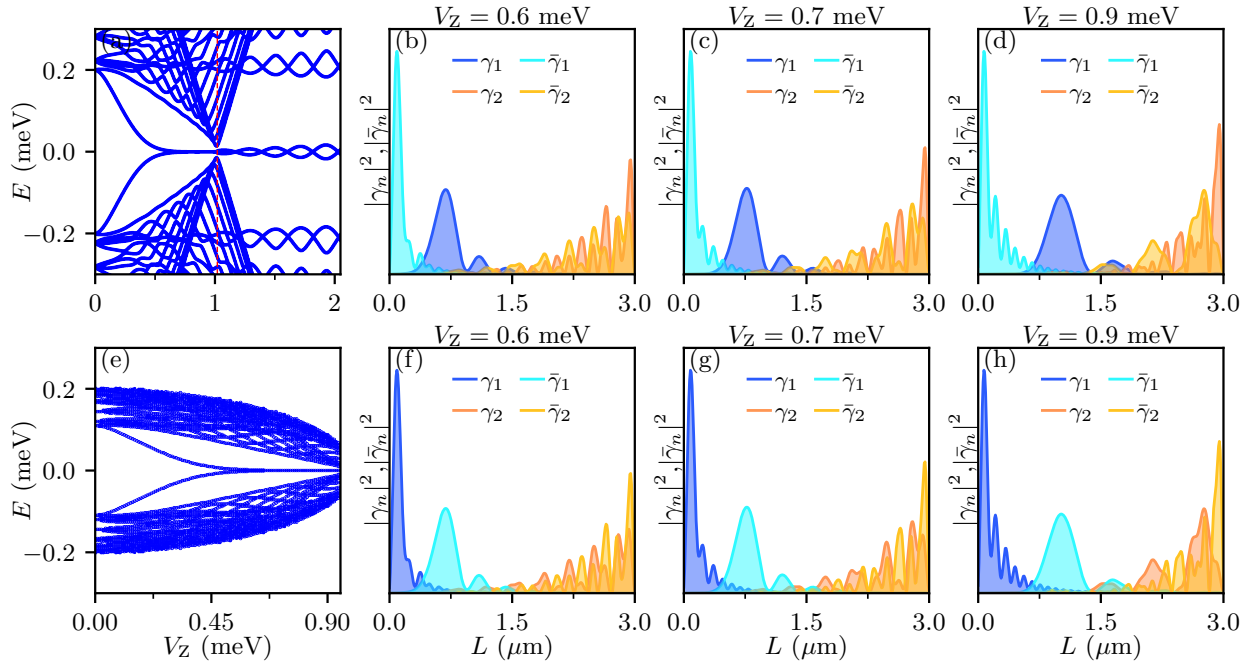

Figure B.7: (a), (b), (c), and (d) correspond to Figs. A.5(c) and A.5(g); (e), (f), (g), and (h) correspond to Figs. A.5(d), and (h).

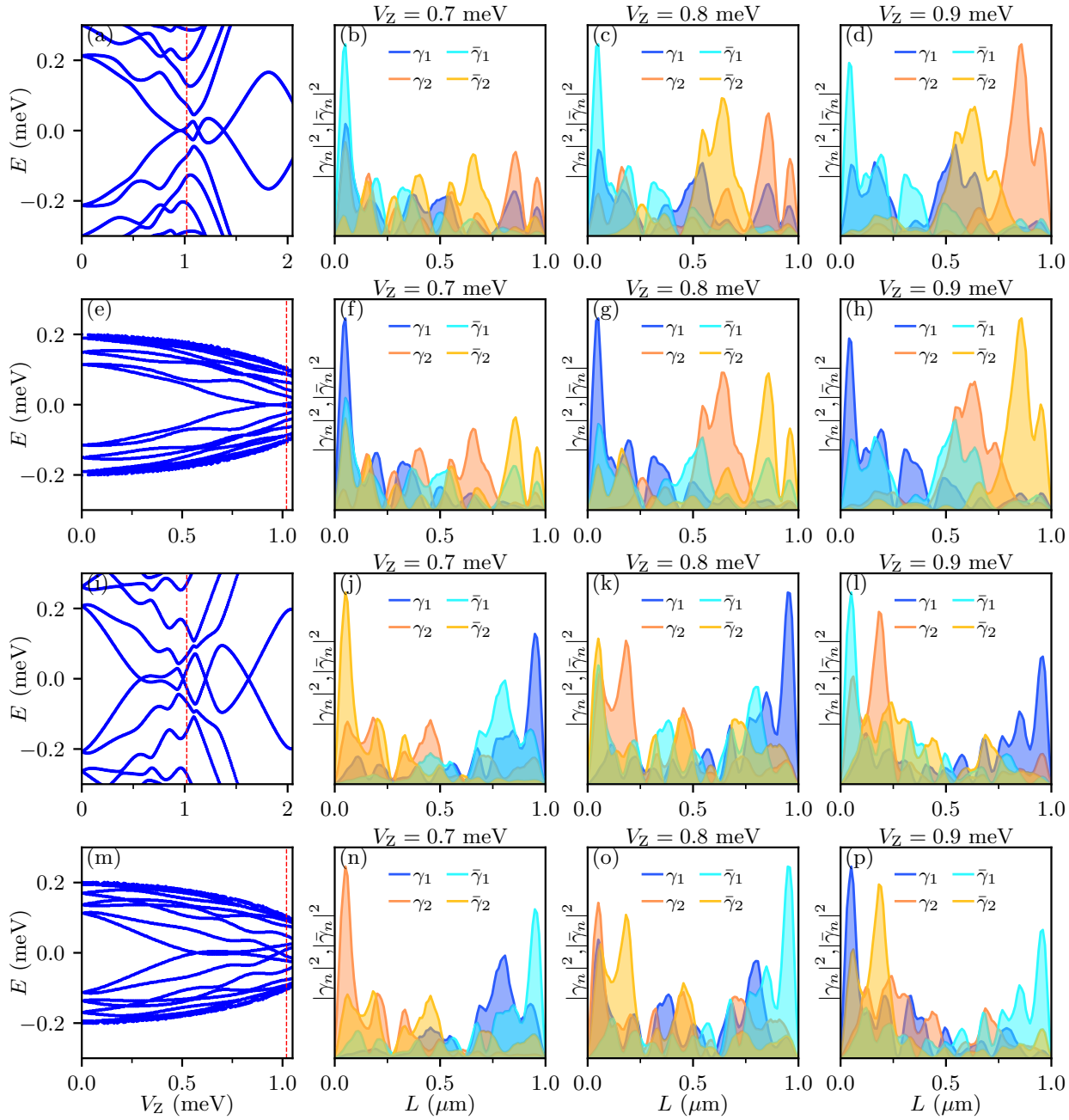

Figure B.8: (a), (b), (c), (d) correspond to Figs. A.6(a) and A.6(b); (e), (f), (g), and (h) correspond to Figs. A.6(c) and A.6(d). (i), (j), (k), (l) correspond to Figs. A.6(e) and A.6(f). (m), (n), (o), and (p) correspond to Figs. A.6(g) and A.6(h).

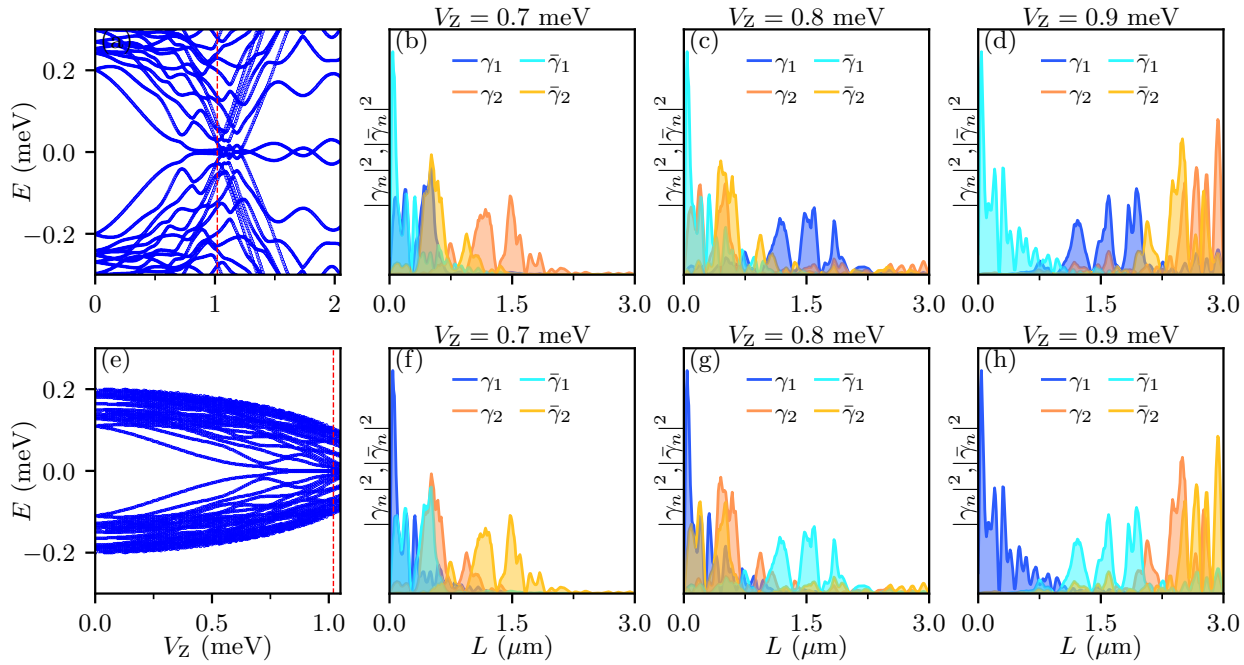

Figure B.9: (a), (b), (c), and (d) correspond to Figs. A.6(i) and A.6(j); (e), (f), (g), and (h) correspond to Figs. A.6(k) and A.6(l).

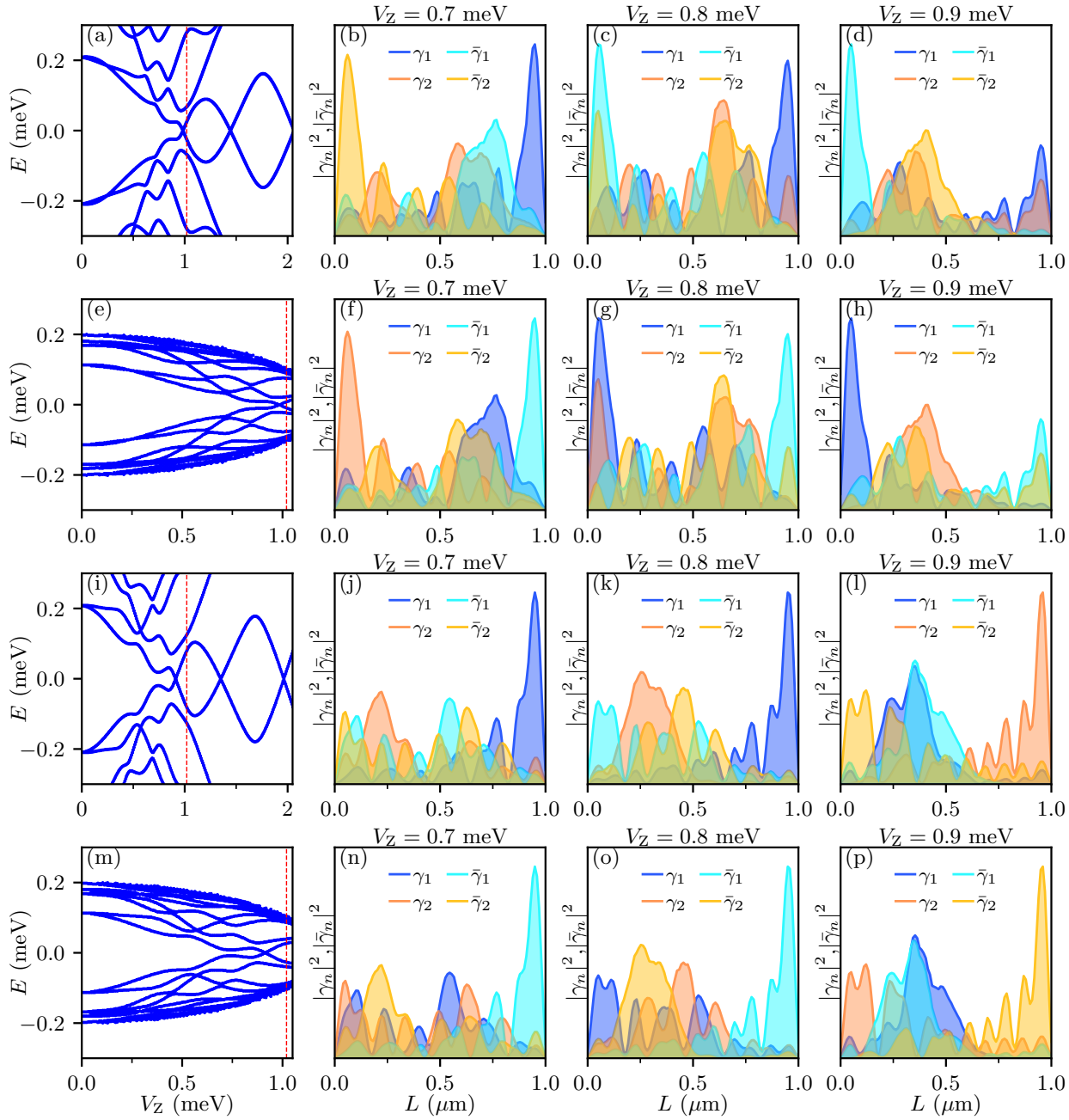

Figure B.10: (a), (b), (c), and (d) correspond to Figs. A.7(a) and A.7(b); (e), (f), (g), and (h) correspond to Figs. A.7(c) and A.7(d). (i), (j), (k), and (l) correspond to Figs. A.7(e) and A.7(f). (m), (n), (o), and (p) correspond to Figs. A.7(g) and A.7(h).

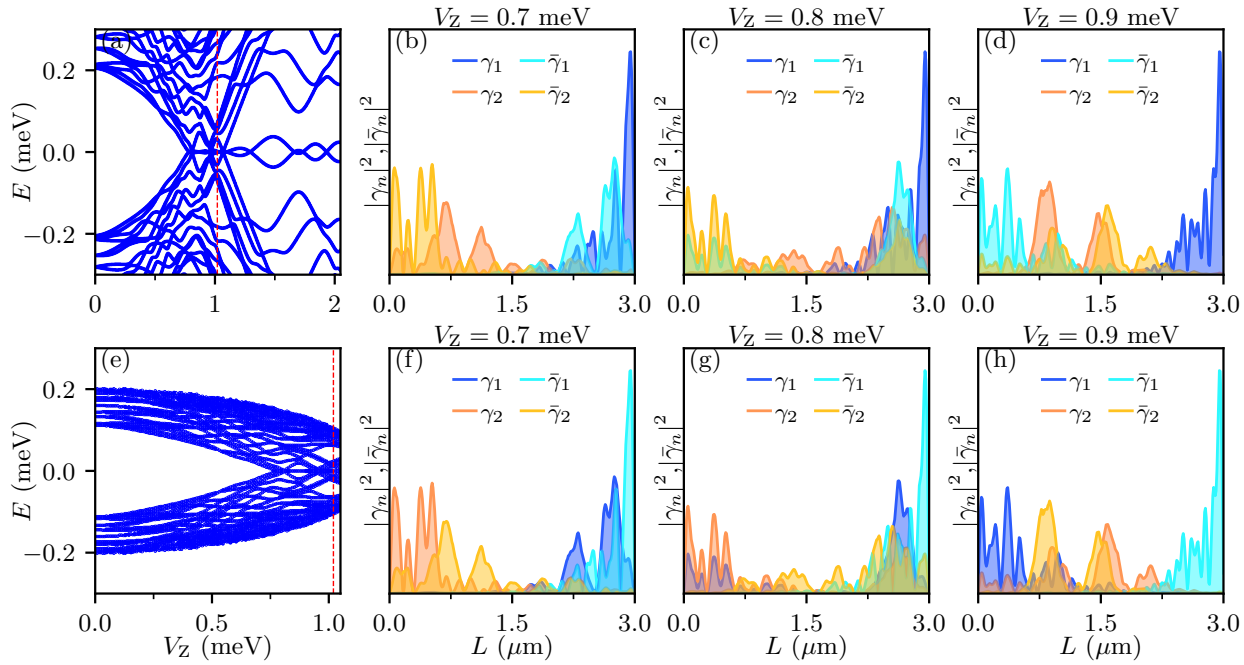

Figure B.11: (a), (b), (c), and (d) correspond to Figs. A.7(i) and A.7(j); (e), (f), (g), and (h) correspond to Figs. A.7(k) and A.7(l).

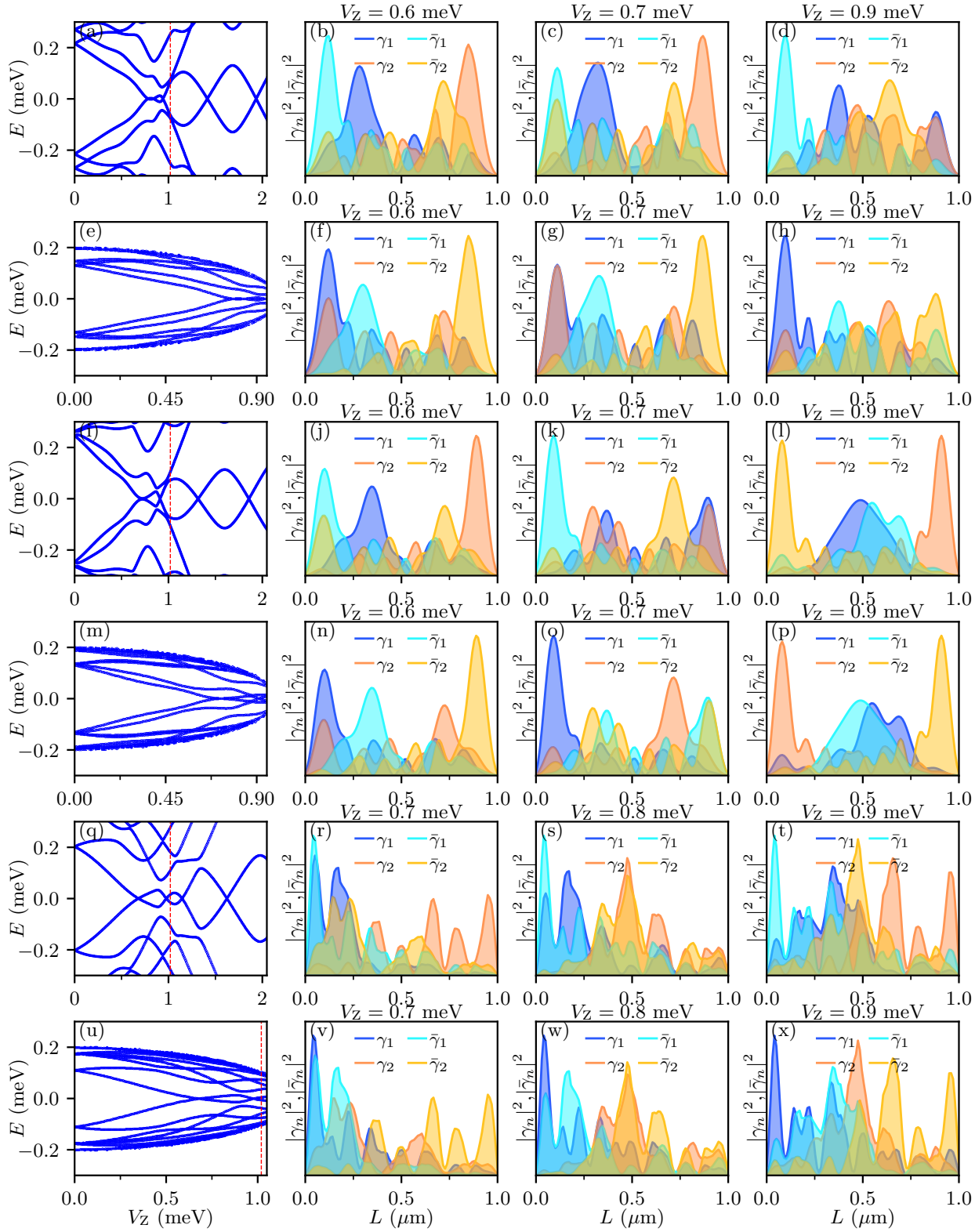

Figure B.12: (a), (b), (c), and (d) correspond to Figs. A.8(a) and A.8(b). (e), (f), (g), and (h) correspond to Figs. A.8(c) and A.8(d). (i), (j), (k), and (l) correspond to Figs. A.8(e) and A.8(f). (m), (n), (o), and (p) correspond to Figs. A.8(g) and A.8(h). (q), (r), (s), and (t) correspond to Figs. A.8(i) and A.8(j). (u), (v), (w), and (x) correspond to Figs. A.8(k) and A.8(l).

Appendix C: More examples of conductance spectra in three-terminal devices

In this section, we show other examples of the good, bad, and ugly ZBCPs in Figs. C.1-C.14.

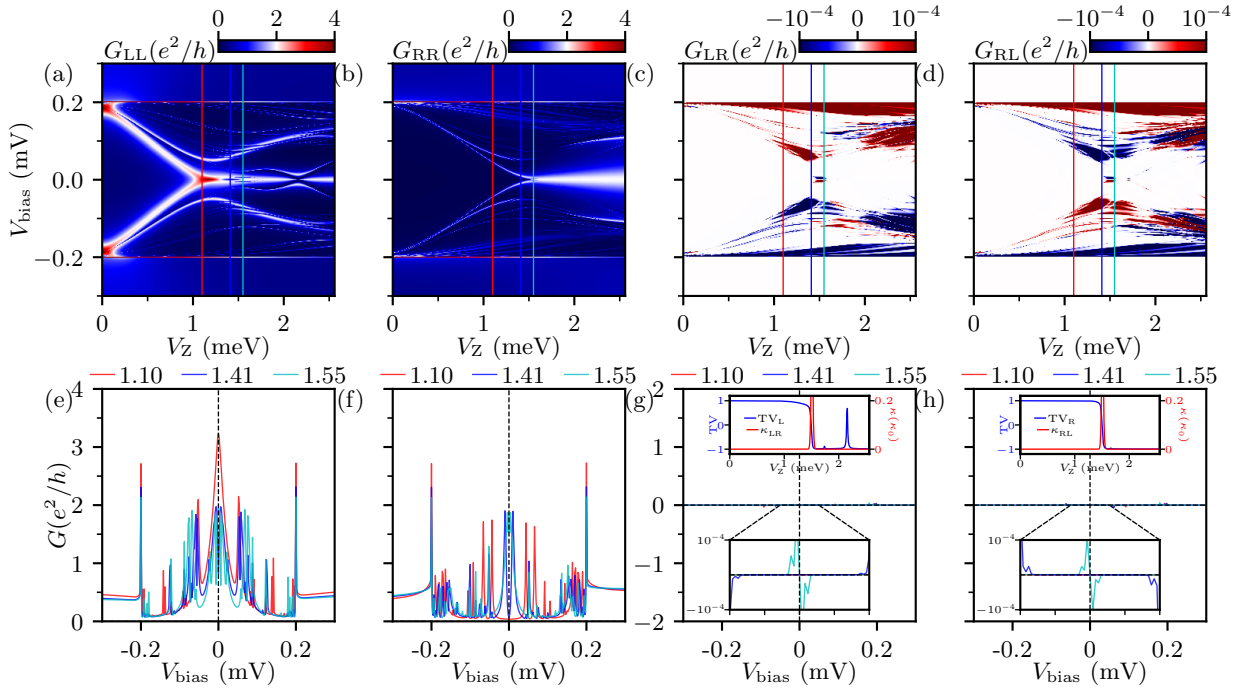

Figure C.1: The ugly ZBCP in a nanowire in the presence of intermediate disorder with $\sigma_\mu/\mu = 2$. (a)-(d) show the local and nonlocal conductance in the "intrinsic" color scale; (e)-(h) are the corresponding line cuts of the conductance as a function of bias at $V_{\rm Z} = 1.1$ meV, 1.41 meV, 1.55 meV. The other parameters are the same as Fig. 3.2. The corresponding TV from the left (right) and thermal conductance $\kappa_{\rm LR}$ ($\kappa_{\rm RL}$) are shown in the inset of (g) [(h)].

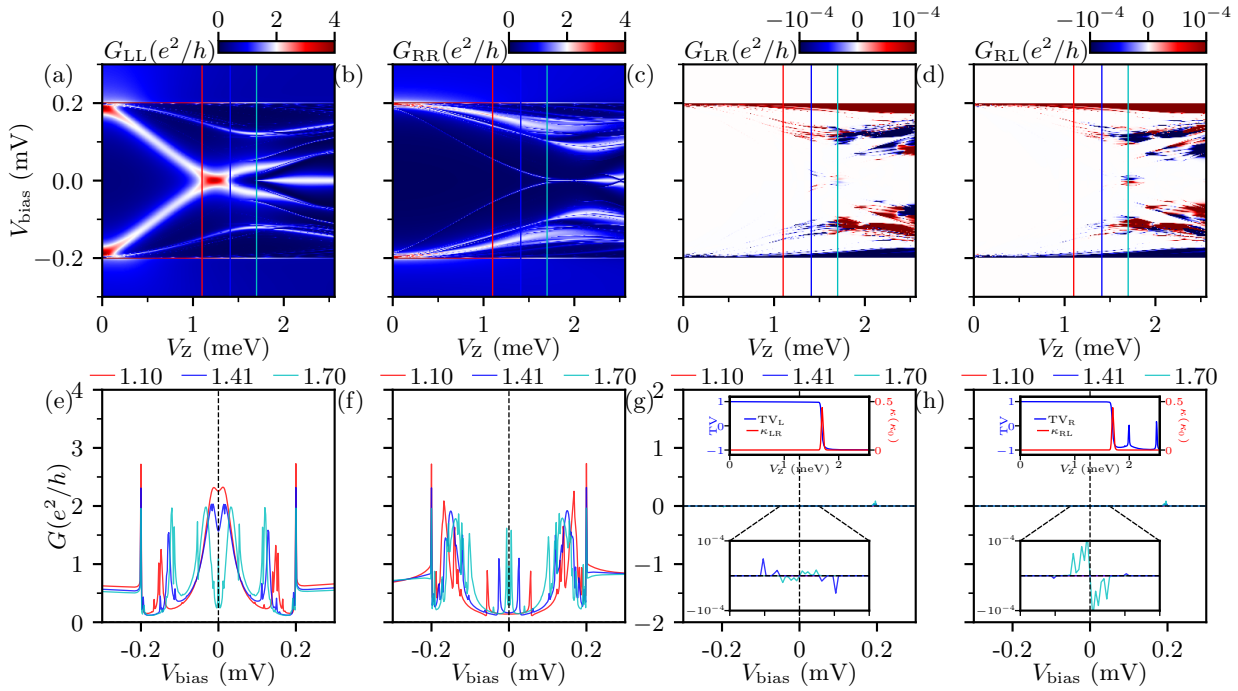

Figure C.2: The ugly ZBCP in a nanowire in the presence of intermediate disorder with $\sigma_\mu/\mu = 2.5$. (a)-(d) show the local and nonlocal conductance in the "intrinsic" color scale; (e)-(h) are the corresponding line cuts of the conductance as a function of bias at $V_{\mathrm{Z}} = 1.1$ meV, 1.41 meV, 1.7 meV. The other parameters are the same as Fig. 3.2. The corresponding TV from the left (right) and thermal conductance κ_{LR} (κ_{RL}) are shown in the inset of (g) [(h)].

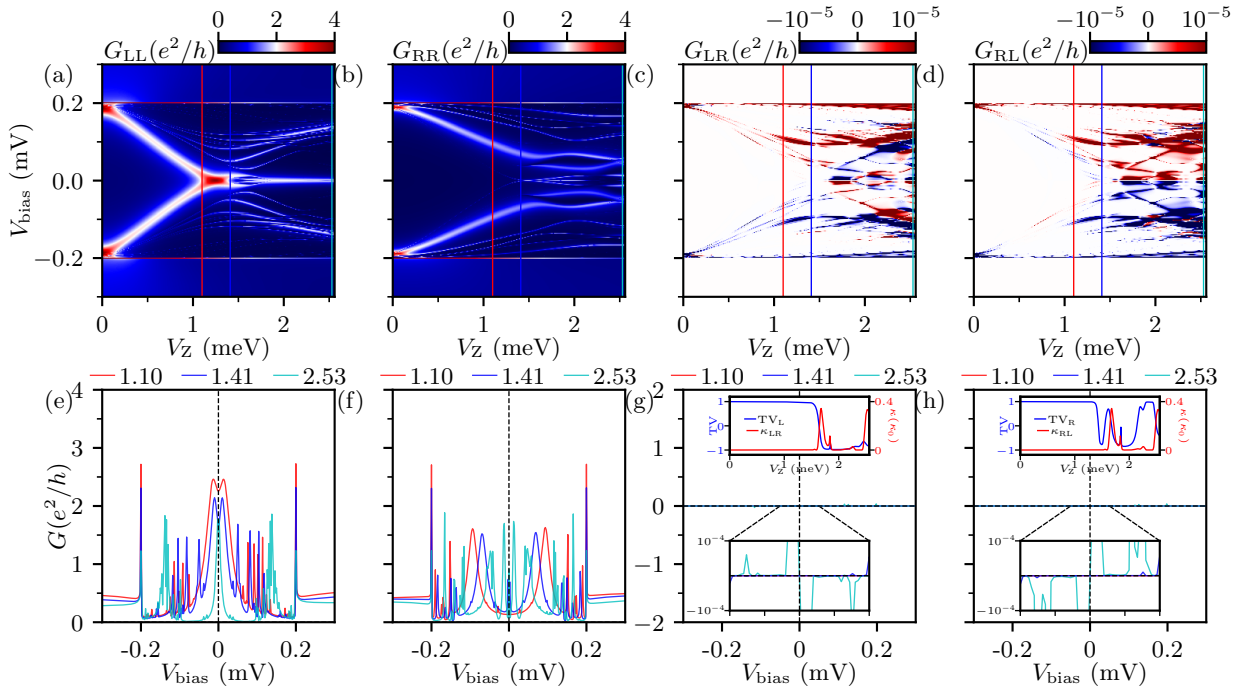

Figure C.3: The ugly ZBCP in a nanowire in the presence of strong disorder with $\sigma_\mu/\mu = 3.5$. (a)-(d) show the local and nonlocal conductance in the "intrinsic" color scale; (e)-(h) are the corresponding line cuts of the conductance as a function of bias at $V_{\rm Z} = 1.1$ meV, 1.41 meV, 2.53 meV. The other parameters are the same as Fig. 3.2. The corresponding TV from the left (right) and thermal conductance $\kappa_{\rm LR}$ ($\kappa_{\rm RL}$) are shown in the inset of (g) [(h)].

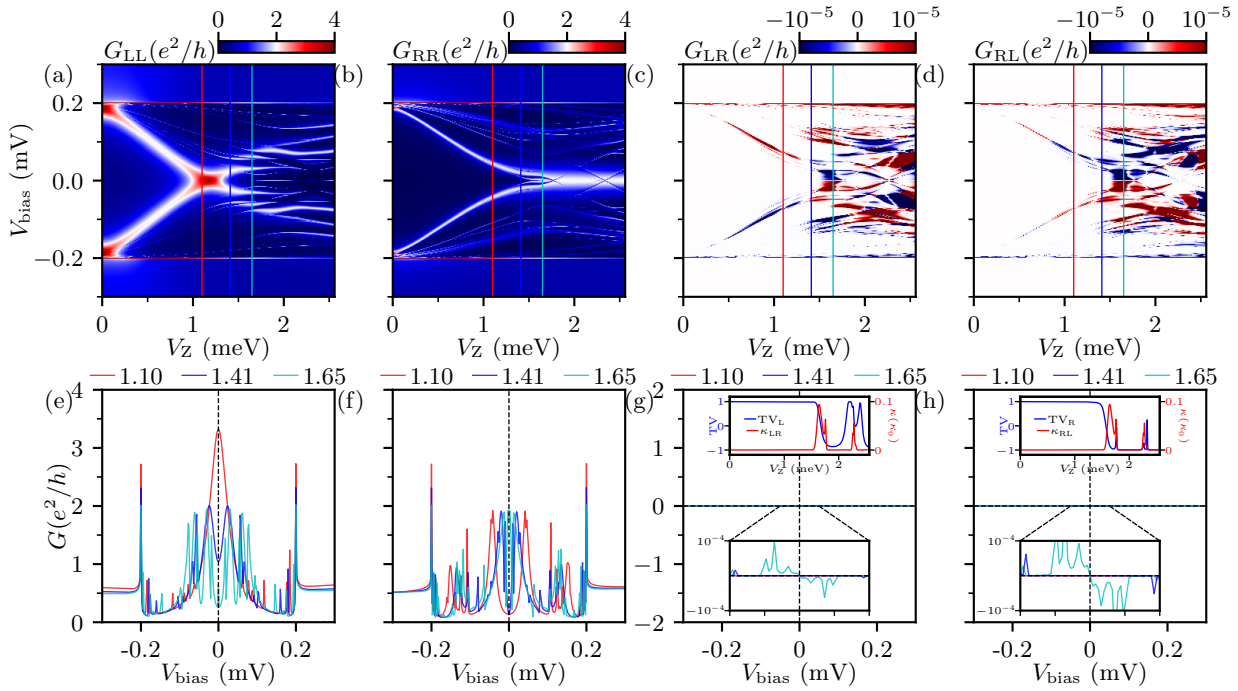

Figure C.4: The ugly ZBCP in a nanowire in the presence of strong disorder with $\sigma_\mu/\mu = 4$. (a)-(d) show the local and nonlocal conductance in the "intrinsic" color scale; (e)-(h) are the corresponding line cuts of the conductance as a function of bias at $V_{\rm Z} = 1.1$ meV, 1.41 meV, 1.65 meV. The other parameters are the same as Fig. 3.2. The corresponding TV from the left (right) and thermal conductance $\kappa_{\rm LR}$ ($\kappa_{\rm RL}$) are shown in the inset of (g) [(h)].

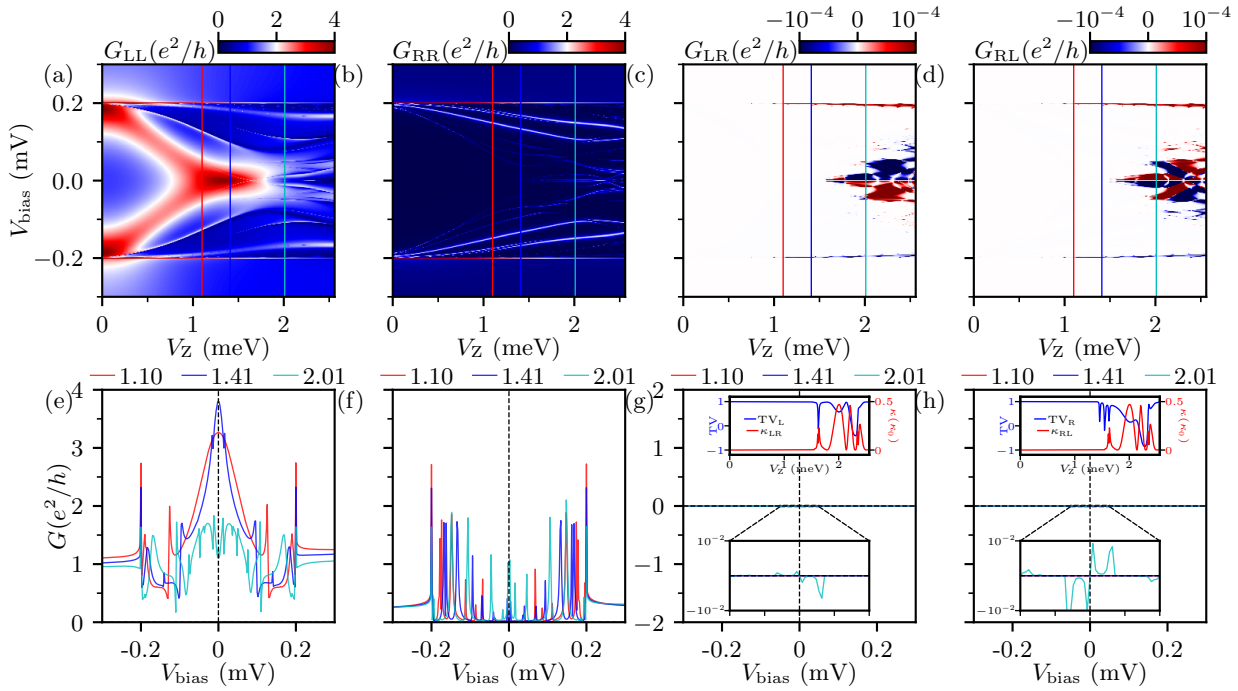

Figure C.5: The ugly ZBCP in a nanowire in the presence of strong disorder with $\sigma_\mu/\mu = 4.5$. (a)-(d) show the local and nonlocal conductance in the "intrinsic" color scale; (e)-(h) are the corresponding line cuts of the conductance as a function of bias at $V_{\rm Z} = 1.1$ meV, 1.41 meV, 2.01 meV. The other parameters are the same as Fig. 3.2. The corresponding TV from the left (right) and thermal conductance $\kappa_{\rm LR}$ ($\kappa_{\rm RL}$) are shown in the inset of (g) [(h)].

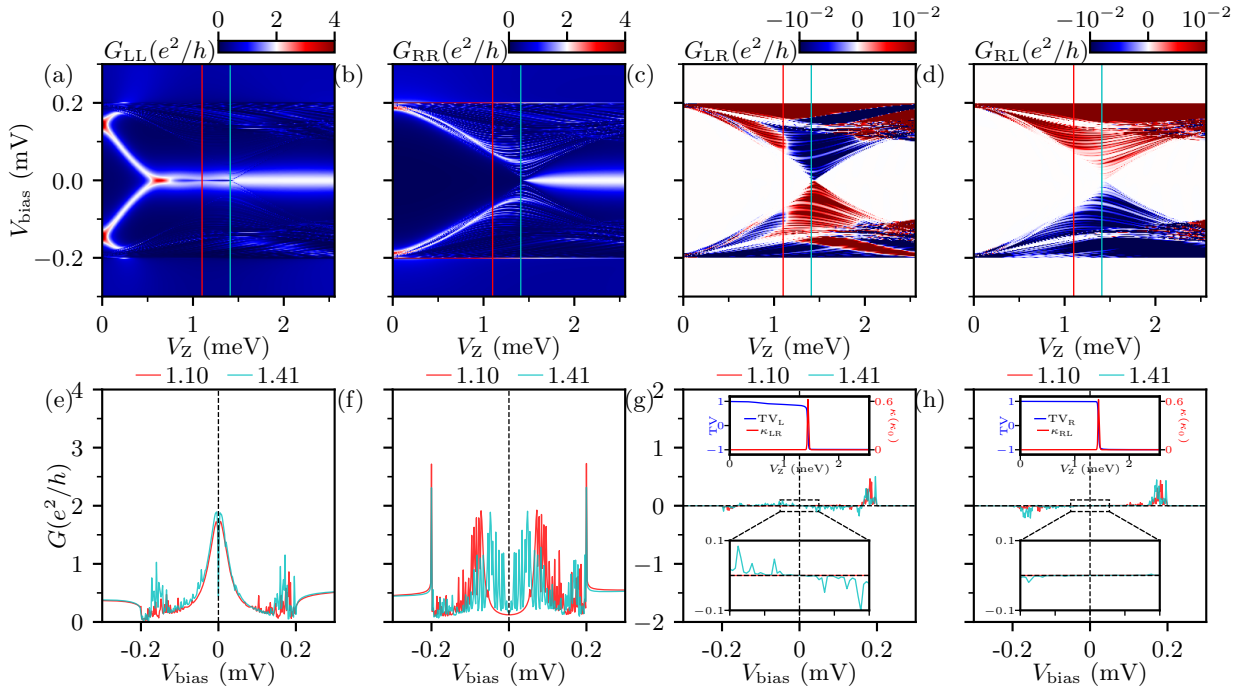

Figure C.6: The wire in the presence of the QD and weak disorder with $\sigma_\mu/\mu = 0.5$. (a)-(d) show the local and nonlocal conductance in the "intrinsic" color scale; (e)-(h) are the corresponding line cuts of the conductance as a function of bias at $V_{\rm Z} = 1.1$ meV, and 1.41 meV. The QD is the same as Fig. 3.3 with $V_{\rm D} = 0.4$ meV and $l = 0.15$ μm. The other parameters are the same as Fig. 3.2. The corresponding TV from the left (right) and thermal conductance $\kappa_{\rm LR}$ ($\kappa_{\rm RL}$) are shown in the inset of (g) [(h)].

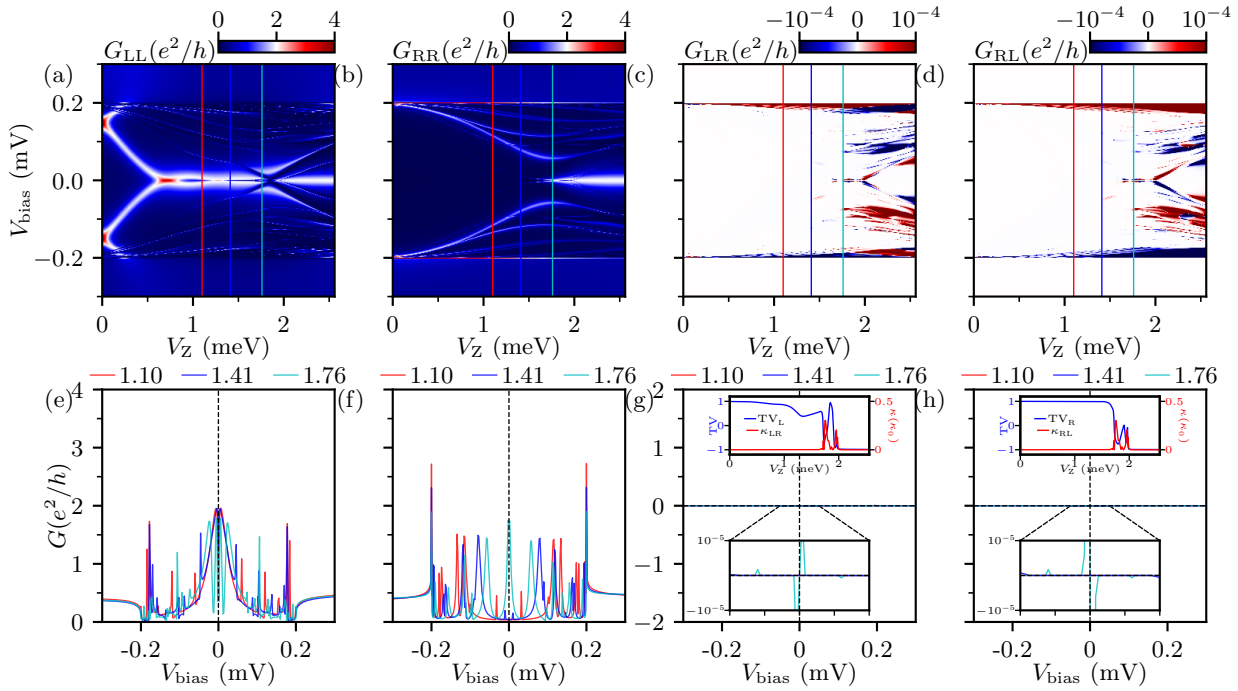

Figure C.7: The wire in the presence of the QD and intermediate disorder with $\sigma_\mu/\mu = 3$. (a)-(d) show the local and nonlocal conductance in the "intrinsic" color scale; (e)-(h) are the corresponding line cuts of the conductance as a function of bias at $V_{\rm Z} = 1.1$ meV, 1.41, and 1.76 meV. The QD is the same as Fig. 3.3 with $V_{\rm D} = 0.4$ meV and $l = 0.15$ μm. The other parameters are the same as Fig. 3.2. The corresponding TV from the left (right) and thermal conductance $\kappa_{\rm LR}$ ($\kappa_{\rm RL}$) are shown in the inset of (g) [(h)].

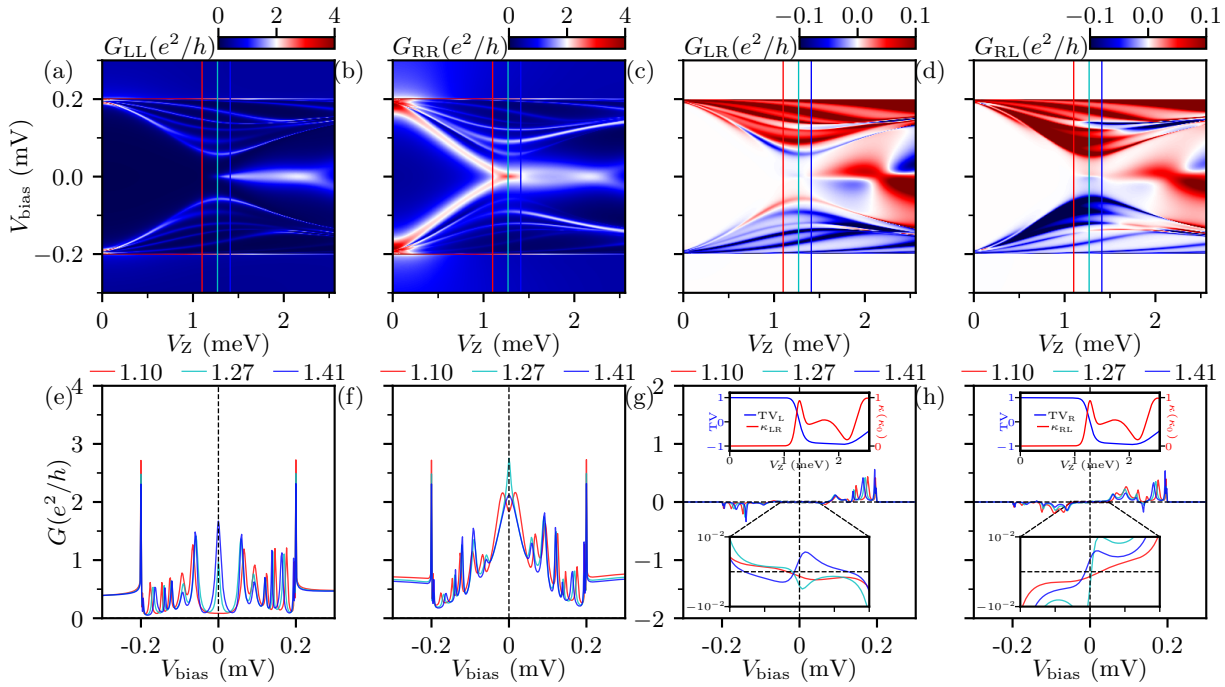

Figure C.8: The short wire ($L = 0.5\ \mu$m) in the presence of intermediate disorder with $\sigma_\mu/\mu = 1.5$. (a)-(d) show the local and nonlocal conductance in the "intrinsic" color scale; (e)-(h) are the corresponding line cuts of the conductance as a function of bias at $V_{\mathrm{Z}} = 1.1$ meV, 1.27 meV, 1.41 meV. The other parameters are the same as Fig. 3.2. The corresponding TV from the left (right) and thermal conductance κ_{LR} (κ_{RL}) are shown in the inset of (g) [(h)].

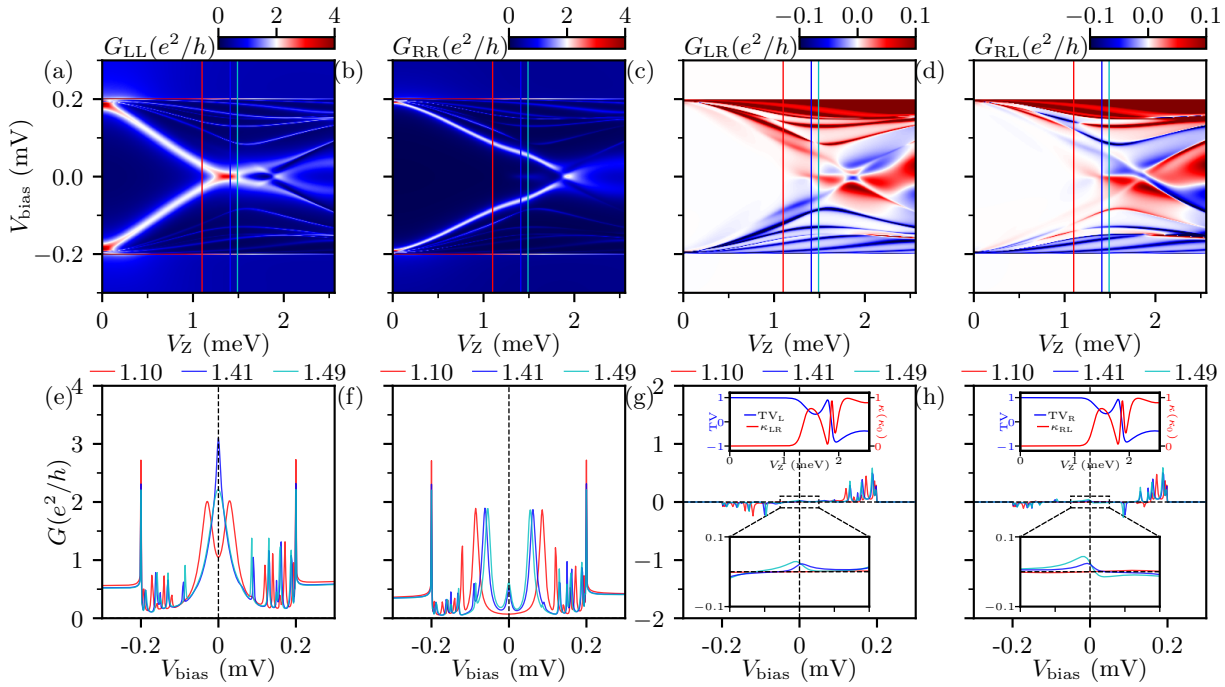

Figure C.9: The short wire ($L = 0.5\ \mu$m) in the presence of intermediate disorder with $\sigma_\mu/\mu = 2$. (a)-(d) show the local and nonlocal conductance in the "intrinsic" color scale; (e)-(h) are the corresponding line cuts of the conductance as a function of bias at $V_{\rm Z} = 1.1$ meV, 1.41 meV, 1.49 meV. The other parameters are the same as Fig. 3.2. The corresponding TV from the left (right) and thermal conductance $\kappa_{\rm LR}$ ($\kappa_{\rm RL}$) are shown in the inset of (g) [(h)].

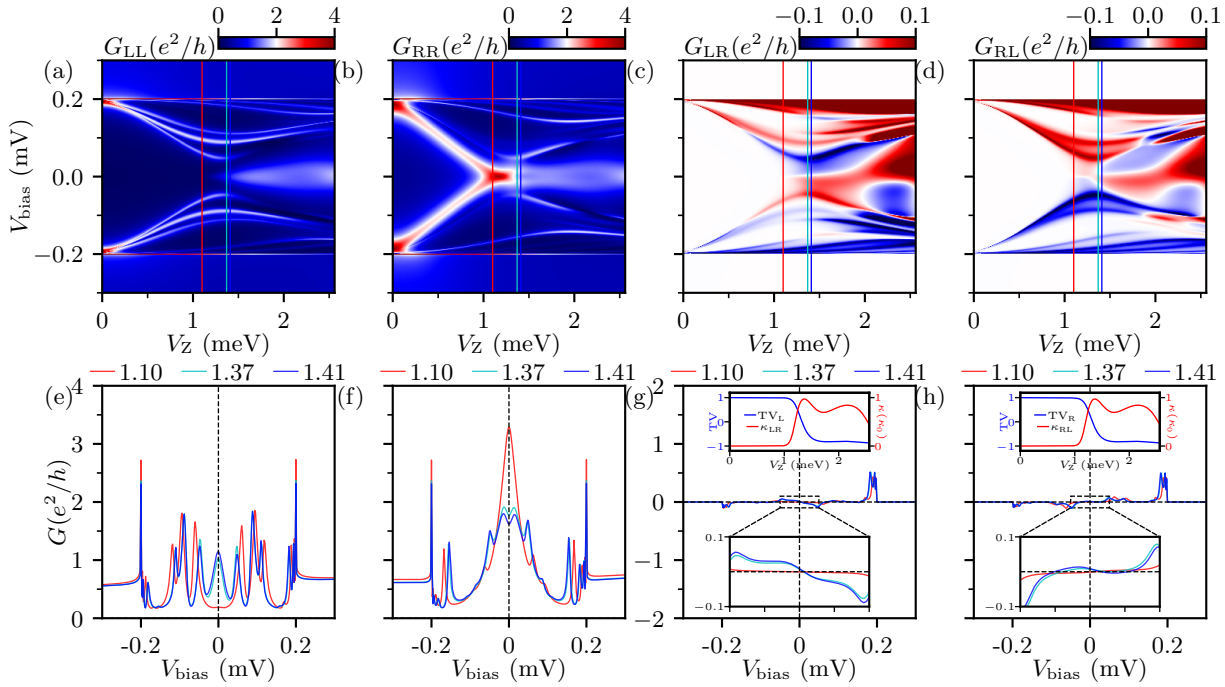

Figure C.10: The short wire ($L = 0.5$ μm) in the presence of intermediate disorder with $\sigma_\mu/\mu = 2.5$. (a)-(d) show the local and nonlocal conductance in the "intrinsic" color scale; (e)-(h) are the corresponding line cuts of the conductance as a function of bias at $V_{\rm Z} = 1.1$ meV, 1.37 meV, 1.41 meV. The other parameters are the same as Fig. 3.2. The corresponding TV from the left (right) and thermal conductance $\kappa_{\rm LR}$ ($\kappa_{\rm RL}$) are shown in the inset of (g) [(h)].

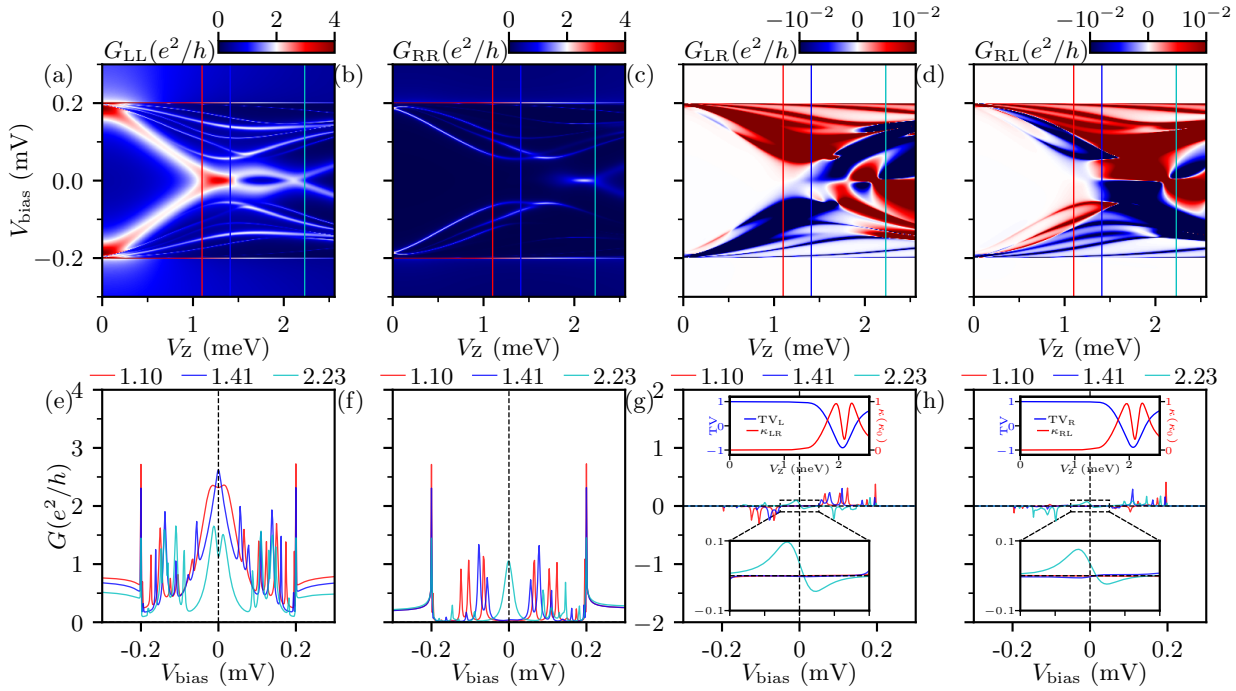

Figure C.11: The short wire ($L = 0.5\ \mu$m) in the presence of strong disorder with $\sigma_\mu/\mu = 3.5$. (a)-(d) show the local and nonlocal conductance in the "intrinsic" color scale; (e)-(h) are the corresponding line cuts of the conductance as a function of bias at $V_{\mathrm{Z}} = 1.1$ meV, 1.41 meV, 2.23 meV. The other parameters are the same as Fig. 3.2. The corresponding TV from the left (right) and thermal conductance κ_{LR} (κ_{RL}) are shown in the inset of (g) [(h)].

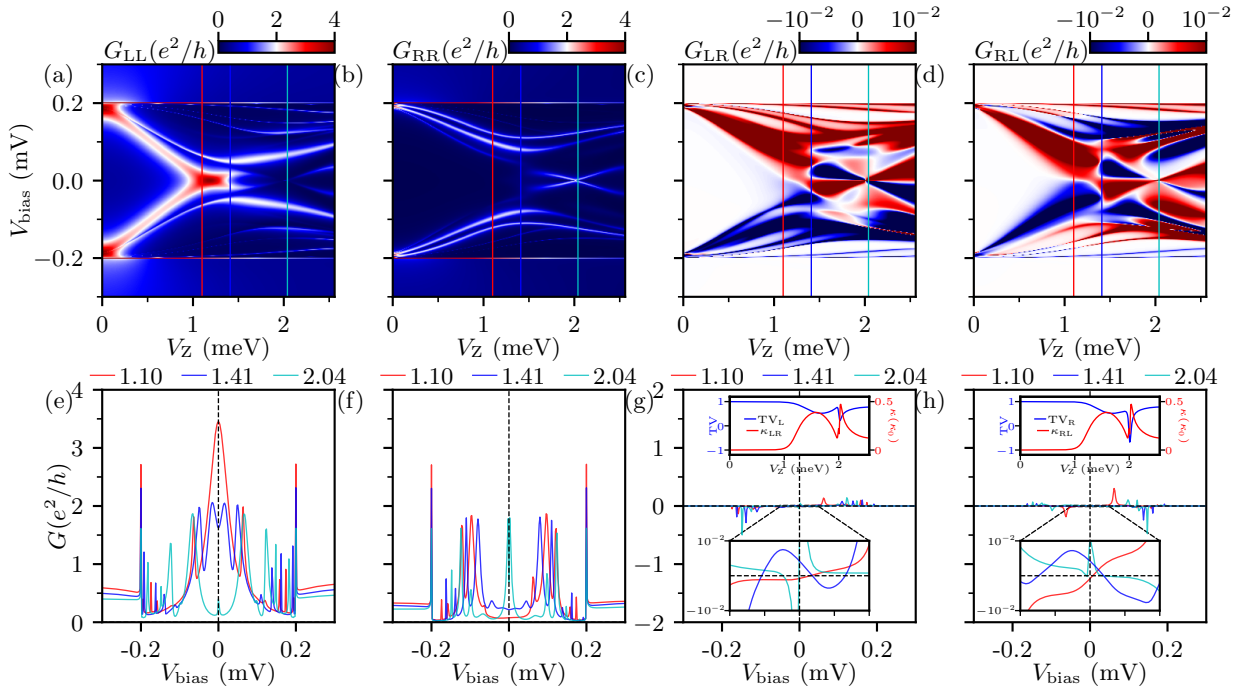

Figure C.12: The short wire ($L = 0.5$ μm) in the presence of strong disorder with $\sigma_\mu/\mu = 4$. (a)-(d) show the local and nonlocal conductance in the "intrinsic" color scale; (e)-(h) are the corresponding line cuts of the conductance as a function of bias at $V_{\rm Z} = 1.1$ meV, 1.41 meV, 2.04 meV. The other parameters are the same as Fig. 3.2. The corresponding TV from the left (right) and thermal conductance $\kappa_{\rm LR}$ ($\kappa_{\rm RL}$) are shown in the inset of (g) [(h)].

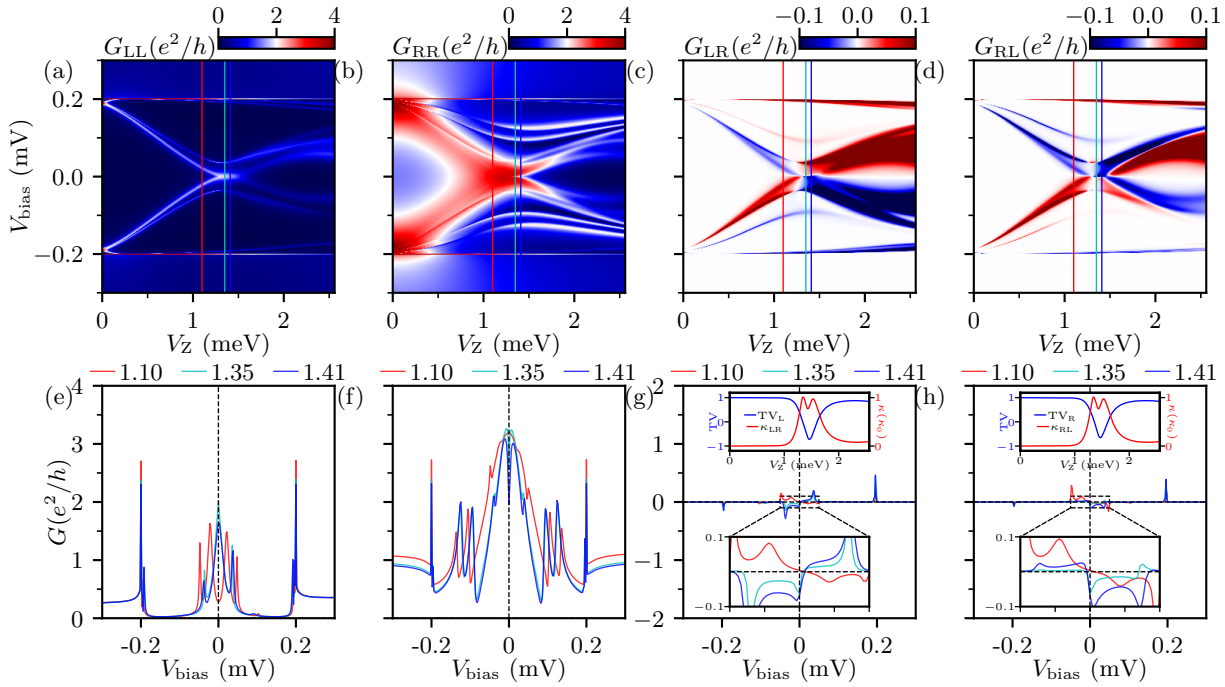

Figure C.13: The short wire ($L = 0.5$ μm) in the presence of strong disorder with $\sigma_\mu/\mu = 4.5$. (a)-(d) show the local and nonlocal conductance in the "intrinsic" color scale; (e)-(h) are the corresponding line cuts of the conductance as a function of bias at $V_{\rm Z} = 1.1$ meV, 1.35 meV, 1.41 meV. The other parameters are the same as Fig. 3.2. The corresponding TV from the left (right) and thermal conductance $\kappa_{\rm LR}$ ($\kappa_{\rm RL}$) are shown in the inset of (g) [(h)].

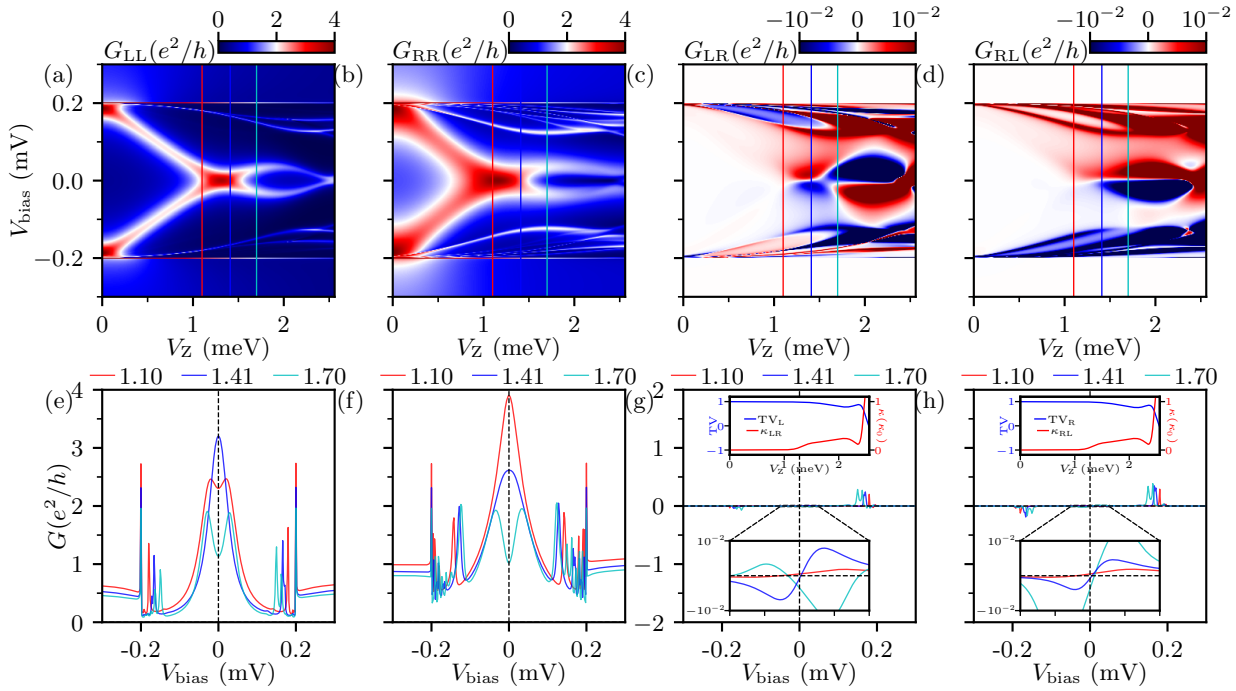

Figure C.14: The short wire ($L = 0.5\ \mu$m) in the presence of very strong disorder with $\sigma_\mu/\mu = 5$. (a)-(d) show the local and nonlocal conductance in the "intrinsic" color scale; (e)-(h) are the corresponding line cuts of the conductance as a function of bias at $V_{\mathrm{Z}} = 1.1$ meV, 1.41 meV, 1.7 meV. The other parameters are the same as Fig. 3.2. The corresponding TV from the left (right) and thermal conductance κ_{LR} (κ_{RL}) are shown in the inset of (g) [(h)].

Appendix D: Code

The codes for all the simulations presented in this dissertation, including the local conductance, nonlocal conductance, thermal conductance, topological visibility, energy spectrum, and wave function in both Nambu space and Majorana basis is accessible on the GitHub repository at https://github.com/hainingpan/Conductance_Kwant, where a "README.md" file is provided to explain the usage, and a directory of "Examples" shows the parameters to reproduce all simulations in this dissertation.

List of Publications

This dissertation is based on the following publications.

[1] H. Pan, W. S. Cole, J. D. Sau, and S. Das Sarma, Generic quantized zero-bias conductance peaks in superconductor-semiconductor hybrid structures, Phys. Rev. B **101**, 024506 (2020).

[2] H. Pan and S. Das Sarma, Physical mechanisms for zero-bias conductance peaks in Majorana nanowires, Phys. Rev. Research **2**, 013377 (2020).

[3] S. Das Sarma and H. Pan, Disorder-induced zero-bias peaks in Majorana nanowires, Phys. Rev. B **103**, 195158 (2021).

[4] H. Pan, J. D. Sau, and S. Das Sarma, Three-terminal nonlocal conductance in Majorana nanowires: Distinguishing topological and trivial in realistic systems with disorder and inhomogeneous potential, Phys. Rev. B **103**, 014513 (2021).

I have also authored the following publications and preprints during my doctoral study.

[1] Y. Huang, H. Pan, C.-X. Liu, J. D. Sau, T. D. Stanescu, and S. Das Sarma, Metamorphosis of Andreev bound states into Majorana bound states in pristine nanowires, Phys. Rev. B **98**, 144511 (2018).

[2] H. Pan, J. D. Sau, T. D. Stanescu, and S. Das Sarma, Curvature of gap closing features and the extraction of Majorana nanowire parameters, Phys. Rev. B **99**, 054507 (2019).

[3] H. Pan, K. Winkler, M. Powlowski, M. Xie, A. Schade, M. Emmerling, M. Kamp, S. Klembt, C. Schneider, T. Byrnes, S. Höfling, and N. Y. Kim, Two-kind boson mixture honeycomb Hamiltonian of Bloch exciton-polaritons, Phys. Rev. B **99**, 045302 (2019).

[4] A. Sett, H. Pan, P. E. Falloon, and J. B. Wang, Zero transfer in continuous-time quantum walks, Quantum Inf Process **18**, 159 (2019).

[5] H. Pan, F. Wu, and S. Das Sarma, Band topology, Hubbard model, Heisenberg model, and Dzyaloshinskii-Moriya interaction in twisted bilayer WSe_2, Phys. Rev. Research **2**, 033087 (2020).

[6] H. Pan, F. Wu, and S. Das Sarma, Quantum phase diagram of a Moiré-Hubbard model, Phys. Rev. B **102**, 201104 (2020).

[7] S. Ahn, H. Pan, B. Woods, T. D. Stanescu, and S. Das Sarma, Estimating disorder and its adverse effects in semiconductor Majorana nanowires, Phys. Rev. Materials **5**, 124602 (2021).

[8] H. Pan and S. Das Sarma, Disorder effects on Majorana zero modes: Kitaev chain versus semiconductor nanowire, Phys. Rev. B **103**, 224505 (2021).

[9] H. Pan and S. Das Sarma, Crossover between trivial zero modes in Majorana nanowires, Phys. Rev. B **104**, 054510 (2021).

[10] H. Pan and S. Das Sarma, Interaction-Driven Filling-Induced Metal-Insulator Transitions in 2D Moiré Lattices, Phys. Rev. Lett. **127**, 096802 (2021).

[11] H. Pan, C.-X. Liu, M. Wimmer, and S. Das Sarma, Quantized and unquantized zero-bias tunneling conductance peaks in Majorana nanowires: Conductance below and above $2e^2/h$, Phys. Rev. B **103**, 214502 (2021).

[12] H. Pan, M. Xie, F. Wu, and S. D. Sarma, Topological Phases in AB-stacked $MoTe_2/WSe_2$: $\mathbb{Z}_2$ Topological Insulators, Chern Insulators, and Topological Charge Density Waves, arXiv:2111.01152 (2021).

[13] H. Pan and S. Das Sarma, Interaction range and temperature dependence of symmetry breaking in strongly correlated two-dimensional moiré transition metal dichalcogenide bilayers, Phys. Rev. B **105**, 041109 (2022).

[14] H. Pan and S. Das Sarma, On-demand large conductance in trivial zero-bias tunneling peaks in Majorana nanowires, Phys. Rev. B **105**, 115432 (2022).

[15] H. Pan, J. D. Sau, and S. D. Sarma, A random matrix theory for the robustness, quantization, and end-to-end correlation of zero-bias conductance peaks in class D ensemble: Searching for Majorana zero modes in disordered quantum dots and wires, arXiv:2204.12505 (2022).

[16] M. Xie, H. Pan, F. Wu, and S. D. Sarma, Nematic excitonic insulator in transition metal dichalcogenide moiré heterobilayers, arXiv:2206.12427 (2022).

Bibliography

[1] K. von Klitzing, G. Dorda, and M. Pepper, New Method for High-Accuracy Determination of the Fine-Structure Constant Based on Quantized Hall Resistance, Phys. Rev. Lett. **45**, 494 (1980).

[2] D. C. Tsui, H. L. Stormer, and A. C. Gossard, Two-Dimensional Magnetotransport in the Extreme Quantum Limit, Phys. Rev. Lett. **48**, 1559 (1982).

[3] M. König, S. Wiedmann, C. Brüne, A. Roth, H. Buhmann, L. W. Molenkamp, X.-L. Qi, and S.-C. Zhang, Quantum Spin Hall Insulator State in HgTe Quantum Wells, Science **318**, 766 (2007).

[4] Y. L. Chen, J. G. Analytis, J.-H. Chu, Z. K. Liu, S.-K. Mo, X. L. Qi, H. J. Zhang, D. H. Lu, X. Dai, Z. Fang, S. C. Zhang, I. R. Fisher, Z. Hussain, and Z.-X. Shen, Experimental Realization of a Three-Dimensional Topological Insulator, Bi2Te3, Science **325**, 178 (2009).

[5] C.-Z. Chang, J. Zhang, X. Feng, J. Shen, Z. Zhang, M. Guo, K. Li, Y. Ou, P. Wei, L.-L. Wang, Z.-Q. Ji, Y. Feng, S. Ji, X. Chen, J. Jia, X. Dai, Z. Fang, S.-C. Zhang, K. He, Y. Wang, L. Lu, X.-C. Ma, and Q.-K. Xue, Experimental Observation of the Quantum Anomalous Hall Effect in a Magnetic Topological Insulator, Science **340**, 167 (2013).

[6] R. L. Willett, L. N. Pfeiffer, and K. W. West, Measurement of filling factor 5/2 quasiparticle interference with observation of charge e/4 and e/2 period oscillations, PNAS **106**, 8853 (2009).

[7] Y. Kasahara, T. Ohnishi, Y. Mizukami, O. Tanaka, S. Ma, K. Sugii, N. Kurita, H. Tanaka, J. Nasu, Y. Motome, T. Shibauchi, and Y. Matsuda, Majorana quantization and half-integer thermal quantum Hall effect in a Kitaev spin liquid, Nature **559**, 227 (2018).

[8] V. Mourik, K. Zuo, S. M. Frolov, S. R. Plissard, E. P. A. M. Bakkers, and L. P. Kouwenhoven, Signatures of Majorana Fermions in Hybrid Superconductor-Semiconductor Nanowire Devices, Science **336**, 1003 (2012).

[9] H. Zhang, C.-X. Liu, S. Gazibegovic, D. Xu, J. A. Logan, G. Wang, N. van Loo, J. D. S. Bommer, M. W. A. de Moor, D. Car, R. L. M. Op het Veld, P. J. van Veldhoven, S. Koelling, M. A. Verheijen, M. Pendharkar, D. J. Pennachio, B. Shojaei, J. S. Lee, C. J. Palmstrøm, E. P. A. M. Bakkers, S. D. Sarma, and L. P. Kouwenhoven, Quantized majorana conductance, [Retracted] Nature **556**, 74 (2018), arXiv:1710.10701.

[10] E. Majorana, Teoria simmetrica dell'elettrone e del positrone, Nuovo Cim **14**, 171 (1937).

[11] J. B. Albert, D. J. Auty, P. S. Barbeau, E. Beauchamp, D. Beck, V. Belov, C. Benitez-Medina, J. Bonatt, M. Breidenbach, T. Brunner, A. Burenkov, G. F. Cao, C. Chambers, J. Chaves, B. Cleveland, M. Coon, A. Craycraft, T. Daniels, M. Danilov, S. J. Daugherty, C. G. Davis, J. Davis, R. DeVoe, S. Delaquis, T. Didberidze, A. Dolgolenko, M. J. Dolinski, M. Dunford, W. Fairbank Jr, J. Farine, W. Feldmeier, P. Fierlinger, D. Fudenberg, G. Giroux, R. Gornea, K. Graham, G. Gratta, C. Hall, S. Herrin, M. Hughes, M. J. Jewell, X. S. Jiang, A. Johnson, T. N. Johnson, S. Johnston, A. Karelin, L. J. Kaufman, R. Killick, T. Koffas, S. Kravitz, A. Kuchenkov, K. S. Kumar, D. S. Leonard, F. Leonard, C. Licciardi, Y. H. Lin, R. MacLellan, M. G. Marino, B. Mong, D. Moore, R. Nelson, A. Odian, I. Ostrovskiy, C. Ouellet, A. Piepke, A. Pocar, C. Y. Prescott, A. Rivas, P. C. Rowson, M. P. Rozo, J. J. Russell, A. Schubert, D. Sinclair, S. Slutsky, E. Smith, V. Stekhanov, M. Tarka, T. Tolba, D. Tosi, K. Twelker, P. Vogel, J.-L. Vuilleumier, A. Waite, J. Walton, T. Walton, M. Weber, L. J. Wen, U. Wichoski, J. D. Wright, L. Yang, Y.-R. Yen, O. Ya. Zeldovich, Y. B. Zhao, and The EXO-200 Collaboration, Search for Majorana neutrinos with the first two years of EXO-200 data, Nature **510**, 229 (2014).

[12] KamLAND-Zen Collaboration, A. Gando, Y. Gando, T. Hachiya, A. Hayashi, S. Hayashida, H. Ikeda, K. Inoue, K. Ishidoshiro, Y. Karino, M. Koga, S. Matsuda, T. Mitsui, K. Nakamura, S. Obara, T. Oura, H. Ozaki, I. Shimizu, Y. Shirahata, J. Shirai, A. Suzuki, T. Takai, K. Tamae, Y. Teraoka, K. Ueshima, H. Watanabe, A. Kozlov, Y. Takemoto, S. Yoshida, K. Fushimi, T. I. Banks, B. E. Berger, B. K. Fujikawa, T. O'Donnell, L. A. Winslow, Y. Efremenko, H. J. Karwowski, D. M. Markoff, W. Tornow, J. A. Detwiler, S. Enomoto, and M. P. Decowski, Search for Majorana Neutrinos Near the Inverted Mass Hierarchy Region with KamLAND-Zen, Phys. Rev. Lett. **117**, 082503 (2016).

[13] A. Y. Kitaev, Fault-tolerant quantum computation by anyons, Annals of Physics **303**, 2 (2003).

[14] S. Das Sarma, M. Freedman, and C. Nayak, Topologically Protected Qubits from a Possible Non-Abelian Fractional Quantum Hall State, Phys. Rev. Lett. **94**, 166802 (2005).

[15] C. Nayak, S. H. Simon, A. Stern, M. Freedman, and S. Das Sarma, Non-Abelian anyons and topological quantum computation, Reviews of Modern Physics **80**, 1083 (2008).

[16] S. D. Sarma, M. Freedman, and C. Nayak, Majorana zero modes and topological quantum computation, npj Quantum Information **1**, 15001 (2015).

[17] A. Ahlbrecht, L. S. Georgiev, and R. F. Werner, Implementation of Clifford gates in the Ising-anyon topological quantum computer, Phys. Rev. A **79**, 032311 (2009).

[18] T. Karzig, C. Knapp, R. M. Lutchyn, P. Bonderson, M. B. Hastings, C. Nayak, J. Alicea, K. Flensberg, S. Plugge, Y. Oreg, C. M. Marcus, and M. H. Freedman, Scalable designs for quasiparticle-poisoning-protected topological quantum computation with Majorana zero modes, Phys. Rev. B **95**, 235305 (2017).

[19] P. Bonderson, M. Freedman, and C. Nayak, Measurement-Only Topological Quantum Computation, Phys. Rev. Lett. **101**, 010501 (2008).

[20] S. Vijay and L. Fu, Teleportation-based quantum information processing with Majorana zero modes, Phys. Rev. B **94**, 235446 (2016).

[21] A. Tran, A. Bocharov, B. Bauer, and P. Bonderson, Optimizing Clifford gate generation for measurement-only topological quantum computation with Majorana zero modes, SciPost Physics **8**, 091 (2020).

[22] N. Read and D. Green, Paired states of fermions in two dimensions with breaking of parity and time-reversal symmetries and the fractional quantum Hall effect, Phys. Rev. B **61**, 10267 (2000).

[23] A. Y. Kitaev, Unpaired Majorana fermions in quantum wires, Phys.-Usp. **44**, 131 (2001).

[24] W. P. Su, J. R. Schrieffer, and A. J. Heeger, Solitons in Polyacetylene, Phys. Rev. Lett. **42**, 1698 (1979).

[25] L. Fu and C. L. Kane, Superconducting Proximity Effect and Majorana Fermions at the Surface of a Topological Insulator, Phys. Rev. Lett. **100**, 096407 (2008).

[26] C. Zhang, S. Tewari, R. M. Lutchyn, and S. Das Sarma, $p_x + ip_y$ superfluid from s-Wave Interactions of Fermionic Cold Atoms, Phys. Rev. Lett. **101**, 160401 (2008).

[27] R. M. Lutchyn, J. D. Sau, and S. Das Sarma, Majorana Fermions and a Topological Phase Transition in Semiconductor-Superconductor Heterostructures, Phys. Rev. Lett. **105**, 077001 (2010).

[28] J. Alicea, Majorana fermions in a tunable semiconductor device, Phys. Rev. B **81**, 125318 (2010).

[29] J. D. Sau, R. M. Lutchyn, S. Tewari, and S. Das Sarma, Generic New Platform for Topological Quantum Computation Using Semiconductor Heterostructures, Phys. Rev. Lett. **104**, 040502 (2010).

[30] J. D. Sau, S. Tewari, R. M. Lutchyn, T. D. Stanescu, and S. Das Sarma, Non-Abelian quantum order in spin-orbit-coupled semiconductors: Search for topological Majorana particles in solid-state systems, Phys. Rev. B **82**, 214509 (2010).

[31] Y. Oreg, G. Refael, and F. von Oppen, Helical Liquids and Majorana Bound States in Quantum Wires, Phys. Rev. Lett. **105**, 177002 (2010).

[32] T. D. Stanescu, J. D. Sau, R. M. Lutchyn, and S. Das Sarma, Proximity effect at the superconductor–topological insulator interface, Phys. Rev. B **81**, 241310 (2010).

[33] J. Alicea, New directions in the pursuit of Majorana fermions in solid state systems, Rep. Prog. Phys. **75**, 076501 (2012).

[34] K. Sengupta, I. Žutić, H.-J. Kwon, V. M. Yakovenko, and S. Das Sarma, Midgap edge states and pairing symmetry of quasi-one-dimensional organic superconductors, Phys. Rev. B **63**, 144531 (2001).

[35] M. T. Deng, C. L. Yu, G. Y. Huang, M. Larsson, P. Caroff, and H. Q. Xu, Anomalous Zero-Bias Conductance Peak in a Nb–InSb Nanowire–Nb Hybrid Device, Nano Letters **12**, 6414 (2012).

[36] A. Das, Y. Ronen, Y. Most, Y. Oreg, M. Heiblum, and H. Shtrikman, Zero-bias peaks and splitting in an Al–InAs nanowire topological superconductor as a signature of Majorana fermions, Nature Physics **8**, 887 (2012).

[37] A. D. K. Finck, D. J. Van Harlingen, P. K. Mohseni, K. Jung, and X. Li, Anomalous Modulation of a Zero-Bias Peak in a Hybrid Nanowire-Superconductor Device, Phys. Rev. Lett. **110**, 126406 (2013).

[38] H. O. H. Churchill, V. Fatemi, K. Grove-Rasmussen, M. T. Deng, P. Caroff, H. Q. Xu, and C. M. Marcus, Superconductor-nanowire devices from tunneling to the multichannel regime: Zero-bias oscillations and magnetoconductance crossover, Phys. Rev. B **87**, 241401 (2013).

[39] E. J. H. Lee, X. Jiang, M. Houzet, R. Aguado, C. M. Lieber, and S. De Franceschi, Spin-resolved Andreev levels and parity crossings in hybrid superconductor–semiconductor nanostructures, Nature Nanotechnology **9**, 79 (2014).

[40] S. M. Albrecht, A. Higginbotham, M. Madsen, F. Kuemmeth, T. S. Jespersen, J. Nygård, P. Krogstrup, and C. Marcus, Exponential protection of zero modes in Majorana islands, Nature (London) **531**, 206 (2016).

[41] J. Kammhuber, M. C. Cassidy, H. Zhang, Ö. Gül, F. Pei, M. W. A. de Moor, B. Nijholt, K. Watanabe, T. Taniguchi, D. Car, S. R. Plissard, E. P. A. M. Bakkers, and L. P. Kouwenhoven, Conductance Quantization at Zero Magnetic Field in InSb Nanowires, Nano Letters **16**, 3482 (2016).

[42] M. Deng, S. Vaitiekėnas, E. B. Hansen, J. Danon, M. Leijnse, K. Flensberg, J. Nygård, P. Krogstrup, and C. M. Marcus, Majorana bound state in a coupled quantum-dot hybrid-nanowire system, Science **354**, 1557 (2016).

[43] H. Zhang, Ö. Gül, S. Conesa-Boj, M. P. Nowak, M. Wimmer, K. Zuo, V. Mourik, F. K. de Vries, J. van Veen, M. W. A. de Moor, J. D. S. Bommer, D. J. van Woerkom, D. Car, S. R. Plissard, E. P. A. M. Bakkers, M. Quintero-Pérez, M. C. Cassidy, S. Koelling, S. Goswami, K. Watanabe, T. Taniguchi, and L. P. Kouwenhoven, Ballistic superconductivity in semiconductor nanowires, Nature Communications **8**, 16025 (2017).

[44] J. Kammhuber, M. C. Cassidy, F. Pei, M. P. Nowak, A. Vuik, Ö. Gül, D. Car, S. R. Plissard, E. P. a. M. Bakkers, M. Wimmer, and L. P. Kouwenhoven, Conductance through a helical state in an Indium antimonide nanowire, Nature Communications **8**, 478 (2017).

[45] J. Chen, P. Yu, J. Stenger, M. Hocevar, D. Car, S. R. Plissard, E. P. A. M. Bakkers, T. D. Stanescu, and S. M. Frolov, Experimental phase diagram of zero-bias conductance peaks in superconductor/semiconductor nanowire devices, Science Advances **3**, e1701476 (2017).

[46] F. Nichele, A. C. C. Drachmann, A. M. Whiticar, E. C. T. O'Farrell, H. J. Suominen, A. Fornieri, T. Wang, G. C. Gardner, C. Thomas, A. T. Hatke, P. Krogstrup, M. J. Manfra, K. Flensberg, and C. M. Marcus, Scaling of Majorana Zero-Bias Conductance Peaks, Phys. Rev. Lett. **119**, 136803 (2017).

[47] Ö. Gül, H. Zhang, J. D. S. Bommer, M. W. A. de Moor, D. Car, S. R. Plissard, E. P. A. M. Bakkers, A. Geresdi, K. Watanabe, T. Taniguchi, and L. P. Kouwenhoven, Ballistic Majorana nanowire devices, Nature Nanotechnology **13**, 192 (2018).

[48] M. W. A. de Moor, J. D. S. Bommer, D. Xu, G. W. Winkler, A. E. Antipov, A. Bargerbos, G. Wang, N. van Loo, R. L. M. O. het Veld, S. Gazibegovic, D. Car, J. A. Logan, M. Pendharkar, J. S. Lee, E. P. A. M. Bakkers, C. J. Palmstrøm, R. M. Lutchyn, L. P. Kouwenhoven, and H. Zhang, Electric field tunable superconductor-semiconductor coupling in Majorana nanowires, New J. Phys. **20**, 103049 (2018).

[49] S. Vaitiekėnas, M.-T. Deng, J. Nygård, P. Krogstrup, and C. M. Marcus, Effective g Factor of Subgap States in Hybrid Nanowires, Phys. Rev. Lett. **121**, 037703 (2018).

[50] A. Grivnin, E. Bor, M. Heiblum, Y. Oreg, and H. Shtrikman, Concomitant opening of a bulk-gap with an emerging possible Majorana zero mode, Nat Commun **10**, 1940 (2019).

[51] G. L. R. Anselmetti, E. A. Martinez, G. C. Ménard, D. Puglia, F. K. Malinowski, J. S. Lee, S. Choi, M. Pendharkar, C. J. Palmstrøm, C. M. Marcus, L. Casparis, and A. P. Higginbotham, End-to-end correlated subgap states in hybrid nanowires, Phys. Rev. B **100**, 205412 (2019).

[52] J. D. S. Bommer, H. Zhang, Ö. Gül, B. Nijholt, M. Wimmer, F. N. Rybakov, J. Garaud, D. Rodic, E. Babaev, M. Troyer, D. Car, S. R. Plissard, E. P. A. M. Bakkers, K. Watanabe, T. Taniguchi, and L. P. Kouwenhoven, Spin-Orbit Protection of Induced Superconductivity in Majorana Nanowires, Phys. Rev. Lett. **122**, 187702 (2019).

[53] J. Chen, B. D. Woods, P. Yu, M. Hocevar, D. Car, S. R. Plissard, E. P. A. M. Bakkers, T. D. Stanescu, and S. M. Frolov, Ubiquitous Non-Majorana Zero-Bias Conductance Peaks in Nanowire Devices, Phys. Rev. Lett. **123**, 107703 (2019).

[54] G. C. Ménard, G. L. R. Anselmetti, E. A. Martinez, D. Puglia, F. K. Malinowski, J. S. Lee, S. Choi, M. Pendharkar, C. J. Palmstrøm, K. Flensberg, C. M. Marcus, L. Casparis, and A. P. Higginbotham, Conductance-Matrix Symmetries of a Three-Terminal Hybrid Device, Phys. Rev. Lett. **124**, 036802 (2020).

[55] D. Puglia, E. A. Martinez, G. C. Ménard, A. Pöschl, S. Gronin, G. C. Gardner, R. Kallaher, M. J. Manfra, C. M. Marcus, A. P. Higginbotham, and L. Casparis, Closing of the induced gap in a hybrid superconductor-semiconductor nanowire, Phys. Rev. B **103**, 235201 (2021).

[56] P. Yu, J. Chen, M. Gomanko, G. Badawy, E. P. a. M. Bakkers, K. Zuo, V. Mourik, and S. M. Frolov, Non-Majorana states yield nearly quantized conductance in proximatized nanowires, Nature Physics **17**, 482 (2021).

[57] H. Zhang, M. W. A. de Moor, J. D. S. Bommer, D. Xu, G. Wang, N. van Loo, C.-X. Liu, S. Gazibegovic, J. A. Logan, D. Car, R. L. M. O. het Veld, P. J. van Veldhoven, S. Koelling, M. A. Verheijen, M. Pendharkar, D. J. Pennachio, B. Shojaei, J. S. Lee, C. J. Palmstrøm, E. P. A. M. Bakkers, S. D. Sarma, and L. P. Kouwenhoven, Large zero-bias peaks in InSb-Al hybrid semiconductor-superconductor nanowire devices, arXiv:2101.11456 (2021).

[58] H. Song, Z. Zhang, D. Pan, D. Liu, Z. Wang, Z. Cao, L. Liu, L. Wen, D. Liao, R. Zhuo, D. E. Liu, R. Shang, J. Zhao, and H. Zhang, Large zero bias peaks and dips in a four-terminal thin InAs-Al nanowire device, arXiv:2107.08282 (2021).

[59] A. Pöschl, A. Danilenko, D. Sabonis, K. Kristjuhan, T. Lindemann, C. Thomas, M. J. Manfra, and C. M. Marcus, Nonlocal signatures of hybridization between quantum dot and Andreev bound states, arXiv:2201.03687 (2022).

[60] A. Pöschl, A. Danilenko, D. Sabonis, K. Kristjuhan, T. Lindemann, C. Thomas, M. J. Manfra, and C. M. Marcus, Nonlocal conductance spectroscopy of Andreev bound states in gate-defined InAs/Al nanowires, arXiv:2204.02430 (2022).

[61] J.-Y. Wang, N. van Loo, G. P. Mazur, V. Levajac, F. K. Malinowski, M. Lemang, F. Borsoi, G. Badawy, S. Gazibegovic, E. P. A. M. Bakkers, M. Quintero-Perez, S. Heedt, and L. P. Kouwenhoven, Parametric exploration of zero-energy modes in three-terminal InSb-Al nanowire devices, arXiv:2203.00773 (2022).

[62] Z. Wang, H. Song, D. Pan, Z. Zhang, W. Miao, R. Li, Z. Cao, G. Zhang, L. Liu, L. Wen, R. Zhuo, D. E. Liu, K. He, R. Shang, J. Zhao, and H. Zhang, Observation of plateau regions for zero bias peaks within 5% of the quantized conductance value $2e^2/h$, arXiv:2205.06736 (2022).

[63] S. Das Sarma, J. D. Sau, and T. D. Stanescu, Splitting of the zero-bias conductance peak as smoking gun evidence for the existence of the Majorana mode in a superconductor-semiconductor nanowire, Phys. Rev. B **86**, 220506 (2012).

[64] H. Pan, C.-X. Liu, M. Wimmer, and S. Das Sarma, Quantized and unquantized zero-bias tunneling conductance peaks in Majorana nanowires: Conductance below and above $2e^2/h$, Phys. Rev. B **103**, 214502 (2021).

[65] T. Ö. Rosdahl, A. Vuik, M. Kjaergaard, and A. R. Akhmerov, Andreev rectifier: A non-local conductance signature of topological phase transitions, Phys. Rev. B **97**, 045421 (2018).

[66] Y.-H. Lai, J. D. Sau, and S. Das Sarma, Presence versus absence of end-to-end nonlocal conductance correlations in Majorana nanowires: Majorana bound states versus Andreev bound states, Phys. Rev. B **100**, 045302 (2019).

[67] H. Pan, J. D. Sau, and S. Das Sarma, Three-terminal nonlocal conductance in Majorana nanowires: Distinguishing topological and trivial in realistic systems with disorder and inhomogeneous potential, Phys. Rev. B **103**, 014513 (2021).

[68] G. Kells, D. Meidan, and P. W. Brouwer, Near-zero-energy end states in topologically trivial spin-orbit coupled superconducting nanowires with a smooth confinement, Phys. Rev. B **86**, 100503 (2012).

[69] D. Rainis, L. Trifunovic, J. Klinovaja, and D. Loss, Towards a realistic transport modeling in a superconducting nanowire with Majorana fermions, Phys. Rev. B **87**, 024515 (2013).

[70] J. Liu, A. C. Potter, K. T. Law, and P. A. Lee, Zero-Bias Peaks in the Tunneling Conductance of Spin-Orbit-Coupled Superconducting Wires with and without Majorana End-States, Phys. Rev. Lett. **109**, 267002 (2012).

[71] T. D. Stanescu and S. Tewari, Nonlocality of zero-bias anomalies in the topologically trivial phase of Majorana wires, Phys. Rev. B **89**, 220507 (2014).

[72] C.-X. Liu, J. D. Sau, T. D. Stanescu, and S. Das Sarma, Andreev bound states versus Majorana bound states in quantum dot-nanowire-superconductor hybrid structures: Trivial versus topological zero-bias conductance peaks, Phys. Rev. B **96**, 075161 (2017).

[73] C. Reeg, O. Dmytruk, D. Chevallier, D. Loss, and J. Klinovaja, Zero-energy Andreev bound states from quantum dots in proximitized Rashba nanowires, Phys. Rev. B **98**, 245407 (2018).

[74] W. DeGottardi, M. Thakurathi, S. Vishveshwara, and D. Sen, Majorana fermions in superconducting wires: Effects of long-range hopping, broken time-reversal symmetry, and potential landscapes, Phys. Rev. B **88**, 165111 (2013).

[75] C. Moore, T. D. Stanescu, and S. Tewari, Two-terminal charge tunneling: Disentangling Majorana zero modes from partially separated Andreev bound states in semiconductor-superconductor heterostructures, Phys. Rev. B **97**, 165302 (2018).

[76] C. Moore, C. Zeng, T. D. Stanescu, and S. Tewari, Quantized zero-bias conductance plateau in semiconductor-superconductor heterostructures without topological Majorana zero modes, Phys. Rev. B **98**, 155314 (2018).

[77] H. Pan and S. Das Sarma, Physical mechanisms for zero-bias conductance peaks in Majorana nanowires, Phys. Rev. Research **2**, 013377 (2020).

[78] T. D. Stanescu and S. Tewari, Robust low-energy Andreev bound states in semiconductor-superconductor structures: Importance of partial separation of component Majorana bound states, Phys. Rev. B **100**, 155429 (2019).

[79] D. Bagrets and A. Altland, Class D Spectral Peak in Majorana Quantum Wires, Phys. Rev. Lett. **109**, 227005 (2012).

[80] O. Motrunich, K. Damle, and D. A. Huse, Griffiths effects and quantum critical points in dirty superconductors without spin-rotation invariance: One-dimensional examples, Phys. Rev. B **63**, 224204 (2001).

[81] P. W. Brouwer, M. Duckheim, A. Romito, and F. von Oppen, Topological superconducting phases in disordered quantum wires with strong spin-orbit coupling, Phys. Rev. B **84**, 144526 (2011).

[82] P. W. Brouwer, M. Duckheim, A. Romito, and F. von Oppen, Probability Distribution of Majorana End-State Energies in Disordered Wires, Phys. Rev. Lett. **107**, 196804 (2011).

[83] A. R. Akhmerov, J. P. Dahlhaus, F. Hassler, M. Wimmer, and C. W. J. Beenakker, Quantized Conductance at the Majorana Phase Transition in a Disordered Superconducting Wire, Phys. Rev. Lett. **106**, 057001 (2011).

[84] C.-H. Lin, J. D. Sau, and S. Das Sarma, Zero-bias conductance peak in Majorana wires made of semiconductor/superconductor hybrid structures, Phys. Rev. B **86**, 224511 (2012).

[85] P. Neven, D. Bagrets, and A. Altland, Quasiclassical theory of disordered multi-channel Majorana quantum wires, New J. Phys. **15**, 055019 (2013).

[86] J. D. Sau and S. Das Sarma, Density of states of disordered topological superconductor-semiconductor hybrid nanowires, Phys. Rev. B **88**, 064506 (2013).

[87] W. DeGottardi, D. Sen, and S. Vishveshwara, Majorana Fermions in Superconducting 1D Systems Having Periodic, Quasiperiodic, and Disordered Potentials, Phys. Rev. Lett. **110**, 146404 (2013).

[88] D. Roy, N. Bondyopadhaya, and S. Tewari, Topologically trivial zero-bias conductance peak in semiconductor Majorana wires from boundary effects, Phys. Rev. B **88**, 020502 (2013).

[89] J. D. Sau and E. Demler, Bound states at impurities as a probe of topological superconductivity in nanowires, Phys. Rev. B **88**, 205402 (2013).

[90] İ. Adagideli, M. Wimmer, and A. Teker, Effects of electron scattering on the topological properties of nanowires: Majorana fermions from disorder and superlattices, Phys. Rev. B **89**, 144506 (2014).

[91] H.-Y. Hui, J. D. Sau, and S. Das Sarma, Bulk disorder in the superconductor affects proximity-induced topological superconductivity, Phys. Rev. B **92**, 174512 (2015).

[92] H. Pan and S. Das Sarma, Disorder effects on Majorana zero modes: Kitaev chain versus semiconductor nanowire, Phys. Rev. B **103**, 224505 (2021).

[93] H. Pan and S. Das Sarma, Crossover between trivial zero modes in Majorana nanowires, Phys. Rev. B **104**, 054510 (2021).

[94] S. Ahn, H. Pan, B. Woods, T. D. Stanescu, and S. Das Sarma, Estimating disorder and its adverse effects in semiconductor Majorana nanowires, Phys. Rev. Materials **5**, 124602 (2021).

[95] L. Lunczer, P. Leubner, M. Endres, V. L. Müller, C. Brüne, H. Buhmann, and L. W. Molenkamp, Approaching Quantization in Macroscopic Quantum Spin Hall Devices through Gate Training, Phys. Rev. Lett. **123**, 047701 (2019).

[96] Q. L. He, L. Pan, A. L. Stern, E. C. Burks, X. Che, G. Yin, J. Wang, B. Lian, Q. Zhou, E. S. Choi, K. Murata, X. Kou, Z. Chen, T. Nie, Q. Shao, Y. Fan, S.-C. Zhang, K. Liu, J. Xia, and K. L. Wang, Chiral Majorana fermion modes in a quantum anomalous Hall insulator–superconductor structure, Science **357**, 294 (2017).

[97] M. Kayyalha, D. Xiao, R. Zhang, J. Shin, J. Jiang, F. Wang, Y.-F. Zhao, R. Xiao, L. Zhang, K. M. Fijalkowski, P. Mandal, M. Winnerlein, C. Gould, Q. Li, L. W. Molenkamp, M. H. W. Chan, N. Samarth, and C.-Z. Chang, Absence of evidence for chiral Majorana modes in quantum anomalous Hall-superconductor devices, Science **367**, 64 (2020).

[98] S. Nadj-Perge, I. K. Drozdov, J. Li, H. Chen, S. Jeon, J. Seo, A. H. MacDonald, B. A. Bernevig, and A. Yazdani, Observation of Majorana fermions in ferromagnetic atomic chains on a superconductor, Science **346**, 602 (2014).

[99] J. D. Sau and P. M. R. Brydon, Bound States of a Ferromagnetic Wire in a Superconductor, Phys. Rev. Lett. **115**, 127003 (2015).

[100] M. Ruby, F. Pientka, Y. Peng, F. von Oppen, B. W. Heinrich, and K. J. Franke, End States and Subgap Structure in Proximity-Coupled Chains of Magnetic Adatoms, Phys. Rev. Lett. **115**, 197204 (2015).

[101] D. Wang, J. Wiebe, R. Zhong, G. Gu, and R. Wiesendanger, Spin-Polarized Yu-Shiba-Rusinov States in an Iron-Based Superconductor, Phys. Rev. Lett. **126**, 076802 (2021).

[102] C.-K. Chiu, J. D. Sau, and S. Das Sarma, Conductance of a superconducting Coulomb-blockaded Majorana nanowire, Phys. Rev. B **96**, 054504 (2017).

[103] Y.-H. Lai, S. Das Sarma, and J. D. Sau, Theory of Coulomb blockaded transport in realistic Majorana nanowires, Phys. Rev. B **104**, 085403 (2021).

[104] S. Takei, B. M. Fregoso, H.-Y. Hui, A. M. Lobos, and S. Das Sarma, Soft Superconducting Gap in Semiconductor Majorana Nanowires, Phys. Rev. Lett. **110**, 186803 (2013).

[105] T. D. Stanescu, R. M. Lutchyn, and S. Das Sarma, Soft superconducting gap in semiconductor-based Majorana nanowires, Phys. Rev. B **90**, 085302 (2014).

[106] D. I. Pikulin, J. P. Dahlhaus, M. Wimmer, H. Schomerus, and C. W. J. Beenakker, A zero-voltage conductance peak from weak antilocalization in a Majorana nanowire, New J. Phys. **14**, 125011 (2012).

[107] E. J. H. Lee, X. Jiang, R. Aguado, G. Katsaros, C. M. Lieber, and S. De Franceschi, Zero-Bias Anomaly in a Nanowire Quantum Dot Coupled to Superconductors, Phys. Rev. Lett. **109**, 186802 (2012).

[108] J. Cayao, E. Prada, P. San-Jose, and R. Aguado, SNS junctions in nanowires with spin-orbit coupling: Role of confinement and helicity on the subgap spectrum, Phys. Rev. B **91**, 024514 (2015).

[109] D. J. Clarke, Experimentally accessible topological quality factor for wires with zero energy modes, Phys. Rev. B **96**, 201109 (2017).

[110] C. Fleckenstein, F. Domínguez, N. Traverso Ziani, and B. Trauzettel, Decaying spectral oscillations in a Majorana wire with finite coherence length, Phys. Rev. B **97**, 155425 (2018).

[111] S. Mi, D. I. Pikulin, M. Marciani, and C. W. J. Beenakker, X-shaped and Y-shaped Andreev resonance profiles in a superconducting quantum dot, J. Exp. Theor. Phys. **119**, 1018 (2014).

[112] H. Pan, W. S. Cole, J. D. Sau, and S. Das Sarma, Generic quantized zero-bias conductance peaks in superconductor-semiconductor hybrid structures, Phys. Rev. B **101**, 024506 (2020).

[113] M. Wimmer, A. R. Akhmerov, J. P. Dahlhaus, and C. W. J. Beenakker, Quantum point contact as a probe of a topological superconductor, New J. Phys. **13**, 053016 (2011).

[114] I. C. Fulga, F. Hassler, A. R. Akhmerov, and C. W. J. Beenakker, Scattering formula for the topological quantum number of a disordered multimode wire, Phys. Rev. B **83**, 155429 (2011).

[115] E. Prada, P. San-Jose, and R. Aguado, Transport spectroscopy of NS nanowire junctions with Majorana fermions, Phys. Rev. B **86**, 180503 (2012).

[116] C.-X. Liu, J. D. Sau, and S. Das Sarma, Distinguishing topological Majorana bound states from trivial Andreev bound states: Proposed tests through differential tunneling conductance spectroscopy, Phys. Rev. B **97**, 214502 (2018).

[117] F. Peñaranda, R. Aguado, P. San-Jose, and E. Prada, Quantifying wave-function overlaps in inhomogeneous Majorana nanowires, Phys. Rev. B **98**, 235406 (2018).

[118] A. Vuik, B. Nijholt, A. Akhmerov, and M. Wimmer, Reproducing topological properties with quasi-Majorana states, SciPost Physics **7**, 061 (2019).

[119] T. D. Stanescu and S. Tewari, Majorana fermions in semiconductor nanowires: fundamentals, modeling, and experiment, Journal of Physics: Condensed Matter **25**, 233201 (2013).

[120] Y. A. Bychkov and E. I. Rashba, Oscillatory effects and the magnetic susceptibility of carriers in inversion layers, J. Phys. C: Solid State Phys. **17**, 6039 (1984).

[121] J. D. Sau, R. M. Lutchyn, S. Tewari, and S. Das Sarma, Robustness of Majorana fermions in proximity-induced superconductors, Phys. Rev. B **82**, 094522 (2010).

[122] R. M. Lutchyn, E. P. A. M. Bakkers, L. P. Kouwenhoven, P. Krogstrup, C. M. Marcus, and Y. Oreg, Majorana zero modes in superconductor–semiconductor heterostructures, Nature Reviews Materials **3**, 52 (2018).

[123] B. D. Woods, J. Chen, S. M. Frolov, and T. D. Stanescu, Zero-energy pinning of topologically trivial bound states in multiband semiconductor-superconductor nanowires, Phys. Rev. B **100**, 125407 (2019).

[124] S. Das Sarma, A. Nag, and J. D. Sau, How to infer non-Abelian statistics and topological visibility from tunneling conductance properties of realistic Majorana nanowires, Phys. Rev. B **94**, 035143 (2016).

[125] W. E. Arnoldi, The principle of minimized iterations in the solution of the matrix eigenvalue problem, Quarterly of applied mathematics **9**, 17 (1951).

[126] W. Chang, S. M. Albrecht, T. S. Jespersen, F. Kuemmeth, P. Krogstrup, J. Nygård, and C. M. Marcus, Hard gap in epitaxial semiconductor–superconductor nanowires, Nature Nanotechnology **10**, 232 (2015).

[127] P. Krogstrup, N. L. B. Ziino, W. Chang, S. M. Albrecht, M. H. Madsen, E. Johnson, J. Nygård, C. M. Marcus, and T. S. Jespersen, Epitaxy of semiconductor–superconductor nanowires, Nature Materials **14**, 400 (2015).

[128] C. Reeg and D. L. Maslov, Transport signatures of topological superconductivity in a proximity-coupled nanowire, Phys. Rev. B **95**, 205439 (2017).

[129] T. D. Stanescu and S. Das Sarma, Proximity-induced low-energy renormalization in hybrid semiconductor-superconductor Majorana structures, Phys. Rev. B **96**, 014510 (2017).

[130] H. Pan, J. D. Sau, T. D. Stanescu, and S. Das Sarma, Curvature of gap closing features and the extraction of Majorana nanowire parameters, Phys. Rev. B **99**, 054507 (2019).

[131] N. B. Kopnin and M. M. Salomaa, Mutual friction in superfluid ^{3}He: Effects of bound states in the vortex core, Phys. Rev. B **44**, 9667 (1991).

[132] T. M. Rice and M. Sigrist, Sr2RuO4: an electronic analogue of ^{3}He?, J. Phys.: Condens. Matter **7**, L643 (1995).

[133] S. Das Sarma, C. Nayak, and S. Tewari, Proposal to stabilize and detect half-quantum vortices in strontium ruthenate thin films: Non-Abelian braiding statistics of vortices in a $p_x + ip_y$ superconductor, Phys. Rev. B **73**, 220502 (2006).

[134] A. C. Potter and P. A. Lee, Engineering a $p + ip$ superconductor: Comparison of topological insulator and Rashba spin-orbit-coupled materials, Phys. Rev. B **83**, 184520 (2011).

[135] R. M. Lutchyn, T. D. Stanescu, and S. Das Sarma, Momentum relaxation in a semiconductor proximity-coupled to a disordered s-wave superconductor: Effect of scattering on topological superconductivity, Phys. Rev. B **85**, 140513 (2012).

[136] Y. Huang, H. Pan, C.-X. Liu, J. D. Sau, T. D. Stanescu, and S. Das Sarma, Metamorphosis of Andreev bound states into Majorana bound states in pristine nanowires, Phys. Rev. B **98**, 144511 (2018).

[137] F. Setiawan, C.-X. Liu, J. D. Sau, and S. Das Sarma, Electron temperature and tunnel coupling dependence of zero-bias and almost-zero-bias conductance peaks in Majorana nanowires, Phys. Rev. B **96**, 184520 (2017).

[138] C. W. Groth, M. Wimmer, A. R. Akhmerov, and X. Waintal, Kwant: a software package for quantum transport, New Journal of Physics **16**, 063065 (2014).

[139] C.-X. Liu, J. D. Sau, and S. Das Sarma, Role of dissipation in realistic Majorana nanowires, Phys. Rev. B **95**, 054502 (2017).

[140] G. E. Blonder, M. Tinkham, and T. M. Klapwijk, Transition from metallic to tunneling regimes in superconducting microconstrictions: Excess current, charge imbalance, and supercurrent conversion, Phys. Rev. B **25**, 4515 (1982).

[141] M. P. Anantram and S. Datta, Current fluctuations in mesoscopic systems with Andreev scattering, Phys. Rev. B **53**, 16390 (1996).

[142] F. Setiawan, P. M. R. Brydon, J. D. Sau, and S. Das Sarma, Conductance spectroscopy of topological superconductor wire junctions, Phys. Rev. B **91**, 214513 (2015).

[143] T. D. Stanescu, R. M. Lutchyn, and S. Das Sarma, Majorana fermions in semiconductor nanowires, Phys. Rev. B **84**, 144522 (2011).

[144] D. Roy, C. J. Bolech, and N. Shah, Majorana fermions in a topological superconducting wire out of equilibrium: Exact microscopic transport analysis of a p-wave open chain coupled to normal leads, Phys. Rev. B **86**, 094503 (2012).

[145] E. Dumitrescu, B. Roberts, S. Tewari, J. D. Sau, and S. Das Sarma, Majorana fermions in chiral topological ferromagnetic nanowires, Phys. Rev. B **91**, 094505 (2015).

[146] J. Stenger and T. D. Stanescu, Tunneling conductance in semiconductor-superconductor hybrid structures, Phys. Rev. B **96**, 214516 (2017).

[147] M. Büttiker, Scattering theory of current and intensity noise correlations in conductors and wave guides, Phys. Rev. B **46**, 12485 (1992).

[148] C.-X. Liu, F. Setiawan, J. D. Sau, and S. Das Sarma, Phenomenology of the soft gap, zero-bias peak, and zero-mode splitting in ideal Majorana nanowires, Phys. Rev. B **96**, 054520 (2017).

[149] C. W. J. Beenakker, Random-matrix theory of quantum transport, Rev. Mod. Phys. **69**, 731 (1997).

[150] T. Guhr, A. Müller–Groeling, and H. A. Weidenmüller, Random-matrix theories in quantum physics: common concepts, Physics Reports **299**, 189 (1998).

[151] P. W. Brouwer, K. M. Frahm, and C. W. J. Beenakker, Distribution of the quantum mechanical time-delay matrix for a chaotic cavity, Waves in Random Media **9**, 91 (1999).

[152] C. W. J. Beenakker, Random-matrix theory of Majorana fermions and topological superconductors, Rev. Mod. Phys. **87**, 1037 (2015).

[153] S. Datta, *Electronic Transport in Mesoscopic Systems*, Cambridge Studies in Semiconductor Physics and Microelectronic Engineering (Cambridge University Press, Cambridge, 1995).

[154] C. Beenakker, Search for Majorana Fermions in Superconductors, Annu. Rev. Condens. Matter Phys. **4**, 113 (2013).

[155] T. Senthil, J. B. Marston, and M. P. A. Fisher, Spin quantum Hall effect in unconventional superconductors, Phys. Rev. B **60**, 4245 (1999).

[156] T. Senthil and M. P. A. Fisher, Quasiparticle localization in superconductors with spin-orbit scattering, Phys. Rev. B **61**, 9690 (2000).

[157] F. Evers and A. D. Mirlin, Anderson transitions, Rev. Mod. Phys. **80**, 1355 (2008).

[158] P. W. Anderson, Absence of Diffusion in Certain Random Lattices, Phys. Rev. **109**, 1492 (1958).

[159] H. Zhang, C.-X. Liu, S. Gazibegovic, D. Xu, J. A. Logan, G. Wang, N. van Loo, J. D. S. Bommer, M. W. A. de Moor, D. Car, R. L. M. Op het Veld, P. J. van Veldhoven, S. Koelling, M. A. Verheijen, M. Pendharkar, D. J. Pennachio, B. Shojaei, J. S. Lee, C. J. Palmstrøm, E. P. A. M. Bakkers, S. Das Sarma, and L. P. Kouwenhoven, Retraction Note: Quantized Majorana conductance, Nature, 10.1038/s41586-021-03373-x (2021).

[160] Y.-J. Doh, J. A. van Dam, A. L. Roest, E. P. A. M. Bakkers, L. P. Kouwenhoven, and S. D. Franceschi, Tunable Supercurrent Through Semiconductor Nanowires, Science **309**, 272 (2005).

[161] A. M. Lobos, R. M. Lutchyn, and S. Das Sarma, Interplay of Disorder and Interaction in Majorana Quantum Wires, Phys. Rev. Lett. **109**, 146403 (2012).

[162] W. S. Cole, S. Das Sarma, and T. D. Stanescu, Effects of large induced superconducting gap on semiconductor Majorana nanowires, Phys. Rev. B **92**, 174511 (2015).

[163] J. D. Sau, S. Tewari, and S. Das Sarma, Experimental and materials considerations for the topological superconducting state in electron- and hole-doped semiconductors: Searching for non-Abelian Majorana modes in 1D nanowires and 2D heterostructures, Phys. Rev. B **85**, 064512 (2012).

[164] B. D. Woods and T. D. Stanescu, Enhanced topological protection in planar quasi-one-dimensional channels with periodically modulated width, Phys. Rev. B **101**, 195435 (2020).

[165] A. Altland and M. R. Zirnbauer, Nonstandard symmetry classes in mesoscopic normal-superconducting hybrid structures, Phys. Rev. B **55**, 1142 (1997).

[166] D. Wang, L. Kong, P. Fan, H. Chen, S. Zhu, W. Liu, L. Cao, Y. Sun, S. Du, J. Schneeloch, R. Zhong, G. Gu, L. Fu, H. Ding, and H.-J. Gao, Evidence for Majorana bound states in an iron-based superconductor, Science **362**, 333 (2018).

[167] S. Zhu, L. Kong, L. Cao, H. Chen, M. Papaj, S. Du, Y. Xing, W. Liu, D. Wang, C. Shen, F. Yang, J. Schneeloch, R. Zhong, G. Gu, L. Fu, Y.-Y. Zhang, H. Ding, and H.-J. Gao, Nearly quantized conductance plateau of vortex zero mode in an iron-based superconductor, Science, 10.1126/science.aax0274 (2019).

[168] B. D. Woods, S. Das Sarma, and T. D. Stanescu, Subband occupation in semiconductor-superconductor nanowires, Phys. Rev. B **101**, 045405 (2020).

[169] F.-M. Dittes, The decay of quantum systems with a small number of open channels, Physics Reports **339**, 215 (2000).

[170] C. Mahaux, *Shell-model approach to nuclear reactions.* (North-Holland Pub. Co., Amsterdam, London, 1969).

[171] T. J. Christiansen and M. Zworski, A mathematical formulation of the Mahaux–Weidenmüller formula for the scattering matrix, J. Phys. A: Math. Theor. **42**, 415202 (2009).

[172] M. Marciani, P. W. Brouwer, and C. W. J. Beenakker, Time-delay matrix, midgap spectral peak, and thermopower of an Andreev billiard, Phys. Rev. B **90**, 045403 (2014).

[173] D. I. Pikulin and Y. V. Nazarov, Two types of topological transitions in finite Majorana wires, Phys. Rev. B **87**, 235421 (2013).

[174] D. I. Pikulin and Y. V. Nazarov, Topological properties of superconducting junctions, Jetp Lett. **94**, 693 (2012).

[175] S. Ryu, A. P. Schnyder, A. Furusaki, and A. W. W. Ludwig, Topological insulators and superconductors: tenfold way and dimensional hierarchy, New J. Phys. **12**, 065010 (2010).

[176] M. Z. Hasan and C. L. Kane, Colloquium: Topological insulators, Rev. Mod. Phys. **82**, 3045 (2010).

[177] X.-L. Qi and S.-C. Zhang, Topological insulators and superconductors, Rev. Mod. Phys. **83**, 1057 (2011).

[178] H. Zhang, D. E. Liu, M. Wimmer, and L. P. Kouwenhoven, Next steps of quantum transport in Majorana nanowire devices, Nat Commun **10**, 1 (2019).

[179] J.-P. Xu, C. Liu, M.-X. Wang, J. Ge, Z.-L. Liu, X. Yang, Y. Chen, Y. Liu, Z.-A. Xu, C.-L. Gao, D. Qian, F.-C. Zhang, and J.-F. Jia, Artificial Topological Superconductor by the Proximity Effect, Phys. Rev. Lett. **112**, 217001 (2014).

[180] S. Das Sarma and H. Pan, Disorder-induced zero-bias peaks in Majorana nanowires, Phys. Rev. B **103**, 195158 (2021).

[181] H. Pan and S. Das Sarma, On-demand large conductance in trivial zero-bias tunneling peaks in Majorana nanowires, Phys. Rev. B **105**, 115432 (2022).

[182] H. Pan, J. D. Sau, and S. D. Sarma, A random matrix theory for the robustness, quantization, and end-to-end correlation of zero-bias conductance peaks in class D ensemble: Searching for Majorana zero modes in disordered quantum dots and wires, arXiv:2204.12505 (2022).